GEOLOGICA ULTRAIECTINA

Mededelingen van de
Faculteit Aardwetenschappen
Universiteit Utrecht

No. 142

Development of porphyroclast geometries during non-coaxial flow

An experimental and analytical investigation

Coen E. ten Brink

GEOLOGICA ULTRAIECTINA

Mededelingen van de
Faculteit Aardwetenschappen
Universiteit Utrecht

No. 142

Development of porphyroclast geometries during non-coaxial flow

An experimental and analytical investigation

Coen E. ten Brink

ISBN 90-71577-97-X

Cover: Photomicrograph of thin section. Quartz-feldspar-mica matrix, laden with quartz and feldspar porphyroclasts. It has a well defined foliation, and several indicators of sense of shear can be recognised: asymmetric extensional shear bands, antithetic microfaults in tiled grains, and σ- and δ-type porphyroclasts at early stages of development. Sense of shear was sinistral. Sardinia; plane light; total width of view is appr. 35 mm.

Development of porphyroclast geometries during non-coaxial flow

An experimental and analytical investigation

Ontwikkeling van porfieroklasten in niet-coaxiale vloeivelden

Een experimentele en analytische benadering
(met een samenvatting in het Nederlands)

Proefschrift

TER VERKRIJGING VAN DE GRAAD VAN DOCTOR AAN DE UNIVERSITEIT UTRECHT,

OP GEZAG VAN DE RECTOR MAGNIFICUS PROF. DR. J. A. VAN GINKEL,
INGEVOLGE HET BESLUIT VAN HET COLLEGE VAN DECANEN
IN HET OPENBAAR TE VERDEDIGEN OP

MAANDAG 23 SEPTEMBER 1996, DES NAMIDDAGS TE 12.45 UUR

door

Coen E. ten Brink

Geboren op 24 september 1961 te Amsterdam

PROMOTORES: PROF. DR. C. J. SPIERS,
FACULTEIT AARDWETENSCHAPPEN,
UNIVERSITEIT UTRECHT
PROF. DR. C. W. PASSCHIER,
INSTITUT FÜR GEOWISSENSCHAFTEN,
JOHANNES GUTENBERG-UNIVERSITÄT, MAINZ

Contents

Komm wir greifen nach den Sternen
Stück für Stück, nach und nach
Ich erzähl Dir mein Geheimnis
und auch mehr, wenn Du mich fragst

(Herbert Grönemeier-Grönland)

Samenvatting

Grofweg gezien is de aarde opgebouwd uit drie delen: de kern, de mantel en de korst. De buitenste 10 tot 70 kilometer van de aarde, de bovenmantel en de korst, bestaat uit relatief harde platen, die horizontaal ten opzichte van elkaar kunnen bewegen. Deze plaatbewegingen worden continentendrift genoemd en gaan gepaard met vervormingen in het materiaal waaruit de aardkorst en bovenmantel bestaat. De verschijnselen van deze deformatie in het gesteente vertonen een enorme variatie in afmetingen: van gebergtevorming tot slechts met een microscoop waarneembare vervormingen. De drie hoofdvormen van deformatie zijn: plooien, waarbij het materiaal min of meer plastisch is vervormd; breuken, waarbij twee massa's langs elkaar schuiven; en grootschalige opheffing of daling, waarbij het gesteente niet of nauwelijks vervormd raakt. Dit proefschrift gaat over verschijnselen die voorkomen bij verschuivingen langs breuken.

Ik wil hierbij benadrukken dat een geoloog een meer omvattende betekenis toekent aan het woord breuk dan gebruikelijk is. De meesten onder ons noemen een barst in een ruit een breuk, strikt geologisch gesproken is dat een 'diaklaas', zolang er geen verplaatsing langs de barst heeft plaatsgevonden. In sommige oude gebouwen (zoals enkele jaren geleden in café 'het Heen en Weer' aan het Wed te Utrecht) ziet men wel eens lakzegels op een barst in de muur. Deze zegels worden aangebracht om te zien of er, en zo ja wat voor, verplaatsingen langs de barst optreden (of de barst een breuk is of niet), zodat men de betrouwbaarheid van het gebouw kan beoordelen. De verplaatsing langs een barst kan zeer langzaam, of met horten en stoten gaan, net zoals bij breuken in natuurlijke gesteentes, en daardoor onwaarneembaar zijn op het moment dat er iemand naar kijkt, vandaar het lakzegel. Mocht er verschuiving optreden, dan is er meestal niet één scherp vlak waarlangs de verplaatsing optreedt, maar een (smalle) zone waarin de bakstenen en het cement verpulverd raken. Zulke gedeformeerde schuifzones kan men in natuurlijke gesteentes ook aantreffen. In tegenstelling tot de scheur in een muur kan in een natuurlijke schuifzone, door de verhoogde temperatuur en druk op grotere diepte, de aanwezige vloeistoffen of de zeer langzame verplaatsing, het materiaal zich plastich gedragen in plaats van breken. Als een gesteente niet homogeen van samenstelling is, kan het voorkomen dat sommige gesteente-mineralen zich plastisch gedragen in vergelijking tot de andere mineralen, die breken of slechts weinig deformeren, in dat geval is er sprake van een 'rheologie-verschil'.

Het kan van belang zijn om te weten wat de verplaatsing langs een schuifzone is geweest. Bijvoorbeeld om een economisch interessante laag of ertsader, gevonden aan de ene kant, aan de andere kant van de zone terug te vinden. Een geoloog heeft in het algemeen te maken met de situatie ná deformatie en omdat niemand in het (verre) verleden lakzegels heeft aangebracht in of aan de schuifzones die we tegenwoordig vinden, zal op een andere manier de verplaatsingen van die zones bepaald moeten worden. Het onderzoek hier beschreven is gericht op een fenomeen dat voorkomt in schuifzones, om te beoordelen of daarmee de richting en afstand van een verschuiving bepaald mogen en/of kunnen worden.

Een 'porfieroklast' in een gedeformeerd gesteente is een overblijfsel van een mineraal-korrel en onderscheidt zich van zijn directe omgeving (de 'matrix') door zijn grotere korrel-diameter. Porfieroklasten ontstaan door rheologie-verschillen in het gesteente gedurende deformatie; relatief harde mineralen vormen porfieroklasten terwijl relatief zachte mineralen de matrix vormen, de kleine korrel-diameter daarvan is meestal het gevolg van uitgebreide dynamische rekristallisatie. Mocht een relatief harde porfieroklast een vervormbare schil (mantel) hebben, dan

zal gedurende deformatie dit mantelmateriaal gemengd worden met de zachtere omgeving (matrix). De manier waarop het mantelmateriaal met de matrix wordt gemengd is het directe resultaat van het verplaatsingsveld of vloeipatroon in de directe omgeving van de harde porfieroklast-kern. De uiteindelijke vorm (of 'geometrie') van het kern-mantel-matrix systeem moet dus in relatie staan tot het vloeipatroon, ofwel de 'kinematiek', van de deformatie. Op dit moment worden porfieroklast-geometrieën gebruikt om de verplaatsingsrichting in schuifzones, met name in 'mylonieten' (erg gedeformeerde schuifzones), te bepalen. Van porfieroklast-geometrieën wordt gedacht dat ze mogelijk ook informatie kunnen verschaffen over materiaal eigenschappen van klast- en matrix-materiaal tijdens hun ontwikkeling. Wanneer de kinematische condities die leiden tot een bepaalde porfieroklast-geometrie bekend zijn, kan deze geometrie mogelijk gebruikt worden om de bewegings richting van de deformatie en de distributie van vervorming en vervormings-snelheid in de schuifzone te bepalen. De meest betrouwbare informatie wordt natuurlijk verkregen van geometrieën die onder unieke condities worden gevormd. In dit proefschrift wordt getracht een systematische basis te verkrijgen voor de kinematische interpretatie van porfieroklast-geometrieën, en dan voornamelijk die van kern-mantel-matrix systemen in 'metamorfe' schuifzones (die bij verhoogde temperatuur en/of druk, een verandering hebben ondergaan in structuur en/of samenstelling).

Een gedetailleerde bespreking van de onderhavige problemen wordt geïntroduceerd in Hoofdstuk 1 en het doel van het onderzoek wordt gedefinieerd.

Hoofstuk 2 rapporteert de ontwikkeling van sterk verlengde ofwel 'gevleugelde', δ-type porfieroklasten[1], experimenteel gemodelleerd in een doorzichtig, cirkelvormig, shuif-apparaat waarin kristallijne materialen werden gebruikt om een natuurlijk gesteente na te bootsen, namelijk kamfer objecten omgeven door een makkelijk deformeerbare octachloropropaan (OCP) matrix. De relatief harde, oorspronkelijk rechthoekige kamfer objecten vervormden tot δ-objecten gedurende voortgaande schuifbeweging. De ontwikkeling van deze δ-objecten, en het vloeipatroon in de omringende OCP-matrix, werden stapsgewijze gevolgd. De vleugels van de δ-objecten vertoonden een geometrie die niet eerder was waargenomen in experimenten met een Newtoniaanse vloeistof als matrix; de vleugels die aan beide kanten van de kern vormden vertoonden een 'traptrede', ze lagen niet in hetzelfde vlak. Bestudering van het verplaatsingsveld liet zien dat dit het gevolg was van een ongebruikelijk vloeipatroon (vlinderdas-vorm) rond de relatief harde kamfer objecten die langzamer roteerden dan gelijksoortige objecten in Newtoniaanse vloei. De niet-Newtoniaanse eigenschappen van de matrix zouden hiervan de oorzaak kunnen zijn. Dit impliceert dat niet-Newtoniaanse materialen beter zijn dan Newtoniaanse materialen, om de geometrieën in niet-Newtoniaans deformerende gesteentes te modelleren, omdat de uiteindelijke geometrie anders kan zijn. In een Addendum bij Hoofdstuk 2 worden de distributies van verplaatsing en verplaatsings-snelheid in een circulaire schuifzone en de daarmee samenhangende rotatiesnelheid van (bijna) onvervormbare objecten, uitvoerig besproken.

In Hoofstuk 3 worden materialen en methoden beschreven die mogelijk gebruikt kunnen worden om de invloed van materiaal-eigenschappen en grens-condities op het vloeigedrag in een klast-matrix systeem te testen. De materiaal eigenschappen van glycerol en een zeer verdunde (0,5 massa%) pAA-oplossing werden vastgesteld. Bevestigd is dat glycerol een New-

[1] de porfieroklast-geometrie typen worden genoemd naar de vorm van de vleugels in een bepaalde doorsnede. De vleugel aan een zijde van de kern van het δ-type lijkt op de Griekse letter δ, de vleugel aan de andere kant is een puntspiegeling in het kern-centrum. Er bestaan tevens σ-, ϕ- en θ-type geometrieën.

toniaans gedrag vertoont bij kamertemperatuur en schuifsnelheden tussen $4 \cdot 10^{-2}$ to 10^{+2} s^{-1}. De pAA-oplossing vertoont een niet-lineair verband tussen shuifspanning (τ) en schuifsnelheid ($\dot{\gamma}$) dat kan worden beschreven in de vorm $\dot{\gamma} = k \cdot \tau^n$ (k is een constante), waar bij 25°C, de exponent (n) oploopt van 1,5 tot 2,8 bij schuifsnelheden van $6 \cdot 10^{-2}$ tot 10^{+2} s^{-1}. Tevens worden de experimentele opzet en de methoden om vloeipatroon en object-rotatiesnelheid te bepalen, die worden gebruikt in het volgende Hoofdstuk (Hst. 4), uitgelegd.

In Hoofdstuk 4 wordt het onderzoek beschreven naar de invloed van de materiaal-eigenschappen en de grens-condities op het vloeipatroon rond, en het rotatie-gedrag van, de objecten gedurende een opgelegde schuifbeweging. Experimenten werden uitgevoerd met ongehinderd drijvende en onvervormbare objecten in glycerol en pAA-oplossing. Deze experimenten demonstreerden dat de, door vloeistof omgeven, objecten allemaal roteren wanneer een schuifbeweging wordt opgelegd aan de vloeistof. In glycerol kan de rotatiesnelheid van de objecten beschreven worden met de bestaande theorieën voor elliptische deeltjes in een Newtoniaanse vloeistof. Als de schuifzone breed is in vergelijking tot de diameter van het object, vertoont het vloeipatroon in glycerol een oog-vormige geometrie die overeenkomstig is met de theorie wanneer de schuifbeweging op oneindig grote afstand wordt opgelegd. Als de schuifzone smal is vertoont het vloeipatroon een vlinderdas geometrie. De rotatiesnelheid van de objecten in de pAA-oplossing is sterk gereduceerd ten opzichte van die in glycerol wanneer de schuifsnelheid groot is, en weinig gereduceerd als de schuifsnelheid klein is. Het vloeipatroon in de pAA-oplossing heeft altijd een vlinderdas geometrie, zelfs bij een zeer brede schuifzone. De analytische oplossing voor vloei rond een afgeremde cylinder werd in de pAA-oplossing, waar een gereduceerde rotatiesnelheid in combinatie met een vlinderdas vloeipatroon werd gevonden, sterk benaderd. Met deze experimenten wordt daarom aangetoont dat, onder bepaalde omstandigheden, vloei in een natuurlijke omgeving kan worden gesimuleerd met de analytische oplossing voor het verplaatsingsveld.

In Hoofstuk 5 wordt het onderzoek gepresenteerd dat werd uitgevoerd om de materiaal-eigenschap te isoleren die verantwoordelijk is voor de gereduceerde rotatiesnelheid van de objecten in de pAA-oplossing en zorgt voor het ontstaan van een vlinderdas-vloeipatroon, zelfs wanneer de schuifzone breed is. De gevolgde methode omvat het in kaart brengen van vloeipatronen met behulp van zowel de analytische stroom-functie, alsook de eindige elementen methode. Tevens werden de factoren, die de uiteindelijke geometrie van een porfieroklast kern-mantel-systeem veroorzaken, systematisch onderzocht. De studie met gebruik van de stroomfunctie laat zien dat wanneer de schuifbeweging op oneindige afstand wordt opgelegd, het vloeipatroon rond een vrij-draaiende cylinder een oog-vormige geometrie heeft. Wanneer de rotatie wordt belemmerd ontstaat er een vlinderdas geometrie. De eindige elementen methode (FEM) werd toegepast om smalle en oneindig brede schuifzones te simuleren. Dit werd gedaan voor Newtoniaanse matrix materialen en voor matrix materialen waarin de schuifsnelheid exponentieel toeneemt met schuifspanning ($\dot{\gamma} = k \cdot \tau^n$; $n>1$, n onafhankelijk van $\dot{\gamma}$). De FEM resultaten laten zien dat het vloeipatroon in een exponentieel matrix materiaal erg weinig verschilt van dat in een Newtoniaans materiaal. Hieruit wordt afgeleid dat een anisotropie-ontwikkeling[2] in de pAA-oplossing verantwoordelijk is voor de in Hoofdstuk 4 beschreven gereduceerde object-rotatiesnelheid en het afwijkende vloeipatroon waneer de schuifzone breed is. De FEM simulaties laten ook zien dat een versmalling van de schuifzone ervoor zorgt dat het vloeipatroon in de

[2] anisotropie wil zeggen dat materiaal-eigenschappen afhankelijk zijn van de richting waarin ze gemeten worden. Bijvoorbeeld: het kost weinig moeite om de losse vellen papier van een stapel over elkaar te schuiven terwijl je er niet inzakt als je erop gaat staan.

matrix van een oog-vormige naar een vlinderdas geometrie veranderd. Als laatste wordt het verplaatsingsveld, afgeleid van de betreffende stroom-functie, gebruikt om te modelleren hoe de vorm van een passieve mantel[3] rond een onvervormbare cylinder ontwikkeld, wanneer aan de matrix een schuifbeweging wordt opgelegd. Hiermee wordt aangetoond dat de primaire factor die de geometrie van de evoluerende mantel bepaalt, de vorm van de mantel is ten opzichte van het oppervlak dat het gebied nabij de kern met gesloten vloeipaden begrenst (waar materiaal weer naar zijn oorspronkelijke positie kan terugkeren). Wanneer een porfieroklast-kern rekristalliseert tijdens deformatie, is dit tevens direct afhankelijk van de snelheid waarmee kern-materiaal wordt omgezet in mantel-materiaal. De resultaten laten tevens zien dat een mantel geometrie sterk afhankelijk is van de hoeveelheid schuifbeweging van de matrix. Een porfieroklast kan evolueren van het ene type naar een ander met toenemende deformatie; bijvoorbeeld van een θ-, via een ϕ- en een σ-, naar een δ-type geometrie. Een gereduceerde rotatiesnelheid van de kern kan mogelijk voorkomen dat bepaalde geometrie-typen niet kunnen ontstaan.

De relatie tussen de resultaten van Hoofdstuk 2 tot en met 5 word besproken in Hoofdstuk 6. Dit leidt tot de conclusie dat voornamelijk δ-type en in mindere mate ook σ-type porfieroklast-geometrieën gebruikt kunnen worden als betrouwbare elementen om de schuifrichting te bepalen. De δ- en σ-typen kunnen ook toegepast kunnen worden om een minimum hoeveelheid verschuiving te schatten die de matrix in de directe nabijheid van de kern heeft ondergaan. Geologisch relevant is verder dat wanneer de vleugels van een δ-klast een trap-trede vertonen, dit diagnostisch is voor een vlinderdas vloeipatroon gedurende de deformatie. Het vlinderdas vloeipatroon duidt ofwel op een anisotropisch gedrag van het matrix-materiaal, ofwel op een breedte van de schuifzone die kleiner is dan ongeveer 20 maal de diameter van de porfieroklast-kern. De trap-trede van de vleugels van een δ-object kunnen niet gebruikt worden om de materiaal eigenschappen van de matrix gedurende deformatie te bepalen, omdat het vlinderdas vloeipatroon wordt gevonden in Newtoniaanse, exponentiële en anisotrope materialen. De ontwikkeling van anisotropie in de matrix heeft een grote invloed op het vloeipatroon rond en de rotatiesnelheid van de kern, en zodoende op de geometrie-ontwikkeling van een vervormbare mantel. Een zwaarwegende conclusie is echter dat de ontwikkeling van een porfieroklast geometrie uiterst complex is en dat in vele gevallen de uiteindelijke geometrie niet eenduidig is. Resterende vragen en suggesties voor toekomstig onderzoek beëindigen het laatste Hoofdstuk van dit proefschrift.

[3] passief betekent in dit geval dat de mantel dezelfde materiaal-eigenschappen heeft als de matrix.

Summary

A porphyroclast is a remnant of a resistant mineral grain, preserved in a deformed rock, which is of a size larger than the grains in the surrounding matrix. Porphyroclasts develop because of a difference in rheology between constituent minerals during deformation; relatively hard minerals tend to form porphyroclasts while relatively soft minerals form the matrix, the finer grain size generally reflecting extensive dynamic recrystallisation. This thesis is concerned with establishing a systematic basis for the kinematic interpretation of porphyroclast microstructures, and in particular mantled porphyroclasts, developed in deformed metamorphic rocks. Provided that a deformable mantle exists at the periphery of a relatively rigid porphyroclast, the final geometry of a core-mantle-matrix system is a direct result of the flow pattern, or velocity distribution, in the immediate vicinity of the core. Porphyroclast geometries therefore in some way reflect the kinematics or pattern of flow. These relatively rigid objects and associated features are widely used as shear sense indicators, particularly in mylonites, and may also hold information on the rheology of the clast and surrounding material during the time of their development. When the kinematic conditions or flow geometry that lead to the development of a particular microstructure are known, the microstructural feature in question can potentially be used to define the sense of shear and the distribution of strain and strain rate. Accordingly, the most reliable information is obtained from microstructures that develop under unique conditions.

In Chapter 1, the problems addressed in this thesis are introduced in detail, and the aims of the present study are identified.

Chapter 2 reports the development of strongly extended or 'winged', δ-type porphyroclasts modelled experimentally in a transparent circular shear rig using crystalline rock analogue materials, namely camphor objects embedded in an easily deformable octachloropropane (OCP) matrix. The relatively rigid, rectangular camphor objects deformed into δ-objects with progressive deformation up to a shear strain of 100. The development of these δ-objects, and of the flow field in the OCP matrix, was followed from step to step during the deformation. The δ-objects that developed showed stair-stepping of wings not observed in previous experiments with Newtonian fluids. Analysis of the flow pattern indicates that this is due to an unusual flow pattern geometry (bow-tie shaped) around the relatively rigid camphor objects, which rotated more slowly than equivalent objects in Newtonian flow. The non-Newtonian (power-law) rheology of the experimental materials may be responsible for this discrepancy. The implication is that non-Newtonian materials are better analogues than Newtonian materials to study the development of structures in rocks with non-Newtonian rheology, since the geometry of the resulting structures can be very different. In an addendum to Chapter 2, the complicated distribution of shear strain rate associated with a circular shear zone, and the possible influence of this on the rotation rates of rigid (or nearly rigid) objects is discussed in detail.

Chapter 3 outlines potential materials and methods that can be used to test the effects of material properties and boundary conditions on flow behaviour in a clast-matrix model system. The rheological properties of glycerol and a dilute (0.5%wt) pAA-solution were established. It is confirmed that glycerol has Newtonian behaviour at room temperature and shear stain rates ranging from $4 \cdot 10^{-2}$ to 10^{+2} s^{-1}. The pAA-solution has a shear-thinning behaviour with a stress vs. strain rate relation that can be described by a relation of the form $\dot{\gamma} = k \cdot \tau^n$, where, at 25°C,

the power-law exponent (n) increases from 1.5 to 2.8, in the range of shear strain rates from $6 \cdot 10^{-2}$ to 10^{2} s^{-1}. Furthermore, the experimental set-up, and methods used to determine flow-pattern and object rotation rate, used in the subsequent Chapter (Ch. 4), are described.

Chapter 4 reports an investigation of the effects of matrix material properties and boundary conditions on the flow pattern around, and rotational behaviour of, rigid objects that are subjected to bulk simple shear. Shear experiments were performed with rigid objects embedded in glycerol and pAA-solution. The experiments all demonstrated that embedded objects rotate when shear deformation is imposed on the fluids. In glycerol, the rotation rate of the objects is described by existing theory for ellipsoidal particles in a Newtonian fluid. When the shear zone is wide with respect to the object-diameter, the flow pattern in glycerol shows an eye-shaped geometry that is also consistent with theory for flow in simple shear imposed at infinity. When the shear zone is narrow, the flow pattern has a bow-tie geometry. In the pAA-solution, the rotation rate of the objects, relative to that in a Newtonian fluid, is strongly reduced when the shear strain rate is increased, and modestly reduced when the shear zone width or the temperature is reduced. In the pAA solution, the flow pattern always has a bow-tie geometry. The analytical solution for the flow around a retarded cylinder was closely approximated in experiments with pAA where the bow-tie flow pattern was reported in combination with a reduced rotation rate of the object. It is therefore shown that, under certain conditions, the analytical solution for the velocity field can simulate flow in natural environments.

Chapter 5 documents research performed to isolate the material property that causes objects to rotate at a reduced rate in the pAA-solution, as well as bringing about the associated bow-tie flow pattern observed even in wide shear zones. The approach followed involved mapping out flow patterns using both analytical stream function, and finite element modelling methods. Furthermore, the factors that determine the final geometry of porphyroclast core-mantle structures are systematically investigated. The stream function work shows that in simple shear flow, imposed at infinity, around a free rotating cylinder, the flow pattern has an eye-shaped geometry. When the rotation rate of the cylinder is retarded, a bow-tie flow pattern results. Finite element modelling (FEM) is performed to simulate narrow and infinitely wide shear zones. This is done for Newtonian matrix materials and matrix materials that have a power-law stress vs. strain rate behaviour with a strain rate independent power-law exponent (n). The FEM results show that flow pattern and object rotation in a (constant n) power-law matrix is nearly equivalent to that in a Newtonian matrix. From these findings, it is inferred that anisotropy development in the pAA-solution is responsible for the reduced rotation rate of embedded objects, and the change in flow pattern in the wide shear zone, as was reported in Chapter 4. The FEM results also confirms that closing in of rigid shear zone walls, causes the flow pattern in the matrix to shift from an eye-shaped to a bow-tie geometry. Finally, the velocity field obtained from the appropriate stream function is used to model the development of passive mantles around rigid cylinders subjected to bulk simple shear. The results show that the most important factor determining the developing mantle geometry is the shape of the mantle with respect to the surface that bounds the region near the core where flow is closed, i.e., where material can return eventually to its initial position. In the case of recrystallising or deteriorating porphyroclasts, this is directly related to the rate at which core material is transformed into mantle material. Secondly, the results show significant changes in mantle geometry with progressive shear strain. Thus, with increasing deformation, the mantle geometry can evolve from one type to another, e.g., from a θ- to a ϕ- to a σ- to a δ-type geometry. Furthermore, a low rotation rate of the core may prevent the development of certain of these geometry-types.

A synthesis of the results of Chapter 2 to 5 is given in Chapter 6. It culminates in the conclusion that in particular δ-type, but also σ-type, porphyroclast geometries offer reliable sense of shear indications, and may be used to estimate a minimum amount of accumulated shear strain in the adjacent matrix material. Other geologically relevant conclusions are that stair stepping of the wings of a δ-clast is diagnostic for a bow-tie flow pattern during deformation. The bow-tie flow pattern indicates either anisotropic behaviour of the matrix or a width of the shear zone that is less than approximately 20 times the diameter of the clast-core. Stair stepping of the wings of a δ-clast is not a gauge of rock rheology since a bow-tie flow pattern can develop in Newtonian, power-law, and anisotropic materials. The development of anisotropy in the deforming matrix has a large effect on the flow pattern around and the rotation rate of the core, and accordingly, on the geometry development of a deformable mantle. A final, inescapable conclusion, however, is that mantle geometry development is complex, and in many cases the final shape is ambiguous. Questions that remain unanswered and suggestions for future research complete the final Chapter of this thesis.

"Zie je, dit is nu het soort dingen waar ik achter moet zien te komen.
Misschien schrijf ik er wel eens een dissertatie over. ...
Pieren bouwen, wegen aanleggen en vissen is goed voor
gewone stervelingen die zich niet bekommeren om de grote samenhang."

(Tove Jansson-Pappa Moem en de mysteriën der zee)

Chapter 1

Definition of problems and aims

1.1 Introduction

Microstructural features preserved in ductily deformed rock form a source of information which can potentially be used to reconstruct the deformation history of the rock. Such features include grain shape fabric (foliation and lineation), crystallographic preferred orientation, grain size distribution, subgrain structures, dislocation structures, deformation lamellae, porphyroblasts, porphyroclasts, fibres, strain shadows, micro-boudins and micro-folding. On the basis of experimental studies on both metals and rocks (see reviews by Schmid 1982 and Knipe 1989), some of these features are known to record information about deformation mechanisms and rheological behaviour (reaction to stress), while others contain information on the geometry of ductile flow (kinematics).

In particular, the mechanical (or rheological) behaviour of rocks and rock-forming minerals has been studied extensively over the last decades. Stress vs. strain and stress vs. strain rate relations have been obtained on the flow-behaviour of rocks and numerous quantitative mechanism-based (or microphysically-based) models describing the rheologies of different rock materials are now at hand (see reviews by Kirby and Kronenberg 1987, Carter and Tseun 1987, Kohlstedt *et al.* 1995). These studies have also yielded valuable information on the dependence of stress-sensitive microstructural features such as dislocation density (Kohlstedt and Weathers 1980, Tullis and Yund 1987, Hirth and Tullis 1992), subgrain size and dynamically recrystallised grain size (Mercier *et al.* 1977, White 1979, Ross *et al.* 1980, Schmid *et al.* 1980, Karato 1984, Twiss 1986, Derby 1990, Michibayashi 1993) on imposed flow stress. Coupling rheological laws with paleo-stress determinations based on such features provides useful constraints for interpreting and modelling rock deformation behaviour.

In contrast, quantitative kinematic investigations are relatively new and focus on strain related aspects of grain shape and orientation (Wenk *et al.* 1987, Erskine *et al.* 1993), fibre-growth (Etchecopar and Malavieille 1987, Urai *et al.* 1991), foliation development, inclusion trails in rotated porphyroblasts (Rosenfeld 1970, Schoneveld 1977, Bell 1985, Bell *et al.* 1986, Bell and Johnson 1989, Passchier and Speck 1994, Gray and Busa 1994), and porphyroclasts (Passchier and Simpson 1986, Passchier 1987b, 1994, Passchier and Sokoutis 1993). A comprehensive and up-to-date review of these investigations is found in Passchier and Trouw (1996). These kinematic studies are done to establish the relationship between the geometry of flow (i.e., displacement or velocity field) within a volume of rock and the (micro)structures that develop as a result. When the kinematic conditions or flow geometry that lead to the development of a particular microstructure are known, the microstructural feature in question can potentially be used to define the sense of shear and the distribution of strain and strain rate. Accordingly, the most reliable information is obtained from microstructures that develop under unique conditions.

This thesis is concerned with establishing a systematic basis for the kinematic interpretation of porphyroclast microstructures, and in particular mantled porphyroclasts developed in deformed metamorphic rocks. These relatively rigid objects and associated features are widely used as shear sense indicators, particularly in mylonites (Hanmer and Passchier 1991 and refer-

ences therein), and may also hold information on the rheology of the clast and surrounding material during the time of their development (Passchier *et al.* 1993).

1.2 Previous work on porphyroclasts

1.2.1 General aspects and terminology

A porphyroclast is a remnant of a resistant mineral grain, preserved in a deformed rock, which is of a size larger than the grains in the surrounding matrix. Porphyroclasts, or simply 'clasts', develop because of a difference in rheology between constituent minerals during deformation; relatively hard (or competent) minerals tend to form porphyroclasts while relatively soft (or less competent) minerals form the matrix, the finer grain size generally reflecting extensive dynamic recrystallisation. Typical examples are large single crystals of feldspar in quartz mylonites and of pyroxene clasts in peridotite mylonites (Tullis and Yund 1985, Passchier and Simpson 1986, Hooper and Hatcher 1988, Vissers *et al.* 1991). Clasts show less internal deformation than the matrix and often display a rim or mantle of recrystallised core material with smaller grain size, or material resulting from reaction at the rim with the matrix due to changing pressure, temperature or chemical conditions (i.e., polycrystalline feldspar, quartz-mica or quartzo-feldspatic aggregates, Hanmer and Passchier 1991).

During deformation, the rim-material around porphyroclasts can be drawn out into the matrix, thus forming a core-mantle geometry which, in some way, reflects the deformation field. Several types of such geometry have been distinguished in natural rocks. Shapes described so far are the θ, ϕ, σ and δ types, thus termed since the outline of the mantle material in a specific orientation resembles the corresponding Greek symbol. The reference orientation is the xz-plane through the centre of the object, that is the section that contains the maximum and minimum principal finite extensions (Passchier 1994). In a deformed rock, this will be the plane perpendicular to the foliation and parallel to the stretching lineation (fig. 1.1a). In this section, the θ-type geometry (Hooper and Hatcher 1988) has a simple spherical or elliptical cross-section and no large extensions or wings are found around the core (fig. 1.1b). The ϕ-type (Passchier and Simpson 1986, Passchier 1994) shows elongated extensions of mantle material, from now on called wings (fig. 1.1c). These wings are symmetrically arranged on two sides of the core. Both θ- and ϕ-types have an orthorhombic symmetry. Characteristic of the σ-type geometry (Simpson and Schmid 1983, Passchier and Simpson 1986) is the triangular or wedge shaped form of the mantle material at two opposite sides of the core which show a 'stair-stepping' effect (Lister and Snoke 1984, fig. 1.1d). Stair stepping of wings means that mantle extensions on either side of the clast do not share the same plane. Passchier and Simpson (1986) made a distinction between σ_a- and σ_b-type porphyroclasts. The σ_a-description was used for isolated σ-clasts in a relatively homogeneously deformed matrix, and the σ_b-description for geometries found in S-C mylonites (Lister and Snoke 1984), i.e. in mylonites characterised by a shape or mineral foliation (S-planes) cut by relatively straight shear band cleavages (C- or C'-planes) (fig. 1.1d). C-planes are the narrow zones of high shear strain and are thought to develop parallel to the shear zone walls, C'-planes are curved and anastomosing and inclined to the shear

Figure 1.1 (next page). Schematic representation of **(a)** the presently chosen reference frame with respect to a deformed rock and **(b-f)** the most common types of deformed mantled porphyroclasts as seen in cross-sections on the observation surface (modified from Passchier 1994, and Passchier and Simpson 1986).

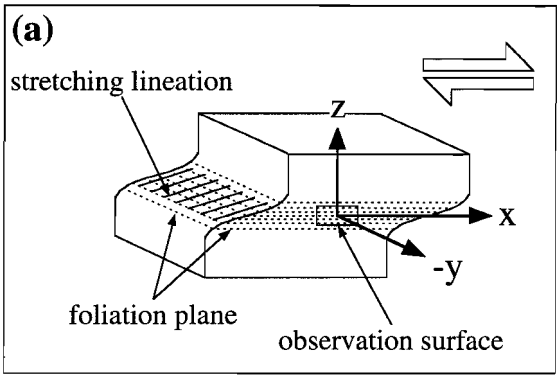

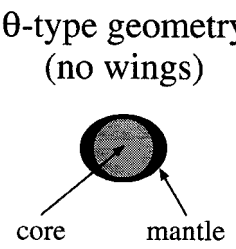

Winged objects

no stair-stepping

stair-stepping

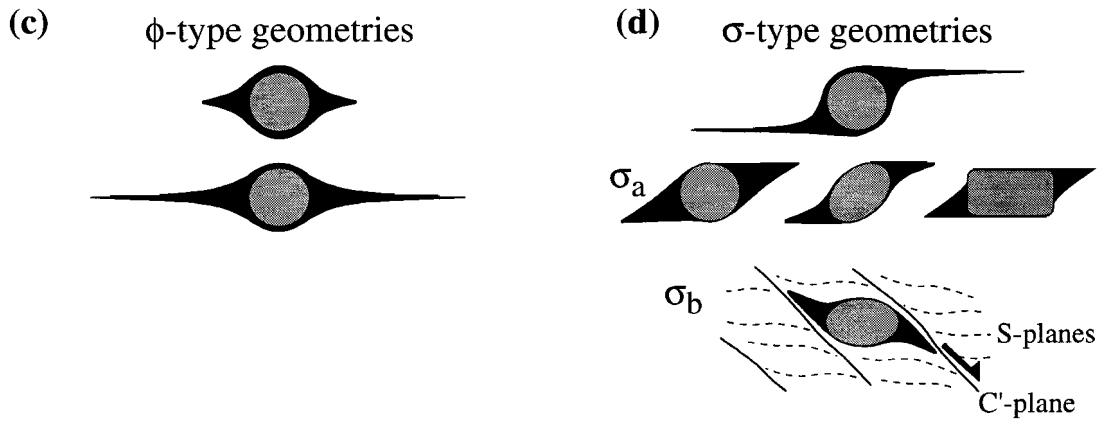

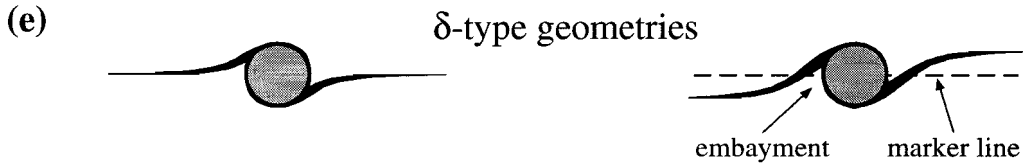

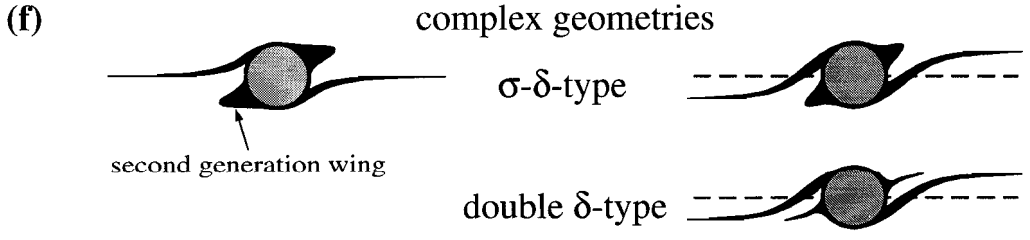

zone boundaries. The σ_b-type has relatively short wings with wing-extremes bending towards the direction of the C-planes. Typical of the δ-clast (Passchier and Simpson 1986) are the triangular embayments of matrix material located between the core and the wings (fig.1.1e). The wings of a δ-clast do not show the wedged shape close to the clast core as do the σ-types. Well-developed wings of a δ-clast thus make two distinct bends before they straighten out away from the core. The wings on either side of the clast may share the same plane but can also be found to show stair-stepping. Both σ- and δ-types have a monoclinic symmetry. Not surprisingly, some porphyroclasts show a mixed character or more than one set of extensions. The latter are called complex systems (Passchier and Simpson 1986, fig. 1.1f). In general, the best developed wings of a complex system are of the δ-type while the less developed extensions (also called second generation wings) are triangular and thus similar to partly developed σ-type wings. Double δ-wings can also be found (fig. 1.1f). Frequently, deformation of natural rocks is so extreme that the porphyroclast geometry is not preserved intact.

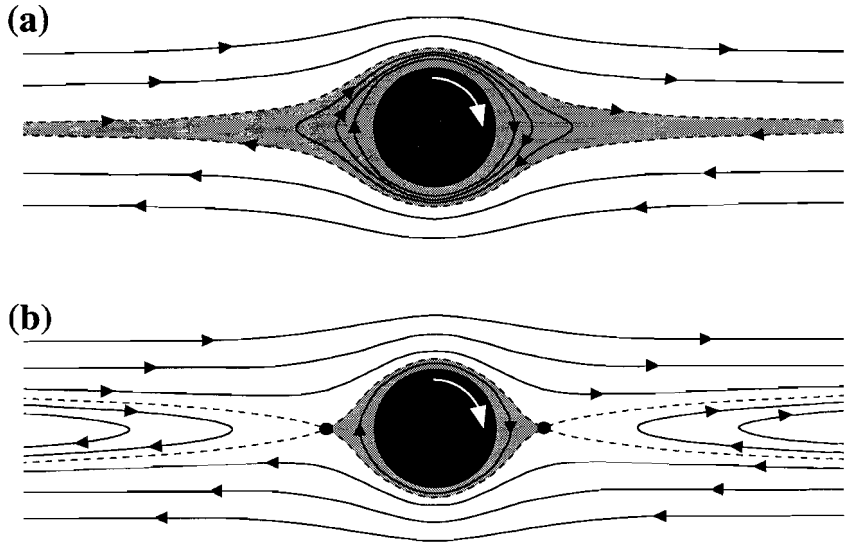

Figure 1.2. Schematic representation of (**a**) an 'eye-shaped', and (**b**) a 'bow-tie-shaped' flow geometry. Black circle: rigid object, dashed lines: separatrices, continuous lines: stream lines, heavy dots: stagnation points, shaded area: region with closed stream lines. The theoretical 'eye-shaped' flow pattern shown in (a) has stagnation points at infinite horizontal distance from the centre of the object.

As already mentioned, core-mantle geometry in some way must reflect the flow field in the deformed rock. On the basis of theoretical and experimental studies of flow around rigid objects, a θ-geometry is thought to reflect either a high effective viscosity of the clast and consequently a very thin or absent mantle (Passchier and Sokoutis 1993) or a small amount of accumulated strain. The φ-geometry is believed to indicate non-coaxial (simple shear) flow around a core with a wide mantle, or flow with a large coaxial component (intermediate to pure shear) (Passchier 1994). The σ-geometry is assumed to result from (approximately) simple shear flow with either an eye-shaped flow pattern (fig. 1.2a) around a 'free floating' core with a relatively wide mantle, or rapidly recrystallising core (Passchier 1994, Passchier and Simpson 1986) or from a mantle around a 'decoupled' core with a high strain rate gradient across the

core-mantle boundary (Bjørnerud and Zhang 1995). The δ-type geometry is thought to reflect rotation of the core with respect to the matrix, therefore indicating non-coaxial flow and a coherent ('well-coupled', 'non-slipping') core-mantle boundary. Presumed constraints on the development of the δ-type geometry are further: the mantle is pre-existing and had an initially elliptical shape; the core is not or very slowly recrystallising to form mantle material; the mantle material has a viscosity close to that of the matrix; and accumulated shear strain must be high (Passchier and Simpson 1986, Passchier and Sokoutis 1993, Ildefonse and Mancktelow 1993, Passchier 1994, Bjørnerud and Zhang 1995). Complex porphyroclast geometries are presumed to reflect periodic recrystallisation of the core. Such periodic mantle production could result from a pulsating rotation rate that is associated with a non-equidimensional core, fluctuations in shear strain rate, or changes in metamorphic conditions (Passchier and Simpson 1986).

Because of their inferred non-coaxial flow history, the two monoclinic types of mantle geometries, σ and δ, are currently used as kinematic indicators, specifically to determine the direction of shear in shear zones. Their use as a shear-sense indicator is supported by other micro structural evidence, i.e., they are usually consistent with the movement direction inferred from microfolds, S-C foliation, refracted or off-set veins, pressure-shadows and -fringes, quarter-, tiling- and domino-structures and/or asymmetric extensional shear bands. In addition, the δ-type geometry is thought to record information on the rheology during deformation; Passchier *et al.* (1993) suggested that stair-stepping of the wings is characteristic for non-linear (or power-law) stress vs. strain rate behaviour of the matrix during deformation, correspondingly, the absence of stair-stepping will be typical for materials deforming with a linear stress vs. strain rate (or Newtonian) behaviour.

Investigation to the rotational behaviour of porphyroblasts has lead to the argument that these do not rotate during non-coaxial deformation (Bell 1985, Bell *et al.* 1986; 1989; 1992a; 1992b, Bell and Johnson 1989; 1992, Bell and Hayward 1991). A porphyroblast is a large single crystal, inferred to have grown in a solidified rock in response to changes in metamorphic conditions. Although the development of (shrinking) porphyroclasts is the counterpart of the development of (growing) porphyroblasts, both represent relatively rigid objects in a, less competent, deforming environment. Therefore, the rotational behaviour of these objects may be comparable. The controversy between non-rotating blasts and and rotating clasts has recently been reason for a heated discussion in the literature (Bell *et al.* 1992a; 1992b; 1992c, Passchier *et al.* 1992, Wallis 1992).

1.2.2 Previous theoretical and numerical work

Flow around rigid objects

Theoretical work on the kinematics of clasts follows fluid mechanics studies of the flow behaviour of fluids around obstacles, such as a river flowing around the pillars of a bridge. These studies were extended to slow Stokes (laminar) flow around buoyant objects. Buoyant objects in this sense neither float nor sink.

Jeffery (1922) theoretically investigated the motion of ellipsoidal particles immersed in an incompressible, viscous, shearing fluid. He showed that the rotation rate of a particle is a function of the strength of the shear flow, the shape of the particle and the orientation of the particle with respect to the direction of flow. A sphere in dextral shear flow rotates clockwise with an angular velocity (in $rad \cdot s^{-1}$) that is equal to half the shear strain rate. Using the xyz reference frame defined in 1.2.1, the axis around which the sphere rotates is the y-direction. A cylinder has the same rotational behaviour as a sphere provided that its long axis is aligned parallel to the

y-direction. Ellipsoidal particles with their long axis in the xz-plane have a fluctuating rotation rate: slower when the long axis is parallel to the direction of flow, faster when the long axis is perpendicular to the direction of flow.

Jeffery (1922) also gave equations that describe the motion in the fluid. However, these are not easily used. Fortunately, the work by Bretherton (1962), considering the first inner expansion of the Stokes solution, resulted in a two-dimensional stream function that, at least to a first approximation, describes the flow field in shear flow around a cylinder. This stream function is also applicable to cylinders that rotate with an arbitrary angular velocity. Differentiation of the stream function allows for the calculation of the components of the velocity vectors at all points in the xz-plane. The stream function can thus be used to construct a flow pattern, i.e., paths that fluid particles will follow during flow past the cylinder.

Using the approach of Bretherton (1962), Robertson and Acrivos (1970) have shown that the shear flow pattern around a cylinder is a function of the rotation rate of the cylinder. They showed that a free floating cylinder gives rise to a so called 'cats-eye' flow geometry (fig. 1.2a) while a small, externally imposed, reduction of the rotation rate of the cylinder results in a 'bow-tie' flow pattern (fig. 1.2b). They included more terms of the Stokes solution in the stream function than Bretherton (1962) and found that inclusion of inertial effects (geologically insignificant) would lead to a lower rate of rotation of a free floating cylinder. At low Reynolds numbers, velocities calculated with the improved stream function deviate very little from those obtained using the stream function given by Bretherton. Furthermore, Robertson and Acrivos found excellent agreement between experimental flow patterns and flow patterns calculated with the stream function given by themselves and by Bretherton (1962).

Chwang and Wu (1975) used another approach to find solutions for the Stokes equations for velocity, pressure, viscosity and external force. Their approach is called the singularity method and is based on single-point disturbances (such as a point source, point sink, point rotation) and combinations and derivatives thereof. Although the singularity method has its main use in solving problems with more difficult geometries, it can also be used for the relatively simple geometries of shear flow around a cylinder or a sphere. The solution of Chwang and Wu (1975) for shear flow past a stationary cylinder is equivalent to that of Bretherton (1962). The angular velocity of a free floating cylinder and a free floating sphere, calculated with the singularity method, is half the shear strain rate and thus equal to the angular velocity calculated by Jeffery (1922).

The numerical investigation by Freeman (1985) shows that departures from particle axisymmetry or from simple shear flow geometries will have significant effects on particle behaviour compared to the predictions of spheroid/simple-shear solutions. This seems a trivial matter but it should be emphasised that any particle in a coaxial deformation (irrotational; pure shear) will eventually reach a stable position. With pure shear flow as one extreme, and simple shear flow as the other extreme, it is clear that intermediate flow will have a range of solutions for particle and matrix motion. Ghosh and Ramberg (1976) theoretically defined the flow-type/particle-shape conditions that determine whether an object will keep rotating or not at ongoing flow for the two-dimensional case. Their conclusion is that in intermediate flow with a considerable pure shear component, objects with a relatively low aspect ratio can reach a stable position and thus stop rotating, even when the deformation continues (their figure 43; Kinematic vorticity number $W_k = \left(1 + 4s_r^2\right)^{-\frac{1}{2}}$; i.e.: $R_{xy}=2$ will become stable when $W_k \geq 0.6$). The theoretically determined reorientation of rigid elongated inclusions in simple shear flow was confirmed by shear box experiments. The paths that axially symmetric, three-dimensional, particles will

follow to reach their stable positions in general three-dimensional flows are given by Passchier (1987b).

In all of the above-mentioned theoretical and numerical studies, a no-slip condition is assumed for the particle-matrix interface. Slip along the object surface, characterised by a loss of coherence at the object-matrix interface, results in a decreased angular velocity of the object, as shown by the experiments of Ildefonse and Mancktelow (1993). In deforming rocks, this 'decoupling' of object and matrix may be caused by deformation and recrystallisation of core material, dissolution and reprecipitation of matrix material, crack-formation at the particle-pressure shadow interface or the development of melt films along grain boundaries (Ildefonse and Mancktelow 1993, and references therein).

Core-mantle-matrix geometries

When the velocities in the material surrounding a rigid object are known, it is possible to model the development of so-called 'passive' mantle geometries. Passive in this usage means rheologically identical to the matrix material. A passive mantle is thus a displacement marker only, equivalent to drawing a circle on the side of a deck of cards before shearing the deck in order to illustrate the strain ellipse. Similarly, it is possible to numerically (and experimentally) model a passive mantle or a passive layering in the deforming matrix that surrounds an object. Bjørnerud (1989) mathematically modelled the development of passive layers in low Reynolds-number shear flow around a free floating rigid sphere. The results of this modelling show evidence to support Simpson and Schmid (1983), who argued that in simple shear the presence of a rigid object causes a progressive asymmetric folding and increasing layer-thickness variation of the original parallel layering.

Numerical simulation of passive mantle development, including the concepts of both clast recrystallisation ('conversion' at outer surface into matrix material), and clast-matrix interface decoupling, has led to the belief that even a small amount of slip along the object-matrix interface will inhibit the development of δ-type porphyroclasts (Bjørnerud and Zhang 1995). Notably, slip (simulated by an increased velocity gradient) along the boundary of an object that is circular in cross-section, does not influence the rotation rate of the object since the resolved shear stresses at the object surface do not depend on the orientation of the core. Numerical simulation of a slipping boundary on a spherical object is, therefore, a entirely hypothetical simplification that gives insight into the complicated aspects of non-spherical objects.

1.2.3 Previous experimental work

Flow around rigid objects

As already mentioned, Robertson and Acrivos (1970) performed experiments using a Newtonian fluid with rigid cylinders and obtained good agreement with theoretical predictions for velocity distributions in the fluid. Ferguson (1979) used polymer solutions to experimentally determine the rotational behaviour of particles in non-Newtonian media. His results indicate that, at least for accumulated shear strains up to 20, the behaviour of spheres and slender rods in pseudoplastic (power-law exponent of flow law (see Ch. 3): n~1.3) and elasticoviscous fluids ('n'~1.3) is very similar to that in a Newtonian fluid (n=1) and is in good agreement with the theoretically determined behaviour in a Newtonian fluid.

The rotation of rigid particles (R_{xy}=3), embedded in a Newtonian matrix deforming by simple shear, was experimentally determined by Ildefonse *et al.* (1992). The influence of the rectangular shape, compared to an elliptical shape, is only minimal; in simple shear, the rectan-

gular particles at a low angle to the shear direction tend to rotate slightly faster that theoretically predicted for ellipsoidal particles. They also show that, in multi-particle systems, the rotation of individual, equal sized, objects is significantly lowered when the distance between particles is shorter than their length. The coalescence of the individual flow perturbations disturb the overall pattern to such a degree that it can no longer be simply related to the external boundary conditions.

Experimental work on rigid, elongated (R_{xy}=3), non-slipping particles in a power-law matrix (n~3) by Ildefonse and Mancktelow (1993) shows good agreement with the theory for rotational behaviour in Newtonian fluids. The results also show that decoupled objects rotate slower in simple shear and faster in pure shear than their non-slipping counterparts. Decoupling also causes higher strain concentrations at the tips of the object. It is argued that in simple shear, the decrease in rotation rate that occurs when the long axis of the particle approaches the shear plane, would inhibit the development of δ-type porphyroclasts and favour the development of σ-type geometries. Slip on the interface may also account for the common observation that some porphyroclast systems indicate a contradictory sense of shear. The different rotation rate, caused by slip, leads to a stronger shape preferred orientation of multi-particle/matrix systems in both simple and pure shear flow geometries. In simple shear, a bimodal orientation distribution of particles develops, with one set of long axes sub-parallel and another set at ~30° to the shear plane. The results of the experimental investigations by Ildefonse *et al.* (1992) and Ildefonse and Mancktelow (1993), provide useful insight for the understanding of clast-behaviour and, due to the complex geometrical lay-out, are probably not easily supported by numerical simulations.

Core-mantle-matrix geometries

Shear box experiments with a (nearly) passive mantle around an oblong (R_{xy}=2) object in a Newtonian matrix show that a high rheological contrast between clast and matrix allows shear induced vorticity in the matrix to be converted into spin of the clast (Van den Driessche and Brun 1987). In these experiments, developing wings extend in the direction of instantaneous stretching and a shear strain (γ) of at least 8 has to accumulate before the characteristic triangular embayment of a δ-clast are apparent. The distance between the wing-tips can be used to define a minimum estimate of the bulk finite shear strain.

Similar experiments on passive mantle development around a circular object, subjected to simple shear, indicate that the 'recrystallisation rate' of the core (i.e., the rate at which mantle material is produced at the core periphery) is highly significant for the developing geometry (Passchier and Simpson 1986). A pre-existing mantle around a non-shrinking core rapidly (γ=~3) develops into a δ-type geometry. A low rate of 'recrystallisation' increases the amount of shear needed to produce the typical δ-type geometry. Increasing the recrystallisation rate of the core inhibits the development of a δ-type and results in the development of a σ-type, while high recrystallisation rates can only produce φ-type wings. These results confirm that relatively large shear strains are needed for the development of a δ-geometry, at least around a non-spherical object. Surprisingly however, a pre-existing mantle around a circular-sectioned and completely rigid core can attain a δ-shape after a shear strain of only 3.

The influence of mantle rheology on the development of core-mantle structures in a shearing Newtonian matrix was investigated experimentally by Passchier and Sokoutis (1993). Their work indicates that the development of a specific type of geometry is determined by the competence contrast between the mantle material and the matrix, and by the thickness of the initial

mantle. It must be noted that these experiments were performed with mantle materials that have power-law stress vs. strain rate behaviour. This means that the competence contrast between mantle and matrix is a function of the shear strain rate. Since the presence of a rigid core induces strain and strain rate gradients, competence variations within the mantle material arise which, in turn, results in a competence-contrast distribution between mantle and matrix that depends on the position with respect to the core. Mantles with a much higher competence than the matrix did not deform and these core-mantle systems behaved as completely rigid spheres. When the competence contrast decreases, the mantle deforms into a 'steady state ellipsoid' that is oriented with its long axis at a small angle to the shear direction (x-axis), independent of the accumulated shear. With a vanishing competence contrast between mantle and matrix, the developing wing geometry shows a ϕ-shape. Passchier and Sokoutis (1993) also showed that a mantle with a lower competence than the matrix can develop σ- or δ-type wings, depending on the width of the initial mantle. The maximum mantle width that may produce a δ-type is of the order of 20 to 30% of the radius of the rigid core. The width of the wings in the y-direction is reduced when the rheology of the matrix material diverges from Newtonian behaviour (increase of stress exponent). Wings that are thin in the y-direction (tube-shape), develop from highly non-Newtonian mantles and tend to neck and boudinage. It seems natural that a mantle with a high competence with respect to the matrix shows a behaviour that is similar to that of a rigid core. However, from these experiments of Passchier and Sokoutis (1993), where the competence of the mantle is not uniform, it is difficult to define the competence contrast limits that constrain a typical geometry. Nevertheless, the experiments clearly show that the material properties of the mantle are of influence for the developing geometry. Furthermore, the experiments confirm that initially wide spherical mantles cannot develop into a δ-geometry.

1.3 Outstanding problems

From the foregoing, it is clear that considerable progress has been made concerning the behaviour of porphyroclast type systems, consisting of a rigid or semi-rigid object embedded in a flowing matrix. However, a number of important questions remain unanswered and impede application to the kinematic interpretation of natural porphyroclast micro-structures. The main problems remaining are as follows:

(1) It is yet to be established if viscous materials and Newtonian flow laws, which are commonly used to simulate porphyroclast development, are acceptable models for a natural mantle-matrix system, and if the core of a porphyroclast system can be represented by a rigid object. Since most rocks consist of crystalline material and often do not deform by Newtonian flow-laws, such models may not achieve the intended goal.

(2) The influence of the rheological behaviour of the matrix on the rotation rate of an embedded object is still poorly understood. When object rotation rates are lowered due to the rheology of the surrounding rock, the amount of shear accumulated by the matrix is no longer simply twice the amount of rotation of the clast. Rheological evidence should be sought to test the hypothesis put forward by Bell and co-workers that, in geological settings, porphyroblasts do not generally rotate (Bell 1985, Bell *et al.* 1986; 1989; 1992a; 1992b, Bell and Johnson 1989; 1992, Bell and Hayward 1991).

(3) Knowledge is lacking on the parameters that control the geometry of the flow pattern. This is particularly important for the interpretation of δ-clast structures which are thought to be the most promising kinematic indicators. Bjørnerud and Zhang (1995) argue that even minor slip

along the core-matrix interface, resulting in a reduced rotation rate of the core, inhibits the formation of a δ-type geometry. A reduced rotation rate of the object will theoretically result in a bow-tie flow pattern in the matrix (Bretherton 1962). Stair-stepping of the wings of a δ-clast is thought to evolve from a bow-tie flow pattern (Passchier and Sokoutis 1993). There is thus a contradiction in the stair-stepping nature of a δ-clast. Instigated by an experiment with a non-Newtonian matrix, Passchier *et al.* (1993) suggested that the bow-tie flow pattern might be related to the power-law stress-strainrate behaviour of the matrix. However, the bow-tie flow pattern itself is not uncommon in experiments with shearing Newtonian matrix material around free floating objects (Van Den Driessche and Brun 1987, Passchier and Simpson 1986, Passchier and Sokoutis 1993). On the other hand, the bow-tie flow pattern seems to be absent in the numerical modelling of free floating cylinders in a Newtonian matrix (Bretherton 1962, Chwang and Wu 1975, Masuda and Ando 1988, Bjørnerud 1989). Therefore, it should be checked what these differences between experimental and numerical work are based on.
(4) It is still insufficiently understood what conditions determine the final geometry of porphyroclast core-mantle structures. Of special interest is the question if δ-type clasts can only be formed when the core has produced mantle material prior to the onset of deformation. This may be indicative of the timing of changing conditions such as temperature, pressure, and chemical environment, with respect to the onset of flow in a rock.

1.4 Present aims

In view of the problems outlined above, this aims of this thesis are as follows.
(1) To establish the characteristics of flow in a clast-(mantle)-matrix system that consist of crystalline materials. A cardinal feature of this aim is to experimentally simulate clast development using crystalline materials for both clast and matrix.
(2) To determine the influence of the material properties and conditions on the rotation rate of an embedded 'free floating' object.
(3) To determine the influence of the material properties and conditions on the flow pattern around an embedded 'free floating' object.
(4) To isolate the characteristic parameters or conditions that lead to a specific geometry. For that purpose, a model should be obtained that includes as many potential parameters and conditions as possible. By comparing the results of changes in individual parameters in such a model, it may be possible to define the relevant effects of each parameter or condition on the final geometry.

Note that aims (2) and (3) are closely related and, therefore, can be investigated simultaneously. Material properties have to be verified for matrix materials suitable for experimental investigation of the characteristics of viscous flow around rigid objects. Experiments with these viscous materials must then include a systematic investigation of changing conditions, i.e., shear strain rate and relative distance of the object to the shear zone margins.

Chapter 2

Modelling of mantled porphyroclasts using non-Newtonian rock analogue materials[1]

2.1 Abstract

The development of δ-type porphyroclasts was modelled experimentally in a circular transparent shear rig using crystalline rock analogue materials. Rectangular camphor objects embedded in a matrix of octachloropropane were deformed in simple shear flow. The camphor deformed into δ-objects with progressive deformation up to a shear strain of 100. The development of these δ-objects and of gradients of flow parameters in the matrix was followed from step to step during the deformation. The δ-objects in this experiment show stair-stepping of wings that did not occur in earlier experiments with Newtonian fluids. Analysis of the flow pattern indicates that this is due to an unusual flow perturbation geometry around the relatively rigid camphor objects which rotate more slowly than equivalent objects in Newtonian flow. The non-Newtonian rheology of the experimental materials may be responsible for this deviant behaviour. This implies that non-Newtonian fluids are better analogues than Newtonian fluids to study the development of structures in rocks with non-Newtonian rheology, since the geometry of the resulting structures can be different.

2.2 Introduction

Mylonite zones are important tectonic elements that accommodate much of the imposed deformation in the crust and mantle. The geometry of microstructures in mylonites is an important source of information on the development of mylonite zones and on the kinematics and dynamics of flow in them. However, microstructures can only yield reliable data if their development is properly understood. Mantled porphyroclasts, one of the more common mylonitic microstructures, consist of a core (the porphyroclast) and a deformed mantle that can have a complex, monoclinic geometry which is commonly used to determine sense of shear in mylonites. The mantle is thought to develop by recrystallisation in the outer rim of a large parent grain, of which the porphyroclast is a relic. Relatively common are mantled feldspar porphyroclasts in quartz-feldspar mylonites (Passchier and Simpson 1986, Hooper and Hatcher 1988, Hanmer and Passchier 1991) and mantled pyroxene porphyroclasts in peridotites (Boudier *et al.* 1988). We investigated the development of mantled porphyroclasts by experimental modelling, in order to determine what data besides sense of shear can be derived from porphyroclast geometry.

Some of the most conspicuous mantled porphyroclast shapes are δ-objects, which have a characteristic spiral shape similar to a Greek letter δ (fig. 2.1; Passchier and Simpson 1986). The development of δ-objects has been investigated by Passchier and Simpson (1986), Van Den Driessche and Brun (1987) and Passchier and Sokoutis (1993). Their work was based on natural

[1] This work has already appeared in an article of the same title: Coen E. ten Brink and Cees W. Passchier, Journal of Structural Geology, Vol. 17, No. 1, pp. 131 to 146, 1995.

δ-objects and on experimental deformation of deformable mantles around rigid objects in Newtonian fluids. The experimental set-up and materials used in these studies have a number of limitations: (1) only small finite strain values were reached in single experimental steps in experiments by Passchier and Simpson (1986) and Van Den Driessche and Brun (1987) whereas natural porphyroclasts commonly develop at high finite strain; (2) the shapes of the 'porphyroclasts' were circular (except for Van Den Driessche and Brun 1987) whereas natural objects usually have a more complex shape; (3) the 'porphyroclasts' were fixed in size - the central object could not add new material to the mantle by recrystallisation; (4) matrix materials were Newtonian fluids (except for Passchier *et al.* 1993) whereas rocks commonly deform by power-law flow; (5) matrix materials were non-crystalline fluids whereas rocks are polycrystals that develop a crystallographic preferred orientation that may influence flow behaviour. We have tried to overcome these restrictions by means of a new, more evolved experiment.

In order to model the development of natural δ-objects in mylonites more closely, we carried out experiments on organic, crystalline rock-analogue materials with non-Newtonian rheology in which the matrix and the 'porphyroclasts' have different rheologies. The 'porphyroclasts' have an initial elongate, approximately rectangular shape and are subject to deformation and recrystallisation. The experiments were carried out in a circular shear rig that has the advantage that very high strains can be obtained and that the deformation process can be observed in transmitted light down to the scale of individual grains.

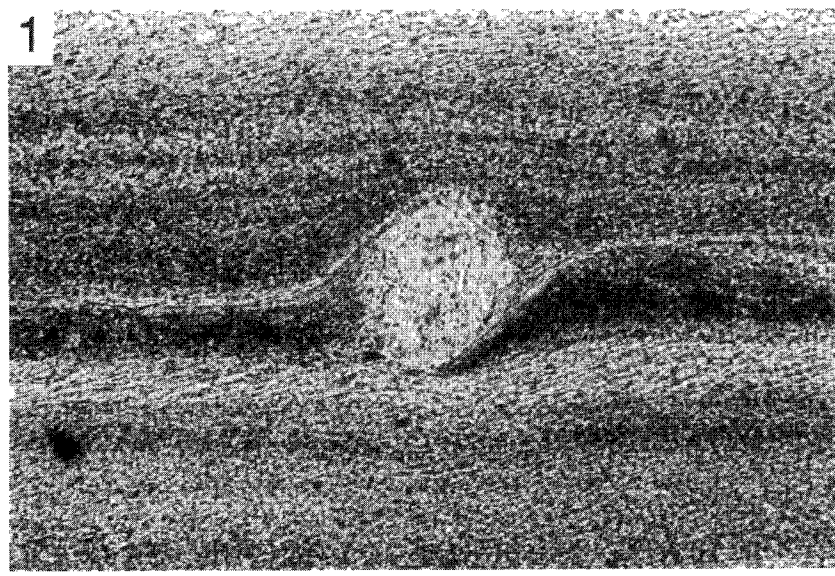

Figure 2.1. Microphotograph of a plagioclase δ-porphyroclast in a matrix of quartz-plagioclase-biotite ultramylonite. The wings of recrystallised feldspar on both sides of the core show stair-stepping. A weak mica preferred orientation is visible in the ultramylonite matrix. Barthélemy Massif, Pyrenees. Width of view is 3 mm, plane polarised light.

2.3 Materials and methods

2.3.1 Apparatus

The ring-shear apparatus used in this experiment can model non-coaxial progressive deformation in a sample material. A sample is wedged between two glass plates (fig. 2.2a) and is deformed in torsion by rotation of the upper glass plate around a central axis while the lower plate remains fixed. The sample can be observed through the glass plates during deformation under a petrographic microscope. An annular shear zone is created in the sample material by the presence of two frosted grips of different diameter, each etched on to one of the glass plates (fig. 2.2a); since the sample material is only connected to the glass plates along the frosted grips, sample material in the annular shear zone is deformed in non-coaxial flow with the vorticity vector parallel to the rotation axis of the upper glass plate (fig. 2.2b).

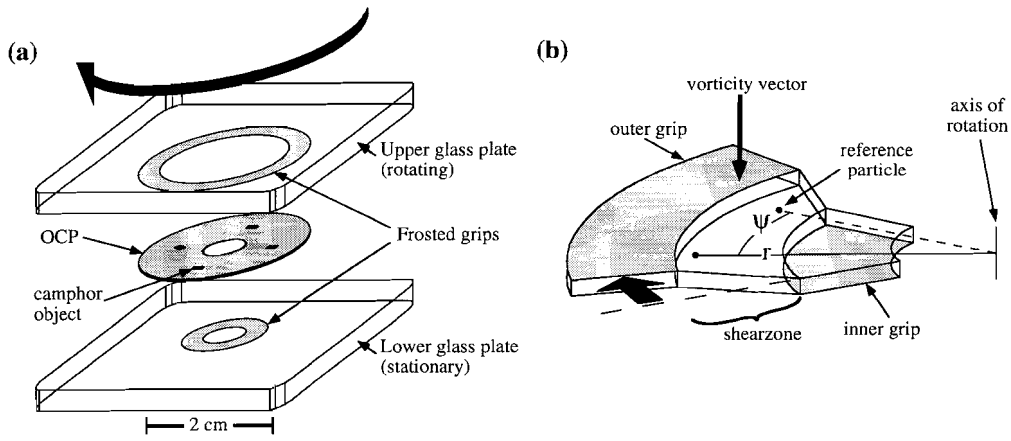

Figure 2.2. (**a**) Simplified exploded view of the ring-shear apparatus. Sample material is contained between two glass plates. Clockwise rotation of the upper plate induces dextral sense of shear in the sample. (**b**) Detail of the deforming part of the sample material showing the location of shear zone development and explanation of the position of marker particles with respect to the rotational origin of the ring-shear apparatus and a certain reference particle.

2.3.2 Experimental materials

Two sample materials were used: octachloropropane (OCP) as a matrix material and camphor for porphyroclasts. OCP (C_3Cl_8) has a hexagonal crystal symmetry with a melting temperature of 160°C. Camphor ($C_{10}H_{16}O$) is either rhombohedral (<92°C) or cubic (>92°C) and its melting temperature is 179°C. The rheological behaviour of both materials between 52°C and 68°C was investigated experimentally by A. Oostra (fig. 2.3, unpublished data). Both materials show power-law flow behaviour with stress exponents of approximately n=5 (OCP) and n=3.5 (camphor). Bons (1993) and Bons and Urai (1994) investigated the rheological properties at 28°C and found similar stress exponents of 4.5±0.3 (OCP) and 3.3±0.3 (camphor). Silicon carbide grit is distributed as a fine powder in the OCP and camphor and acts as marker particles for flow analysis.

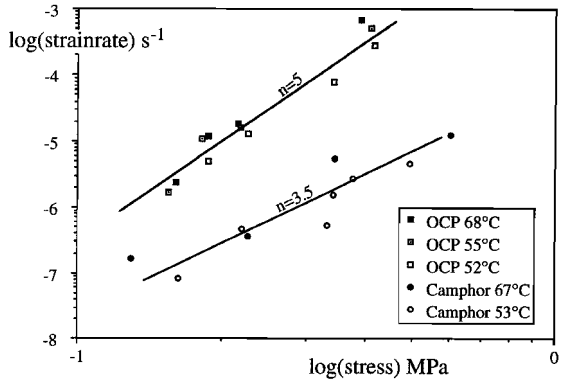

Figure 2.3. Log(stress)-log(strain rate) plot for OCP and camphor with superposed lines for n=5 and n=3.5 in a power-law relationship: $\dot{\gamma}=C\cdot\sigma^n$. Unpublished data from A. Oostra.

2.3.3 Sample preparation

Sample preparation is similar to the technique described in Means (1983) and Jessell (1986). Approximately 5 g of laboratory grade OCP is chopped to a fine powder using a razor blade. It is mixed with 0.2%wt silicon carbide grit with an average particle size of 26 μm and pressed between teflon foil into a disk of approximately 0.4 mm thick and 25 mm in diameter using a hand operated press. The sample disk is optically checked for uniform distribution of the grit particles; if the distribution is far from uniform, the process of chopping and pressing is repeated. A camphor disk is prepared in the same way.

The surfaces of the two glass plates, except for the frosted grips, are coated with a thin film of silicon grease. This is done in order to reduce friction between the deforming material and the glass plates; a sample will only deform homogeneously if it is not attached to the glass plates between the frosted grips. The OCP disk is pressed onto the glass plate with the larger frosted grip using a hand press. Excess material outside the larger grip and inside the smaller grip is removed. With a preparation needle four depressions are made in the part of the OCP that will be the future shear zone. Four slightly oblong pieces of approximately 0.4x0.4x0.5 mm are cut from the camphor disk and placed in the depressions. The voids around the camphor fragments are closed by addition of a small slice of OCP and gentle pressure on the sample.

The second glass plate is now emplaced on the sample material and the assembly is placed in the ring-shear apparatus which is then heated to 60°C (0.77 T_m of OCP) and left to anneal for 3 days. A dead weight of 3 kg, placed on the upper glass plate, is used to attain full contact between the sample material and the glass plates over the entire area of the frosted grips. During annealing, the thickness of the sample is reduced to approximately 0.3 mm. When complete contact is established between the sample and both glass plates, the top of the ring-shear apparatus is tightened so that a rubber ring applies a normal stress on the sample.

The resulting sample has no large voids and shows four approximately rectangular camphor objects in a homogeneous OCP matrix (figs. 2.4 and 2.5a). For both OCP and camphor, average grain size after annealing is 0.1-0.15 mm, the grain shape is equidimensional, and grain boundaries are straight or slightly curved. There is no apparent grain-shape foliation, though sample preparation has probably introduced a weak crystallographic preferred orientation (Jessell 1986). The four oblong camphor objects are numbered C1 to C4 and have initial aspect ratios (R_{xy}) of 2 (C1), 1.4 (C2), 1.5 (C3) and 1.2 (C4). The initial angles between their long axes and the frosted grip circle are 6° (C1), 67° (C2), 53° (C3) and 95° (C4), respectively (fig. 2.4).

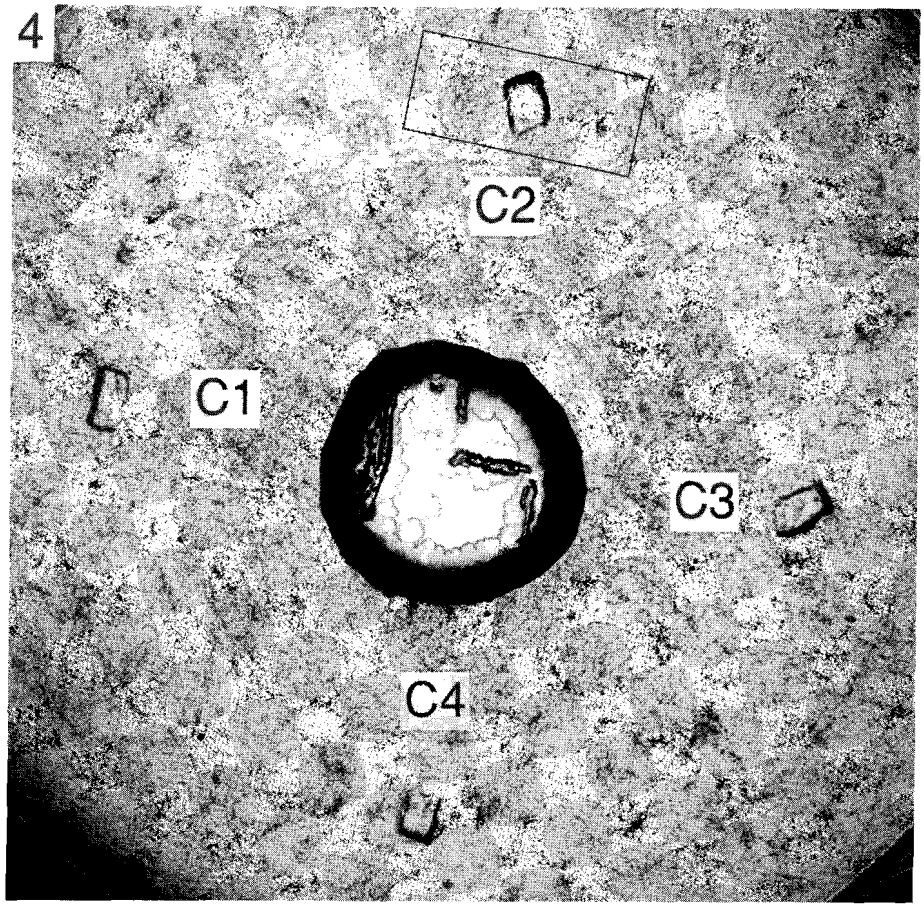

Figure 2.4. Overview of the entire sample of OCP with camphor objects before deformation, seen from above. Object numbers are indicated. 'Dust' in the sample are marker particles. The outline shows the area of figure 2.5a. Width of view is 18 mm, plane polarised light.

2.4 Experimental conditions

A small motor was used to rotate the upper glass plate at a constant rate of 0.5 revolutions per hour, which imposed a bulk shear-strain rate ($\dot{\gamma}$) of about $2{,}6 \cdot 10^{-3}$ (s^{-1}) over the annular shear zone between the frosted grips. This produced a relatively homogeneous, non-coaxial circular Couette flow in the OCP matrix in the shear zone. Flow lines are circular but parallel to the frosted grips and the flow pattern bears a resemblance to simple shear in that no stretching occurs parallel to the grips. We define a 'flow circle' as a circle parallel to the grips, similar to the 'flow plane' of simple shear.

The temperature was kept at 60±0.5°C during the first 12 hours of deformation. The motor was switched off for approximately 6 minutes at regular intervals to take photomicrographs of the sample. After the first 12 hours of deformation, the imposed finite shear strain (γ) was about 113 (fig. 2.6). γ is calculated as circular displacement of the outer frosted grip, divided by shear zone width (Passchier and Sokoutis 1993).

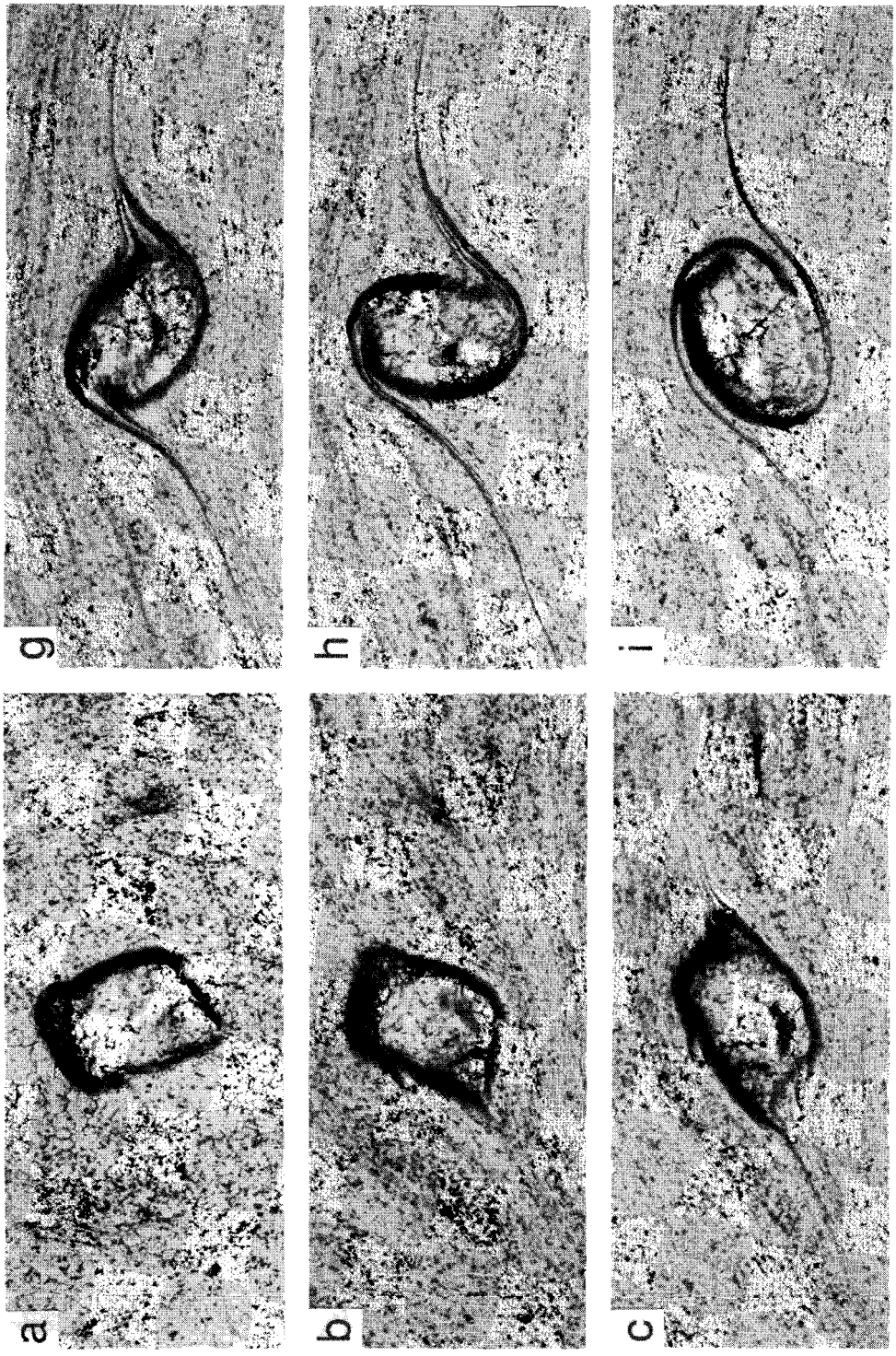
g
h
i
a
b
c

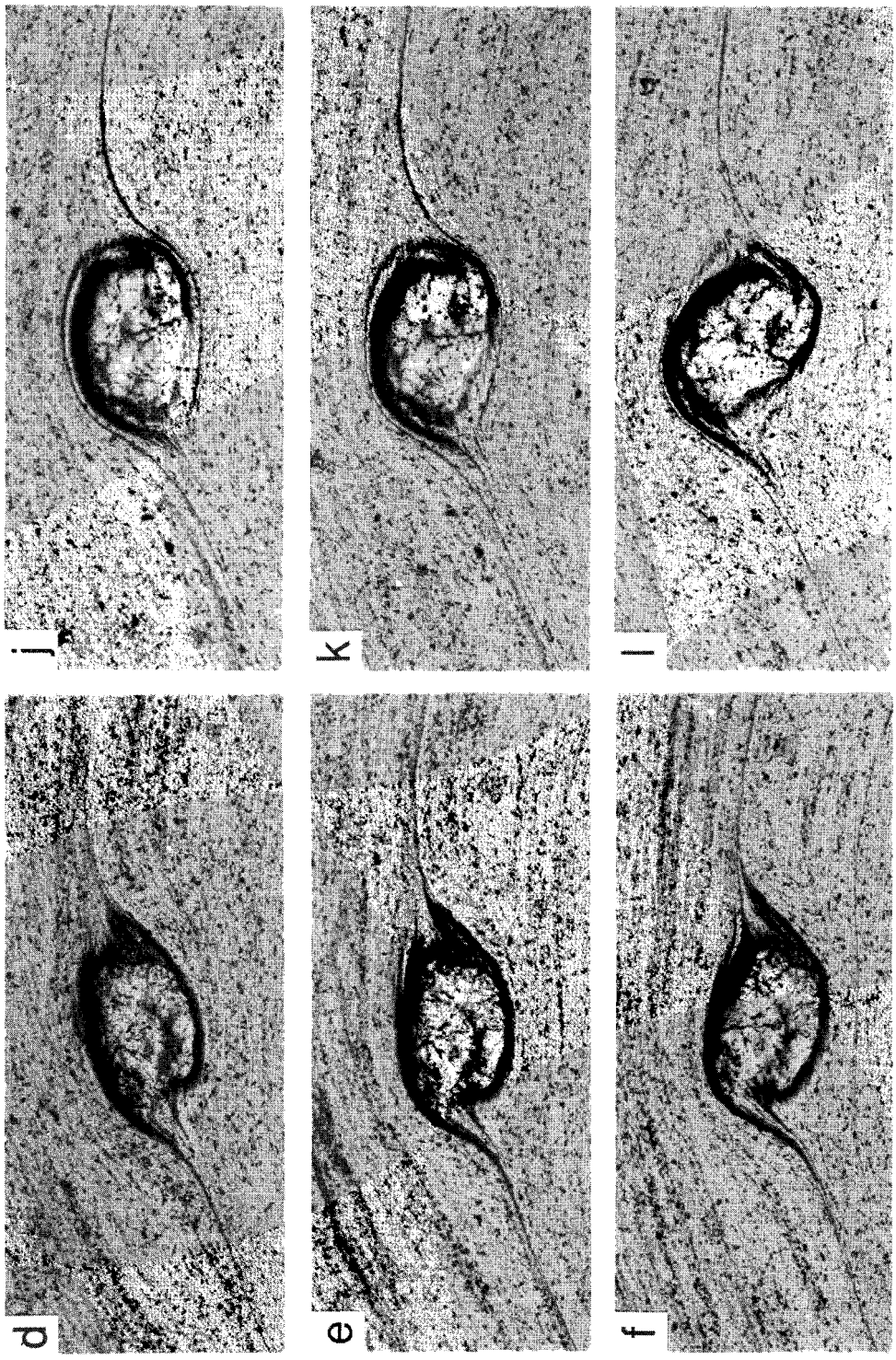
j
k
l
d
e
f

Figure 2.5 (previous pages). Sequence of microphotographs of the camphor object C2, showing the gradual development of a complex δ-shape. The centre of rotation of the ring-shear apparatus is downward in all photographs. Running time and shear strain (γ) for these photographs was: **(a)** 0 min.; γ=0, **(b)** 60 min.; γ=9, **(c)** 120 min.; γ=19, **(d)** 180 min.; γ=28, **(e)** 240 min.; γ=37, **(f)** 300 min.; γ=47, **(g)** 360 min.; γ=56, **(h)** 420 min.; γ=66, **(i)** 480 min.; γ=75, **(j)** 540 min.; γ=84, **(k)** 570 min.; γ=89, and **(l)** 630 min.; γ=98. Width of view is 4.5 mm, plane polarised light.

Several times during the experiment the sample seemed to break at the inner grip. In that case the motor and the temperature control were shut off and a dead weight of 3 kg was placed on the upper glass plate. After the contact was restored, the ring-shear apparatus was tightened and the sample heated up before restarting the deformation. These interruptions did not visibly affect the already developed microstructures in the zone around the camphor objects, though they did flatten the whole sample by a few μm.

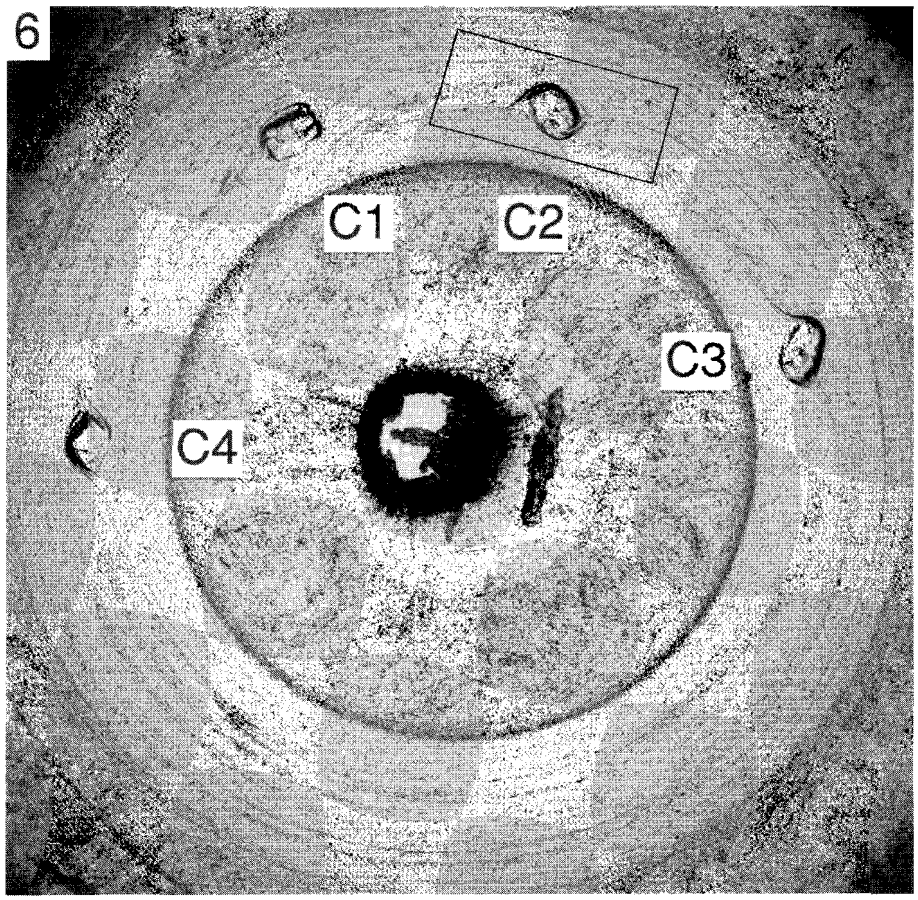

Figure 2.6. Overview of the entire sample after 630 minutes of deformation (γ=98). Object numbers correspond to text and other figures. Marker particles in the shear zone have been aligned while those outside are still undisturbed. Camphor objects have drifted together due to a difference in distance to the centre of rotation of the ring-shear apparatus. The outline shows the area of figure 2.5l. Width of view is 18 mm, plane polarised light.

2.5 Experimental observations

2.5.1 Deformation of the OCP matrix

Soon after deformation started, a grain-shape preferred orientation (GSPO) developed in the OCP close to the inner grip while little deformation was visible in the rest of the sample. This zone of higher strain gradually widened during the experiment but the inner part of the shear zone retained the best grain-shape foliation. This means that finite strain was not homogeneously distributed over the sample but increased towards the inner grip. This effect results from the circular shape of the specimen chamber which induces a gradient of increasing flow stress and strain rate over the sample towards the inner grip. This gradient is an inherent property of any circular shear zone set-up. The foliation, defined by the GSPO, is at a small angle to the imposed flow circle in areas that are only little influenced by the camphor objects while it is deflected around the objects (fig. 2.7).

Besides a GSPO, a crystallographic preferred orientation developed in the OCP matrix. The trace of the long axis of the indicatrix is preferentially perpendicular to the flow circle in the domain outside the zone of contact strain around the camphor objects. Near the top-left and bottom-right of the camphor objects, this trace is orientated approximately 30° counter-clockwise from the general orientation.

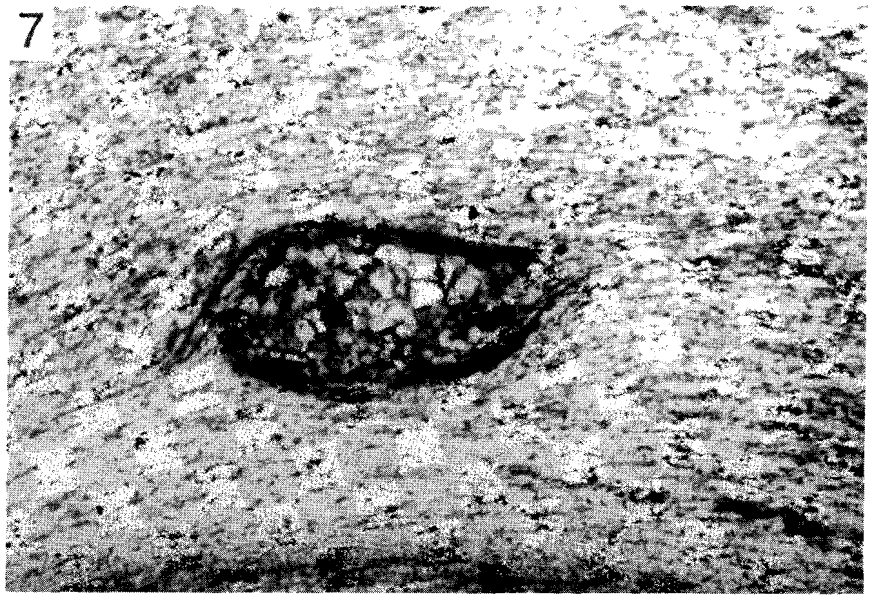

Figure 2.7. Microphotograph of C3 at 180 minutes running time (γ=28) showing the grain shape preferred orientation of the matrix material around the object. Crossed nicols at 45° to the sides of the photograph, width of view is 4.5 mm. Note that this is not the same object as the one shown in figure 2.5.

2.5.2 Deformation of camphor

During the experiment the camphor objects deformed and rotated with respect to the flow circle. The initial rectangular objects (figs. 2.4 and 2.5a) started to shed fine grained mantle material from their rims, probably by dynamic recrystallisation (fig. 2.5b). Up to γ=19, this fine grained material stretched into the surrounding OCP matrix at the two opposite corners of the

rectangular object that were in the extensional quadrant of the flow (fig. 2.5c). With continuing deformation the other two corners rotated into a similar position and also started to shed material (fig. 2.5e). The resulting 'wings' of fine grained material did not detach from the camphor core and with increasing deformation they stretched, thinned and even 'wrapped around' the central object (figs. 2.5f to 2.5l); they were smoothly curved and have a remarkably regular thickness. Embayments of OCP formed between the central object and the wings and caused the typical δ-shape. After initial development of the wings, the camphor objects did not shed any new fine grained material but continued to deform internally. The wings did not stretch along a single circlar arc through the centre of the objects as would be expected, but show 'stair-stepping'; they 'step-up' over the object, similar to some natural mantled porphyroclasts (Lister and Snoke 1984, Passchier and Simpson 1986 and Passchier *et al.* 1993) (fig. 2.1).

The set-up of our experiment allows not only direct observation of the change in geometry of a deforming object, but also allows quantification of deformation parameters based on the displacement of inserted silicon carbide marker particles (Means 1983, Jessell 1986). We used the displacement patterns to study: (1) the gradients of individual deformation parameters, and (2) the perturbation in the flow pattern around camphor objects.

2.6 Deformation parameter gradients

2.6.1 Tensor calculations

For any small area, confined by at least three marker particles for which the relative positions before and after a deformation increment are known, a local deformation tensor can be calculated (Ramsay 1967, Jessell 1986). Since the tensor describes a homogeneous deformation, we cannot resolve deformation inhomogeneities on a scale smaller than that between marker particles. In practice this means that we cannot calculate the difference in deformation behaviour for individual crystals in the sample. For the ring-shear apparatus we used a curvilinear reference frame (fig. 2.2b) with the origin at the centre of rotation of the upper glass plate and a reference axis defined by the origin and one of the marker particles. The position of every marker particle at time (t) is thus defined by its distance to the origin (r) and its polar angle (ψ) to the reference particle (fig. 2.2b).

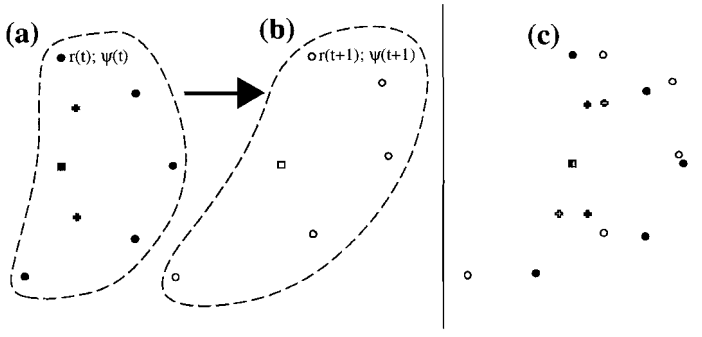

Figure 2.8. Information used to calculate the deformation tensors and the position of gridnodes for a deformation increment. **(a)** Particles and gridnodes before the deformation increment. **(b)** Particles after the deformation increment. **(c)** Superposition of the two states with the reference particle as local origin. Circles - marker particles; square - reference particle; crosses - grid nodes. Closed symbols: before deformation increment; open symbols: after deformation increment. r and ψ are polar co-ordinates of gridpoints as shown in figure 2.2b.

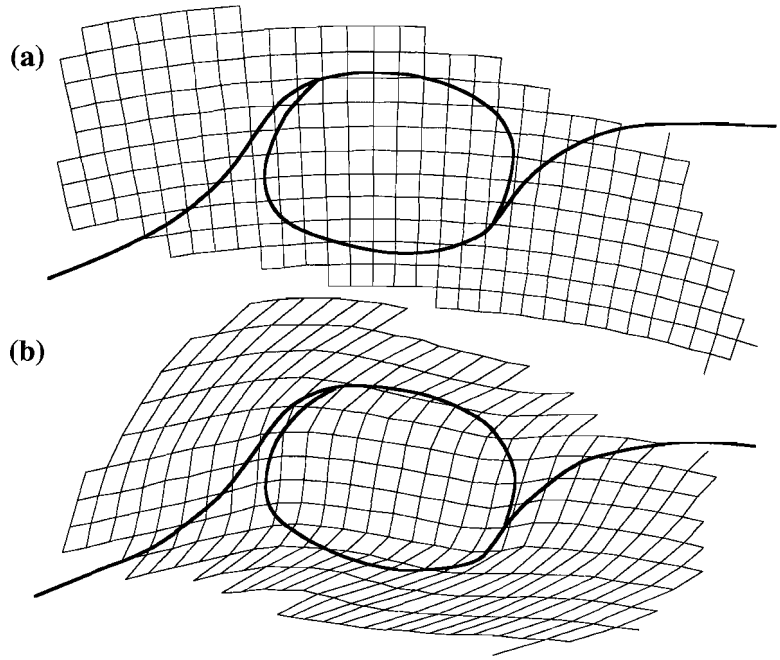

Figure 2.9. Example of (**a**) an undeformed polar grid superposed on the sample material and object C2 after 570 minutes of deformation. (**b**) The deformed polar grid of (a) after an extra increment of 20 minutes of deformation. The outline of object C2 is indicated by a solid line. An increment of 20 minutes imposes a shear strain of approximately 3 over the entire shear zone; due to shear localisation at the inner grip, the shear strain over the shear zone segment outlined by the grid is about 1.

In this experiment we use the following method to calculate the local deformation tensor (**F**) (Bons *et al.* 1993). A regularly spaced imaginary polar grid is superposed on the sample (figs. 2.8a and 2.9a). The position of each grid node is defined with respect to four adjacent marker particles occupying at least 3 different quadrants. After a deformation step, these particles are displaced (fig. 2.8b) and if one marker particle is used as a reference, the translation component of deformation can be deleted and the relative displacement of marker particles can be measured (fig. 2.8c). A least squares best fit method is now used to determine the displacement of each gridnode from the displacement of the four adjacent marker particles (fig. 2.8c). Using this technique, a deformed polar grid can be constructed (fig. 2.9b) and the deformation tensor for the deformation increment can be calculated for each individual gridnode (Bons *et al.* 1993). A slight error in the determination of the position of a marker particle may introduce a significant error in the calculation of the finite strain tensor. This implies that the deformation increments should not be too small when this method is being used.

We studied deformation patterns around camphor object C2. Enlarged photographs of C2 taken at 10 minute intervals between 570 and 630 minutes of deformation (imposed γ of 89 and 98 respectively) were studied in detail. On each photograph more than 1000 marker particles were traced, numbered and digitised. Inaccuracy in the orientation of enlarged photographs can cause a significant error in the rotational component of the deformation, therefore photographs of the entire specimen chamber (as figs. 2.4 and 2.6) were used to determine the centre of rotation and the exact orientation of the enlarged photographs with respect to this origin. The results of an interval of 20 minutes running time (between 570 (γ=89) and 590 (γ=92) minutes) are presented

as a deformed grid (fig. 2.9b) and in plots showing the gradients of individual deformation parameters (fig. 2.10). The increments from 590 to 610, and 610 to 630 minutes show similar results. The ring-shear apparatus was not tightened during these 20 minutes intervals.

2.6.2 Deformed grid

The undeformed and deformed grids in figure 2.9 show that flow is not homogeneously distributed over the annular shear zone in the sample, but partitioned: zones of high shear strain are located above and below the camphor object along the grips. Deformation of the camphor object is mainly a passive rotation: gradients of deformation intensity are rather small except in the region close to the object boundary. This is the domain where progressive deformation changes from a non-coaxial pattern towards rigid body rotation. The gridnode spacing is too large to give an accurate estimate of the width of this transition.

2.6.3 Gradient plots

Since our experiment is virtually two-dimensional, the deformation tensor **F** can be fully described by only four independent coefficients, whose values depend on the chosen reference frame. However, **F** can also be expressed by four 'invariant' deformation parameters (see Appendix) such as finite strain R_f, a finite 'mean' vorticity number W_f (introduced in Passchier 1988 and there labelled W_n^m), finite dilatation A_f (the total area change) and the orientation of the long axis of the finite strain ellipse with respect to the flow circle (β_f). R_f is equal to (undeformed state) or larger than 1; A_f is 1 for absence of dilatation, and may be smaller (area decrease) or larger (area increase) than 1. W_f is a measure of the rotational component of the deformation normalized for strain (Appendix, Truesdell 1953, Passchier 1988). We use a positive sign for W_f to indicate a bulk clockwise rotation. W_f is 0 for a pure shear deformation history, 1 for a dextral simple shear deformation history and goes to infinity for a rigid body rotation. We have chosen to use these four parameters because, although they are not independent, they completely describe the finite deformation, do not change with reference frame orientation and are easier to understand as physical entities than four coefficients that depend on reference frame. Figure 2.10 shows the gradients of the four deformation parameters of **F** and shows the amount of detail about heterogeneous deformation that can be made visible with our method. The plots represent an interval of 20 minutes; though the imposed strain is 3, the strain is about 1 over the grid which only displays part of the shear-zone width.

The contour plot of R_f (fig. 2.10a) shows values around 1 within the camphor object, and values exceeding 2.5 in bands parallel to the grips above and below the object; finite strain increases towards the inner grip due to the circular shape of the specimen chamber (Passchier and Sokoutis 1993).

The contour plot of W_f (fig. 2.10b) shows high values within the object that indicate approximately rigid body rotation conditions. Values around 1, which represent simple shear, are located below the object, and away from it to the left and right. Interesting are domains of negative W_f on each side and close to the object that represent anticlockwise rotation. These domains of 'inverse' vorticity were theoretically predicted by Masuda and Ando (1988) and arise from the fact that the

Figure 2.10 (next page). Contour plots of **(a)** R_f, **(b)** W_f, **(c)** A_f, and **(d)** β_f for the deformation increment between 570 and 590 minutes running time around object C2, shown as a deformed grid in figure 2.9. The area within the clast in (d) shows the actual long axes instead of contours due to the large variation in orientation. The reference axis in (d) has unit length, dashed line indicates flow-circle through centre of clast.

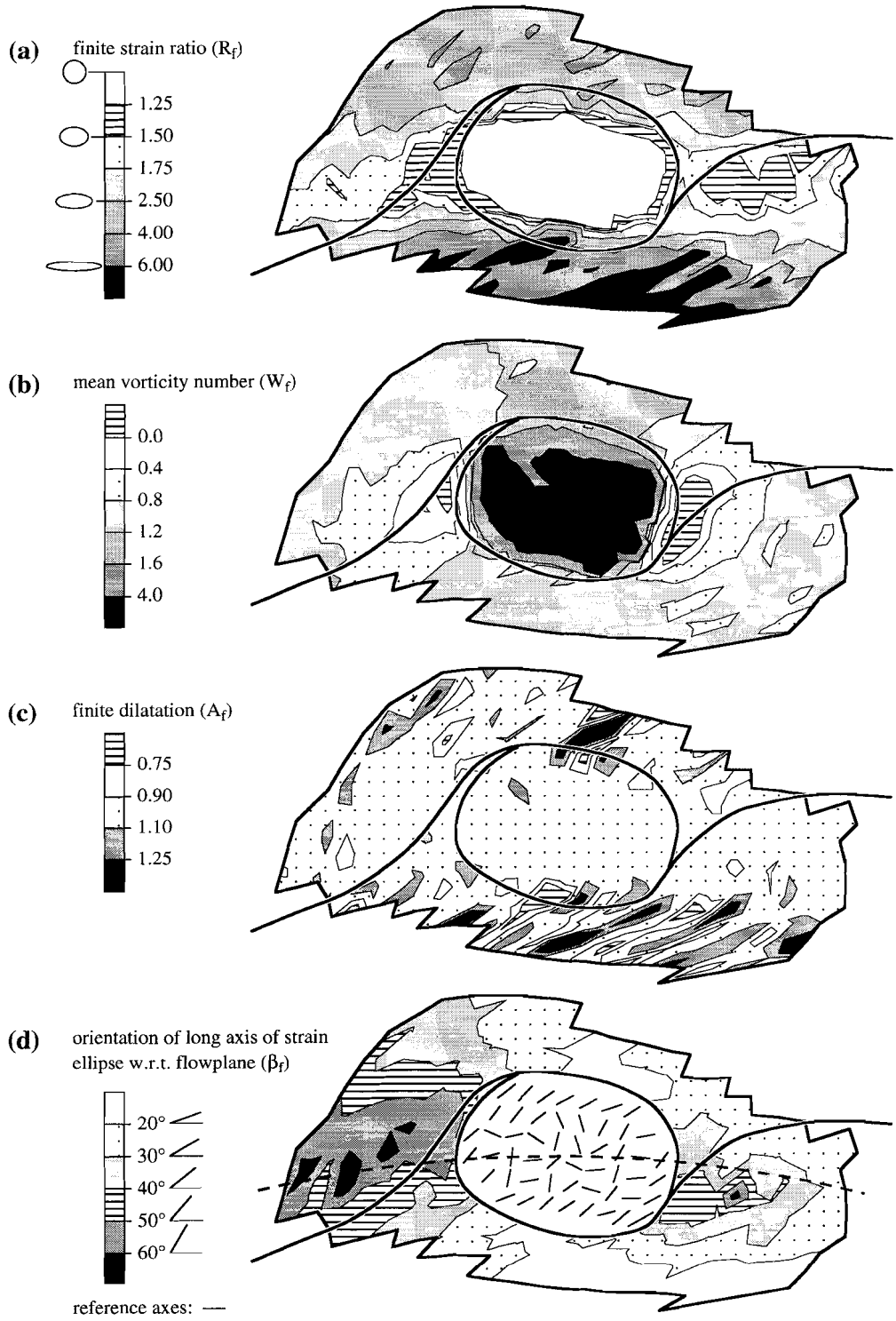
(a)
finite strain ratio (R_f)
1.25
1.50
1.75
2.50
4.00
6.00
(b)
mean vorticity number (W_f)
0.0
0.4
0.8
1.2
1.6
4.0
(c)
finite dilatation (A_f)
0.75
0.90
1.10
1.25
(d)
orientation of long axis of strain ellipse w.r.t. flowplane (β_f)
20°
30°
40°
50°
60°
reference axes: —

drag-effect of the rotating object on the matrix in the strain shadow is negative and locally exceeds the 'positive' vortical effect of bulk simple shear.

The contour plot of A_f (fig. 2.10c) shows a mean value of 1 with some small local deviations. The specimen chamber is closed and volume should be conserved during deformation. Finite dilatation is therefore a function of changes in thickness of the specimen, or development of voids in the sample; an overall thickening or thinning of the sample material would result in a relatively constant deviation of a dilatation value of 1. The material is (nearly) incompressible at the stresses applied in this experiment and few voids develop within the shear zone. The local dilatation values can therefore be used as an indication of the errors made by tracing the exact positions of the marker particles.

The plot of β_f (fig. 2.10d) shows the orientation distribution of the long axis of the strain ellipse with respect to the flow circle at the end of the deformation increment. It agrees well with the patterns of grain shape orientation visible in figure 2.7. In the camphor object, the large variation in β_f values can be attributed to the fact that strain is small here. This variation is probably the combined effect of small errors in locating the marker particles and small inhomogeneities in the deformation.

2.7 Flow perturbation

The presence of a rigid object causes perturbation of homogeneous flow. In a non-coaxial flow a rigid object will rotate if no shear localisation occurs (Jeffery 1922). Rotation of the rigid object is associated with the generation of circular or ellipsoidal flow lines in the adjacent matrix; such flow lines can be approximately closed, i.e. a particle on a flow line will return approximately to its initial position. Somewhere in such a flow pattern there must be a transition between the open flow lines of far field flow and closed flow lines. Such a transition is a sharp boundary known as a 'separatrix' (Ottino 1989).

Tracing of the relative displacements of marker particles can give a good indication of the pattern of flow around the camphor objects. Figure 2.11 shows the streamline pattern (the paths of individual particles as seen by an observer fixed to the reference frame for a reference particle at

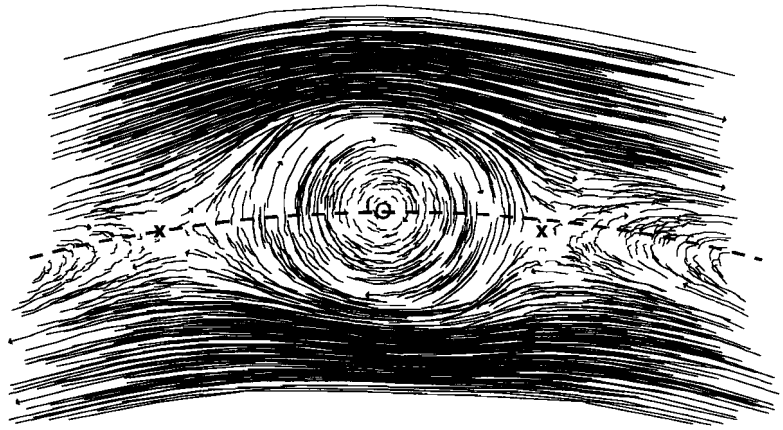

Figure 2.11. Streamline pattern of the marker particles around C2 for 6 successive intervals of 10 minutes of deformation (between 570 and 630 minutes running time); sense of shear is dextral. Crosses are hyperbolic stagnation points; circle is parabolic stagnation point, dashed line indicates flow-circle through centre of clast.

the centre of the object) around object C2 for six successive increments of 10 minutes of deformation. The pattern shows deflection of the open streamlines of simple shear away from the central object and ellipsoidal closed streamlines close to the object, as predicted by Ottino (1989). A separatrix can be envisaged between both domains and an additional domain of curved streamlines exists on either side of the object. This 'bow-tie shaped' flow perturbation pattern has three separatrices which end on two 'immobile' points (particles without relative displacement) on both sides of the central object. Such 'immobile' points are common where separatrices meet, and are known as 'hyperbolic stagnation points' (Ottino 1989, Passchier 1994). Material points on the separatrices move towards and away from such hyperbolic stagnation points.

2.8 Model for development of complex δ-objects

Passchier *et al.* (1993) argued that a 'bow-tie' flow pattern will result in stair-stepping δ-objects when the ductile mantle of a rigid circular object is situated partly outside the separatrix. Such a flow pattern, however, cannot result in a more complex shape of the porphyroclast, like the double wings on either side of the object which started to develop after an imposed shear strain of 28 (fig. 2.5d). Passchier and Simpson (1986) modelled the development of mantled porphyroclasts and succeeded in reproducing the double-winged examples sometimes found in nature by an instantaneous decrease in diametre of the rigid object. The 'mantle' of their clasts consisted of matrix material (the wings evolved from a passive markerline drawn on the matrix).

Our experiment shows both a bow-tie flow pattern and a core decreasing in diameter. The camphor objects are deformable and develop from a rectangular shape into an elliptical core with curved wings. The flow pattern can therefore be expected to have changed with time; this change in flow geometry has been found in the interval between 570 and 630 minutes running time (the experiment did not yield enough data to study the flow in detail over the whole time span). This makes it possible that parts of a clast that were at first 'trapped' within the domain of elliptical flow lines became part of the domain of open flow lines, thus forming the base of a new generation of wings (Passchier 1994).

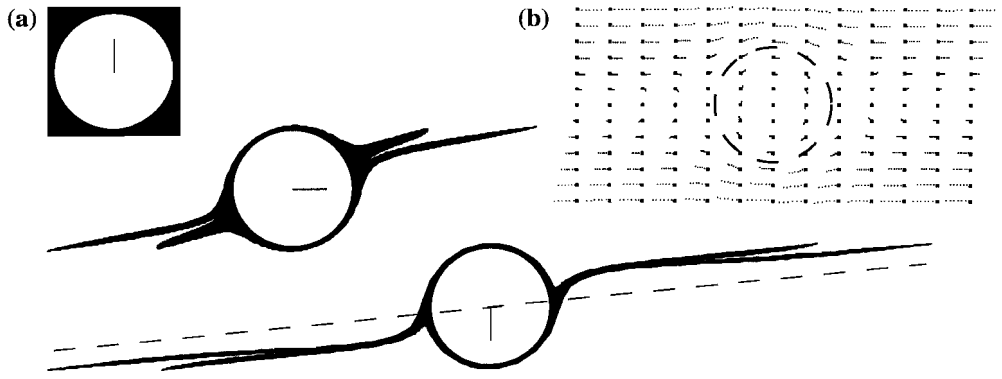

Figure 2.12. (**a**) Evolution of a rigid circular object with a passive square mantle into a double winged stair-stepping δ-clast when subjected to deformation according to flow in (b). The dashed line through the centre of the rigid body is shown to clearly illustrate the stair-stepping geometry of the wings.(**b**) Particle displacements for 6 strain increments in a computer-generated, time-independent, deformation with a bow-tie flow pattern: heavy dots denote original positions; dashed circle indicates position of rigid object.

In our experiment, the observed small change in the flow pattern alone cannot account for the secondary set of wings as the geometry of the separatrix adapts to the orientation of the elliptical core. During a 90° rotation not enough 'mantle material' had been located far enough from the core to eventually 'escape' the central domain of the separatrix.

Due to stress concentration, the corners of a rectangular clast are more susceptible to degradation than the core. In our experiment this would make the camphor objects act as an elliptical core with a rectangular, more or less passive mantle. Computer modelling of a square passive marker around a circular rigid object shows that stair-stepping δ-objects with double wings can develop in a time independent 'bow-tie' flow pattern (ten Brink *et al.* 1993; fig. 2.12).

2.9 Object rotation rate

Rigid ellipsoidal objects in a Newtonian fluid subject to simple shear flow rotate at a variable rate (Jeffery 1922). When an object lies with its long axis parallel to the flow plane the rotation rate has a minimum value, and when the long axis is perpendicular to the flow plane it has a maximum value. The variation in rotation rate is also proportional to the aspect ratio (R_{xy}) of the object (Jeffery 1922, Simpson and De Paor 1993). A circular object has a constant rotation rate, while objects with increasing R_{xy} values show an increasingly pulsating character.

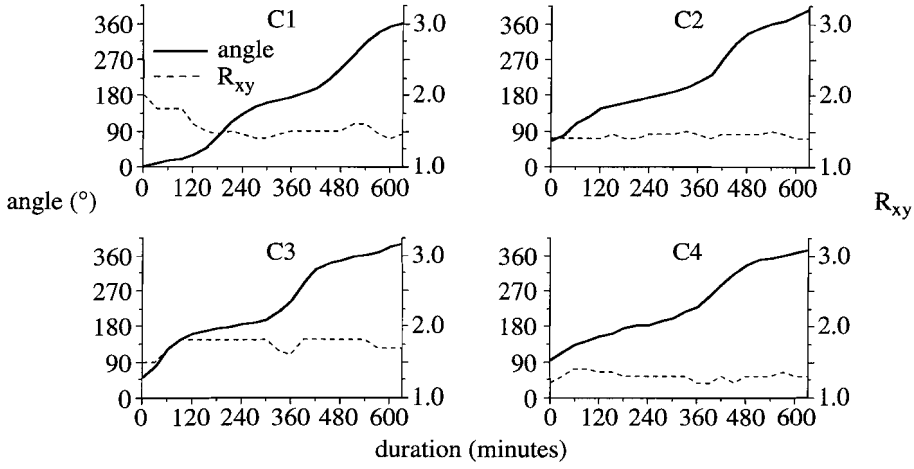

Figure 2.13. Graphs showing the orientation of the objects long axis (solid line) and change in shape (dashed line) of the objects plotted against duration of deformation. See figure 2.14 for explanation of orientation.

We have monitored the rotational behaviour and change in shape of the oblong camphor objects in our experiment. Only the shape of the core was measured; the developing wings were not taken into account. Figure 2.13 shows the orientation of the object long axis with time. Figure 2.14 shows the theoretically expected and experimentally determined rotation rates against object orientation. The objects show a pulsating rotation rate and the orientation at which the experimental minimum and maximum values occur, parallel and perpendicular to the flow plane, respectively, fit well with the theoretically expected values for elliptical objects in a Newtonian fluid. However, the rotation rate of the objects in our experiment is relatively low compared to theoretically expected values for objects with the same aspect ratio (fig. 2.14). Figure 2.15 shows the comparison of our results with other values; again, our experiment shows consistently low rota

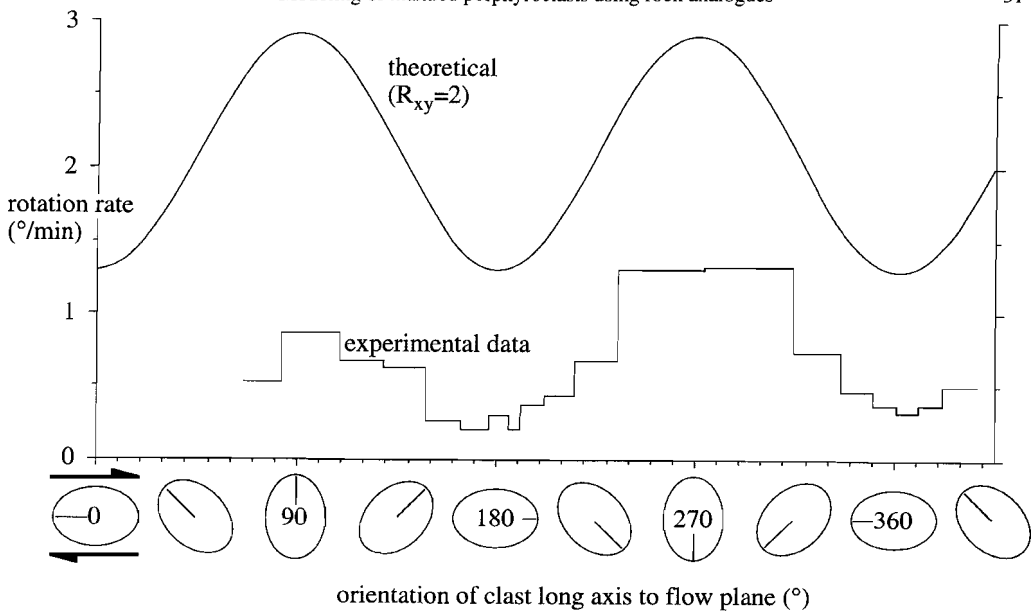

Figure 2.14. Graph showing rotation rate versus the angle of the object long axis of clast C2 to the flow circle. The lower curve shows the mean experimental values. The upper curve shows the rotation rate of an elliptical object with an aspect ratio of 2 subjected to Newtonian simple shear at $\dot{\gamma}=2.6\cdot10^{-3}$ (s^{-1}).

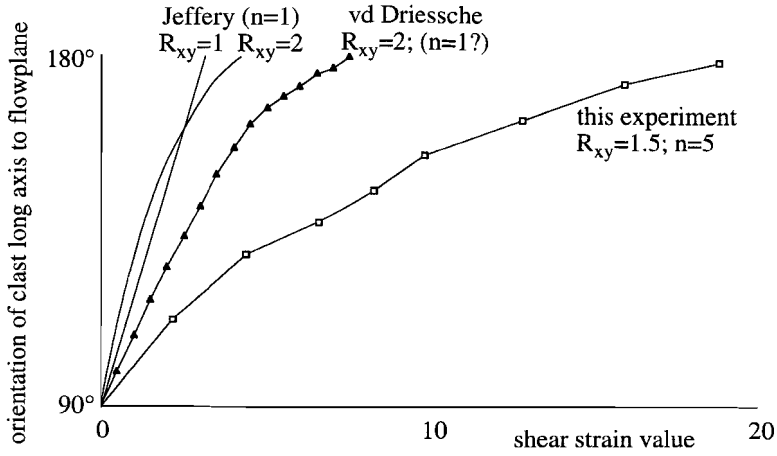

Figure 2.15. Graph of orientation versus shear strain showing the difference in rotational behaviour of objects in simple shear flow. Shown are theoretical data derived from Jeffery (1922), data from an experiment by Van Den Driessche and Brun (1987) and data from object C2 in this experiment. R_{xy} = length/width of the object; n = stress exponent of power-law flow.

tion rates. Recent experiments by Passchier and Sokoutis also give a first indication of lower rotation rates in non-Newtonian materials (Passchier and Sokoutis pers. comm.).

Besides the rotation rate, the aspect ratio of the camphor objects changes with progressive orientation; it varies with time as the object is periodically shortened and extended in response to its orientation in the incremental flow field. Such behaviour can be expected in non-coaxial flow (Simpson and De Paor 1993). Another deviation from the theoretical model is that the minimum

rotation rate does not seem to depend on the R_{xy} value of the objects (fig. 2.16). This may be due to the existence of the wings which make the objects respond as if they had higher R_{xy} values when they are positioned with the long axis parallel to the flow plane.

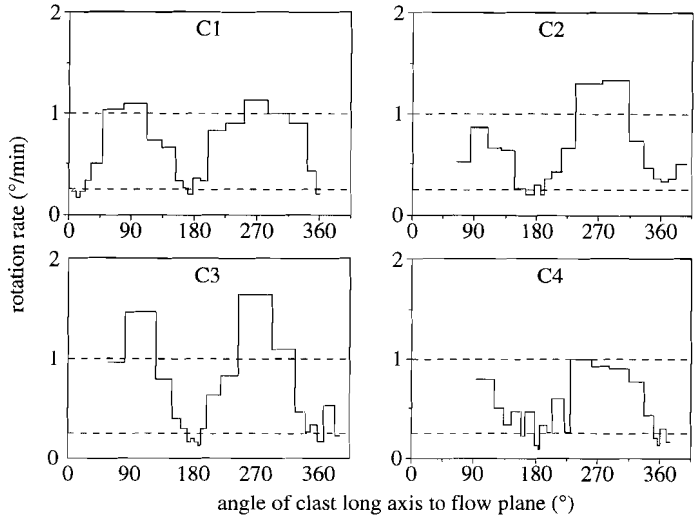

Figure 2.16. Graphs showing the mean rotation rate versus orientation for all four objects.

2.10 Discussion

The results of our experiment partly confirm those of earlier work with Newtonian fluids, but also shows a number of differences that are partly due to the experimental set-up that we have chosen. In our case, wings of δ-objects develop from material created in the rim of deformable objects that were homogeneous at the onset of the deformation. This may be comparable to the development of natural mantled porphyroclasts that form by development of a core and mantle structure, and subsequent deformation of the recrystallised mantle. It is difficult to explain, however, why recrystallisation in our experiment was restricted to the initial stages of deformation. It may be due to the stress gradient set up by the rectangular object; this stress gradient would cause stress concentration at the corners of the object. After the object obtained a rounded shape, recrystallisation may have stopped.

The high shear strain values reached in our experiment serve to illustrate that once a δ-object is established, and if the central object does not recrystallise further, the δ-shape is stable up to high strain. The wings wrap in an elliptical way around the central object, and eventually thin to such an extent that they become almost invisible (figs. 2.5l and 2.6). This confirms the model proposed by Passchier and Simpson (1986).

During the experiment, a strong crystallographic preferred orientation developed in the crystalline OCP matrix. However, no change in the symmetry of the flow patterns or in the distribution of incremental strain values and orientations was observed to coincide with this development.

It seems that, at least in our experiment, the development of a crystallographic preferred orientation in the matrix has little influence on the history of development of δ-objects.

The ellipsoidal shapes of the porphyroclasts did not have a significant effect on the development of wings, but the porphyroclasts did show the expected pulsating rotation rate of elliptical objects.

Our experimental results differ from those of previous workers in two important aspects: 'bow-tie' shaped flow perturbations developed around the objects, rather than the 'eye-shaped' perturbations expected theoretically and observed in earlier experiments; and camphor objects rotated significantly more slowly than theoretical expectations and other earlier experiments.

One of the main differences between the rheology of our sample materials and those of other workers is that ours are strongly non-Newtonian, and follow power-law behaviour (fig. 2.3; Bons and Urai 1994). It is therefore possible that the non-Newtonian behaviour of our materials is responsible for the deviant behaviour. Experimental work by C. Passchier and D. Sokoutis (Passchier *et al.* 1993) on Newtonian and non-Newtonian non-crystalline fluids suggests that stair-stepping mantled objects only form in non-Newtonian fluids. Newtonian fluids give wings that are in line and lack stair-stepping. Observations on the rotation rate of a spherical rigid central object in the mantles of objects studied by Passchier *et al.* (1993), show that these objects also rotate more slowly than would be theoretically expected, though not as slowly as the values obtained in the experiment described in this paper. The set-up of our experiment, however, makes it possible that the camphor objects were subject to drag against the glass plates and the effect may therefore partly be caused by drag and partly by the non-Newtonian nature of the OCP matrix.

2.11 Consequences for the interpretation of natural δ-objects

Our experiment shows that natural δ-objects can be successfully modelled if high strain values are accumulated by non-coaxial flow. This experiment indicates that δ-objects with shapes like figures 2.5g and 2.5h, which are relatively common, must have experienced a considerable amount of shear strain to develop. However, quantification of shear strain from natural δ-objects is generally difficult since deformational conditions (rheologies of matrix and object, strain rate, homologous temperature, etc.) are usually unknown. δ-objects with spiral wings as shown in figures 2.5i to 2.5l are comparatively rare, possibly because such high strain values are not often reached in nature.

2.12 Conclusions

The flow perturbation around camphor objects in a non-Newtonian matrix of OCP subjected to overall simple shear has a bow-tie shape which is different from that predicted theoretically and observed experimentally for Newtonian fluids. As a consequence of the bow-tie shaped perturbation, the δ-objects in our experiment develop a stair-stepping geometry. The wings of the δ-objects spiral around the central object and gradually become thin and vague with progressive deformation, since no material can be added to the wings while they continue to stretch. Deformation is strongly variable around a developing δ-object; it ranges from approximately simple shear in the far-field to nearly rigid body rotation within the porphyroclast. Rotation rates of the porphyroclasts are relatively low when compared to theoretical values for elliptical objects

in Newtonian fluids.

This experiment shows that non-Newtonian, crystalline analogues give more and better information than Newtonian fluids, as the geometry of the resulting structures can be different.

Acknowledgements -We thank Paul Bons and Mark Jessell for writing the application 'Marker Analysis' and refining it to our needs. C. E. ten Brink thanks Paul Bons for the endless discussions on deflection and his effort to create the program that generated figure 2.12. J. Van Den Driessche and an anonymous reviewer are thanked for their comments on the original manusript. T.H. Bell encouraged us to do this experiment by his critical remarks on rotation.

Appendix

The way in which deformation parameters are defined is shown in figure 2.A1 which is a Mohr representation for a deformation tensor **F** (Passchier 1988):

$$\mathbf{F} = \begin{bmatrix} a & b \\ c & d \end{bmatrix}$$

Useful equations to determine deformation parameters from the Mohr diagram are:

$$R_f = \frac{1+e_1}{1+e_2} = \frac{T+R}{T-R} \qquad \text{A1.1}$$

$$W_f = \frac{Q}{R} \qquad \text{A1.2}$$

$$A_f = (1+e_1)\cdot(1+e_2) = (T+R)\cdot(T-R) \qquad \text{A1.3}$$

$$\beta_f = \varphi - \alpha \qquad \text{A1.4}$$

where:

$$T = \tfrac{1}{2}\cdot\sqrt{(a+d)^2+(b-c)^2}$$

$$R = \tfrac{1}{2}\cdot\sqrt{(a-d)^2+(b+c)^2}$$

$$Q = \tfrac{1}{2}\cdot(b-c)$$

$$S = \tfrac{1}{2}\cdot(d+a)$$

$$\sin\alpha = \frac{Q}{T}$$

$$\sin 2\varphi = \frac{(a-S)\cdot S-(c+Q)\cdot Q}{R\cdot T}$$

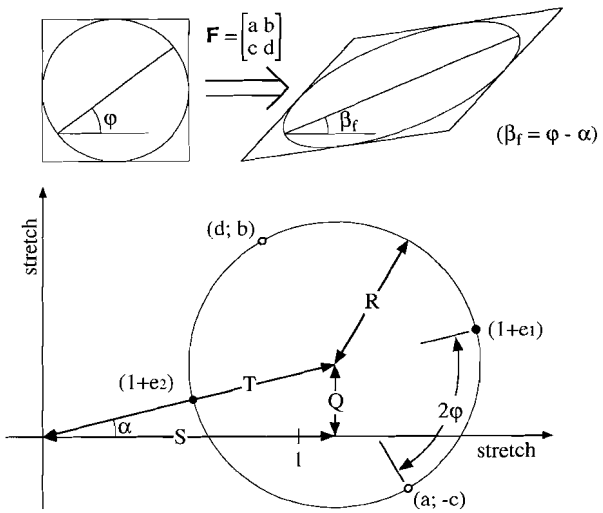

Figure 2.A1. Top - deformation of a square showing the orientation of the strain ellipse. Bottom - Mohr diagram for the deformation tensor **F**, illustrating the derivation of deformation parameters. See explanation in the text.

Addendum to Chapter 2

Strain rates and object rotation rate in a circular shear zone

The preceding Chapter is reprinted from the article by Ten Brink and Passchier, 1995, Journal of Structural Geology, Vol. 17, No. 1, pp 131 to 146. In this article, no explicit attention was given to:

1- The distribution of angular velocities and associated shear strain rates in a circular shear zone; consequently, it is not clear what the 'imposed shear strain (rate)' represents, especially since the matrix in Chapter 2 has a power-law stress-strain rate relation.

2- The rotation rates of rigid (or nearly rigid) objects in a circular shear zone.

These are important points which require discussion, in order to permit easy comparison of the results and conclusions of Chapter 2 to the experiments described in subsequent Chapters. The aim of this addendum is to clarify points not discussed in Ten Brink and Passchier (1995). Furthermore, some minor errors present in Chapter 2 are corrected.

2A.1 Shear strain (rate) in a circular shear zone

Shortly after publication of the preceding Chapter (Ten Brink and Passchier, 1995), a paper by Masuda *et al.*, which is highly relevant to Chapter 2 was published (Masuda *et al.*, 1995). Masuda (pers. comm.) pointed out an error in Chapter 2 regarding the strain (rate) estimates. What follows is based on Masuda *et al.* (1995).

2A.1.1 Object free case

Masuda *et al.* (1995) derived expressions for the angular velocity and shear strain rate in a circular shear zone (Couette flow) without embedded objects. In this case, the basic equation of the time-independent flow of non-Newtonian material is given by:

$$\dot{\gamma} = k\tau_{r\theta}^{n}, \qquad \text{A2.1}$$

where $\dot{\gamma}$ is the tangential shear strain rate, k is a constant, $\tau_{r\theta}$ is the tangential shear stress and n is the stress exponent. The angular velocity ($\dot{\theta}$) and shear strain rate ($\dot{\gamma}$) at radial distance (r) are given by (Masuda *et al.* 1995, equations 7 and 8):

$$\dot{\theta}(r) = \frac{\dot{\omega}_i - \dot{\omega}_e}{R_i^{-2n} - R_e^{-2n}} \cdot \frac{1}{r^{2n}} + \frac{R_i^{2n}\dot{\omega}_i - R_e^{2n}\dot{\omega}_e}{R_i^{2n} - R_e^{2n}}, \qquad \text{A2.2a}$$

and:

$$\dot{\gamma}(r) = \frac{\dot{\omega}_i - \dot{\omega}_e}{R_i^{-2n} - R_e^{-2n}} \cdot \frac{-2n}{r^{2n}}. \qquad \text{A2.3a}$$

Here, $\dot{\omega}_i$ and $\dot{\omega}_e$ are the angular velocities at the inner ($r=R_i$) and outer ($r=R_e$) boundaries respectively. Using the values of the experiment described in Chapter 2: $R_i=6.0\cdot10^{-3}$ m, $R_e=9.0\cdot10^{-3}$ m, $\dot{\omega}_i=0$, $\dot{\omega}_e=0.5$ RPH$=8.7\cdot10^{-4}$ rad s^{-1} and n=5, the angular velocity and shear strain rate as a function of r are given by:

$\dot{\theta}(r)=8.85\cdot10^{-4} - 5.35\cdot10^{-26}\cdot r^{-10}$ rad s^{-1} and A2.2b

$\dot{\gamma}(r)=5.35\cdot10^{-25}\cdot r^{-10}$ s^{-1}. A2.3b

Figure 2A.1 shows how $\dot{\theta}$ and $\dot{\gamma}$ vary as a function of r within a circular shear zone using equations A2.2b and A2.3b. Note that this is directly comparable to the experimental shear zone when no objects are present. The same functions drawn for n=1 and n=3 are shown for comparison. As shown by Masuda *et al.* (1995) and in figure 2A.1a, the angular velocity is not linearly distributed (broken line) over the width of the circular shear zone, not even for Newtonian materials (n=1). This means that the shear strain rate is not constant over the shear zone, as was assumed in Chapter 2. The shear strain rate in that part of the shear zone where the clasts of the experiment of Chapter 2 were situated (r=6.7-7.5·10^{-3} m) ranges from ~3·10^{-3} to ~1·10^{-3} s^{-1} for n=5. The value for the shear strain rate as used in Chapter 2 was 2.6·10^{-3} s^{-1} and is mostly higher than the theoretical values when no object is present.

The values for shear strain rate within the shear zone are not affected by adding a constant to the angular velocity for every radius. This means that the shear strain rate would remain the same when the outer grip is stationary and the inner grip is rotating at 8.7·10^{-4} rad s^{-1} but in the opposite direction.

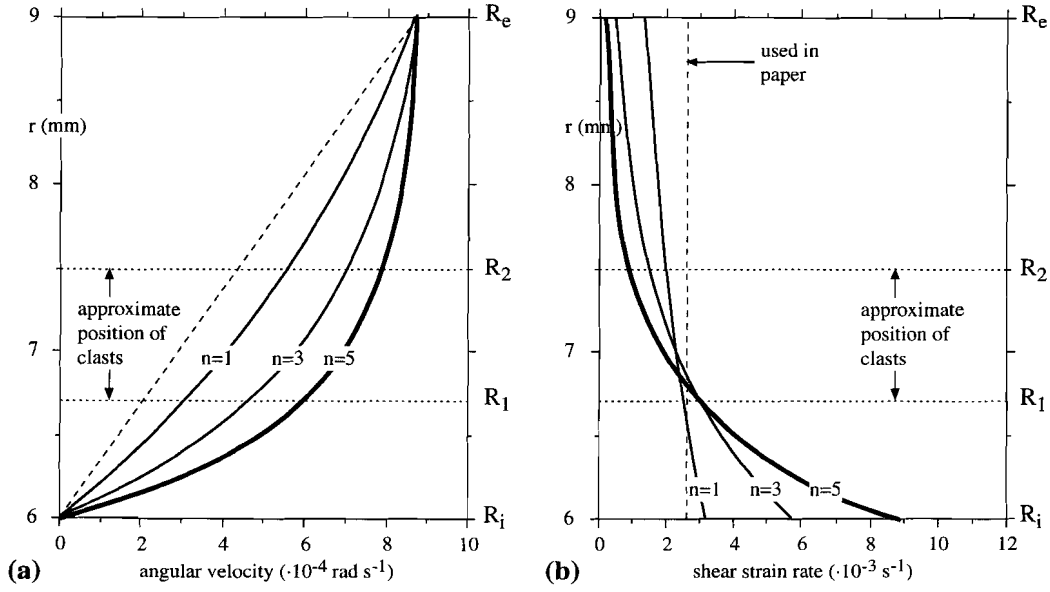

Figure 2A.1. Graphs showing the variation of **(a)** angular velocity and **(b)** shear strain rate over a circular shear zone for power-law materials with n=1, 3 and 5. The dashed line in (a) shows a linear increase in angular velocity with radius. The dashed line in (b) indicates the value for shear strain rate that was used in Chapter 2. The approximate position of the clasts described in Chapter 2 is indicated.

2A.1.2 The effect of a rigid object

When a (relatively) rigid object is present in a circular shear zone, the dependence of $\dot{\theta}$ and $\dot{\gamma}$ on r are altered. As a first step to gain insight into this problem, consider a ring of rigid material placed in the shear zone and rotating along with the flow (fig. 2A.2). In addition, assume that the outer grip rotates as fast as in the case without a rigid ring. This will result in

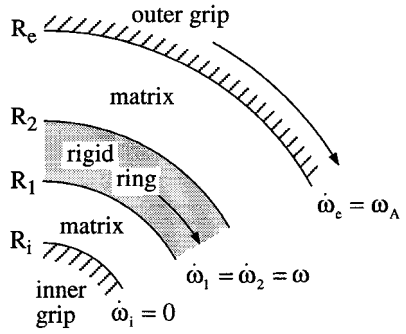

Figure 2A.2. Line drawing showing the ring placed in the circular shear zone to simulate the effect of the presence of a rigid object.

more deformation in the parts of the shear zone that are not occupied by the rigid ring. The angular velocity within the ring must remain constant since it is rigid. Furthermore, the torque (M) applied on the outer grip is completely transferred over the matrix material and rigid ring towards the inner grip. In order to calculate the angular velocity of the ring, I use equation 9 from Masuda *et al.* (1995) for the shear stress ($\tau_{r\theta}$) in a circular shear zone:

$$\tau_{r\theta} = \left(\frac{1}{k} \cdot \frac{\dot{\omega}_i - \dot{\omega}_e}{R_i^{-2n} - R_e^{-2n}} \cdot \frac{-2n}{r^{2n}} \right)^{\frac{1}{n}}, \qquad \text{A2.4}$$

where k is the same constant as in equation A2.1. Now, the fundamental equations for torque (M) and force (F) are given by:

$M = F \cdot r$ and
$F = \tau \cdot A$, (A=area, for a cylinder of height h: $A = 2\pi rh$),

which, for an annular shear zone give:

$M = \tau \cdot A \cdot r = \tau \cdot 2\pi rh \cdot r$ or

$$M(r) = r^2 \cdot \tau_{r\theta} \cdot 2\pi h. \qquad \text{A2.5}$$

Using equations A2.4 and A2.5, the torques at the inner and outer boundaries of the shear zone in which a rigid ring occupies the space from R_1 to R_2 (radii $R_i<R_1<R_2<R_e$ with respective angular velocities $\dot{\omega}_i, \dot{\omega}_1, \dot{\omega}_2, \dot{\omega}_e$) are hence given by:

$$M(R_i) = R_i^2 \cdot \left(\frac{1}{k} \cdot \frac{\dot{\omega}_i - \dot{\omega}_1}{R_i^{-2n} - R_1^{-2n}} \cdot \frac{-2n}{R_i^{2n}} \right)^{\frac{1}{n}} \cdot 2\pi h \quad \text{and}$$

$$M(R_e) = R_e^2 \cdot \left(\frac{1}{k} \cdot \frac{\dot{\omega}_2 - \dot{\omega}_e}{R_2^{-2n} - R_e^{-2n}} \cdot \frac{-2n}{R_e^{-2n}} \right)^{\frac{1}{n}} \cdot 2\pi h.$$

Since the torque in the shear zone is constant:

$M(R_i)=M(R_e)$.

If we now use $\dot{\omega}_1 = \dot{\omega}_2 = \omega$ (the angular velocity of the rigid ring), $\dot{\omega}_i=0$ and $\dot{\omega}_e=\omega_A$, this yields:

$$\left(\frac{-\omega}{R_i^{-2n} - R_1^{-2n}}\right)^{\frac{1}{n}} = \left(\frac{\omega - \omega_A}{R_2^{-2n} - R_e^{-2n}}\right)^{\frac{1}{n}}. \qquad \text{A2.6}$$

Therefore, the angular velocity of the rigid ring is given by:

$$\omega = \omega_A \cdot \frac{R_1^{-2n} - R_i^{-2n}}{R_e^{-2n} - R_2^{-2n} + R_1^{-2n} - R_i^{-2n}}. \qquad \text{A2.7}$$

The experimental data of Chapter 2 ($R_i=6\cdot10^{-3}$, $R_e=9\cdot10^{-3}$ m and $\omega_A=8.7\cdot10^{-4}$ rad s^{-1}) together with the values $R_1=6.7\cdot10^{-3}$ and $R_2=7.5\cdot10^{-3}$ m can be inserted in equation A2.7. These values of R_1 and R_2 are chosen to represent a rigid ring occupying the space equivalent to the approximate positions of the clasts in the shear zone of Chapter 2. The resulting value of ω is:

$\omega=0.881\cdot\omega_A$.

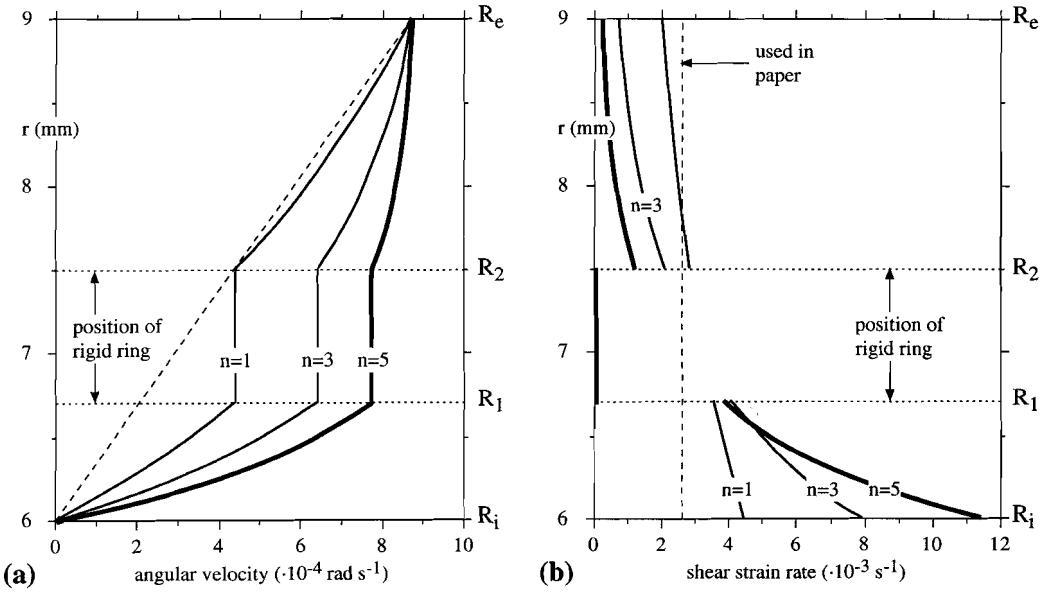

Figure 2A.3. As fig.2A.1 but with a rigid ring placed within the shear zone.

Figure 2A.3 shows how $\dot{\theta}$ and $\dot{\gamma}$ are a function of r within the circular shear zone of the experimental set up, when a rigid ring with radii approximating the positions of the clasts is present in the shear zone. Within the ring, the shear strain rate is zero. Similar plots for n=1 and n=3 are shown for comparison. These graphs, based on equations A2.2, A2.3 and A2.7, show that the shear strain rate in the deforming matrix is increased compared to the situation where no rigid

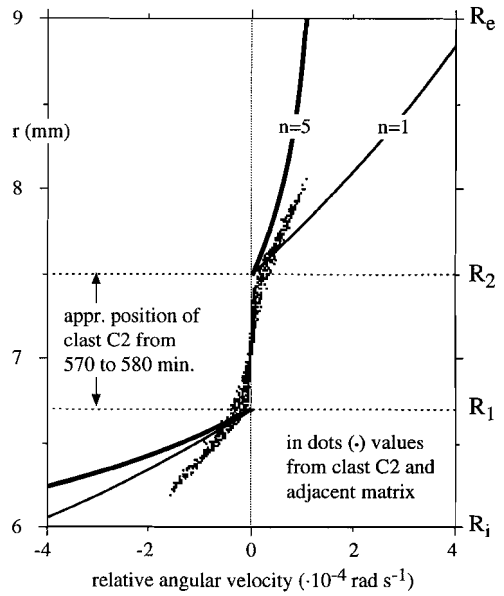

Figure 2A.4. Graph showing relative angular velocities of the markers in the experiment of Chapter 2 and the theoretical values in a circular shear zone where a rigid ring is present at the approximate position of the clast in the experiment for power-law materials with n=1 and 5.

ring is involved. It can be seen that the shear strain rates adjacent to the inside and outside of the rigid ring are very different: $\sim 4 \cdot 10^{-3}$ and $\sim 1 \cdot 10^{-3}$ s^{-1} respectively for n=5. The value used in Chapter 2 ($2.6 \cdot 10^{-3}$ s^{-1}) is only a little lower than the average value ($\sim 2.5 \cdot 10^{-3}$ s^{-1}) for shear strain rate when a rigid ring is considered to rotate along with the flow.

The relative displacements of the marker particles in the clast and the adjacent matrix in the experiment of Chapter 2 were used to evaluate their angular velocities with respect to the reference frame. Since in the experiment it was not possible to work with an external reference frame, the angular velocities are calculated from a co-ordinate system that rotates along with the chosen reference particle (see fig. 2.2b in Ch. 2). In the experiment, the reference particle was a marker at the approximate centre of clast C2 (see fig. 2.11 in Ch. 2). Looking at the relative displacements, the particles near the inner grip rotate anti-clockwise and particles near the outer grip rotate clockwise with respect to the reference particle. Likewise, the angular velocities of the particles will show a change in sign from inner to outer grip. The relative angular velocities of the marker particles can be compared to the theoretical values, as shown in figures 2A.1 and 2A.3, when a constant is added to the theoretical values such that, at a radius equivalent to that of the centre of the clast, the theoretical angular velocity is zero. Figure 2A.4 shows the relative angular velocities (dots) of markers in clast C2 and its adjacent OCP-matrix (between 570 and 580 minutes running time) together with the relative angular velocities for a matrix with n-values of 5 and 1 respectively, when a rigid ring is present (lines). The experimental values are calculated from the displacement parallel to the flow direction, displacements perpendicular to the flow direction are not considered. The slope of the dot cluster at the approximate position of the clast indicates that clast C2 is rotating. The continuous curves are calculated with equations A2.2, A2.3 and A2.7, while the difference in angular velocity ($\dot{\omega}_e$-$\dot{\omega}_i$) between inner and outer grip was set at $8.7 \cdot 10^{-4}$ rad s^{-1}. It can be seen that the absolute value of the relative angular

velocity in the OCP at the side of the inner grip is lower than the theoretical values, even when n=1. The relative angular velocity in the OCP at the side of the outer grip is in between the theoretical values for n=5 and n=1. The shear strain rate is related to the reciprocal of the slope of the $\dot{\theta}$-curves in figures 2A.1a, 2A.3a and 2A.4. Due to the distributed nature of the data, it is not possible to find a single curve describing the experimental values of relative angular velocities (dots in fig. 2A.4) on either side of the clast. However, an estimate can be made which can be converted into shear strain rate using (Masuda *et al.* 1995, eq. 1):

$$\dot{\gamma} = r \cdot \frac{d\dot{\theta}}{dr}. \qquad \text{A2.8}$$

The calculated shear strain rates at the sides of the inner and outer grip are in the order of $1.5 \cdot 10^{-3}$ and $1.0 \cdot 10^{-3}$ s^{-1} respectively and certainly do not reach the value of $2.6 \cdot 10^{-3}$ s^{-1} that was used in Chapter 2. The data describing the relative angular velocities of the markers in the 5 succeeding 10 minute intervals (up to 630 minutes of deformation) lead to similar shear strain rates. The low value of shear strain rate at the inner grip side of clast C2 should be considered with care since it falls completely out of the range of the theoretical values.

In relation to these considerations, it should be noted that the clasts in the experiment do not form a complete and totally rigid ring. Therefore, the values for $\dot{\theta}$, $\dot{\gamma}$ and ω, as calculated without a rigid ring and with a rigid ring, represent the maximum range of the experimental values, assuming that interfacial slip resistance between the deforming material (matrix and clasts) and the glass plates can be neglected.

2A.1.3 The effect of interfacial slip resistance on shear strain (rate)

The experimental data, presented in figure 2A.4, demonstrate that the shear strain rates on the sides of both inner and outer grip of the clasts differ less than the shear strain rates that were calculated for the inner and outer area of the matrix when a rigid ring was supposed to rotate along with the flow. A cause that can diminish the difference in shear strain rate between inner and outer area is a lower angular velocity of the rigid ring. When the ring rotates slower than the calculated value of $0.881 \cdot \omega_A$, the difference in angular velocity and, hence, the shear strain rate in the matrix, between the ring and the outer grip is increased. Concomitantly, the difference in angular velocity, and the associated shear strain rate in the matrix, between the ring and the inner grip is reduced. The question now arises what could cause a reduction of the angular velocity of the rigid ring.

A pure frictional resistance can account for a lower angular velocity of the ring, but only in a stick-slip way. To clarify this, consider two parallel plates exerting equivalent normal stresses on opposing sides of a rigid block. Assuming that the frictional shear stress (τ_f) is linearly related to the friction coefficient (f) and the applied normal force (σ_n; $\tau_f = f \cdot \sigma_n$), a resisting stress originates when a tangential force is applied to one plate while the other is kept stationary. Sliding starts when the tangential force exceeds the frictional shear stress. In real situations, two interfaces will not be identical and sliding will only occur along the interface with the lower friction coefficient. When only one of the plates in the rings-shear apparatus is rotating, this would imply that the rigid ring is either stationary, or rotating at the same angular velocity as the driven plate.

This is certainly not the case in the ring-shear experiment since sticking of the clasts to the upper or the lower glass plate would imply the absence of shear in the outer or the inner matrix region, which is not observed. With only frictional resistance, slip along both interfaces may happen (although never simultaneously) in a 'stick-slip' situation when the maximum friction coefficient transfers from one interface to the other. However, such stick-slip behaviour is not found in the ring-shear experiment, at least not on a measurable time-scale.

Now consider that a viscous layer is present on both sides between the block and the confining plates. A tangential force exerted on one plate will cause both of the viscous layers to shear since the shear stress (τ) is proportional to the shear strain rate ($\dot{\gamma}$) and to the viscosity of the layer (η; in a Newtonian material: $\tau=\dot{\gamma}\cdot\eta$). The shear strain rate will be equivalent and uniform in both viscous layers in order to keep the shear stress in the layers at a minimum. The velocity difference between the block and both plates will be equivalent, provided that the viscous layers on both sides have the same thickness (and flow in the layers is laminar and that the layers are Newtonian). When one layer is thinner than the other, the block will have a lower velocity difference with the plate adjacent to the thinner layer and, concomitantly, a higher velocity difference with the other plate. Viscous layers between a rigid ring and the glass plates can thus account for a reduced (but also increased!) angular velocity of the rigid ring.

The glass plates of the ring-shear apparatus were coated with a thin film of silicon grease. A viscous layer is therefore present between the clasts (and the matrix) and the glass plates. Even when this silicon grease film is 'scraped off' from the clasts during the experiment, it is possible that strain softening, of either OCP or camphor, along the camphor-glass contact may have a similar effect as a viscous layer. The velocity contrast between the clasts and the confining glass plates is, however, no longer linearly related to the difference in thickness of the softer camphor layers. This is due to the power-law log(stress)-log(strain rate) behaviour of the camphor.

Not considering the matrix and resisting forces within the apparatus, a frictional resistance between the clasts and the plates will increase the torque that is needed before the upper plate of the ring-shear apparatus starts rotating. As soon as the frictional resistance is exceeded by the applied torque, the rotation rate of the driven plate would accelerate, even when the driving torque remains constant. In contrast, viscous clast-glass interfaces would lead to instantaneous rotation of the upper plate when a torque is applied and the rate of rotation will be a function of the applied torque and the viscosity and thickness of the layers.

The shear induced deformation of the matrix and resisting forces within the apparatus would reduce the rotation rate of the upper plate when a constant torque was the driving mechanism. However, they will have the same effect in both cases. In the ring-shear experiment of Chapter 2, the upper glass plate is driven at constant angular velocity and the torque, needed to rotate the upper plate, is not measured. Up to this point, it is impossible to distinguish between rapidly changing stick-slip behaviour or viscous behaviour of the clast-glass interfaces.

2A.2 Rotation rates of the clasts

As shown above, the assumption of a uniform shear strain rate of $2.6\cdot10^{-3}$ s^{-1} in the experimental shear zone of Chapter 2 is not correct. As a consequence, the rotation rates of the clasts have to be reconsidered. The effect of interfacial resistance as well as the effect of wings developing on a clast will be discussed.

2A.2.1 The effect of shear strain rate on rotation rate of an elliptical object

Figure 14 in Chapter 2 shows that clast C2 (which is, unfortunately, not mentioned in text or caption) rotates at a lower rate than that of an equivalent elliptical object in a Newtonian matrix as predicted by equation 47 of Jeffery (1922):

$$\left(a^2 + b^2\right)\dot{\phi} = \kappa\left(a^2\cos^2\phi + b^2\sin^2\phi\right). \qquad \text{A2.9}$$

Applied to the experimental (2-dimensional) conditions, a and b are the axial dimensions (a>b) of the elliptical object, ϕ represents the angle between axis a and the normal to the direction of shear, $\dot{\phi}$ represents the angular velocity of the object and κ is the shear strain rate. Subject to the constrain that ϕ=0 when t=0, the orientation of the ellipse in time is given by (Jeffery 1922, eq. 48):

$$\tan\phi(t) = \frac{a}{b}\cdot\tan\frac{\kappa\, t\, ab}{a^2 + b^2}. \qquad \text{A2.10}$$

Since a is the long axis of the ellipse, $a/b=R_{xy}$ (the aspect ratio). I introduce α, the angle between the ellipse long axis and the direction of shear ($\alpha = \phi - 90°$, fig. 2A.5), $\dot{\alpha} = \dot{\phi}$ and $\dot{\gamma}=\kappa$. Equations A2.9 and A2.10 can hence be written as:

$$\dot{\alpha} = -\frac{\dot{\gamma}}{R_{xy}^2 + 1}\cdot\left(\left(R_{xy}^2 - 1\right)\sin^2\alpha + 1\right) \text{ and} \qquad \text{A2.11}$$

$$\frac{1}{\tan\alpha(t)} = -R_{xy}\cdot\tan\left(\frac{\dot{\gamma}\, t\, R_{xy}}{R_{xy}^2 + 1}\right). \qquad \text{A2.12}$$

The negative signs appearing here are the result of the chosen mathematical convention (anti-clockwise rotation is positive) and the assumption that dextral simple shear has a positive value. For better comparison, α and $\dot{\alpha}$ are shown in absolute values in figures 2A.6 and 2A.7.

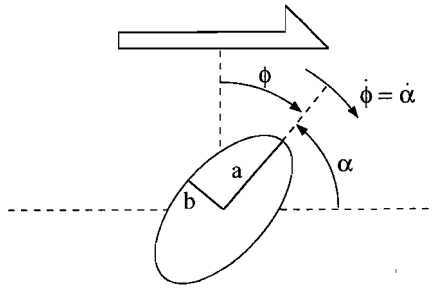

Figure 2A.5. Line drawing showing the relation between a; b, ϕ; $\dot{\phi}$ and α; $\dot{\alpha}$.

From equations A2.9 and A2.11, it is clear that the rotation rate of an ellipse in a Newtonian matrix is linearly related to the shear strain rate. The evolution of orientation and aspect ratio of all 4 clasts in the experiment of Chapter 2 is shown in Figure 13 of Chapter 2. For example, clast C1 has an aspect ratio and orientation of 2.0 and 4° respectively at start. After 630 minutes of deformation the aspect ratio and orientation are 1.45 and 361° respectively.

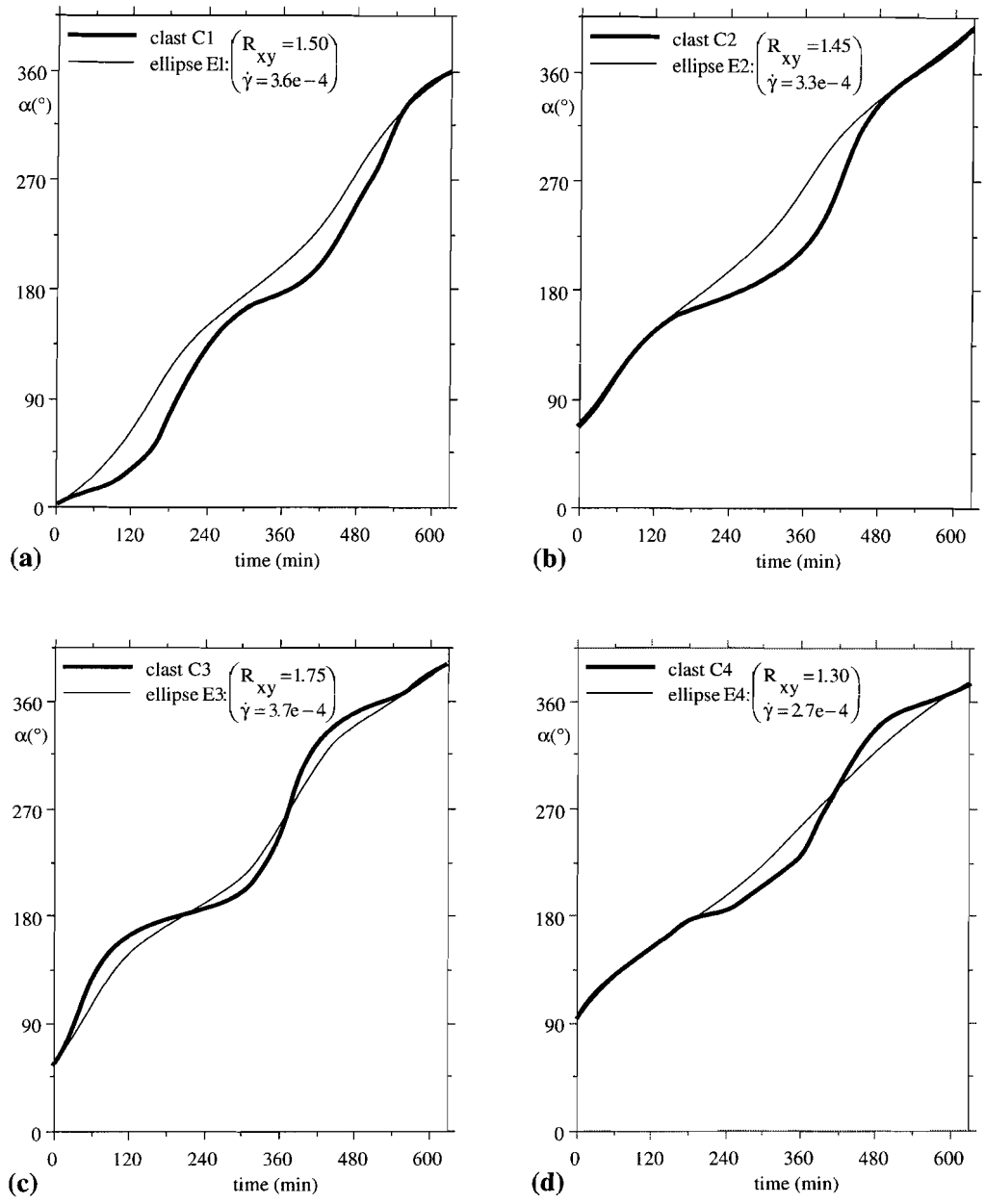

Figure 2A.6. Graphs showing the orientation (α) of the long axis against time of the clasts in Chapter 2 (C1..C4) plus the theoretical curves for elliptical objects (E1..E4) with equivalent aspect ratio (R_{xy}). Shear strain rates ($\dot{\gamma}$) given in the legend. ($\dot{\gamma}$=3.6e-4 means: $\dot{\gamma}=3.6\cdot10^{-4}\ s^{-1}$)

With the aid of equation A2.10 or A2.12 we can evaluate the theoretical average shear strain rates for the individual clasts in Chapter 2. In order to do so, ellipse E1 is defined as the ellipse with an aspect ratio equivalent to the average aspect ratio of clast C1 and an initial orientation equivalent to that of clast C1 ($R_{xy}(E1)=\overline{R}_{xy}(C1)=1.5$; $\alpha_{t=0}(E1)=\alpha_{t=0}(C1)=4°$). Using

equation A2.12 we can calculate that a shear stain rate of $3.6 \cdot 10^{-4}$ s^{-1} will rotate ellipse E1 from $\alpha=4°$ to $\alpha=361°$ in 630 minutes. The shear strain rate value of E1 ($3.6 \cdot 10^{-4}$ s^{-1}) is attributed to the average shear strain rate for clast C1. In a similar way, the average shear strain rates evaluated for clasts C2, C3 and C4 are 3.3, 3.7 and 2.7 ($\cdot 10^{-4}$ s^{-1}) respectively. It should be emphasised that these individual average shear strain rates are in the order of 10 to 15% of the imposed shear strain rate of $2.6 \cdot 10^{-3}$ s^{-1} used in Chapter 2.

The slopes of the curves in Figure 13 of Chapter 2 and figure 2A.6 represent the rotation rate. It can be seen in figure 2A.6 that the difference in slope (or 'amplitude' of the rotation rate) of a clast in the experiment is larger than that of the equivalent elliptical object. This is better shown in figure 2A.7 (similar to Fig. 14 in Chapter 2). The dotted curves in figure 2A.7 show the result of the shear strain rates that were calculated for the ellipses E1 to E4 and are used to draw the thin curves in figure 2A.6. It is inferred that the difference in rotational behaviour is probably the combined result of interfacial resistance between the clasts and glass plates and the development of the wings.

2A.2.2 The effect of interfacial resistance on clast rotation rate

The torque associated with the interfacial resistance between a clast and the glass plates is opposite to the torque exerted by the matrix on the clast. This resistance torque is proportional to the area of the clast. Frictional interface behaviour implies that the resistance torque is also proportional to the normal stress on the glass plates and the camphor-glass friction coefficient. In contrast, viscous interface behaviour implies that the resistance torque is a function of the rotation rate of the object and the thickness and viscosity of the viscous layer.

First consider viscous interface layers. With the restriction that the layers are Newtonian and have a constant thickness, the resistance torque is linearly related to the rotation rate of the clast. This implies that the viscous interface resisting torque will reduce the rotation rate of a clast as a function of its orientation and is similar to a decrease in shear strain rate. In a graph like the ones shown in figure 2A.7, this would lower the curve and reduce its amplitude. So, by scaling the shear strain rate we can eliminate the effect of a Newtonian viscous interface resisting torque. To do this, an average shear strain rate of $6.0 \cdot 10^{-4}$ s^{-1} is used to calculate the rotation rates of the ellipses E1 to E4 (fig. 2A.7, thin continuous curves). This is equivalent to the assumption that a viscous interface layer would reduce the rotation rate proportionally. The maximum rotation rates of the objects now agree quite well with the experimental maxima. This value for shear strain rate ($6.0 \cdot 10^{-4}$ s^{-1}) is only half the value that would be expected from the experimental data for angular velocities in figure 2A.4; it should be noted that the shear strain rates calculated from figure 2A.4 average at $1.25 \cdot 10^{-3}$ s^{-1}.

The thin continuous curves in figure 2A.7 show that it is not possible to obtain the experimental values by scaling the theoretical values for rotation rate of an elliptical object: multiplying the theoretical values by a constant might give the appropriate 'amplitude' but will also increase the minimum rotation rate. Therefore, constant-layer-thickness Newtonian-viscous interface behaviour cannot account for the rotational behaviour of the clasts. It not feasible to evaluate the effect of a power-law viscous interface since the individual interface widths are not known.

Now consider frictional interfaces. The resistance torque is constant when the area of the clast is not changed, sliding of the clasts over the glass plates has no effect on the friction coefficient (for example by reducing the grain size at the glass contact) and there is no change in

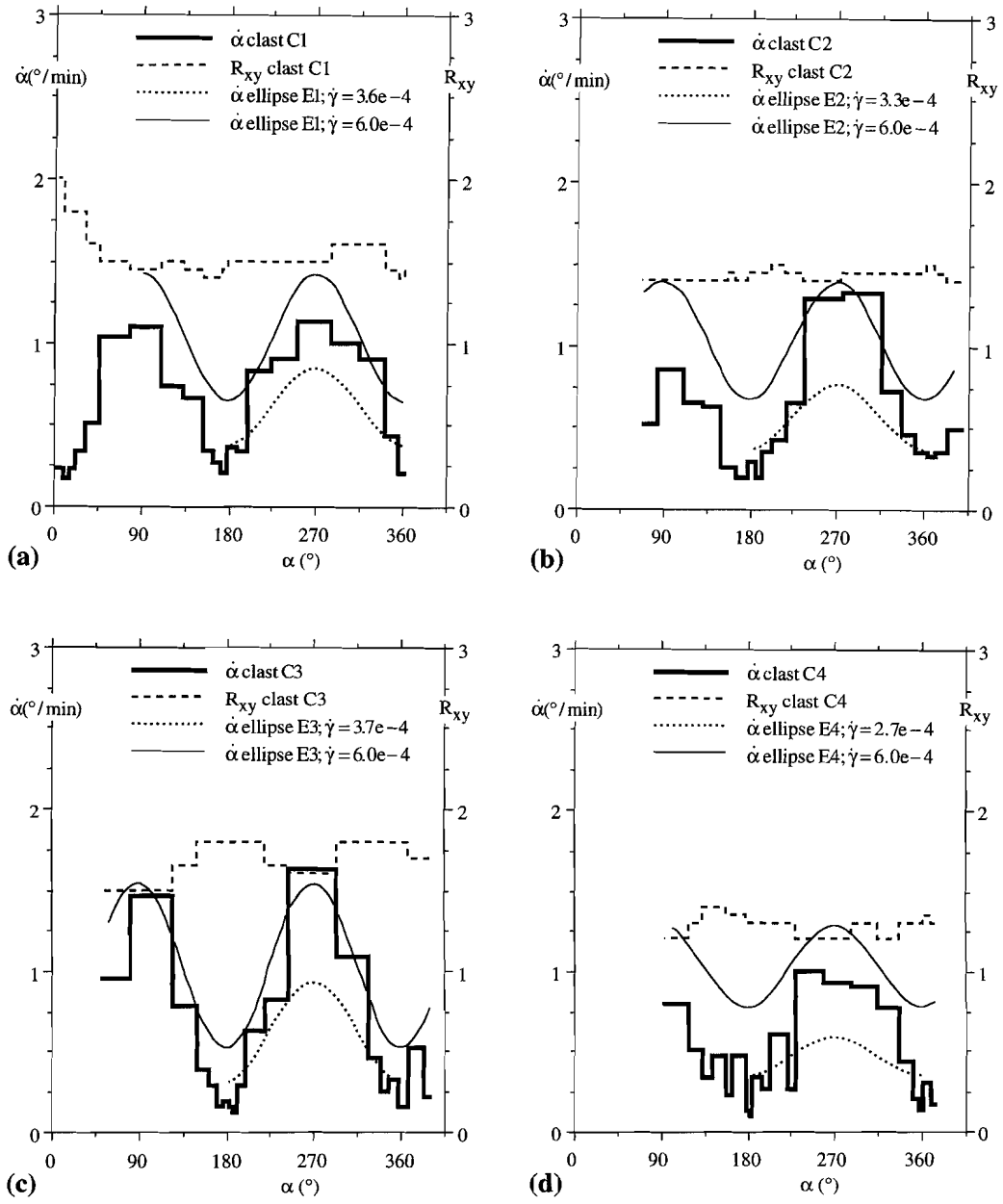

Figure 2A.7. Graphs showing the rotation rate ($\dot{\alpha}$) and aspect ratio (R_{xy}) vs. orientation (α) of the clasts in Chapter 2 (C1..C4) as well as theoretical curves for rotation rate of elliptical objects (E1..E4) at the shear strain rates ($\dot{\gamma}$) given in the legend.

normal stress of the glass plates on the clasts (the confining plates are absolutely flat and cannot move in the 3rd dimension). When we assume that the area of the clast, the normal stress and the friction coefficient are constant, the frictional resistance torque is constant. A frictional resistance torque would thus reduce the forward rotating torque of the matrix on the clast by a

constant value that is independent of the orientation of the clast. This implies that the rotation rate of the clast would be lowered by a constant as well. In a graph like the ones shown in figure 2A.7, this would lower the curve but not change its amplitude.

It is possible that a frictional interface behaviour is responsible for the rotational behaviour but it is impossible to check this in the ringshear apparatus since the normal stress on the clasts cannot be measured. The normal stress can certainly not be taken as constant because the glass slides were pressed more closely together several times during the experiment in order to restore the contact at the grips. For the same reason, there is no use in trying to combine the effects of both friction and Newtonian viscous interface behaviour, in order to evaluate the rotational behaviour of the clasts.

2A.2.3 The effect of the developing wings on clast rotation rate

It was mentioned in Chapter 2 that developing wings may have an influence on the effective aspect ratio of clasts and thus on their effective rotation rate. At the start of the experiment no wings exist and the calculated rotation rates for elliptical objects (E1 to E4) are close to the experimental values as can be seen in figure 2A.6 (for clast C1 this is not directly visible in fig. 2A.6a; This clast shows a diminishing aspect ratio in the first 90 minutes, when an aspect ratio of 2 is used at start, the slope of the experimental curve is closely approximated). If wings develop, part of the wings may possibly be considered to act as an extension of the clast. Since the wings are always at the same position with respect to the flow-plane, this will give the clast a pulsating effective aspect ratio; higher when the clast long axis is parallel to the flow, lower when the clast long axis is perpendicular to the flow (fig. 2A.8). Incorporating an 'effective' aspect ratio for winged objects could explain a lower rotation rate of the clast in all orientations.

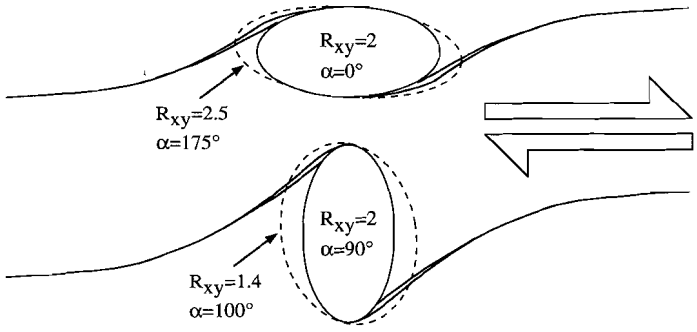

Figure 2A.8. Line drawing indicating how the 'effective' area of the clast (dashed line) changes the aspect ratio and orientation when part of the wings can be considered to act as an extension of the clast.

As wings evolve, material is shed from the clast and its area will diminish. In order to maintain proper contact between sample material and glass plates, the ring-shear apparatus was tightened several times during the experiment, thus flattening the sample by a few μm. The area of the clasts would thus be increased as well as the normal stress on the sample. The glass plates used during the experiment did show a thickness variation of ± 4 μm and it was not possible to check if the plates were mounted absolutely perpendicular to the rotation axis of the ring-shear apparatus. This means that we cannot assume a constant area and normal stress. If, and in what way, the interfacial resistance forces change during the experiment is thus a question still unanswered. Therefore, it is difficult to evaluate the 'effective' aspect ratio's of the clasts in Chapter 2.

2A.3 Conclusions

The shear strain rate, and thus also the accumulated shear, in a circular shear zone is not linearly distributed over the shear zone, not even for Newtonian materials. When relatively rigid objects are incorporated in the shear zone, the distribution of shear strain (rate) within the deforming material becomes more difficult to describe. Resistance between the confining plates and the deforming material has a complicated effect on the rate of deformation within the circular shear zone of a ring-shear apparatus. This implies that, even when the results at first sight appear consistent with existing theories, special care is needed when quantitative measurements are made with experimental data from a ring-shear apparatus. The shear strain rate in the immediate vicinity of the clasts in Chapter 2 is lower than the 'imposed shear strain rate' of $2.6 \cdot 10^{-3}$ s^{-1}. The best estimate of the shear strain rate in the immediate vicinity of a clast is $\sim 1.25 \cdot 10^{-3}$ s^{-1}. This value is evaluated from the relative displacements of marker particles in and around one clast during the last 60 minutes of the experiment. However, it is not certain if this shear strain rate of $\sim 1.25 \cdot 10^{-3}$ s^{-1} existed throughout the duration of the experiment and it may also not apply to the other clasts.

The camphor clasts in Chapter 2 show a pulsating rotation rate which is consistent with the theory; the highest rotation rates are found when the long axis of the clast is perpendicular to the flow plane and the lowest rotation rates are found when the long axis is parallel to the flow plane. The statement in Chapter 2: "Rotation rates of the porphyroclasts are relatively low when compared to theoretical values for elliptical objects in Newtonian fluids." and following text, did not fully take into account the possible complications that may occur in the experiment described there. The distribution of shear strain rate within the circular shearzone can account for a ~50% reduction of the rotation rates of the clasts in Chapter 2. Further reduction of the rotation rates cannot be attributed to a constant (indicating friction) or proportional (indicating viscous interfaces) resistance force alone. It is obvious that resistance forces must be present in the ring-shear apparatus and that these will reduce the rotation rate of the clasts. However, it is not certain on which mechanism these resistance forces are based. The developing wings or the power-law rheology of the matrix may possibly reduce the rotation rate as well. The results of resistance forces, wing development and matrix material together, should account for the still missing ~35% reduction in rotation rate. Unfortunately, their individual contributions cannot be evaluated with the present data.

The implications of the deformational geometry, the non-linearity of the rheology and the effect of the wings on the effective shape of the clasts have been discussed and quantified as much as possible. Nevertheless, too many unknown parameters remain to fully and accurately describe (or model) the rotational behaviour of the clasts in Chapter 2[1]. In future experiments one should try to measure the torque and quantify the friction between sample and glass plates as well as improve the measurements of positions of material points with respect to the overall deformation geometry. Inscribing a reference frame on one but preferably both glass plates will be extremely useful.

[1] I do not think the ending can be right. Donald Justice; Night light.

There is always an easier method.

(Iles' law)

Er is altijd een gemakkelijker manier.

(wet van Iles)

Chapter 3

A linear fluid shear apparatus to model ongoing simple shear allowing direct observation

3.1 Introduction

In Chapter 2 the experimental simulation of the development of a winged clast is shown using a transparent ringshear apparatus and crystalline materials as clast and matrix. A close geometrical resemblance between the experimental results and natural winged clasts was found. Detailed analysis of the experiments revealed that the displacements in and around the objects showed a 'bow-tie' flow pattern and that the objects rotated slower than initially expected.

A suggestion was made that the non-linear rheology of the matrix could lead to the establishment of the bow-tie flow pattern, as found in the ringshear apparatus. The bow-tie flow pattern has been theoretically predicted and experimentally established by Robertson and Acrivos (1970). They found this pattern in simple shear flow of Newtonian material around a cylinder forced to rotate slower than the rate predicted by Jeffery (1922) for a suspended particle.

The Addendum to Chapter 2 gives more insight into the problem of the rotation rates of the clasts. However, it could not be established with certainty if the slower rotation of the objects was due to the rheology of the matrix, friction in the ringshear apparatus or the effect of developing wings.

If the bow-tie flow pattern in Chapter 2 was not the result of impeded rotation rate of the clasts, it remains unsolved if the rheology of the matrix, the boundary conditions of the experiment or possibly other factors determine the flow pattern around the objects. The matrix material in Chapter 2 (OCP) is a well known material as far as rheological properties are concerned. Despite investigation on several organic compounds (Bons 1993), no other relatively user-friendly rock analogues were found to test the influence of the rheology of a crystalline matrix with the use of a ringshear apparatus. The boundary conditions in the ringshear apparatus are difficult, though not impossible, to change or test and experiments with the apparatus are tedious and time consuming.

To circumvent some of the difficulties mentioned above, another approach was taken as described in this and the next Chapter. An apparatus was used with the following characteristics. The use of a linear shear rig reduces the problem of the (shear) strain rate distribution although insertion of an object must result in gradients of shear strain (rate) and stress within the matrix. A belt-mechanism in the apparatus allows the user to impose ongoing shear and a gearbox allows for different experimental shear strain rates. The use of a fluid as matrix material simplifies sample preparation and allows the objects to be free-floating, thus eliminating frictional forces acting on them. By choosing the right fluids, the influence of rheology on the flow pattern can be tested. Using fluids as matrix materials seems to be appropriate since no detectable influence of a developing crystallographic preferred orientation on the flow pattern was found in Chapter 2. The lay-out of the newly developed linear fluid shear apparatus also allows us to investigate the effect of different boundary conditions on the flow.

After an introduction in fluid dynamics, this Chapter introduces the two fluids that were chosen for the experiments: glycerol to model a Newtonian matrix and a solution of polyacrylamide (pAA) to simulate a non-linear matrix. A description of the linear fluid shear apparatus, the additional equipment, and the methods that were used to determine the flow pattern in the fluids and the rotation rate of the objects concludes this Chapter.

3.2 Flow behaviour of fluids; theory and measurements

Viscosity (η) is a measure of resistance of a substance to a change in shape taking place at a given speed. The viscosity of most liquids decreases with an increase in temperature. When the viscosity is not influenced by the shear strain rate (at constant temperature) the fluid is termed Newtonian. Fluids also change their viscosity with pressure. Most fluids have a positive viscosity/pressure coefficient. Non-Newtonian fluids show a variable viscosity with shear- or strain rate. The addition of dissolved or fine suspensions of material can greatly increase the viscosity of the now impure fluid volume.

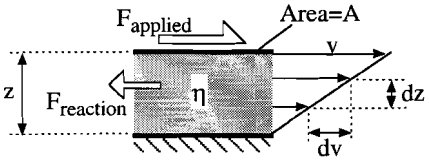

Figure 3.1. Physical system of simple shear flow.

3.2.1 Linear and non-linear viscosity

In this section, a brief description of the possible responses of liquids to shear stresses and shear strain rates is given. Some general definitions of fluid behaviour are stated. Consider two parallel and plane surfaces of area A at a distance z, and a fluid of η viscosity between these plates (fig. 3.1). If one of the surfaces is moved in its own plane at a velocity v by an applied force F, then the magnitude of this force, assuming laminar flow conditions, is proportional to the viscosity η of the fluid, to the ratio v/z, and to the surface A. The ratio F/A is called the shear stress τ:

$$\tau = \frac{F}{A} \text{ (Pa)}. \qquad 3.1$$

The ratio v/z is called the shear strain rate $\dot{\gamma}$:

$$\dot{\gamma} = \frac{v}{z} \text{ (s}^{-1}\text{)}. \qquad 3.2$$

The shear stress is proportional to the shear strain rate and to the viscosity:

$$\tau = \dot{\gamma} \cdot \eta \left(\text{or} \quad \dot{\gamma} = \frac{\tau}{\eta} \right). \qquad 3.3\ (3.4)$$

Viscosity therefore is:

$$\eta = \frac{\tau}{\dot{\gamma}} \text{ (Pa s)}. \qquad 3.5$$

Shown in figure 3.1 is a linear velocity distribution between the two planes. This is not necessarily the case in other flow geometries. For flow in round pipes, the shear stain rate is given by:

$$\dot{\gamma} = \frac{dv}{dz} \text{ or } \frac{dv}{dr}. \qquad 3.6$$

For flow between two concentric cylinders, one of which is rotating, the shear strain rate is:

$$\dot{\gamma} = -r\frac{d\omega}{dr}. \qquad 3.7$$

This type of flow is known as Couette flow. Generalising for Newtonian fluids under laminar conditions:

$$\eta = \tau\frac{dz}{dv}. \qquad 3.8$$

Typical rheograms of a Newtonian (*or linear*) liquid are shown in figure 3.2. η is called the dynamic viscosity and is by geologists normally expressed in SI-units as Pascal seconds (Pa s).

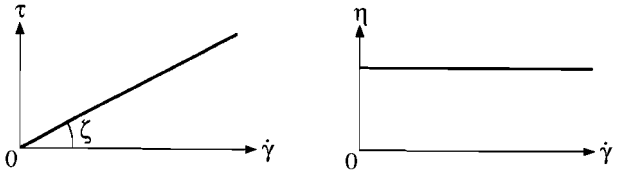

Figure 3.2. Typical rheograms of a Newtonian liquid. Dynamic viscosity (η)=tan ζ=constant.

In fluid dynamics, the dynamic viscosity is normally expressed in Poises (P) or Centipoises (cP): 1 (Pa s) = 10 (P) = 10^4 (cP). When using measuring devices in which the specific gravity of the medium or the gravity of the measuring device itself is involved, the dynamic viscosity cannot be measured directly. The viscosity measured by such methods is called the kinematic viscosity (ν) and expressed in SI-units as meter squared per second (m^2s^{-1}), in fluid dynamics the kinematic viscosity is normally expressed in Stokes (St) or Centistokes (cSt); 1 (m^2s^{-1}) = 10^4 (St) = 10^6 (cSt). The relationship between the dynamic and kinematic viscosity is:

$$\nu = \frac{\eta}{\rho}, \text{ where } \rho \text{ is the density of the fluid.} \qquad 3.9$$

The flow behaviour of a solution or suspension is also largely determined by shape, configuration and distribution of the dissolved or suspended molecules. The concentration of large molecules in a solvent, their solvation and their tendency to form micelles is most important. Starting from a pure Newtonian solvent to which chain molecules are added, the viscosity will increase with increasing concentration, and the fluid will cease to be Newtonian when a certain concentration is exceeded. These fluids also tend to decrease their viscosity with increasing shear strain rate. This flow behaviour is called shear-thinning (*sometimes referred to as: pseudoplastic*). Two simple explanations for this non-linear phenomenon can be given though it should be stressed that these explanations are simplifications that serve to illustrate the nature of factors influencing the rheology of suspensions:

- Molecules behave as a suspension of rigid rods in a Newtonian liquid: At rest the rod-shaped molecules are in an ideal disorientation due to the Brownian movement in the liquid. During shear, the rods tend to orient themselves in the direction of shear. A strong preferred orientation

results in a lower viscosity. The random Brownian movement opposes the trend toward a preferred orientation so that for any given shear strain rate a certain state of dynamic equilibrium is reached, which determines the viscosity.
- Molecules behave as a suspension of elastic coils in a Newtonian liquid: Filamentary macromolecules have a relatively high mobility of atom groups around their mutual electron pairs so that their shape is irregular. At rest they form porous solvated coils. When the suspension is sheared, the resultant forces disentangle the coils in the direction of flow. The disentanglement of the coils depends on their elasticity and the shear strain rate. Through this disentangling action a part of the liquid, previously bound to the molecule by solvation, is released. The interaction of orientation, disentanglement and dilution by released solvent results in a reduction of internal friction and hence the viscosity with increasing shear strain rate.

Shear-thinning flow behaviour as such is a characteristic of a solution or suspension. Furthermore, flow behaviour is dependent on the concentration of a solution or suspension. It is for this reason that equations are valid only over a certain range.

Compared to a fluid with short molecules, the decrease in viscosity of a fluid with long molecules is, with the two explanations given above, thus accompanied by an increase in anisotropy. With respect to natural rocks, this increase in anisotropy can be compared to the evolution of a granite into a gneiss where the micaceous minerals tend to line up in the direction of the flow. Shear-thinning is not necessarily related to anisotropy: in a single phase material for instance, the establishment of a smaller equilibrium grain-size as result of a higher strain rate can account for a decrease in viscosity while no preferred orientation (crystallographic or grain shape) develops.

For shear-thinning flow, a formula describing the relation between shear strain rate and shear stress has been proposed by Ostwald:

$$\dot{\gamma} = k \cdot \tau^n, \text{ with } n>1, \qquad 3.10$$

in which k and n are material parameters. This flow-law is generally assumed to apply to rocks deforming in the ductile regime (Poirier 1991). This would mean that, at shear strain rates approaching zero, the limit of the slope (ζ) of the $\dot{\gamma}$-τ curve is 90° and the viscosity would be infinite (fig. 3.3). However, shear-thinning materials show a positive and finite viscosity value at zero shear strain rate. Therefore, equation 3.10 can give a good description of the flow behaviour of a material at higher rates of shear but at low rates it does not describe the behaviour in a realistic way.

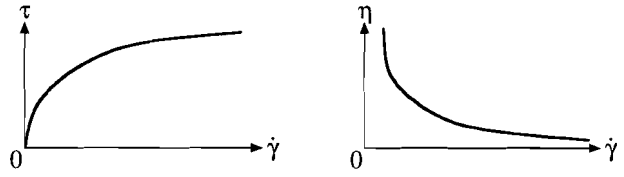

Figure 3.3. Rheograms of a shear-thinning fluid according to the flow-law of Ostwald.

An alternative formula, which takes the finite viscosity at zero shear strain rate into account, has been proposed by Steiger/Ory:

$$\dot{\gamma} = a \cdot \tau^3 + c \cdot \tau, \text{ with } c>0. \qquad 3.11$$

The two factors a and c are material parameters. For non-Newtonian materials 'a' is a measure of the deviation from true Newtonian behaviour (fig. 3.4).

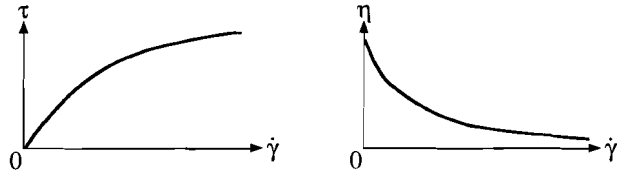

Figure 3.4. Rheograms of a pseudoplastic fluid according to the flow-law of Steiger/Ory.

In some fluids the viscosity is, in addition to its relationship with shear strain rate, also time or strain dependent. A substance whose viscosity decreases when subjected to shear is called thixotropic (*also referred to as: rheopectic*) if this phenomenon is reversible. If, in a thixotropic substance shearing is discontinued for a certain time, its viscosity will again increase (fig. 3.5).

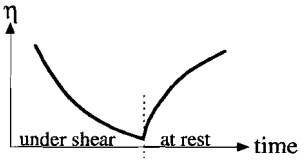

Figure 3.5. Reversible behaviour of a thixotropic material when subjected to a certain time of shear.

3.2.2 Relation between viscosity and strain rate sensitivity on stress

The viscosity is proportional to the relation (or flow-law) between stress and strain rate (equation 3.5). A relation, postulated for minerals and rocks deforming in the ductile regime is often used in only one dimension (Poirier 1991), is given by:

$$\dot{\varepsilon}_{11} = A e^{-\frac{Q}{R \cdot T}} (\sigma_{11} - \sigma_{33})^n. \qquad 3.12$$

Here, stress and strain rate are presented as scalars, with the stress usually defined as the difference between the maximum and the minimum principle stresses. The pre-exponential factor (A), the stress exponent (n) and the activation enthalpy (Q) are material constants. R is the gas-constant and T the absolute temperature.

In the experiments presented in this thesis, the temperature was kept constant and the deformation was essentially simple shear flow. Therefore, equation 3.12 can be simplified with a pre-exponential factor B, which incorporates the temperature. The strain rate ($\dot{\varepsilon}$) and the differential stress (σ_{11}-σ_{33}) are represented by shear strain rate ($\dot{\gamma}$) and shear stress (τ) respectively:

$$\dot{\gamma} = B \cdot \tau^n \left(\text{or} \quad \tau = \left(\frac{1}{B} \right)^{1/n} \dot{\gamma}^{1/n} \right). \qquad 3.13\ (3.13a)$$

Note that equation 3.13 is similar to the equation proposed by Ostwald (eq. 3.10) for shear-thinning materials. Inserting equation 3.13a in equation 3.5 leads to:

$$\eta = (1/B)^{1/n} \dot{\gamma}^{(1/n)-1}, \qquad 3.14$$

which can be written as:

$$\log(\eta) = C + p\log(\dot{\gamma}). \qquad 3.15$$

Where $C=(1/B)^{1/n}$ and $p=(1/n)-1$ or $n=(1+p)^{-1}$. The constant p is the slope of the curve in a $\log(\eta) - \log(\dot{\gamma})$ graph (see fig. 3.6). The viscosity in the case of a Newtonian material is independent of strain rate so the $\log(\eta) - \log(\dot{\gamma})$ curve is a horizontal line, p equals zero and the stress exponent n is 1. For most non-Newtonian materials the $\log(\eta) - \log(\dot{\gamma})$ curve is a descending line, p is negative and the stress exponent is larger than 1. If the $\log(\eta) - \log(\dot{\gamma})$ curve is not a straight line, the above evaluation is not correct for the determination of the pre-exponential factor C. However, at a given strain rate ($\dot{\gamma}$), the stress exponent n will be related to the slope of the $\log(\eta) - \log(\dot{\gamma})$ curve by:

$$n(\dot{\gamma}) = \frac{1}{1 + p(\dot{\gamma})}. \qquad 3.16$$

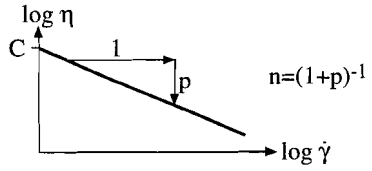

Figure 3.6. Showing the relation between stress exponent n and slope p of a $\log(\eta) - \log(\dot{\gamma})$ curve.

3.2.3 Measurements of viscosity

The viscosity of a fluid can be measured in two distinct ways. The kinematic methods (which use gravity as driving force) include the flow rate of a fluid through a pipe and the velocity of a falling sphere in a fluid. The dynamic techniques (which use movement as driving force) are basically available as Couette rheometer and cone-and-plate rheometer. Dynamic methods are relevant for discussion in this thesis.

Couette rheometer

A Couette flow rheometer consists of two concentric cylinders of different diameter (fig. 3.7), a motor and a torque transducer. If the internal cylinder rotates (radius R_i, angular velocity ω_A) while the external cylinder (with radius R_e) is held stationary, the fluid in the annular zone between the two cylinders will be subjected to a shear strain rate and, in response to the viscosity (η), a state of stress will exist in the fluid. If the effects at the top and bottom of the internal cylinder are neglected, the torque (M) applied to the internal cylinder has to be transferred entirely through the fluid to the external cylinder. This implies that the torque ($M=F \cdot r$) over the concentric gap must be constant. At a point of radius r ($R_i \leq r \leq R_e$) the shear stress $\tau(r)$ is:

$$\tau(r) = \frac{M}{2\pi h}\frac{1}{r^2}. \qquad 3.17$$

From this equation it is clear that there is a radial stress gradient over the fluid filled annulus and that the shear strain rate from internal to external cylinder will vary accordingly. The stress gradient and thus shear strain rate are also dependent on the flow behaviour of the liquid (see addendum to Chapter 2). For a Newtonian liquid (n=1), this method is acceptable since the viscosity is not a function of shear strain rate and the viscosity can be determined using equations 3.5, 3.17 and A2.3a. For a non-Newtonian liquid, extensive corrections have to be made before a viscosity can be determined. In practice, when using a Couette rheometer, the effects at

the top and bottom of the internal cylinder are not negligible and a correction for these effects is used (end correction).

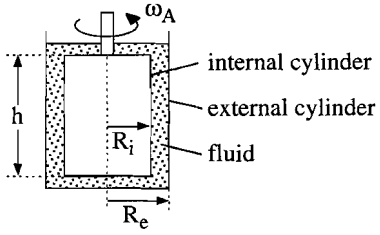

Figure 3.7. Simplified Couette rheometer.

Cone and plate rheometer

In a cone-and-plate rheometer, a fluid is sheared in an annulus that linearly increases in thickness outwards. As a result, the imposed shear strain rate is constant throughout the annulus (fig. 3.8). This implies that viscosities can be measured as a function of shear strain rate. The shear strain rate in a cone and plate rheometer can be described by:

$$\dot{\gamma} = \frac{\omega_A}{\beta}\ (s^{-1}), \qquad 3.18$$

where β (expressed in radians) is small and ω_A (the angular velocity of the cone) is expressed in radians per second. Since for any radius r the velocity $v(r) = \omega_A \cdot r$, the distance between the plates $z = r \cdot \tan\beta = r \cdot \beta$ if the angle β is very small and the shear strain rate $\dot{\gamma} = v/z$ (fig. 3.8a). When the shear strain rate is constant, the shear stress is also constant (fig. 3.8b):
$\tau = dF/dA$ = constant.
The torque dM resulting from shear on area dA is:
$dM = r \cdot dF = r \cdot \tau \cdot dA = r \cdot \tau \cdot 2\pi \cdot r \cdot dr = 2\pi \cdot \tau \cdot r^2 \cdot dr$.
Integrating of dM between r=0 and r=R and rearranging the components results in:

$$\tau = \frac{3 \cdot M}{2\pi \cdot R^3}. \qquad 3.19$$

The torque (M) and the angular velocity of the cone (ω_A) are measured and the viscosity can be calculated using equations 3.5 and 3.19.

The method of determination of the viscosities presented in this study is a 'steady rate sweep' with a cone and plate rheometer. This means that the rotation rate of the cone is set at a certain value and the actual torque measurement is done after a delay time, then the cone is set to rotate at another rate and, after the delay time, a new measurement is made. Inaccuracies are to be expected with thixotropic materials when the delay time is too short to reach a 'steady state'

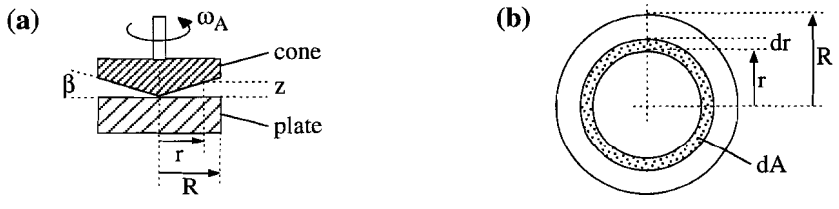

Figure 3.8. (**a**) Simplified cone and plate rheometer. (**b**) Explanation used for stress determination.

viscosity. It is possible to check the validity of the chosen delay-time by doing two series of measurements, one by increasing the shear strain rate and a second by decreasing the shear strain rate. If the two sets of data don't match, especially at the lower shear strain rates, the delay time was probably too short. Short delay-times are favourable not only for time management, since the material being examined can be destroyed when subjected to long periods of high shear strain rates, or the heat produced in the sheared fluid can cause a temperature gradient in the material. One should take into account how a viscosity is measured. The viscosity of a fluid is typically determined with a rheometer where (approximately) simple shear is imposed on the material. The lower viscosity at high shear strain rates, as observed in shear thinning fluids, is only applicable to the imposed shearing. If the movement direction could be instantaneously changed, a different viscosity measurement might be obtained. A single scalar representing viscosity (η) is only applicable to Newtonian isotropic materials. The viscosity of a true power-law isotropic material can be described by a function: $\eta=f(\dot{\gamma})$. In an anisotropic medium more numbers are needed to fully describe the viscosity (which is then orientation dependent as well). When, for an anisotropic material a scalar is used for the viscosity, this represents the effective viscosity for a particular deformation geometry in relation to a particular anisotropy type and orientation.

3.2.4 Viscosities of glycerol and pAA-water solutions

Glycerol and a polyacrylamide(pAA)-water solution were chosen as fluids to model Newtonian and non-Newtonian matrix materials respectively. These fluids are non-toxic, colourless and have such high viscosities that a light current of air over their surfaces does not have an considerable perturbation effect. During the experiments, a small amount of suspended particles made it possible to determine the flow pattern in the fluids.

Existing data on glycerol

Glycerol (*also known as glycerine*) is the common name for 1,2,3-tri hydroxy propane, chemical formula: $C_3H_5(OH)_3$. It is a colourless, viscous, fluid that is slightly hygroscopic with a relative density of 1.2611 gr cm^{-3} at 20°C. Figure 3.9 shows that the viscosity of pure glycerol decreases rapidly with increasing temperature. In the literature, glycerol and mixtures of glycerol and water are stated to be Newtonian. The table in figure 3.10 shows the relative density (ρ), kinematic viscosity (ν) and dynamic viscosity ($\eta=\nu\cdot\rho$) of water-glycerol mixtures at 20°C. The graph in figure 3.10 shows the increase of dynamic viscosity of the mixtures with

temperature [°C]	viscosity [Pa s]
30	0.629
25	0.954
20	1.49
15	2.33
6	6.26
0	12.11
-4.2	14.9
-10.8	35.5
-15.4	66.5
-20	134
-25	262
-36	2050
-42	6710

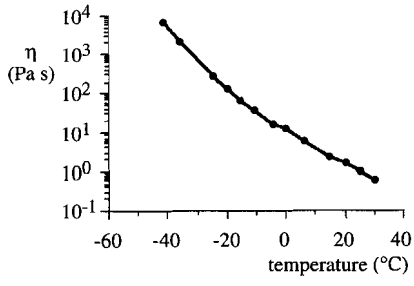

Figure 3.9. Table and graph showing viscosity of pure glycerol as a function of temperature. Data from Handbook of Chemistry and Physics, 64th ed., 1983-1984, table F41.

decreasing water content. Note that η does not increase linearly with %wt glycerol of the mixture, especially above 80%wt.

glycerol %wt	ρ [gr cm^{-3}]	kin.visc. ν [cSt]	dyn.visc. η [Pa s]
0	0.9982	1.004	$1.0019 \cdot 10^{-3}$
5	1.0097	1.116	$1.227 \cdot 10^{-3}$
10	1.0215	1.263	$1.290 \cdot 10^{-3}$
20	1.0459	1.661	$1.737 \cdot 10^{-3}$
40	1.0984	3.326	$3.653 \cdot 10^{-3}$
60	1.1530	9.264	$1.068 \cdot 10^{-2}$
80	1.2085	49.57	$5.991 \cdot 10^{-2}$
84	1.2192	69.18	$8.434 \cdot 10^{-2}$
88	1.2299	119.9	$1.475 \cdot 10^{-1}$
92	1.2404	310.0	$3.845 \cdot 10^{-1}$
96	1.2508	624.0	$7.805 \cdot 10^{-1}$
100	1.2611	1181.3	1.490

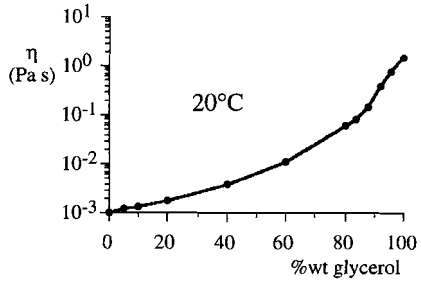

Figure 3.10. Table and graph showing viscosity of glycerol-water mixtures (at 20°C) as a function of glycerol content. Data from Handbook of Chemistry and Physics, 64th ed., 1983-1984, table D235-236.

Existing data on poly-acrylamide (pAA)-water solutions

Poly-acrylamide (pAA) is a polymer consisting of a large number of acrylamide components that build a chain molecule. Depending on the amount of components per molecule, pAA is available in a range of molecular weights. Pure pAA is commercially available as white, opaque crystals. When mixed with water, the crystals dissolve to form a clear viscous fluid. Chiba *et al.* (1986) investigated the rheological behaviour of pAA solutions made from Separan AP-30, manufactured by Dow Chemical Co.. They used solutions ranging from 0.02%wt to 0.25%wt and a Couette rheometer. All their solutions were found to be Newtonian at very low shear strain rates. The 0.25%wt solution began to show non-Newtonian behaviour at about 10^{-2} s^{-1}. The shear strain rate at which transition occurred from Newtonian to shear thinning behaviour was shifted towards lower values and the degree of shear thinning increased as the polymer concentration increased. A semi-empirical equation derived by Cross (1965) describes their experimental data over a wide range of shear strain rates:

$$\eta = \eta_\infty + \frac{\eta_0 - \eta_\infty}{1 + \alpha \cdot \dot{\gamma}^{2/3}}, \qquad 3.20$$

where η_0 is the limiting viscosity at zero shear strain rate, η_∞ the limiting viscosity at infinite shear strain rate and α is a material parameter. Figure 3.11 shows the viscosity curves of three of the pAA solutions examined by Chiba et al (1986) according to equation 3.20.

concen-tration %wt	Tempe-rature [°C]	η_0 [Pa s]	η_∞ [Pa s]	α
0.25	14.2	5.567	0.0120	4.333
0.10	28.3	0.0717	0.0027	0.231
0.05	27.6	0.0289	0.0021	0.187
0.02	18.1	0.0042	0.0002	0.018

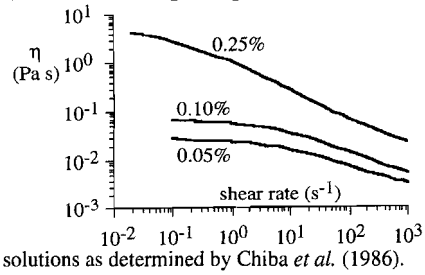

Figure 3.11. Table and graph of viscosity data of pAA solutions as determined by Chiba *et al.* (1986).

3.2.5 Determination of the rheological properties of the experimental fluids

Glycerol is a hygroscopic fluid and the viscosity of glycerol-water mixtures changes with water content. Furthermore, the poly-acrylamide Separan AP-30 is no longer available from the Dow Chemical Co.. Therefore, the viscosities of the glycerol and the pAA-solution that were used during the experiments described in this thesis were examined, instead of using the available data. The rheological properties of the fluids used in this study were determined with a Rheometrics RFS II cone-and-plate rheometer with cone and plate radii of 25 mm and a cone angle of 0.02 radians. The torque-transducer of the used rheometer has a specified range down to $2.5 \cdot 10^{-7}$ Nm, which inhibits accurate viscosity determination at low shear strain rates. The temperature of the sample during measurements was set at 25.3±0.15°C and 25.0±0.25°C for the glycerol and pAA-solution respectively. The investigated liquids did not contain the suspended particles that were used during the experiments as these particles could jam between the cone and the plate, thus disturbing the measurements. As the concentration of suspended particles during the experiments is 0.017±0.001%wt, they have a negligible effect on the viscosity (Yoon and Chen 1990; eq. 12, p. 1556).

Glycerol

The glycerol used in this study was tested in series of increasing and decreasing rates of shear strain. The data presented figure 3.12 are from a 'steady rate sweep' from high to low shear strain rate and is typical of all series measured. It shows a constant viscosity of 0.31±0.02 Pa s (at 25.3±0.15°C) at all shear strain rates and is therefore Newtonian. At rates below 0.1 s^{-1} large errors in determining the viscosity emerged as the torque-transducer of the rheometer reaches the limit of specification. The water content of the glycerol used in this study is not known since it was not tested, from the viscosity measurements it can be deduced that it was in the order of 3 to 7 %wt.

shear rate (s^{-1})	viscosity (Pa s)	torque (Nm)
$1.000 \cdot 10^{2}$	0.3067	$1.004 \cdot 10^{-3}$
$6.309 \cdot 10^{1}$	0.3061	$6.321 \cdot 10^{-4}$
$3.981 \cdot 10^{1}$	0.3056	$3.981 \cdot 10^{-4}$
$2.512 \cdot 10^{1}$	0.3062	$2.517 \cdot 10^{-4}$
$1.585 \cdot 10^{1}$	0.3057	$1.585 \cdot 10^{-4}$
$1.000 \cdot 10^{1}$	0.3070	$1.005 \cdot 10^{-4}$
6.309	0.3055	$6.308 \cdot 10^{-5}$
3.981	0.3052	$3.977 \cdot 10^{-5}$
2.512	0.3032	$2.493 \cdot 10^{-5}$
1.585	0.3024	$1.568 \cdot 10^{-5}$
1.000	0.3050	$9.979 \cdot 10^{-6}$
$6.309 \cdot 10^{-1}$	0.3045	$6.286 \cdot 10^{-6}$
$3.981 \cdot 10^{-1}$	0.3079	$4.011 \cdot 10^{-6}$
$2.512 \cdot 10^{-1}$	0.3102	$2.549 \cdot 10^{-6}$
$1.585 \cdot 10^{-1}$	0.3168	$1.643 \cdot 10^{-6}$
$1.000 \cdot 10^{-1}$	0.3298	$1.079 \cdot 10^{-6}$
$6.310 \cdot 10^{-2}$	0.3207	$6.621 \cdot 10^{-7}$
$3.981 \cdot 10^{-2}$	0.3310	$4.312 \cdot 10^{-7}$
$2.512 \cdot 10^{-2}$	0.2879	$2.366 \cdot 10^{-7}$
$1.585 \cdot 10^{-2}$	0.2643	$1.371 \cdot 10^{-7}$
$1.000 \cdot 10^{-2}$	0.1233	$4.035 \cdot 10^{-8}$
$6.309 \cdot 10^{-3}$	0.4920	$1.016 \cdot 10^{-7}$

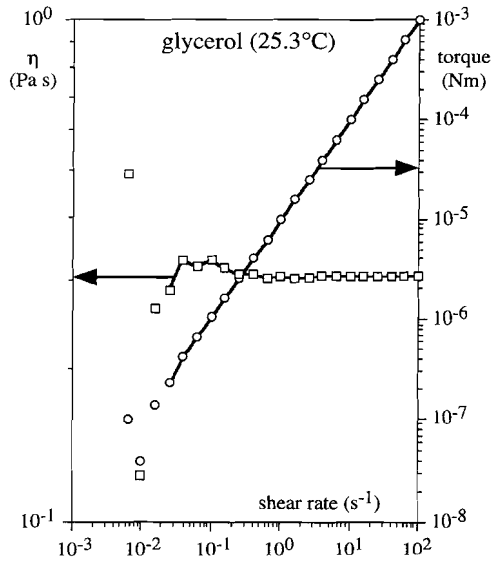

Figure 3.12. Table and graph showing rheological data of the glycerol used in this study. Curves are only drawn down to $2.5 \cdot 10^{-2}$ s^{-1} since measurements at lower shear strain rates are inaccurate.

pAA-solution

The pAA used in this study is Flocculant AP 30 E, obtained from SNF Floerger®, Saint-Etienne, France. Flocculant AP 30 E has a molecular weight of $1 \cdot 10^7$ to $2 \cdot 10^7$. A 0.5%wt solution was made by dissolving 15.00±0.005 gr pAA in 3000.0±0.05 gr (ordinary tap) water. From the 'steady rate sweeps' with increasing shear strain rate it was found that the pAA-solution is thixotropic with a relatively long delay until 'steady state' is reached. The 'relaxation' time, however, is short. Therefore, the data presented here are from a 'steady rate sweep' from high to low shear strain rates, which is thought to be the most accurate. The viscosity of the pAA-solution (at 25.0±0.25°C) decreases from almost 11 Pa s at a shear strain rate of $6 \cdot 10^{-3}$ s^{-1} to 0.06 Pa s at a shear strain rate of $1 \cdot 10^2$ s^{-1} and is clearly shear-thinning[1] (fig. 3.13). The decreasing viscosity with increasing shear strain rate is most likely the effect of the disentanglement and the alignment in the direction of flow of the pAA-molecules and thus an increase in anisotropy as discussed in section 3.2.1.

shear rate (s^{-1})	viscosity (Pa s)	torque (Nm)
$1.000 \cdot 10^2$	0.063	$2.075 \cdot 10^{-4}$
$6.310 \cdot 10^1$	0.094	$1.959 \cdot 10^{-4}$
$3.981 \cdot 10^1$	0.126	$1.651 \cdot 10^{-4}$
$2.512 \cdot 10^1$	0.170	$1.405 \cdot 10^{-4}$
$1.584 \cdot 10^1$	0.230	$1.194 \cdot 10^{-4}$
$1.000 \cdot 10^1$	0.312	$1.023 \cdot 10^{-4}$
6.310	0.412	$8.526 \cdot 10^{-5}$
3.981	0.555	$7.242 \cdot 10^{-5}$
2.512	0.749	$6.160 \cdot 10^{-5}$
1.584	1.004	$5.205 \cdot 10^{-5}$
1.000	1.312	$4.293 \cdot 10^{-5}$
$6.310 \cdot 10^{-1}$	1.700	$3.510 \cdot 10^{-5}$
$3.981 \cdot 10^{-1}$	2.170	$2.827 \cdot 10^{-5}$
$2.512 \cdot 10^{-1}$	2.693	$2.214 \cdot 10^{-5}$
$1.584 \cdot 10^{-1}$	3.328	$1.726 \cdot 10^{-5}$
$1.000 \cdot 10^{-1}$	4.054	$1.326 \cdot 10^{-5}$
$6.310 \cdot 10^{-2}$	4.834	$9.981 \cdot 10^{-6}$
$3.981 \cdot 10^{-2}$	5.760	$7.503 \cdot 10^{-6}$
$2.512 \cdot 10^{-2}$	6.797	$5.586 \cdot 10^{-6}$
$1.584 \cdot 10^{-2}$	7.928	$4.111 \cdot 10^{-6}$
$1.000 \cdot 10^{-2}$	9.351	$3.060 \cdot 10^{-6}$
$6.310 \cdot 10^{-3}$	10.987	$2.268 \cdot 10^{-6}$

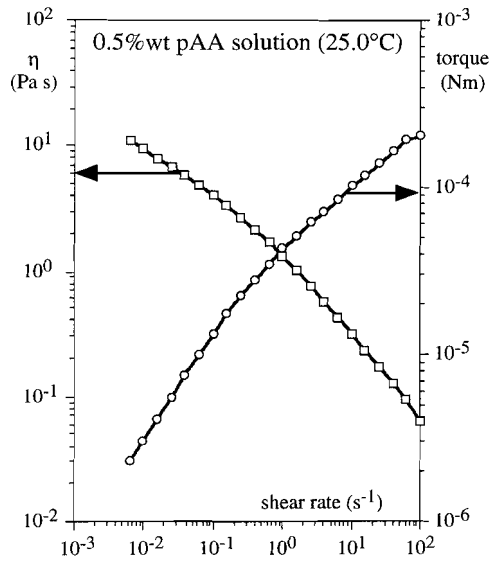

Figure 3.13. Table and graph showing rheological data of the 0.5%wt pAA solution used in this study. Notice that the slope of the viscosity and torque curves is not constant but show a decrease at shear strain rates above 10^{-1} s^{-1}.

[1] Gauthier *et al.* (1971) use the term elasticoviscous, according to the terminology suggested by Reiner and Scott Blair (1967), to describe this type of liquid while 'liquids which exhibit a continuous decrease in viscosity with increasing rate of shear strain without any appreciable elastic recovery when the shearing action is stopped' are called pseudoplastic. In the slow flow of the experiments, the pAA-solutions did not show an appreciable amount of elastic recovery, in faster flow elastic recovery was noticeable.

Stress exponent (n) of glycerol and pAA-solution

As mentioned before (eq. 3.16), there is a relation between the slope (p) of the $\log(\eta) - \log(\dot{\gamma})$ curve and the stress exponent (n) of a material:

$$n(\dot{\gamma}) = \frac{1}{1 + p(\dot{\gamma})}. \qquad 3.16$$

Since the viscosity measurements of the glycerol and pAA solution are not continuous but discrete, it is not possible for these materials to define the exact slope of the $\log(\eta) - \log(\dot{\gamma})$ plot at every rate of shear strain. Therefore, the value for n at a certain rate of shear strain ($\dot{\gamma}_m$) was calculated as the mean value over the previous (m-1) and next (m+1) data points as follows:

$$n(\dot{\gamma}_m) = \frac{1}{1 + p_m}, \qquad 3.21$$

in which the slope of the curve p_m at $\dot{\gamma}_m$ is defined as:

$$p_m = \frac{\log(\eta_{m+1}) - \log(\eta_{m-1})}{\log(\dot{\gamma}_{m+1}) - \log(\dot{\gamma}_{m-1})}. \qquad 3.22$$

Figure 3.14 shows that the stress exponent (n) of glycerol is very close to unity at shear strain rates above 0.04 s^{-1} thus indicating a linear relationship between shear stress and shear strain rate: the fluid shows a Newtonian behaviour. The variable n-values at lower shear strain rates are the result of inaccuracies of the rheometer at these low rates. The stress exponent of the pAA solution (at 25.0±0.25°C) increases from 1.5±0.1 at shear strain rates below 0.06 s^{-1} to 2.8±0.2 at shear strain rates above 2.5 s^{-1}. This indicates that the n-value of the pAA solution is shear strain rate controlled and that there is no single power-law relation between shear stress and shear strain rate: the solution is shear-thinning but the power-law relation has no constant n-value over the range of shear strain rates. The high n-value of 4 at a shear strain rate of 63 s^{-1} is probably due to an erroneous torque-reading at the beginning of this measurement series; it was not found in tests with increasing rate of shear strain. These results of these measurements are in accordance with the data provided by Mena *et al.* (1987), from which a stress-exponent of approximately 2.5 can be estimated for a 0.8%wt pAA solution at shear strain rates ranging from 0.7 to 40 s^{-1}. The temperature at which those measurements were made is not stated.

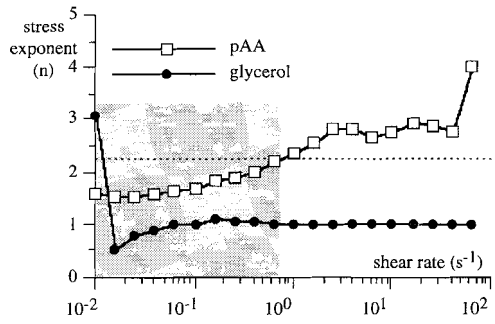

Figure 3.14. Showing the stress exponent (n) of glycerol and pAA solution used in this study calculated according to equations 3.21 and 3.22. The shaded area indicates the range of shear strain rates of the experiments described in Chapter 4.

3.3 Experimental set-up with the linear fluid shear apparatus

3.3.1 Apparatus

The apparatus (fig. 3.15), used during the experiments to investigate the flow pattern around and rotational behaviour of objects during flow, was designed to impose ongoing simple shear at different shear strain rates in liquids at room temperature. It is similar to the shear flow apparatus used by Robertson and Acrivos (1970). It consists of a belt-drive mechanism placed in a transparent box that contains the liquid. Two 50 mm high timing belts protruded above the level of the liquid and moved in opposite direction with the same speed, such that a flow pattern was imposed with straight flow-lines, and a plane of no relative displacement exsisted between the two belts. The set-up thus induced a simple shear deformation in the liquid with no extension in the y-direction (plane strain flow) in the zone where the observations were made.

The belts are driven by an electric motor, connected to a gear-box. The power-supply (internal design) of the motor can be adjusted between 0 and 24 V and the gear-box has 10 different fixed reductions ranging from 1:1 to 1:1000 (fig. 3.16). This set-up makes it possible to vary the belt-speed between $1.0 \cdot 10^{-6}$ and $5.7 \cdot 10^{-3}$ m s^{-1}. Guiding blocks at the inside of each belt can be positioned and fixed to the lid by pins and bolts in order to set the shearzone width between 15 and 40 mm. The pins that are used to position the guiding blocks make the shearzone width adjustable at 5 mm intervals, without the need to remove the lid of the shearbox. These pins (and corresponding slots in the lid and guiding blocks) are a modification of the apparatus made after a first series of experiments. During the earlier experiments, the shearzone width was fixed by using 16.5 mm wide spacers between the belts before the guiding blocks were fastened to the lid. The combination of variable belt speed and shearzone width allows the shear strain rate to be adjusted between $5.0 \cdot 10^{-5}$ and 0.76 s^{-1}.

The elastic energy within the experimental set-up, which is probably the result of friction between the belts and the guiding blocks and the elasticity of the entire system, is released as small variations in belt-speed. At higher belt-speeds, these variations have a high frequency and do not noticeably disturb the observations. At belt-speeds lower than $8 \cdot 10^{-5}$ m s^{-1}, the frequency of the elastic relaxation influences the strain rate significantly and thus inhibits experiments at shear strain rates lower than $5.9 \cdot 10^{-3}$ s^{-1}.

	DETAILS OF EXPERIMENTAL APPARATUS AND MATERIALS
transparent box	polymethylmethacrylate (PMMA)
belts	Synchroflex®; type: 50-T5-620; polyurethane with steel thread inlay
motor	VDO; 24 V DC, 3 Ncm, 3000 rpm with a fixed gear of 1:375 resulting in an output of 8 rpm at 10 Nm
gearbox	APCOR; type: 2412, multiratio speed reducer
apparatus designed and built by:	G.J. Kastelein
tracers	Flakes: aluminium; Ø=30-150 μm; thickness <10 μm (used in early pAA experiments) Micro spheres: polystyrene divinylbenzene (DVB); Ø=50-120 μm (not used) Chalk-dust: blackboard crayon, scraped with razor blade; Ø=20-70μm
He-Ne laser	LAP; type: 8P/ZO3; 8 mW, λ=632.8 nm with focusing lens
cylindrical lens	Spindler & Hoyer; type: 06 3427, f=200 mm; placed at 50 mm from the laser optics
video camera	COHU; type: 4722-2, B/W CCD, 699x580 active picture elements fitted with a f=80 mm Leitz Wetzlar lens
computer	MacintoshII; 8 MB 120 ns RAM, 16 MHz MC68020 processor and MC68881 co-processor

Figure 3.15 (next page). Drawing of the linear fluid shear box used in the experiments described in this thesis. View is from the top. Drive belts rotate clock-wise at the same speed, generating sinistral simple shear between the two guiding blocks. Position of the plane of no displacement is indicated by the dashed line.

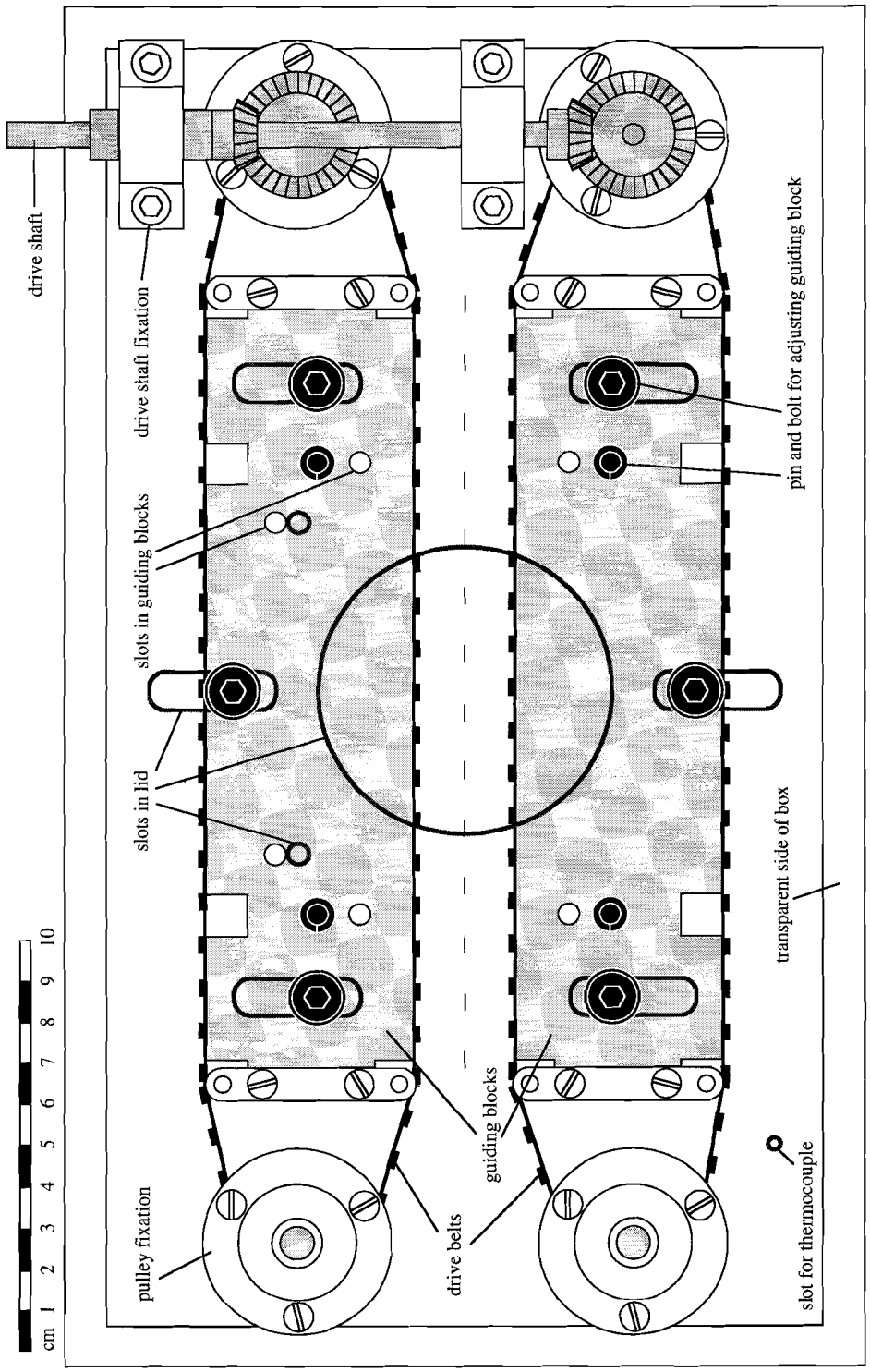
drive shaft
drive shaft fixation
slots in guiding blocks
slots in lid
pulley fixation
drive belts
guiding blocks
pin and bolt for adjusting guiding block
transparent side of box
slot for thermocouple
cm 1 2 3 4 5 6 7 8 9 10

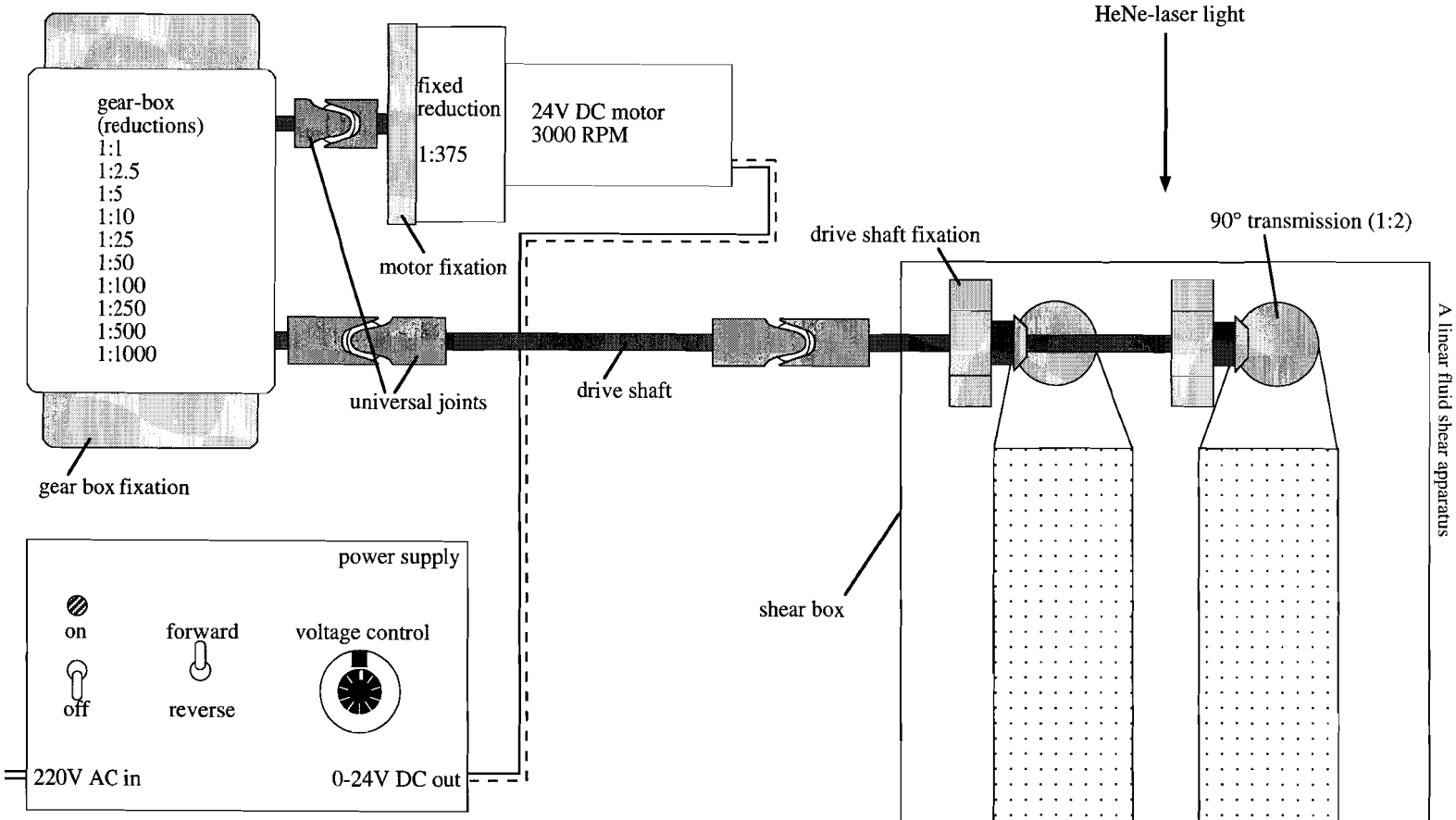
HeNe-laser light
gear-box
(reductions)
1:1
1:2.5
1:5
1:10
1:25
1:50
1:100
1:250
1:500
1:1000
fixed
reduction
1:375
24V DC motor
3000 RPM
motor fixation
drive shaft fixation
90° transmission (1:2)
universal joints
drive shaft
gear box fixation
shear box
power supply
on
off
forward
reverse
voltage control
220V AC in
0-24V DC out

Figure 3.16 (previous page). Schematic drawing showing the layout of the experimental set-up, as seen from above.

3.3.2 Data acquisition and analysis

Particles and laser set-up

Several materials were investigated trying to produce reflecting particles that could trace the flow in the shearing fluids. At the experimental conditions in this study, aluminium flakes and DVB micro spheres, which are often used in flow-examination experiments, are not buoyant enough and sink out of the top layer of the fluid in which the flow is examined in a relatively short time. Furthermore, the aluminium flakes tend to line up with the flowplane which makes them difficult to trace. The best results were obtained with an amount of 0.02%wt of powdered blackboard crayon (Ø=20-70 μm) mixed in the fluids. These chalk-dust tracers are inert and buoyant for several months at the conditions of the experiments in this study. The particles were illuminated by a Helium-Neon laser which produced a Ø=1.2 mm beam of light that passed through a cylindrical, positive lens in order to make a diverging horizontal plane of light. In the centre of the shear-box, at a distance of 90 cm from the positive lens, it was 1.2 mm high and 20 mm wide in cross-section (fig. 3.17). Only those particles in the fluid that were illuminated by the plane of light were visible. By adjusting the plane of light up or down, it is possible to analyse any level in the shearing fluid.

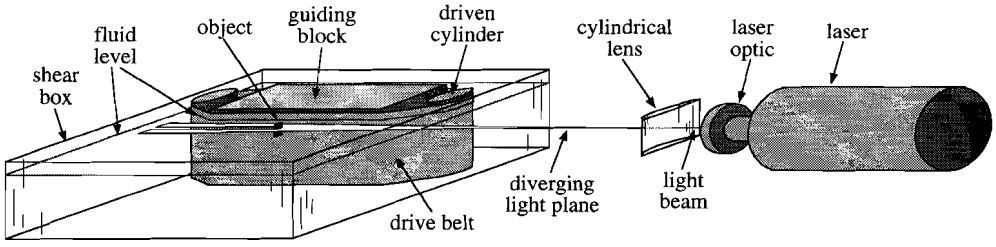

Figure 3.17. Schematic three dimensional drawing of laser and lens position with respect to shear box. The drive mechanism in front (belt, cylinders and guiding block) has been left out for clarity. Note the shadow of the object.

Time-lapse digital imaging

During the experiments, a digital video-camera placed above the central opening in the lid of the shear box, recorded the reflection of the marker particles and/or a white strip fixed to the top of the object, and sent the 256 greyscale image to a computer. Such an image represents information of a specific, 1.2 mm high, horizontal level in the fluid. A time-lapse film of images can be created when separate frames are taken at a constant time interval. The time interval depends on the number of pixel elements of the individual frames since the processor has a limited capacity. The maximum number of frames per film depends on the RAM capacity of the computer since the frames are temporarily stored in this memory. The maximum number of full frames (768x512 pixels) is 16 with the equipment available. The shortest time interval between each full frame is 2 seconds. When the frame-size is reduced to 300x250 pixels it is possible to make up to 60 frames at 0.3 second intervals. Obviously, a faster processor and a larger RAM capacity can shorten the time interval and extend the number of frames per film.

Rotation rate of objects

The image analysis program used for this study (NIH-Image (public domain): versions 1.29q and 1.52) can do a particle analysis on density slices of the digital images made during the experiment: A density slice is a binary image where a user-defined selection of a range of grey-values in the image is set to 1. Narrow white strips at the top of inserted objects can thus be selected as 'particles' to be examined. The analysis can give information on parameters such as: area, position of 'centre of gravity' and orientation of the long axis of an best fit ellipse of a particle. During determination of the rotation rates it is sufficient to record only the area of the object, which allowed the time-lapse film to comprise 60 frames with short time intervals. Version 1.52 of NIH-Image has the advantage over version 1.29q in that it can handle a large number of frames as a single file in stead of separate images.

The time-lapse method implies that only average values during a time interval can be calculated. If the amount of rotation during one interval is small, the error in object orientation (±0.5°) becomes relatively large and the average values will have a wide spread. It was found that an error occurs by determination of the object orientation with version 1.52 of NIH-Image. Part of this error is systematic and can be corrected. The procedure of error determination and correction is explained in the appendix. After correction the error was reduced to 0.3-0.9°, depending on the size and shape of the adhesive label attached to the object.

For simple shear, when one of the axes of the ellipsoid (c) coincides with the direction of the vorticity vector, the velocity of rotation ($\dot{\alpha}$) of a rigid elliptical inclusion in a Newtonian medium is given by (Jeffery 1922):

$$\dot{\alpha} = \frac{\dot{\gamma}\,(R_{xy}^2 \sin^2\alpha + \cos^2\alpha)}{R_{xy}^2 + 1}, \qquad 3.23$$

where $\dot{\gamma}$ is the rate of shear strain, R_{xy} is the axial ratio (a/b with a≥b) of the inclusion, and α is the angle of the long axis (a) with respect to the flowplane (fig. 3.18). For a cylinder with its axis of revolution parallel to the vorticity vector, a=b and thus R_{xy}=1. The theoretical rotation rate of a cylinder in a Newtonian fluid ($\dot{\alpha}_{th,cyl}$) that is being sheared at shear strain rate $\dot{\gamma}$is therefore:

$$\dot{\alpha}_{th,cyl} = \frac{\dot{\gamma}}{2}. \qquad 3.24$$

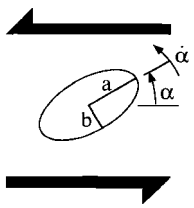

Figure 3.18. Relation of a, b, α and $\dot{\alpha}$ of an ellipsoid in simple shear flow. Axis c of the ellipsoid and the vorticity vector of the flow are perpendicular to the page.

In order to compare the data for several shear strain rates the rotational data are shown as Ω_{rel} (relative rotation rate):

$$\Omega_{rel} = \dot{\alpha}_{m,ob} / \dot{\alpha}_{th,cyl}, \qquad 3.25$$

in which $\dot{\alpha}_{m,ob}$ is the measured rotation rate of the object during the experiments. The unit of Ω_{rel} is a dimensionless number. For simple shear the maximum Ω_{rel}-value of a free floating object is 2 since a material line ($R_{xy}=\infty$) will rotate at a maximum rate when it is perpendicular to the flowplane ($\alpha=90°$). The limiting case for $\dot{\alpha}$ is thus:

$$\lim\left\{\dot{\alpha}\left(\alpha = 90°, R_{xy} \rightarrow \infty\right)\right\} = \dot{\gamma}. \qquad 3.26$$

Flow patterns

The flow patterns shown in paragraph 3.3.4 and in Chapter 4 emerge from time-lapse digital films made during the experiments. In order to determine the flow pattern with respect to the object, some individual frames were repositioned so that the centre of the floating object remained stationary. A maximum horizontal displacement of 0.3 mm (in real space) was sufficient. This repositioning was necessary as it was in practice not possible to place the object exactly in the centre of the shearzone, i.e. with the object's centre in the plane of no displacement. The repositioned individual frames were averaged to obtain an image showing marker particle positions at succeeding times (similar to a multiflash photograph). The quality of this image was improved with digital contrast enhancement and the data were stored on disk and/or written on photographic material with a slide-writer to get 'hard-copies'. All images of the flow pattern in this Chapter and Chapter 4 are shown in inverted gray-scales and show the markers as darker dots in a bright background (similar to a negative of a photograph).

During the experiments it was found that a change in shearzone-width (while the shear strain rate was kept constant by also changing the belt speed) had a strong influence on the flow pattern (Chapter 4); for this reason a 'relative shearzone width' is defined as the width of the shearzone divided by the diameter of the object:

$$SW_{rel} = \frac{\text{shearzone width}}{\text{object diameter}}. \qquad 3.27$$

Stagnation points are defined as places where no displacement occurs. Theoretically, two kinds of stagnation points can exist (Jeffrey and Sherwood 1980); a centre stagnation point and a saddle stagnation point (sometimes referred to as hyperbolic stagnation point). The difference is that around the latter, material points do not return to their original position (fig. 3.19).

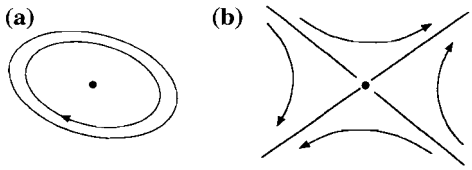

Figure 3.19. Showing the two basic types of stagnation points (heavy dots); **(a)** centre stagnation point, **(b)** saddle stagnation point.

The boundary between different types of flow lines, i.e. open and closed flow lines, is known as a separatrix (Ottino 1989). In a 'bow-tie' shaped flow pattern (fig. 3.20a, see also Chapter 2) the separatrices on either side of the object meet at a stagnation point. The area in between the far-field separatrices, where flow lines are open on the far-field side and closed on the central side, is called a back-flow region. In a bow-tie flow pattern, there are thus five regions with different types of flow: the central region with closed flow lines, the two back-flow regions with

half-closed flow lines, and the two regions with open flow lines. I use the term 'eye-shaped' for a three-region flow pattern in which the region with closed flow lines horizontally extends to infinity and is above and below bounded by regions with open flow lines (fig. 3.20b). Passchier (1994), introduced the term 'eye-shaped' perturbation for a three-region flow pattern, where the separatrices end on a stagnation plane (Passchier and Sokoutis 1993, Passchier *et al.* 1993, Passchier 1994). However, that flow pattern is theoretically not possible (see Chapter 5).

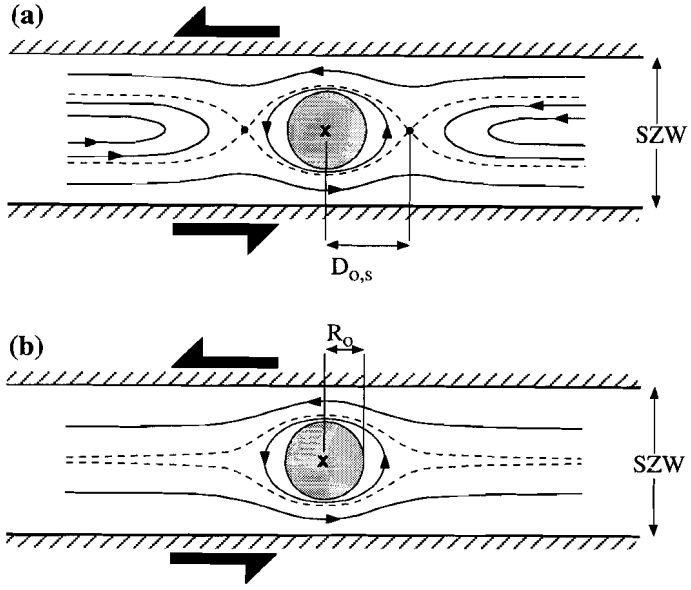

Figure 3.20. Explanation of the features of (**a**) a bow-tie shaped, and (**b**) eye-shaped flow pattern. SZW: shearzone width, broken lines: separatrices, lines with arrows: flow paths, heavy dots: saddle stagnation points, cross: centre stagnation point & centre of object, $D_{o,s}$: distance from centre of object to saddle stagnation point, dot-shading: object, line-shading: shearzone walls (belts).

For comparison purposes, the dimensionless relative distance of the stagnation point to the centre of the object (D_s) is defined as:

$$D_s = \frac{D_{o,s}}{R_o}, \qquad 3.28$$

in which $D_{o,s}$ is the distance between the stagnation point and the centre of the object and R_o is the radius of the object (fig. 3.20).

The procedure of repositioning 'creates' a centre stagnation point in the centre of the object. The saddle stagnation points will be simply further referred to as 'stagnation points' in this work. Since this thesis mainly deals with flow-patterns around objects, one of the main aspects in the analysis of the flow experiments was the determination of the positions of the stagnation points. If there is no reflecting marker exactly at a stagnation point, the position of this point can only be estimated by the trajectories of particles in the immediate surrounding. Since the displacements close to the stagnation point are small, such an estimation is not very accurate. Increasing the time interval gives a better determination of the position of the stagnation point since it increases the total displacement of the particles. However, a long time interval has the disadvan

tage that the flow-paths of particles in the far-field flow, which have larger displacements, are more difficult to determine. The time-intervals of the flow pattern experiments are chosen as a compromise between accuracy in position of the stagnation points and distinction of the far-field particle paths.

With an inaccurate identification of the stagnation points it is also impossible to determine the exact positions of the separatrices. Extrapolating the particle paths into flow-lines can help in estimating the positions of the separatrices and can thus be of use to approximate the positions of the stagnation points. The laser is placed on one side of the object, thus creating a shadow on the other side which makes it impossible to trace marker particles on both sides of the object. Since the experimental set-up has a two-fold symmetry axis in the centre of the object and perpendicular to the plane of view it is assumed that flow on one side of the object is the two-fold symmetry of the other side. Therefore it is sufficient to study the flow on one side of the object.

3.3.3 Flow patterns of glycerol and pAA-solution in the linear fluid shear apparatus

Figure 3.21 shows two images of the flow pattern in glycerol (3.21a) and pAA-solution (3.21b) without an object in the top layer of the fluid. The horizontal lines with different dash-intervals represent particle traces and show that particle paths are straight. The oblique lines compare displacements of particles at different positions in the shearzone and prove that the displacements vary linearly with distance to the belts: the flow is a simple shear in the region of interest when no object is inserted in the fluid ($v_x(x;z)=C\cdot z$, $v_z(x;z)=0$). The flow pattern changes with depth because the (horizontal) layer of fluid at the bottom of the apparatus is stationary. It was found that the transition from simple shear at the top to stationary at the bottom takes place almost entirely in the lowest 10 mm of the fluid while no deviation from simple shear was detected in the upper layer of 25 mm. The objects that will be inserted (next Chapter) have a depth of 5 mm and are floating with their tops nearly flush to the surface of the liquids. Therefore, the assumption that the objects will be subjected to simple shear is valid.

3.4 Conclusions

- The glycerol used for the experiments in Chapter 4 is analysed and proven to be a Newtonian fluid.
- The 0.5%wt polyacrylamide (pAA) in watery solution is a clear fluid that shows a shear thinning behaviour at shear strain rates in between $6.3\cdot10^{-3}$ and 100 s^{-1}. The stress exponent (n) of the pAA-solution in a power-law stress-strain rate relation increases from 1.5 to 3 in this range of shear strain rates and is thought to be related to an increase in anisotropy of the solution.
- Glycerol and pAA-solutions can be used to model Newtonian and non-Newtonian matrix materials respectively.
- Deformation in the central part of the linear fluid shear apparatus is simple shear flow, at least in the top layer, when no object is inserted in the fluid.
- The fluid shear box can impose arbitrarily high simple shear at direct observation.
- By changing the belt speed and/or shearzone width in the fluid shear apparatus, it is possible to vary the shear strain rate from $5.9\cdot10^{-3}$ to 0.76 s^{-1}.
- Changing the shearzone width while keeping the shear strain rate constant allows investigation of the influence of the shearzone width on the flow pattern.

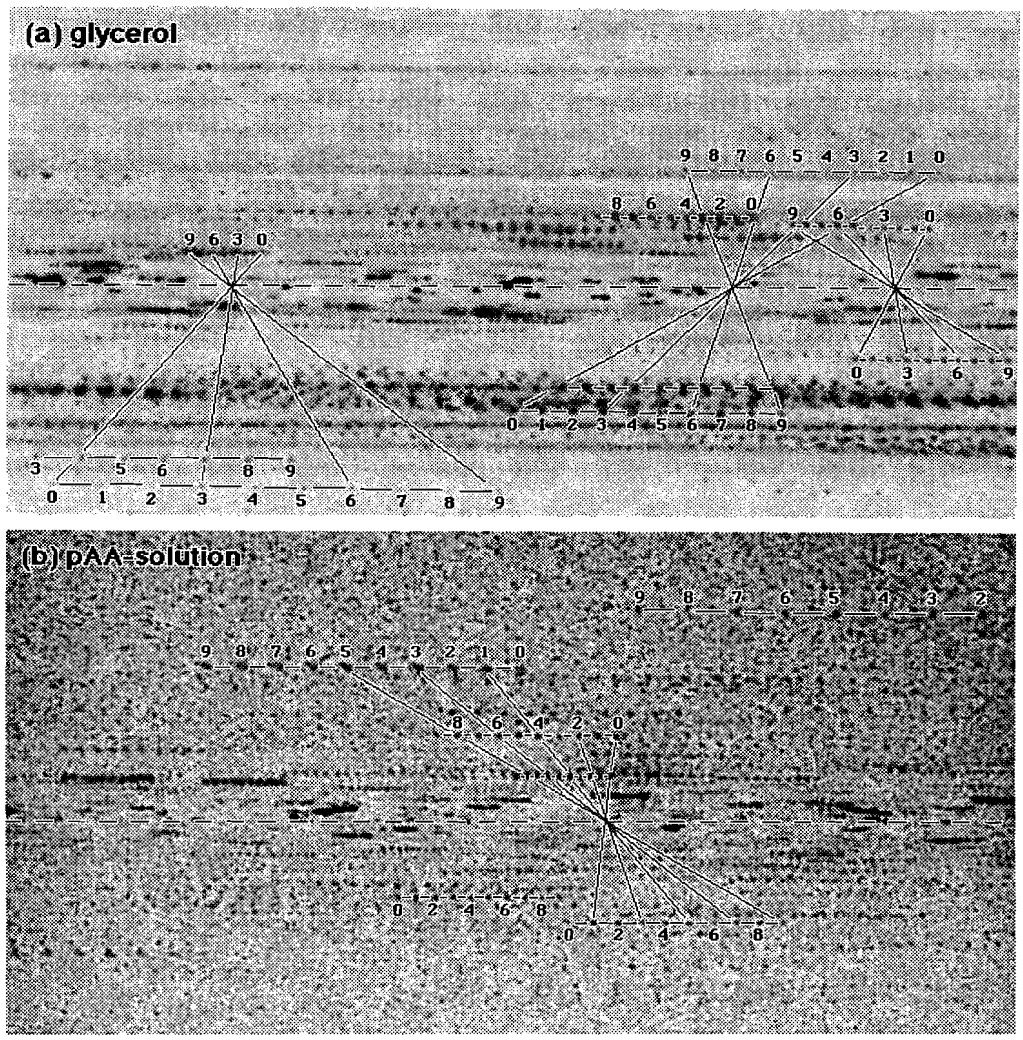

Figure 3.21. Images of the area of interest of shearing **(a)** glycerol and **(b)** pAA-solution when no object is involved. Dashed line at centre of image is the plane of no displacement, numbers indicate successive positions of different particles, oblique lines that connect more than 2 particles remain straight over successive intervals proving simple shear. $\dot{\gamma}$=0.117 s^{-1}, 21°C, average of 10 frames at 2 second intervals, field width is 17.7 mm, shearzone width in (a) is 20 mm and in (b) 40 mm.

Correcting angles measured with NIH image 1.52

During the determination of the rotation rates of the cylindrical object it was found that even this object always showed a pulsating Ω_{rel}-value, depending on the orientation of the object. This led to the belief that the angles measured by the image analysis program, version 1.52 of NIH Image, were not correct and a test was performed to find a possible measurement error. The error in the set-up used can have its origin in the lens, the camera, the frame-grabber, the analysis program or a combination of these. The systematic error was, however, not found while using the program version 1.29q of NIH Image. Since program version 1.29q has other limitations, the later experiments have been analysed with version 1.52.

To examine the accuracy of the measured angles, an object oriented file with 36 numbered rectangles at 5° orientation intervals was made with Canvas™ 3.0.6 and subsequently printed with a QMS-PS 810 laser printer. This print was transformed into TIFF files using the same digital camera, lens, computer and program as during the experiments. The print was 'shot' at two (nearly) perpendicular orientations as the accuracy of the print is not known. The rectangles on these two TIFF files (A and B) were then analysed (with the same procedure as used for the object orientations) with NIH image 1.52 in order to get two orientations ($\alpha(i)_A$ and $\alpha(i)_B$) for each rectangle with number i. If there is no error in either print or analysis, the orientations of the subsequent rectangles in 1 file should have an interval of 5° and the difference in orientation of each rectangle on the two files should be constant and (nearly) 90°. Since this was not the case, the data were treated as follows (see fig. 3A.1):

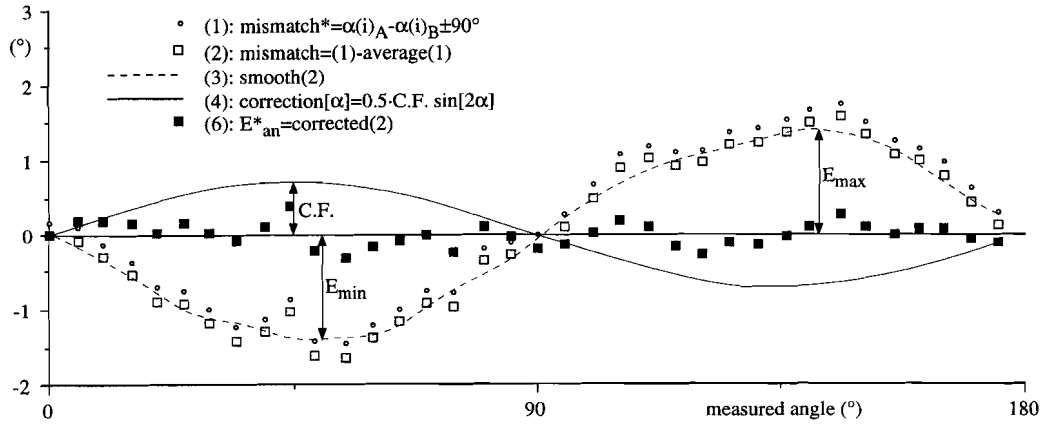

Figure 3A.1. Graph explaining the succeeding steps (between brackets) for correction of the measured angles as described in the text. In this case, the rectangles had a R_{xy} of ~8 and an area on the TIFF files of ~800 pixels. The analytical error in orientation determination (E_{an}) is smaller than 0.3° for this type and size of rectangle.

1) To eliminate the appr. 90° difference in orientation and to shift the values to appr. 0°:
If $(\alpha(i)_A > \alpha(i)_B)$; then mismatch*(i)=$(\alpha(i)_A - \alpha(i)_B - 90°)$;
else mismatch*(i)=$(\alpha(i)_B - \alpha(i)_A + 90°)$;

2) To correct for the possible non-perpendicularity of $\alpha(i)_A$ and $\alpha(i)_B$:
mismatch(i)= mismatch*(i)-average(mismatch*(i));

3) To find the maximum and minimum cyclic error (E_{max} and E_{min} resp.) the mismatch(i)-data were then smoothed.

4) A function was found to correct the orientation data for a cyclic error:
$\text{correction}[\alpha(i)]=0.5 \cdot E_{max} \cdot \sin[2 \cdot \alpha(i)]$;

(The factor 0.5 is because two data-sets had to be corrected in this particular case.)
E_{max} is the correction factor (C.F.) for a certain type (depending on area and R_{xy}) of rectangle.

5) The data are then corrected:
$\alpha(i)_A=\alpha(i)_A+\text{correction}[\alpha(i)_A]$
$\alpha(i)_B=\alpha(i)_B+\text{correction}[\alpha(i)_B]$

6) To find the analysis error in orientation measurements (E_{an}) that cannot be corrected for:
if$(\alpha(i)_A > \alpha(i)_B)$; then $E^*_{an}(i)=(\alpha(i)_A - \alpha(i)_B - 90°)\text{-average}[(\alpha(i)_A - \alpha(i)_B - 90°)]$;
else $E^*_{an}(i)=(\alpha(i)_A - \alpha(i)_B + 90°)\text{-average}[(\alpha(i)_A - \alpha(i)_B - 90°)]$;

This results in a value that represents a maximum of twice the error since it evolves from the difference between two data-sets, each containing its own error; $E_{an}=E^*_{an}/2$. Several types of rectangles were tested, the results are shown in Table 3A.1. From this examination it is clear that the rectangles to be studied should be as large as possible and have a preferably high aspect ratio.

R_{xy}	2		3		8		8	
Area (pixels)	400	800	400	800	400	800	400	800
C.F.	1.4	1.2	0.95	0.85	0.8	0.75	0.7	0.7
E_{an} (°)	0.9	0.8	0.7	0.6	0.5	0.4	0.4	0.3

Table 3A.1. Listing the correction factor (C.F.) and the analysis error (E_{an}) for the orientation of 8 types of rectangles measured with the set-up used during the experiments described in Chapter 4.

Chapter 4

Experimental determination of flow pattern around and rotation rate of floating rigid objects in a linear fluid shear box

4.1 Introduction

This Chapter presents the experiments that were done with the equipment, materials and techniques described in Chapter 3. The experiments were performed in order to determine the effects of matrix material, boundary conditions and object geometry on the flow pattern around, and rotation rate of, floating objects in a shearing medium. A series of tests was first done on the behaviour of free floating cylinders in a shearing Newtonian liquid (glycerol), since available theoretical and experimental work has given insight into this phenomenon. The experimental work was then expanded to objects with different geometries and to test the effects of changing boundary conditions (4.3.2). The influence of non-Newtonian behaviour of the matrix material is described in section 4.3.3 by using a watery 0.5%wt poly-Acrylamide (pAA) solution under identical conditions as for the experiments with glycerol. The results are discussed in 4.4, a speculation about the cause of the unexpected rotational behaviour of objects in the non-Newtonian fluid is given in 4.5.

4.2 Objects

Four objects used in these experiments were made from PVC and had the following dimensions (fig. 4.1): (a&b) Cylinders: Ø=5 x5 and Ø=2 x5 mm, (c) Cube: 5x5 x5 mm, and (d) Rectangular prism: 3x6 x5 mm. As this investigation was two-dimensional (see discussion Chapter 3) the cube and rectangular prism are referred to as square and oblong respectively. All objects had a hole (1 mm diameter, 4 mm deep) drilled in the bottom with the intention to place these objects on an axis. During preliminary experiments, there seemed to be significant friction between the axis and the object which inhibited the modelling of free rotation of the object. PVC has a relative density of 1.3 and would normally sink in the glycerol and the pAA-solution. However, the holes decrease the weight of the objects to such an extent that surface tension keeps the objects from sinking, thus eliminating the need for an axis. When placed in the liquids, the objects 'float' upright with their tops just below the surface of the liquid which shows a meniscus that bends towards the edge of the objects. The Ø=2 mm object actually was too light and, to prevent it from turning 'upside down', the hole was partially filled with dentists putty.

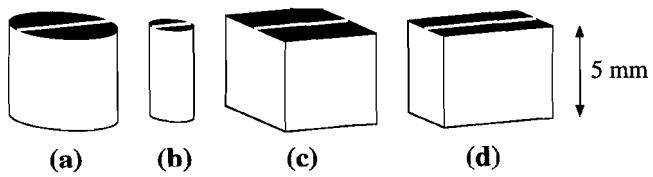

Figure 4.1. The PVC and wooden (except b) objects used in the experiments. **(a)** Ø=5 x5 mm cylinder. **(b)** Ø=2 x5 mm cylinder. **(c)** 5x5 x5 mm 'square' object. **(d)** 3x6 x5 mm 'oblong' object.

During some experiments the cylindrical object did not rotate at a constant rate. This led to the suspicion that static electricity in the PVC influenced the rotational behaviour (see also 4.3.2). In order to circumvent possible static electric charges, objects with the same dimensions as described above (except the Ø=2 mm cylinder) were made from wood with a density of approximately 1.1 g cm^{-3}. To be able to track the rotational behaviour of the rigid objects, a narrow strip (~0.5 mm wide) of white self-adhesive label was fixed to the top side of each object.

4.3 Results

4.3.1 Experimental programme

Table 4.1 lists the experiments that have been performed to analyse the rotational behaviour of the objects. Most of the experiments were done at 20-21°C while some were done at 18 and 24°C to study the influence of different temperatures. During each experiment, the temperature did not vary more than ±0.25°C. The small temperature variation during the individual experiments was not a steady increase and, therefore, cannot be the result of shear-heating. Tests were done with shear zone widths (SZW) in the range of 15 to 40 mm. The electric motor ran at full power (except for experiments G11 to G15) and the different shear strain rates were obtained

EXPERIMENTS WITH GLYCEROL

short name	experimental code	date dd-mm-yy	mixed?	Temp. (°C)	from start?	strainrate (s-1)	SWrel	C.F.	Ωrel av.	Ωrel std.
G1	Ø=5;16.5;1.0;15(2)	24-02-94	y	21.5	y	0.700	3.3	0.0	0.952	0.021
G2	Ø=5;20;1.0;60(1)-1	11-01-95	y	20.0	y	0.574	4.0	0.7	1.019	0.013
G3	Ø=5;20;1.0;60(1)-2	11-01-95	y	19.0	y	0.574	4.0	0.7	1.022	0.016
G4	Ø=5;16.5;2.5;15(5)	24-02-94	y	21.5	y	0.280	3.3	0.0	0.965	0.018
G5	Ø=5;16.5;5.0;15(10)	24-02-94	y	21.5	n	0.140	3.3	0.0	0.966	0.012
G6	Ø=5;20;5.0;60(3)-1	11-01-95	y	20.0	y	0.117	4.0	0.7	1.007	0.015
G7	Ø=5;20;5.0;60(3)-2	11-01-95	y	20.0	y	0.117	4.0	0.7	1.003	0.012
G8	Ø=5;16.5;10;15(10)	24-02-94	y	21.5	y	0.070	3.3	0.0	0.970	0.036
G9	Ø=5;16.5;25;15(25)	03-03-94	y	20.0	n	0.028	3.3	0.0	1.020	0.024
G10	Ø=5;16.5;50;15(50)	03-03-94	y	20.0	n	0.014	3.3	0.0	1.007	0.048
G11	S=5;40;2.5;55(4)	24-01-95	y	20.0	y	0.114	8*	0.7	1.007	0.015
G12	S=5;40;2.5;60(2)-1	24-01-95	y	20.0	y	0.114	8*	0.7	1.005	0.019
G13	S=5;40;2.5;60(2)-2	24-01-95	y	20.0	y	0.114	8*	0.7	1.006	0.018
G14	S=5;16.5;2.5;15(2)	04-03-94	n	room	y	0.280	3.3*	0.0	1.021	0.042
G15	S=5;16.5;5.0;15(5)-1	01-03-94	n	21.5	y	0.140	3.3*	0.0	0.983	0.030
G16	S=5;16.5;10;15(7)	04-03-94	n	room	y	0.070	3.3*	0.0	0.993	0.071
G17	O=6;40;2.5;59(1)	24-01-95	y	20.0	n	0.114	8*	0.7	n.a.	n.a.
G18	O=6;40;2.5;60(2)-2	24-01-95	y	20.0	n	0.114	8*	0.7	n.a.	n.a.
G19	O=6;16.5;5.0;15(5)	02-03-94	n	room	n	0.140	3.3*	0.0	n.a.	n.a.
G20	R=4;16.5;5.0;43(2)	10-06-94	n	21.0	n	0.140	3.3*	0.7	n.a.	n.a.

Table 4.1 (continued on next page). Table listing the experiments described in this work. Short names are included for use in graphs and text. The column "mixed" shows if the liquid was homogenised prior to the start of the experiment. Y in the column "from start?" means that the first frame was taken at the onset of deformation; n means that the first frame was taken after an amount of shear at least equivalent to that needed for a cylindrical object to reach a 'steady state' rotation rate. A * in column "SW_{rel}" means that the object is not round so SW_{rel} changes with orientation; an average diameter of 5 mm has been used to calculate SW_{rel} for these cases. Column "C.F." (glycerol experiments) states the correction factor used while determining the orientations in glycerol experiments; C.F. for all pAA experiments was 0.7. The columns "Ω_{rel} av." and "Ω_{rel} std." give average and standard deviation of Ω_{rel}-values (if appropriate). The column "γ" (pAA experiments) indicates the shear value chosen as begin of 'steady state' rotation and the start of computing av. & std. Ω_{rel}; † indicates that steady state rotation rate was reached before first frame was taken. Values in bold show influence of the column variable most prominent. Values in italics show a negative temperature dependency of Ω_{rel}.

EXPERIMENTS WITH pAA-SOLUTION (new solution after 13-12-94)

name	experiment	date dd-mm-yy	mixed?	Temp. (°C)	from start?	strainrate (s-1)	SWrel	γ	Ωrel av.	Ωrel std.
P1	Ø=2;40;10;60(15)-2	06-12-94	y	20.0	y	0.029	**20.0**	4	0.778	0.017
P2	Ø=2;40;10;51(15)-1	06-12-94	y	20.0	y	0.029	20.0	6	0.809	0.019
P3	Ø=2;20;5.0;60(4)-2	19-12-94	y	20.0	y	0.117	10.0	7	0.629	0.015
P4	Ø=2;20;5.0;120(4)-3	19-12-94	y	20.0	y	0.117	10.0	7	0.634	0.019
P5	Ø=2;20;5.0;60(4)-1	19-12-94	y	19.5	y	0.117	10.0	7	0.658	0.026
P6	Ø=2;40;2.5;60(4)-1	25-11-94	n	21.0	y	0.117	20.0	7	0.565	0.015
P7	Ø=2;40;2.5;56(8)-3	15-12-94	y	21.0	y	0.117	**20.0**	7	0.621	0.011
P8	Ø=2;40;2.5;60(4)-2	14-12-94	y	20.0	y	0.117	20.0	7	0.592	0.016
P9	Ø=2;40;1.0;60(1)	05-12-94	y	21.0	y	0.287	**20.0**	7	0.489	0.018
P10	Ø=5;40;50;60(30)	30-11-94	n	21.0	n	**0.006**	8.0	0†	0.951	0.019
P11	Ø=5;40;25;22(10)	30-11-94	n	21.0	n	0.012	8.0	0†	0.953	0.054
P12	Ø=5;40;10;59(5)-4	02-12-94	y	22.0	y	0.029	8.0	4	0.865	0.024
P13	Ø=5;40;10;55(15)-3	02-12-94	y	22.0	n	0.029	8.0	0†	0.861	0.013
P14	Ø=5;40;10;40(15)-1	07-12-94	y	20.5	y	0.029	8.0	4	0.801	0.014
P15	Ø=5;40;10;49(15)-2	07-12-94	y	20.5	y	0.029	8.0	4	0.819	0.016
P16	Ø=5;40;10;60(15)-5	06-12-94	y	20.0	y	**0.029**	**8.0**	4	0.809	0.011
P17	Ø=5;40;5.0;60(7)-2	05-12-94	y	20.5	y	**0.059**	8.0	5	0.730	0.012
P18	Ø=5;40;5.0;37(7)-1	05-12-94	y	20.0	y	0.059	8.0	5	0.716	0.008
P19	Ø=5;15;10;60(6)-2	21-12-94	y	**24.0**	y	0.077	3.0	7	0.741	0.018
P20	Ø=5;15;10;60(6)-3	22-12-94	y	**21.0**	y	0.077	3.0	7	0.726	0.032
P21	Ø=5;15;10;60(6)-1	20-12-94	y	**18.5**	y	0.077	3.0	7	0.714	0.028
P22	Ø=5;20;5.0;60(4)-1	16-12-94	y	21.0	y	**0.117**	**4.0**	7	0.649	0.013
P23	Ø=5;20;5.0;60(4)-2	16-12-94	y	*21.0*	y	0.117	4.0	7	*0.646*	0.016
P24	Ø=5;20;5.0;60(4)-4	19-12-94	y	*19.5*	n	0.117	4.0	0†	*0.683*	0.015
P25	Ø=5;20;5.0;60(4)-3	19-12-94	y	*19.0*	y	0.117	4.0	7	*0.667*	0.019
P26	Ø=5;20;5.0;60(4)-5	20-12-94	y	*18.5*	y	0.117	4.0	7	*0.673*	0.011
P27	Ø=5;40;2.5;60(4)-1	24-11-94	y	21.0	n	0.117	8.0	0†	0.659	0.008
P28	Ø=5;40;2.5;60(4)-2	05-12-94	y	20.5	y	0.117	8.0	7	0.628	0.014
P29	Ø=5;40;2.5;60(4)-5	16-12-94	y	21.0	y	0.117	8.0	7	0.640	0.009
P30	Ø=5;40;2.5;50(8)-4	15-12-94	y	21.0	y	0.117	8.0	7	0.623	0.011
P31	Ø=5;40;2.5;60(4)-3	14-12-94	y	20.0	y	0.117	8.0	7	0.606	0.010
P32	Ø=5;15;5.0;60(3)-2	21-12-94	y	**24.0**	y	0.154	3.0	7	0.649	0.015
P33	Ø=5;15;5.0;60(3)-3	22-12-94	y	**21.0**	y	0.154	3.0	7	0.631	0.025
P34	Ø=5;15;5.0;60(3)-1	20-12-94	y	**18.5**	y	0.154	3.0	7	0.611	0.024
P35	Ø=5;40;1.0;60(1)	05-12-94	y	21.0	y	0.287	**8.0**	8	0.497	0.018
P36	Ø=5;15;2.5;60(1)-2	21-12-94	y	**24.0**	y	0.308	3.0	8	0.544	0.015
P37	Ø=5;15;2.5;60(1)-3	22-12-94	y	**21.0**	y	**0.308**	3.0	8	0.519	0.019
P38	Ø=5;15;2.5;60(1)-1	20-12-94	y	**18.0**	y	0.308	3.0	8	0.483	0.021
P39	Ø=5;20;1.0;60(1)	16-12-94	y	21.0	y	**0.574**	4.0	8	0.398	0.015
earlier experiments: Ø=5;16.5;1.0;...(..)				room		±0.70	3.3		±0.35	
P40	S=5;40;2.5;48(4)-1	25-11-94	n	21.0	n	0.117	8*	n.a.	n.a.	n.a.
P41	S=5;40;2.5;49(4)-2	25-11-94	n	21.0	n	0.117	8*	n.a.	n.a.	n.a.
P42	O=6;40;2.5;53(4)-1	25-11-94	n	21.0	n	0.117	8*	n.a.	n.a.	n.a.
P43	O=6;40;2.5;39(4)-2	25-11-94	n	21.0	n	0.117	8*	n.a.	n.a.	n.a.
P44	O=6;40;2.5;60(2)	25-11-94	n	21.0	n	0.117	8*	n.a.	n.a.	n.a.
P45	O=6;15;5.0;60(3)	22-12-94	y	21.0	n	0.154	3*	n.a.	n.a.	n.a.

Table 4.1 (continued).

using different reductions of the gear-box and widths of the shear zone. The shear strain rates used in these experiments are chosen in the range where the n-value of the pAA solution changes from 1.5 to 2.3: from 0.006 to 0.70 s^{-1}.

The experimental codes in the table denote the most prominent features and can be read as follows: object type; shear zone width; gearbox setting in revolutions out:revolutions in; number of frames in film (interval time between frames)-repetition {when appropriate}. As an example, the experiment G7 with code: Ø=5;20;5.0;60(3)-2 means: {glycerol experiment number 7} 5 mm diameter cylinder; shear zone width = 20 mm; gears = 5:1; 60 frames (at 3 second intervals)

- repetition of G6. The earlier experiments were done using a spacer of 16.5 mm between the belts before fixing the guiding blocks to the lid of the shearbox and were analysed with version 1.29q of the program NIH-Image (see Chapter 3). These experiments produced statistically acceptable results for the experiments in glycerol and these have not been repeated although an investigation of the influence of the shear zone width (SZW) was done at a later stage. The rotational behaviour of the objects in the pAA experiments could only be examined with a larger number of (smaller sized) frames. The results of the earlier experiments with pAA are therefore not included, except for the average relative rotation rate at 0.70 s^{-1} since this shear strain rate has not been repeated during later experiments. The rotation rates of the objects are all shown as Ω_{rel}-values; the rotation rate of the object relative to the rotation rate of a cylinder in a Newtonian matrix that is sheared at the same rate (see also Chapter 3, section 3.3.2).

4.3.2 Experiments with glycerol as the shearing medium

Cylindrical object

Rotation rate

The graphs of shear-strain (γ) versus Ω_{rel}-value for a cylindrical object (Ø=5 mm PVC or wood) in glycerol show an Ω_{rel}-value of 1.0±0.075 (figure 4.2). The rotation rates agree well with the theoretical value of Jeffery (1922) and Freeman (1985). No influence of shear strain rate on the rotation rate of a cylinder in a Newtonian fluid was found. An influence of the relative shear zone width (SW_{rel}; definition in Ch. 3) on rotation rate cannot be evaluated from the data for cylinders in shearing glycerol since the difference in SW_{rel} between experiments was too small.

Experiment G10 shows a larger variation in Ω_{rel}-value than ±0.075. This variation is related to the orientation of the white label on the top of the cylinder, the minimum is found at an orientation of ~20°, the maximum at ~110° (fig. 4.3a). The object in experiment G10 was made from PVC and the variation is thought to be the effect of electric forces due to a charge of the object and the guiding blocks. Since this was the experiment with the lowest rate of shear strain, the absolute rotation rate was also lowest. The possible attracting and repelling electrical forces thus had a longer period of time to act on the object than during experiments at higher shear strain rates. From experiment G10 it was decided to use wooden objects instead of objects made from PVC. Where this was impossible (the Ø=2 mm cylinder), care was taken to ground the guiding blocks and the object before the cylinder was placed in the liquid.

Figure 4.2 (next page). Graphs showing the relative rotation rates of a floating Ø=5 mm cylinder in glycerol at shear strain rates ranging from 0.014 to 0.7 s^{-1} (experiments G1-G10). **(a)** Graphs showing Ω_{rel}-value versus accumulated shear (γ) for a shear zone width of 16.5 mm. **(b)** As (a); shear zone width is 20 mm. **(c)** Composite graph for a shear zone width of 16.5 mm. **(d)** Composite graph for a shear zone width of 20 mm. c/d show that the average Ω_{rel}-value is close to unity. Dashed boxes around shear strain rate value in (a) and (b) correspond to dashed curves in (c) and (d) resp.. Note that the scales of the graphs are not all the same.

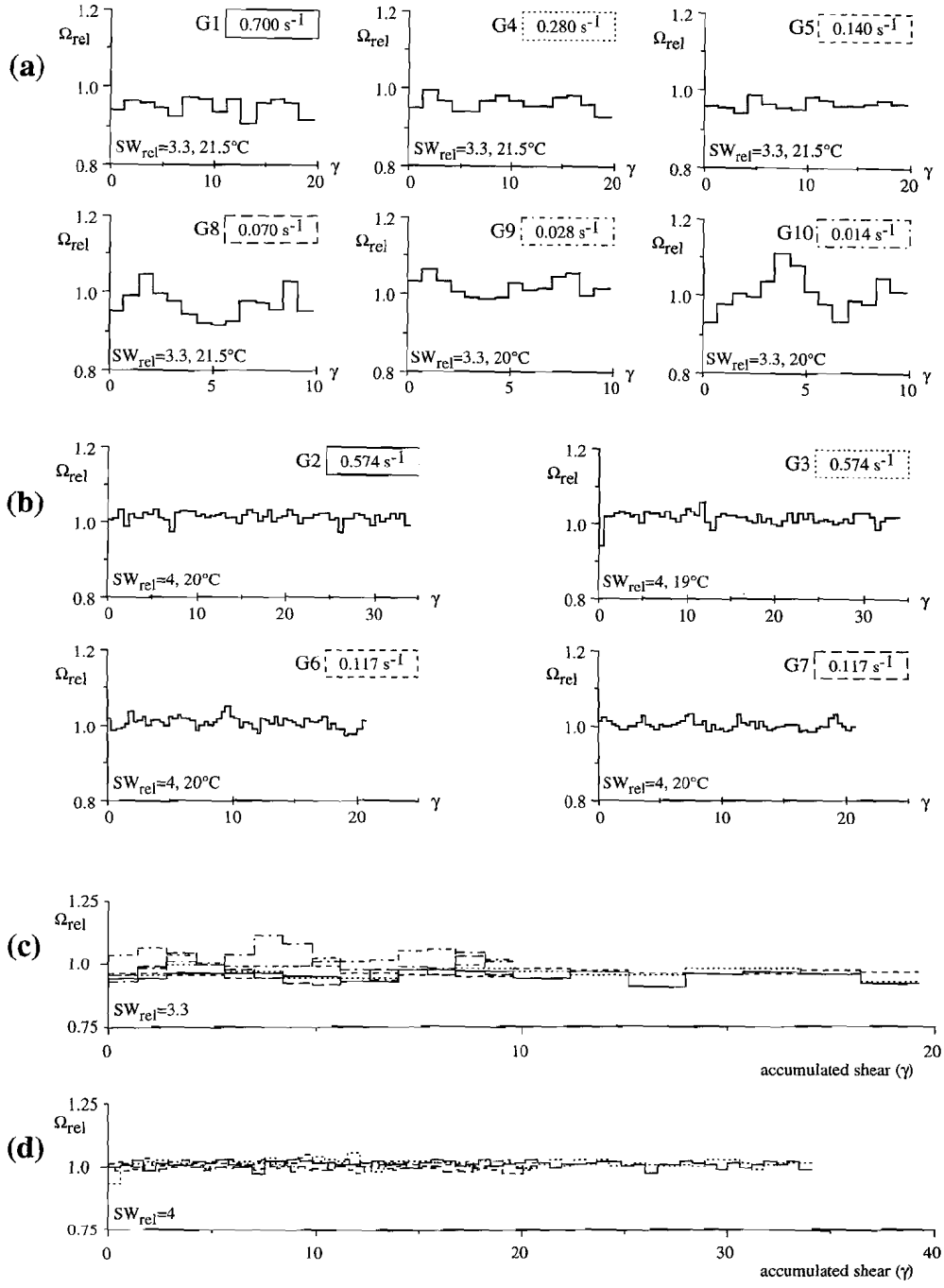
(a)
G1 0.700 s-1
G4 0.280 s-1
G5 0.140 s-1
G8 0.070 s-1
G9 0.028 s-1
G10 0.014 s-1
SWrel=3.3, 21.5°C
SWrel=3.3, 20°C
(b)
G2 0.574 s-1
G3 0.574 s-1
G6 0.117 s-1
G7 0.117 s-1
SWrel=4, 20°C
SWrel=4, 19°C
(c)
SWrel=3.3
accumulated shear (γ)
(d)
SWrel=4
accumulated shear (γ)
Ωrel
γ

Flow pattern

Shear zone width was found to have a strong influence on the flow pattern in glycerol around a floating cylindrical object. The particle paths, illustrated in figure 4.3, show that a time independent bow-tie flow pattern develops around a cylindrical object when the relative shear zone width (SW_{rel}) is smaller than 20. The relation between the relative distance of the stagnation points to the centre of the object (D_s; definition in Ch. 3) and SW_{rel} is ambiguous. In figures 4.3a-c, SW_{rel} is 4, 8 and 10 while D_s is 1.8, 2.4 and 2.3 respectively. In figure 4.3d (SW_{rel} is 20) the position of the stagnation point cannot be determined as the region with closed flow lines is wider than the image: the flow resembles an eye-shaped pattern. The general trend indicates an

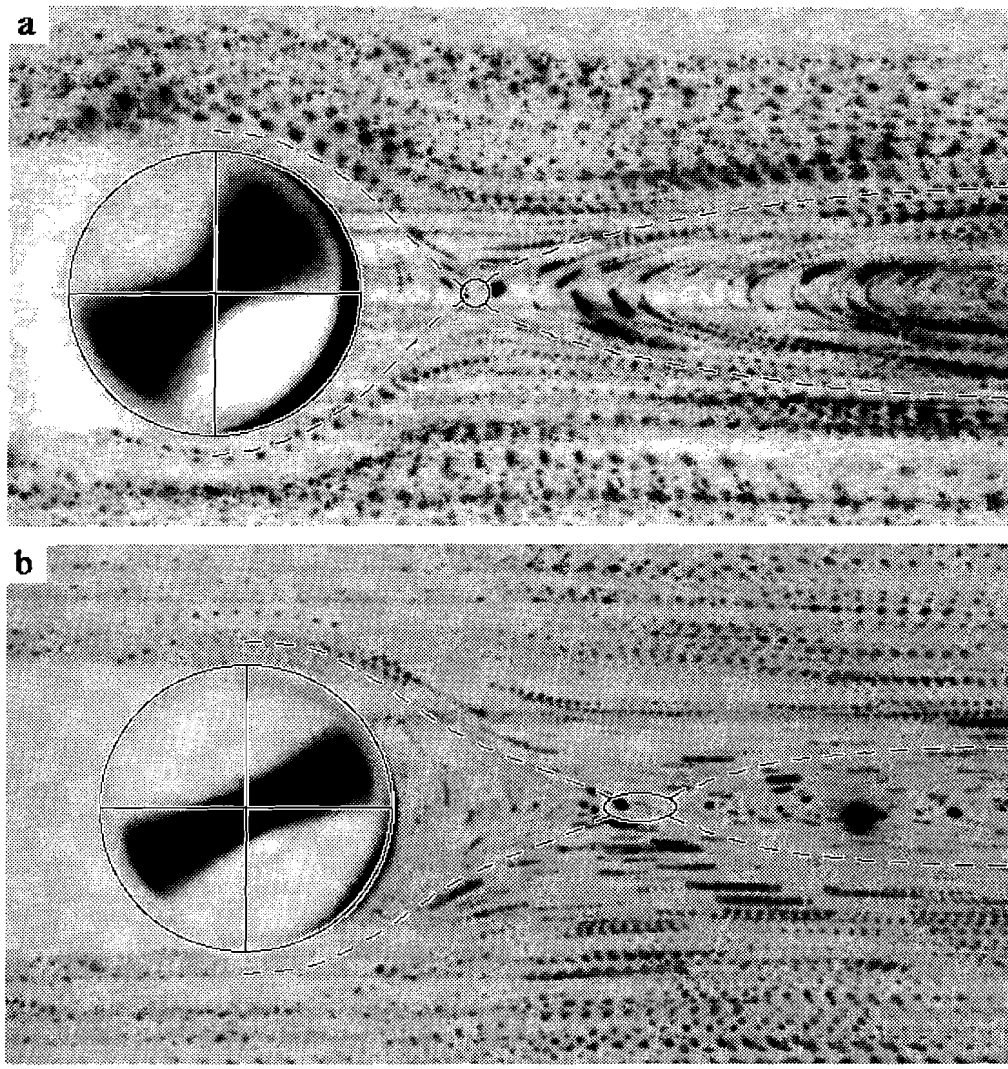

Figure 4.3. Images (averages of 10 frames) showing the bow-tie flow pattern in glycerol around a floating cylinder at a shear strain rate of 0.117 s^{-1}, sinistral shear. Dashed lines and circle (or ellipse) in (a) to (c) indicate interpreted position of separatrices and stagnation point resp.. **(a&b)** Object is a Ø=5 mm cylinder. **(a)** Shear zone width is 20 mm (SW_{rel} is 4), 2 second intervals, D_s is 1.8. The amount of rotation is shown by the exposure of the strip at the

increase in D_s with an increase in SW_{rel} and the small difference in SW_{rel} between figures 4.3b and 4.3c, combined with the poorly defined position of the stagnation point, may account for the deviation from the general trend.

The width of the backflow region is also dependent of SW_{rel}: when SW_{rel} is large, the backflow region is narrow with respect to the cylinder and the far-field separatrices are parallel to the shear zone boundary at a small distance from the object (figs. 4.3b,c); if SW_{rel} is small, the backflow region is nearly as wide as the diameter of the cylinder and the separatrices continue to diverge over a longer distance (fig. 4.3a).

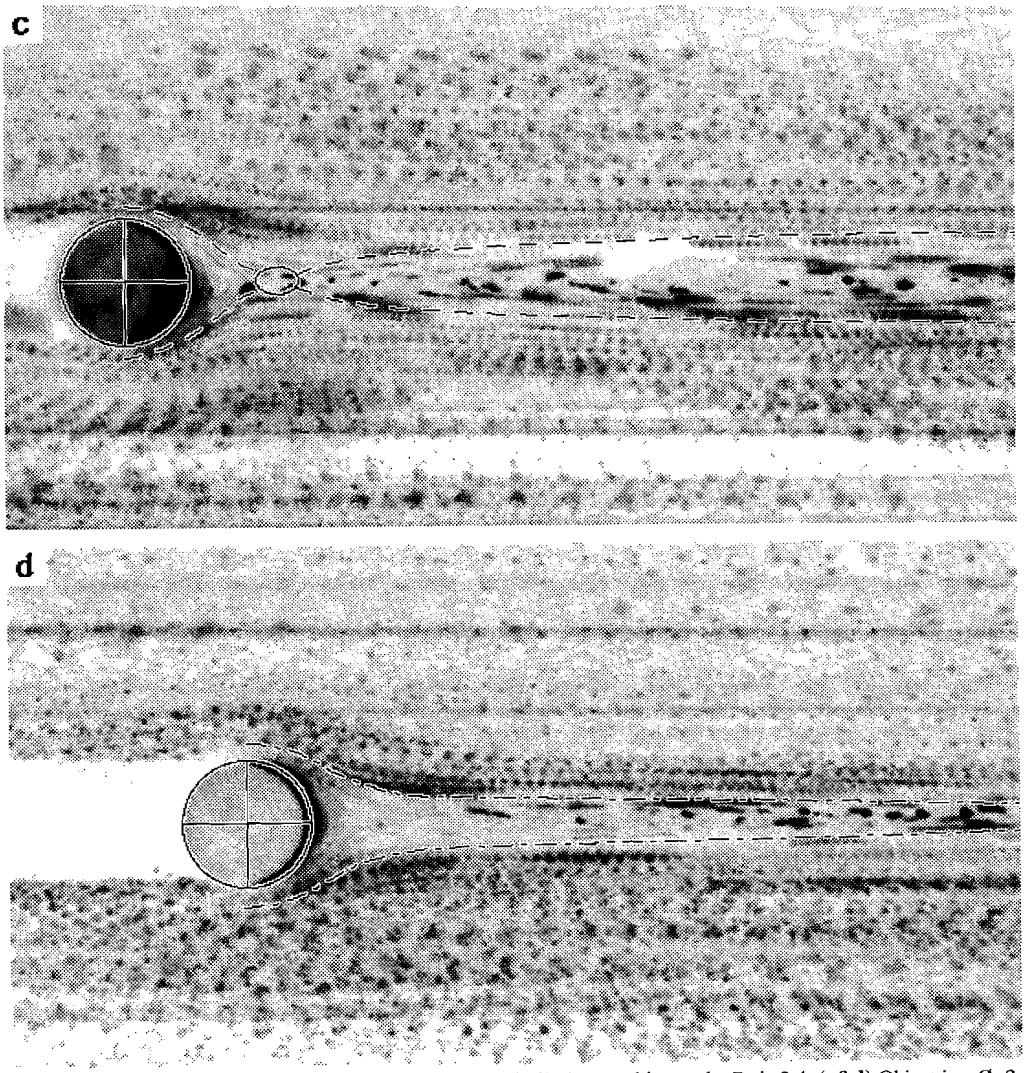

top of the object. (**b**) Shear zone width is 40 mm (SW_{rel} is 8), 1 second intervals, D_s is 2.4. (**c&d**) Object is a Ø=2 mm floating cylinder. (**c**) Shear zone width is 20 mm (SW_{rel} is 10), 2 second intervals. D_s is 2.3. The object had no white strip at the top during this experiment. (**d**) Shear zone width is 40 mm (SW_{rel} is 20), 2 second intervals, eye-shaped flow pattern (D_s cannot be determined), dashed lines represent interpreted flow paths.

Square object

Rotation rate

The graphs of shear-strain (γ) and orientation (α) versus Ω_{rel}-value for a square object (5x5 mm PVC or wood) show an Ω_{rel}-value of 1.0 ($\pm$0.1) which is independent of the shear zone width (figs. 4.4a,b). The orientation of the object with respect to the flow-plane cannot be traced in figs. 4.4a-c. Apparently, there is no 90° cycle in Ω_{rel}-value which might be expected from the geometry of the object (fig. 4.4d). The rotational behaviour of the square object in a Newtonian fluid is thus equal to that of the cylindrical object under similar circumstances.

Figure 4.4 (next page). Graphs showing the rotational behaviour of a floating 5x5 mm square object in glycerol at shear rates ranging from 0.070 to 0.280 s^{-1} (experiments G11-G16). **(a&b)** Graphs showing Ω_{rel}-value versus accumulated shear (γ). Arrows indicate when object has rotated to α=180°. Thick part of curve in a corresponds to curves in (d). **(a)** SW_{rel}=8 (experiments G11-G13). **(b)** SW_{rel}=3.3 (experiments G14-G16). **(c)** Composite graph showing Ω_{rel}-value versus accumulated shear (γ). **(d)** Ω_{rel}-value versus object orientation (α). Bottom pictorial explains object orientation. Dashed boxes around shear rate values in (a) and (b) correspond to dashed curves in (c) and (d). Note that axes do not have the same scale.

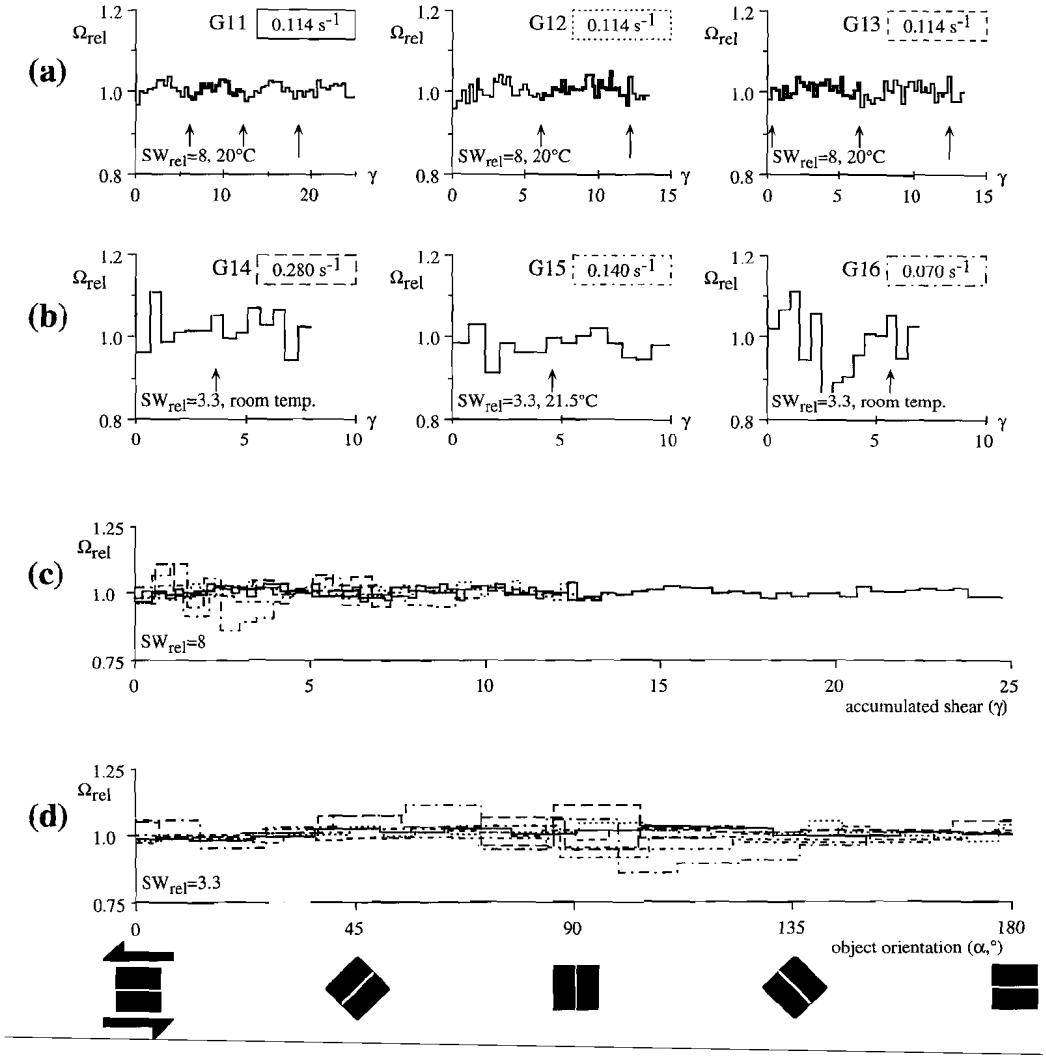
(a)
G11 0.114 s-1
G12 0.114 s-1
G13 0.114 s-1
Ωrel
SWrel=8, 20°C
γ
(b)
G14 0.280 s-1
G15 0.140 s-1
G16 0.070 s-1
SWrel=3.3, room temp.
SWrel=3.3, 21.5°C
(c)
SWrel=8
accumulated shear (γ)
(d)
SWrel=3.3
object orientation (α,°)

Flow pattern

The flow pattern in glycerol around a square object (fig. 4.5) shows a bow-tie geometry and is orientation-, and thus shear- and time-, dependent. With rotation of the object, the stagnation points and the separatrices change position with respect to the centre of the object. When one side of the cube is parallel to the direction of shear, (α=0° or 90°), the stagnation points are situated at the same level (with respect to the shear zone boundaries) as the centre of the object. During rotation, the stagnation point to the right of the object starts to shift upwards until it reaches a maximum level when α=~22°, then downwards crossing the 'centre' level again when α=45°. It continues to shift downwards until a minimum when α=~57° after which it starts to shift upwards again. The distance of the stagnation point to the centre of the object is smallest when α=0° and largest when α=45° but this difference is relatively small (fig. 4.5e). The width of the backflow region mimics the width of the obstacle: it increases from α=0° to α=45° and then decreases until α=90°.

To obtain detailed information on the position of the stagnation points or separatrices in a time dependent flow, means that the flow paths should be recorded in such a shear- (or time-) interval that the rotation of the object is small. During a small increment of shear, the particle displacements are short, especially near the stagnation points. Therefore, it was only possible to obtain rough estimates of the position of the stagnation points and separatrices. Since the flow around the object is time dependent, the question can be raised if the terms 'stagnation point' and 'separatrices' are used correctly in those cases. Although the displacements at the interpreted stagnation points were small, they were not absent. Furthermore, in a time independent flow pattern, each particle always remains in the same flow region (far field, backflow or elliptical flow) which is no longer true in a time dependent flow.

Figure 4.5 (next page). Images showing one cycle of 90° of the orientation dependent bow-tie flow pattern in glycerol around a 5x5 mm floating square object. $\dot{\gamma}$=0.140 s^{-1}, sinistral shear, SZW=16.5 mm, 21°C, average of 5 frames at 1 second intervals, field width is 24 mm. Dashed lines and circle (or ellipse) indicate interpreted position of separatrices and stagnation point resp.. During a time interval of 4 seconds as shown in these images, the object rotates ~16°. **(a)** Object has an orientation with one side approximately parallel to the direction of shear; α=90±8° (the marker on the object is faintly visible). **(b)** α=113±8°. **(c)** α=135±8°. **(d)** α=158±8°. **(e)** Cartoon shows different positions of stagnation point as traced in (a) to (d). The arrowed line connects the centres of the circles that indicate approximate positions.

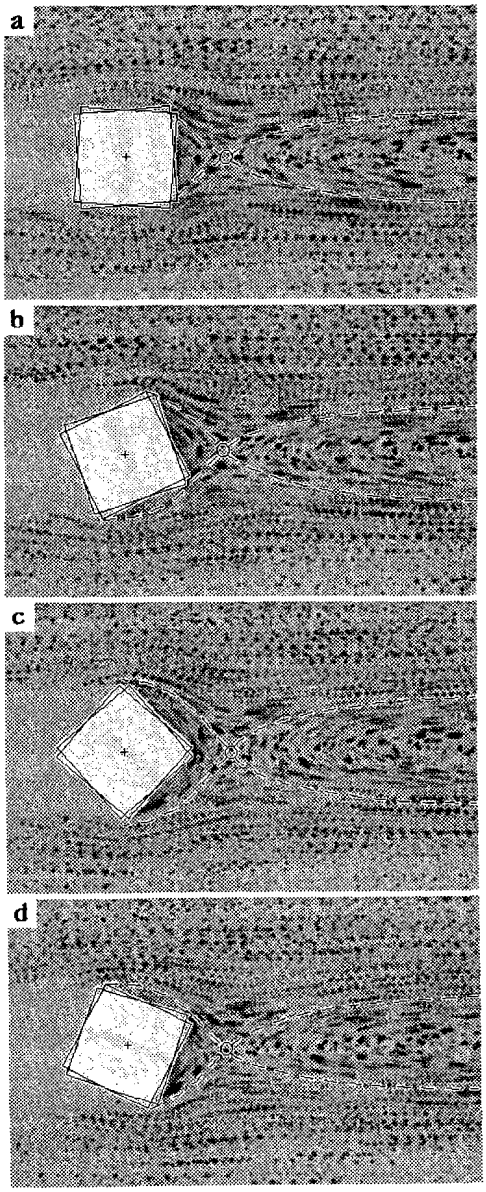
a
b
c
d

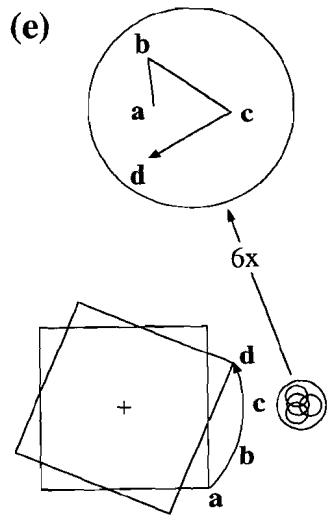
(e)
b
a
c
d
6x
d
c
b
a

Oblong object

Rotation rate

The α versus Ω_{rel} graph (fig. 4.6) for an oblong object with an aspect ratio (R_{xy}) of 2 (experiments G17-G19: 3x6 mm PVC; SZW: G17&G18: 40 mm, G19: 16.5 mm) shows a curve with a maximum Ω_{rel}-value of 1.5 when α=~90°, and a minimum Ω_{rel}-value of 0.5 when α=~0°. These experiments show that no influence of SW_{rel} on Ω_{rel} was present. To investigate the influence of R_{xy} on Ω_{rel}, an oblong object with an aspect ratio of 4 was made from eraser-gum (Staedtler 526 50; experiment G20: 1.3x5.4x11.5 mm, SZW=16.5 mm). This object also shows a pulsating rotational behaviour with maximum and minimum Ω_{rel}-values of 1.85 (α=~90°) and 0.15 (α=~0°) respectively (figs. 4.6b,c). Figure 4.6c shows that an oblong object in glycerol has a rotational behaviour that is close to the theoretical behaviour of an ellipsoid in a Newtonian medium, when a 12.5% smaller aspect ratio for the equivalent ellipsoid is chosen.

Figure 4.6 (next page). Graphs showing Ω_{rel}-value versus object orientation (α) of a floating oblong object in glycerol at shear strain rates of 0.114 and 0.140 s^{-1} (experiments G17-G20) and the theoretical behaviour of ellipsoids of axial ratios (R_{xy}) 1.75 and 3.50 in a Newtonian medium. **(a)** Experiments G17&G18 (SZW=40 mm, R_{xy} of the object is 2) and the theoretical behaviour for R_{xy}=1.75. **(b)** Experiments G19&G20 (SZW=16.5 mm, R_{xy} of the object is 2 and 4 resp.) and the theoretical behaviour for R_{xy}=3.50. **(c)** Composite graph of (a) and (b). Bottom pictorial explains object orientation, dashes correspond to dashed boxes around shear strain rate value in (a) and (b), smooth curves are theoretical values for ellipsoids with axial ratios as indicated.

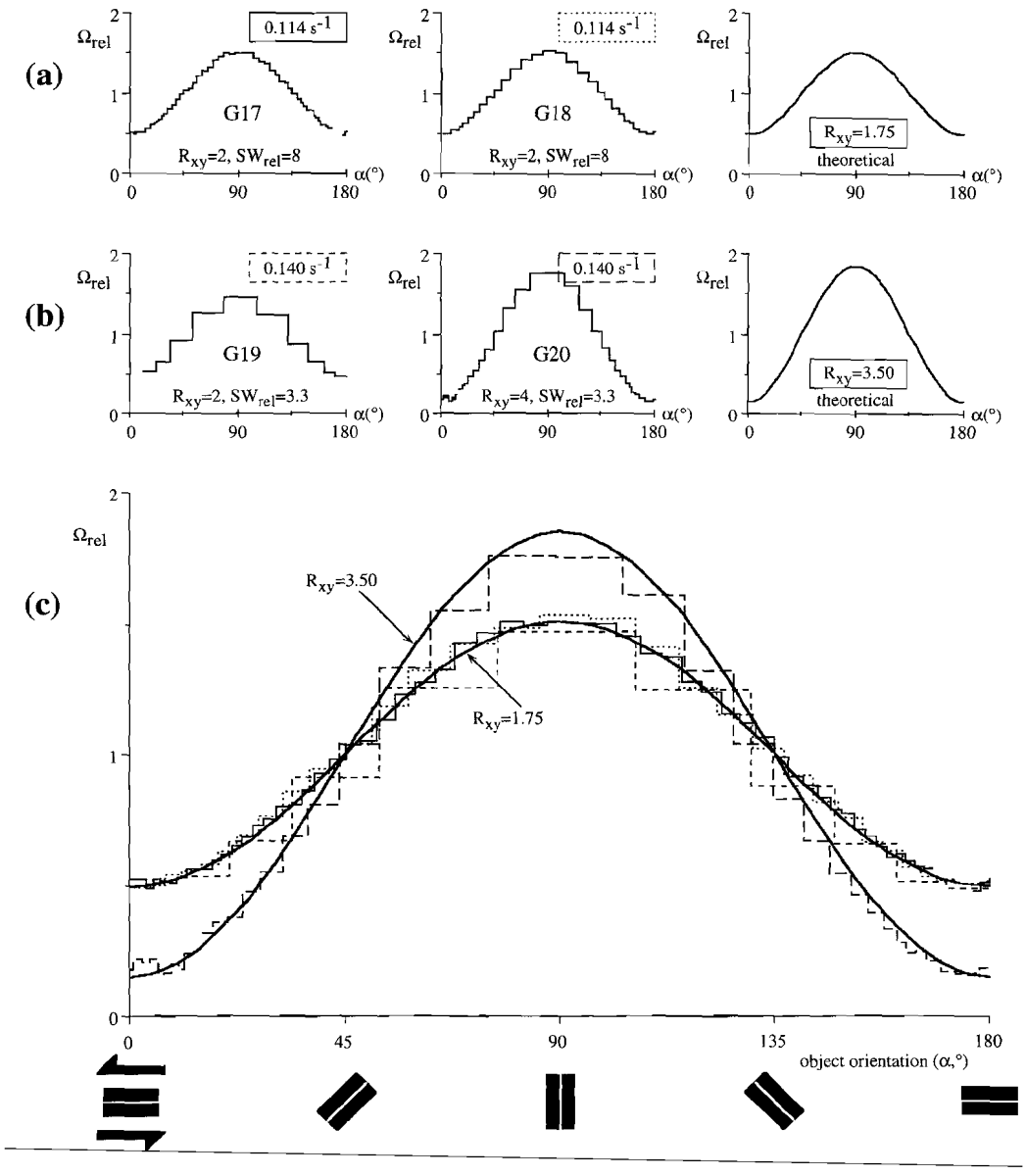
(a)
0.114 s-1
G17
Rxy=2, SWrel=8
G18
Rxy=1.75
theoretical
(b)
0.140 s-1
G19
Rxy=2, SWrel=3.3
G20
Rxy=4, SWrel=3.3
Rxy=3.50
(c)
Ωrel
α(°)
0
45
90
135
180
object orientation (α,°)

Flow pattern

The flow pattern in glycerol around a floating oblong object (fig. 4.7) shows a bow-tie geometry and is orientation dependent, and thus shear- and time- dependent. This makes it difficult to establish accurate positions of stagnation points and separatrices. Within the limit of accuracy, the position of the stagnation point does not seem to shift vertically although D_S appears to be smallest when α=~0° and largest when α=~25° (fig. 4.7e). The width of the backflow region changes with the orientation of the object. A minimum width is reached when α=~0° or α=~90°, a maximum is reached at intermediate orientations. The interpreted far-field separatrices at intermediate orientations are skewed: they cannot be mirrored in a horizontal plane through the stagnation point, as was the case with the square object. Particle trajectories within the central part of the separatrices can be described by semi-circles.

The best example of the difficulties that arise in locating the stagnation points and separatrices is found when the long axis of the object is perpendicular to the flowplane (fig. 4.7d). A region where displacements are very small is found at approximately the same position as in the other orientations and this is interpreted as a stagnation point. When the particle displacements from this point on are extrapolated, the separatrices end on the surface of the object. Linking or extrapolating particle displacements from the corners of the object results in paths that keep dilating from the object.

Figure 4.7 (next page). Images showing part of the cycle of 180° of the bow-tie flow pattern in glycerol around a 6x3 mm floating oblong object. $\dot{\gamma}$=0.140 s^{-1}, sinistral shear, SZW=16.5 mm, 21°C, average of 5 frames at 1 second intervals, field width is 24 mm. Dashed lines and circle (or ellipse) indicate interpreted position of separatrices and stagnation point resp.. **(a)** The object has an orientation with the long side parallel to the direction of shear: α=0±4°. **(b)** α=25±5°. **(c)** α=40±8°. **(d)** α=88±12°. Note that the particle paths close to the object are semi-circular. The central part of the separatrices in (d) seem to end on the surface of the object. **(e)** Cartoon shows different positions of stagnation point as traced in (a) to (d). The arrowed line connects the centres of the circles that indicate the approximate positions.

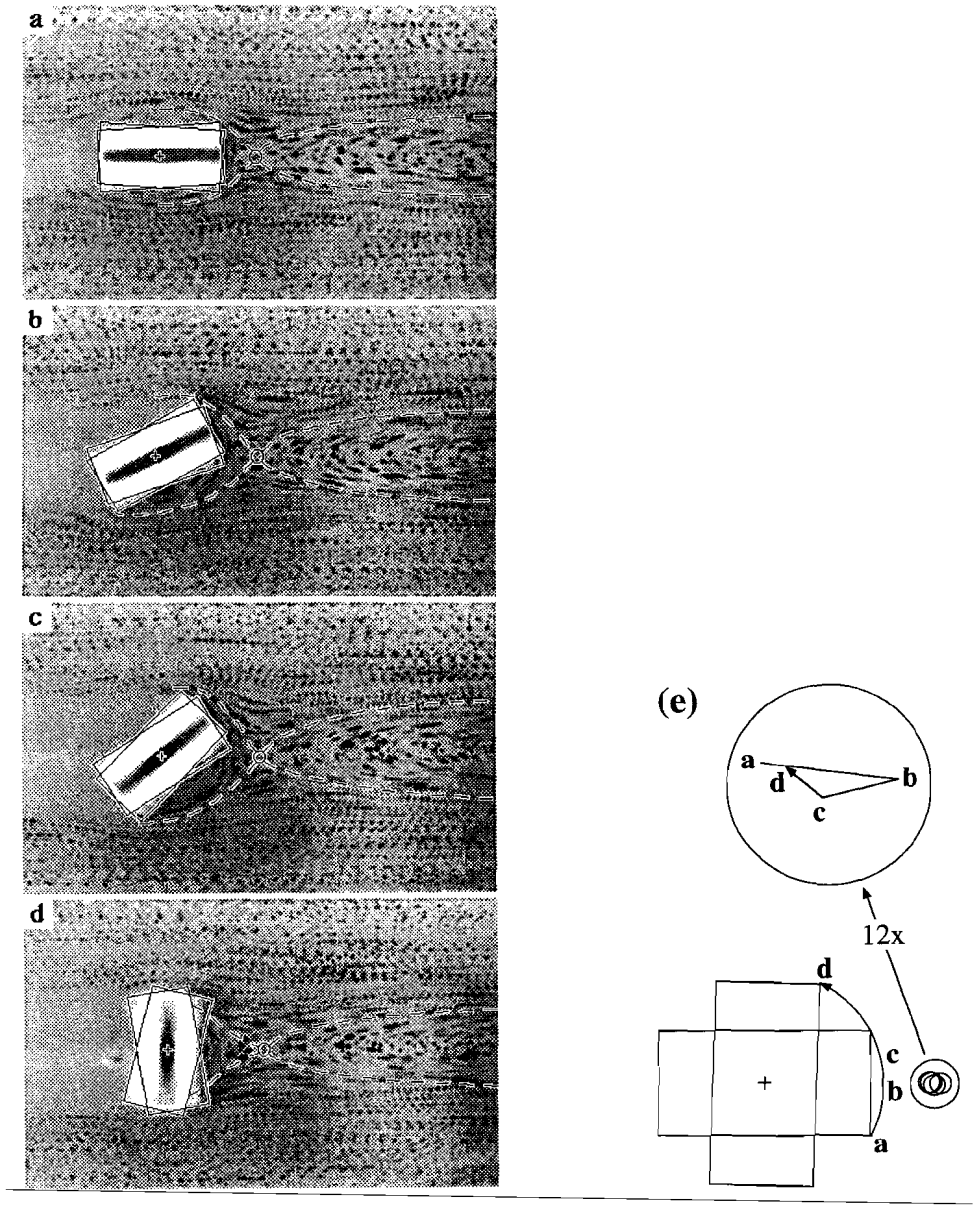
a
b
c
d
(e)
a
b
c
d
12x
d
c
b
a

4.3.3 Experiments with a 0.5%wt pAA-solution as the shearing medium

Cylindrical object

Rotation rate

In contrast to the rotational behaviour of a cylinder in glycerol, equivalent experiments in a 0.5%wt pAA-solution lead to different Ω_{rel}-values. Figure 4.8a shows the relative rotation rate of a cylindrical object (Ø=5 mm PVC or wood) as a function of accumulated shear strain value for different shear strain rates. There is a minor effect of changes in temperature and relative shear zone width (see below). The graph shows a value for Ω_{rel} around 1.0 at the onset of deformation that decreases to an approximately unique plateau value with ongoing shear. This 'steady state' relative rotation rate decreases with increasing shear strain rate. A range of average 'steady state' Ω_{rel}-values between 0.951 and 0.35 is found for shear strain rates from 0.006 to 0.70 s^{-1}. Since the objects in these experiments were floating in the liquid, no forces other than those of the liquid itself can account for the lower rates of rotation.

The effect of the relative shear zone width (SW_{rel}) on the rotational behaviour of the cylinder was also examined. In figure 4.8b, three pairs of experiments with a different SW_{rel} within each pair are shown. Each pair of experiments was done at the same temperature and with the same solution and although the curves with a larger SW_{rel} are mostly below the curves with a smaller SW_{rel}, the differences are just larger than one standard deviation of the mean.

Experiments P19-P21, P32-P34 and P37-P38 were done to establish the effect of the temperature on the value of Ω_{rel} at 'steady state'. The average Ω_{rel}-values of these experiments

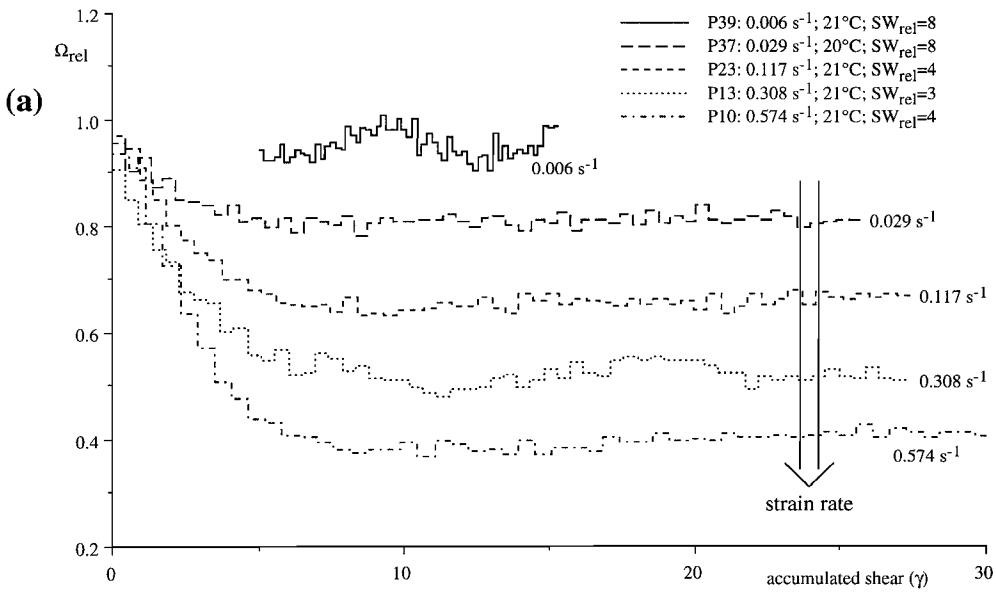

Figure 4.8 (continued on next page). Graphs of Ω_{rel}-value versus accumulated shear showing the effects of changing conditions on the rotation rate of a cylindrical object in shearing pAA-solution. **(a)** Experiments P37, P23, P13 and P10 show a relative rotation rate of 1.0 at the onset of deformation which decreases to a 'steady state' value as shear progresses; P39 had no data from the onset of deformation. The 'steady state' rotation rate clearly decreases with increasing shear strain rate. **(b)** Experiments P37&P9, P23&P4 and P14&P1 showing very little effect of relative shear zone width on 'steady state' rotation rate. **(c)** Experiments P19&P21, P32&P34 and P36&P38 show a positive effect of temperature on rotation rate which increases with shear strain rate.

show an increase when the temperature is increased by 6°C (fig. 4.8c) and is most obvious at higher rates of shear. The steady state rotation rate increase is approximately 2% per °C at 0.308 s^{-1} and 1% per °C at 0.154 s^{-1}. At 0.077 s^{-1} the temperature-effect is within one standard deviation of the mean. The general trend of most other experiments also shows a positive effect of temperature on the average Ω_{rel}-value. However, in experiments P23-P26 the temperature had a negative effect on the rotation rate. Since the difference in temperature of the experiments evaluating the effects of shear rate or shear zone width was mostly within 1°C, the maximum effect on rotation rate of the temperature changes in these experiments is in the order of 2%. The temperature effect is certainly not significant in figure 4.8a, although it may account for the small difference in average Ω_{rel}-value between P4 and P23 shown in figure 4.8b.

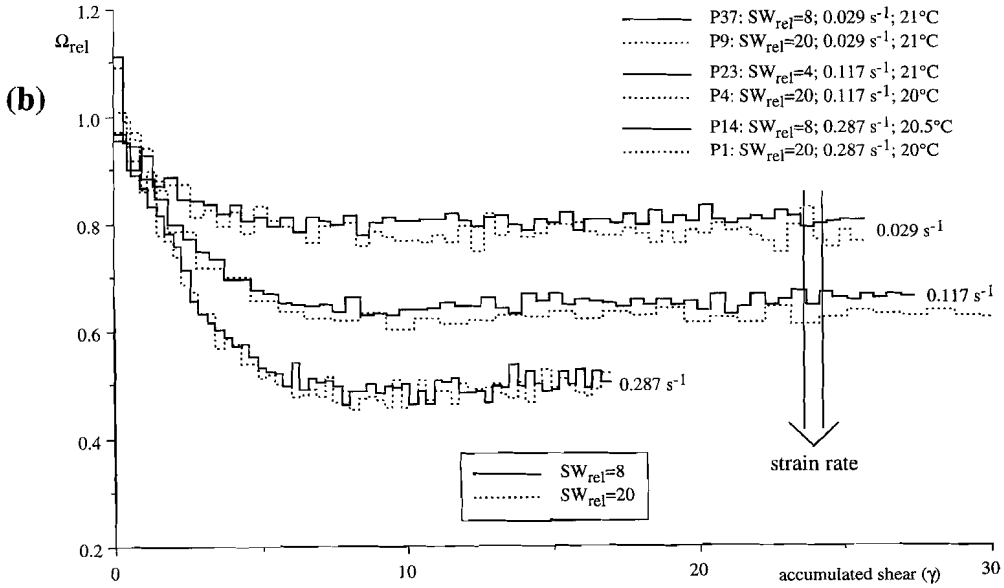

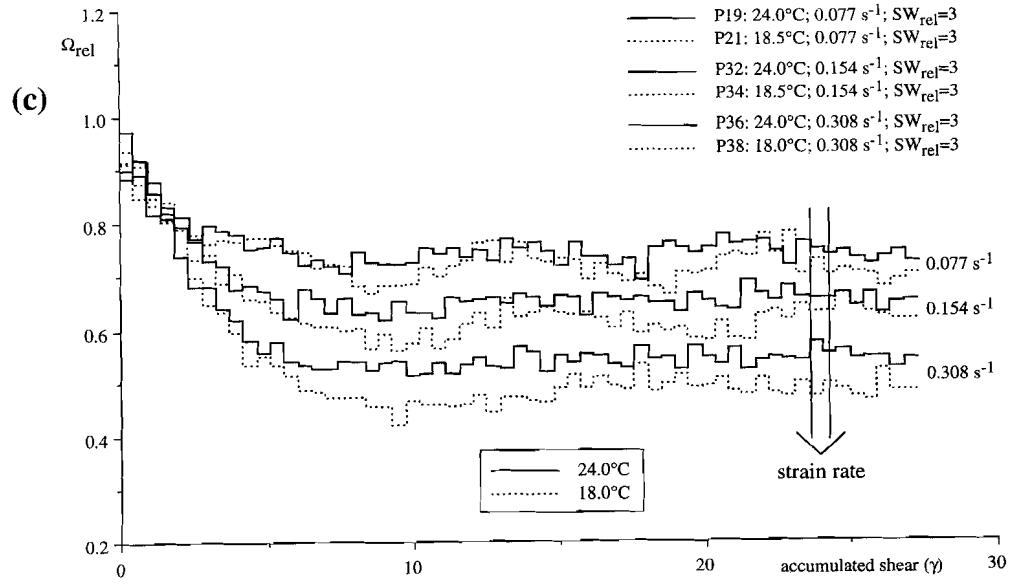

Flow pattern

The flow pattern around cylinders floating in a shearing 0.5%wt pAA-solution is time independent and shown in figure 4.9. It has a bow-tie shape that depends on shear strain rate and relative shear zone width. At lower shear strain rates (fig. 4.9a: $\dot{\gamma}$=0.012), the diameter of the central area with closed flow-lines exceeds that at higher shear strain rates (fig. 4.9b: $\dot{\gamma}$=0.117). Similarly, the stagnation points are at a smaller relative distance (D_S) from the centre of the

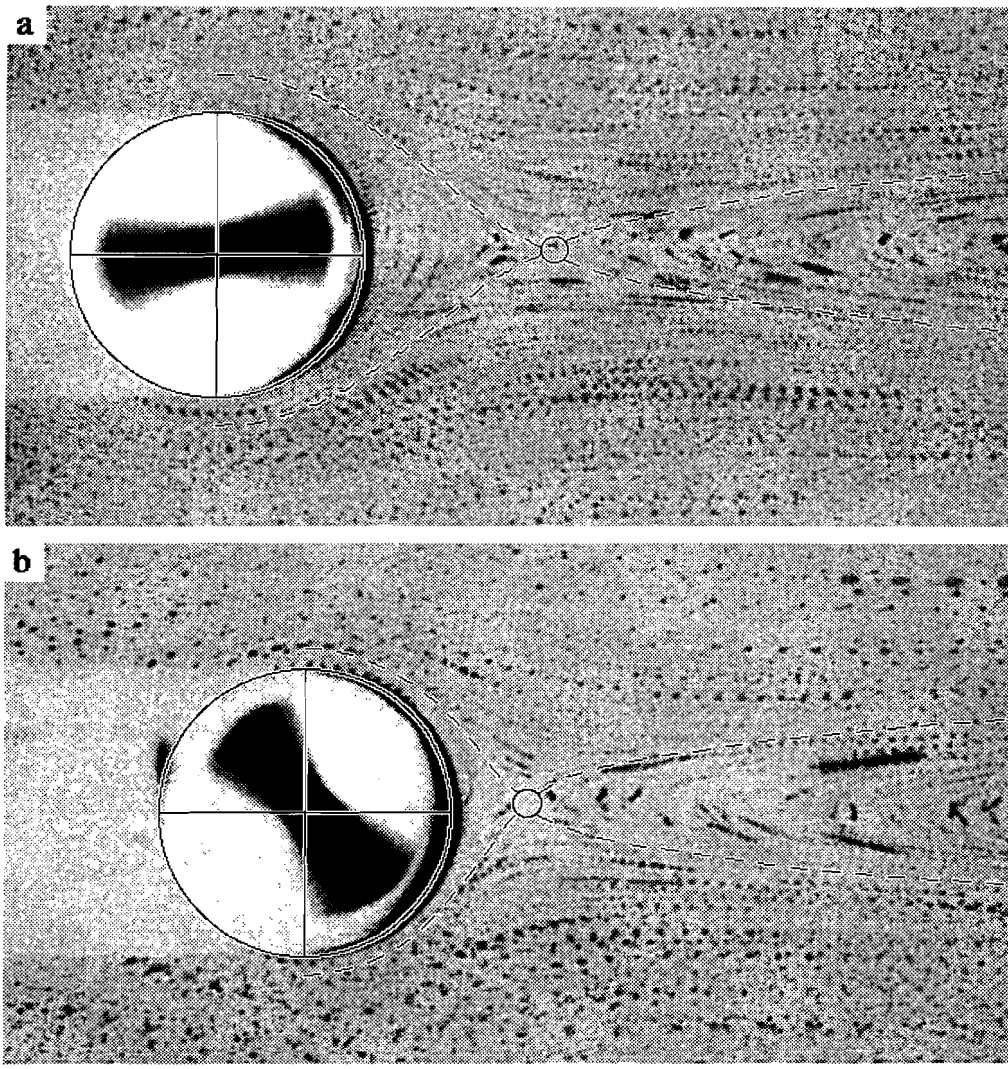

Figure 4.9. Images (averages of 10 frames) showing the bow-tie flow pattern around a floating cylinder in a sinistral shearing 0.5%wt pAA-solution. Dashed lines and circle (or ellipse) indicate interpreted position of separatrices and stagnation point resp.. **(a)** 10 second intervals, $\dot{\gamma}$=0.012 s^{-1}, Ø=5 mm cylinder, SZW=40 mm (SW_{rel}=8).

object (figs. 4.9a,b: D_S=2.3 and 1.5 resp.). Increasing the relative shear zone width results in an increase of D_S (figs. 4.9c,b&d: SW_{rel}=4, 8 and 20; D_S=1.4, 1.5 and 2.3 resp.; $\dot{\gamma}$=0.117 s^{-1}) although the 'height' of the central area with closed flow lines with respect to the object diameter remains constant. The far-field separatrices are diverging over a distance of several object-diameters.

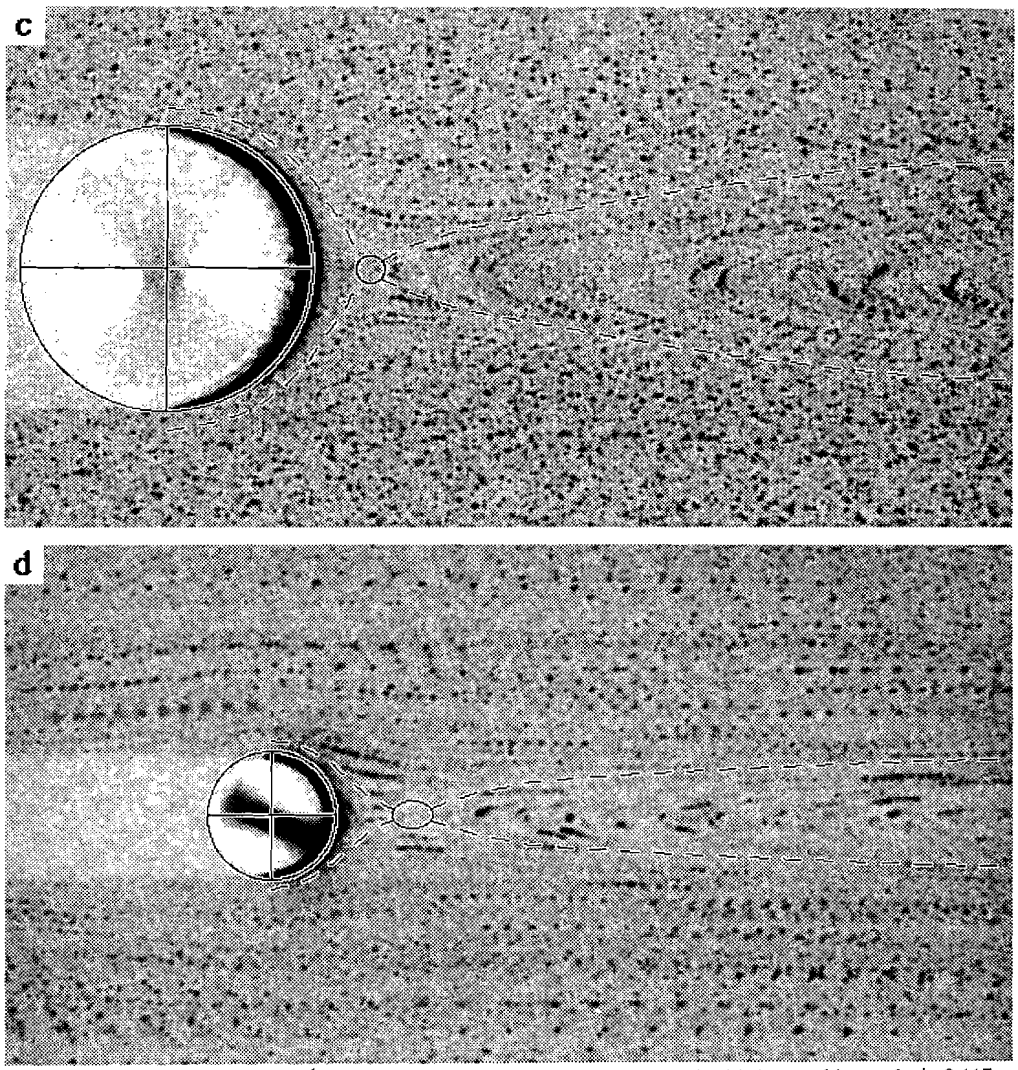

(b) 2 second intervals, $\dot{\gamma}$=0.117 s^{-1}, Ø=5 mm cylinder, SZW=40 mm (SW_{rel}=8). **(c)** 4 second intervals, $\dot{\gamma}$=0.117 s^{-1}, Ø=5 mm cylinder, SZW=20 mm (SW_{rel}=4.) **(d)** 2 second intervals, $\dot{\gamma}$=0.117 s^{-1}, Ø=2 mm cylinder, SZW=40 mm (SW_{rel}=20).

Square object

Rotation rate

In contrast to the behaviour in glycerol, the rotation of a 5x5 mm square object in shearing pAA-solution shows a pulsating rate. This rotation rate is orientation dependent and related to the 4-fold symmetry of the object (fig. 4.10): the curve shows a cycle of 90°. The mean rotation rate of the square object (Ω_{rel}(mean) P40&P41=0.65±0.02) is similar to the 'steady state' rotation rate of a cylinder at the same shear strain rate (Ω_{rel} P27=0.659±0.008). The minimum and maximum Ω_{rel}-value are found at an orientation of 37.5 and 82.5° respectively to the shear direction. At 21°C, a shear rate of 0.117 s^{-1} and a shear zone width of 40 mm the rotational behaviour is described by: $\Omega_{rel}(\alpha)= 0.11 \cdot \sin(4\alpha+120°)+0.65$.

In earlier, less detailed, experiments using the same square object in a 16.5 mm wide shear zone and a shear rate of 0.14 s^{-1}, a minimum, average and maximum Ω_{rel}-value of 0.43, 0.56 and 0.70 respectively was found. The orientation at which the extremes in Ω_{rel} were found in the earlier experiments are similar to those in the later experiments. Unfortunately, no experiments with a cylinder were done using an equivalent shear zone width and shear strain rate.

Flow pattern

During the experiments with pAA solution aluminium flakes were used as tracers in order to determine the flow pattern. These experiments were not repeated with chalk-dust tracers, as was done for most other experiments. The aluminium flakes tend to line-up in the flowplane and very few of the flakes are thus in such a position that they reflect the plane of light in the direction of the camera. For this reason, the flow pattern is difficult to resolve and reproduce in images. Observing the films 'live' on the monitor gives a fair impression of the flow pattern. Therefore the flow around the square and oblong objects in pAA-solution are shown schematically in figures 4.11 (square object) and 4.13 (oblong object).

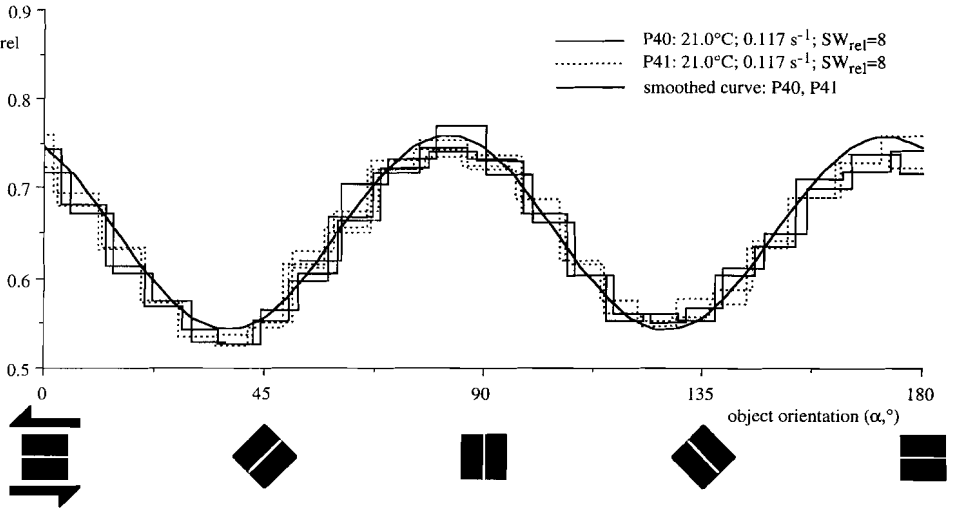

Figure 4.10. Graph of Ω_{rel}-value versus object orientation (α) of a 5x5 mm square object floating in a shearing 0.5%wt pAA-solution; experiments P40&P41 and a smooth curve over the data. Note that the minimum and maximum value for Ω_{rel} are not found at 0 and 90° but at 37.5 and 82.5° resp.. The smooth curve is described by: $\Omega_{rel}(\alpha)=0.11 \cdot \sin(4\alpha+120°)+0.65$.

The interpretations show, within the limited accuracy of these films, that the flow pattern is orientation dependent and that the far-field back-flow regions have slightly skewed displacement paths when the object is in other orientations than at 0 or 45° of one side to the flow direction. From these paths the geometry of the separatrices and position of the stagnation points is interpreted as shown in figure 4.11. At orientations other than 45°, there are two intersection points on either side of the object. These must then be connected by a segment of the central part of the separatrices where no displacement takes place; a line section of stagnation points (thick line sections in figs. 4.11a,b&d). This line decreases and increases in length when the object rotates towards and from an orientation of 45° to the flow.

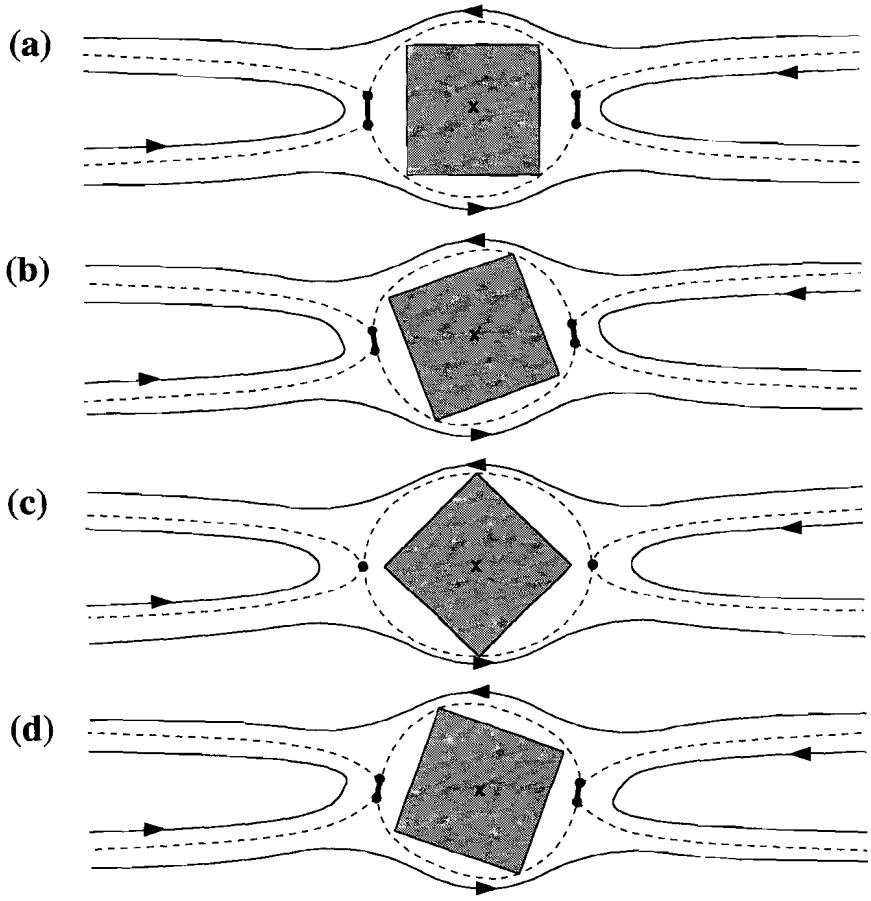

Figure 4.11. Interpretation of one cycle of 90° of the orientation dependent flow around a 5x5 mm square object floating in a shearing 0.5%wt pAA solution. Experimental conditions: $\dot{\gamma}$=0.140 s^{-1}, sinistral shear, SZW=16.5 mm, 21°C. Lines with arrows are flow lines, dashed lines and heavy dots are separatrices and stagnation points resp., heavy line indicates line segment of stagnation points. Notice the skewed backflow regions in (b) and (d).

Oblong object

Rotation rate

The rotation of a 3x6 mm oblong object in shearing pAA-solution shows a pulsating rate, is orientation dependent and related to the 2-fold symmetry of the object (fig. 4.12); the curve shows a cycle of 180°. The curve is skewed and the minimum and maximum Ω_{rel}-values are found at orientations α=~23° and α=~87° respectively.

Reducing the shear zone width results in a larger amplitude of the curve. The decrease in shear zone width from 40 (P42-P44) to 15 mm (P45), raises the maximum Ω_{rel}-value from 1.5 to 1.7, while the minimum value is decreased from 0.2 to well below 0.1. The low Ω_{rel}-value in experiment P45 when the object has an orientation in between 0 and 45°, indicates that when the shear zone is relatively narrow, the amount of accumulated shear strain needed to rotate the object is very high. In experiment P45 the shear zone width is 15 mm, the amount of accumulated shear strain needed to rotate the object from 0 to 45° is approximately 14. In a shear zone of 40 mm wide (P42-P44), the same rotation is found after an accumulated shear strain of 6. Preliminary experiments with a shear zone width of 16.5 mm in which the aspect ratio of the object (R_{xy}) was 4 (1.3x5.4x11.5 mm) have shown that the object nearly stops rotating at an orientation of ~12°.

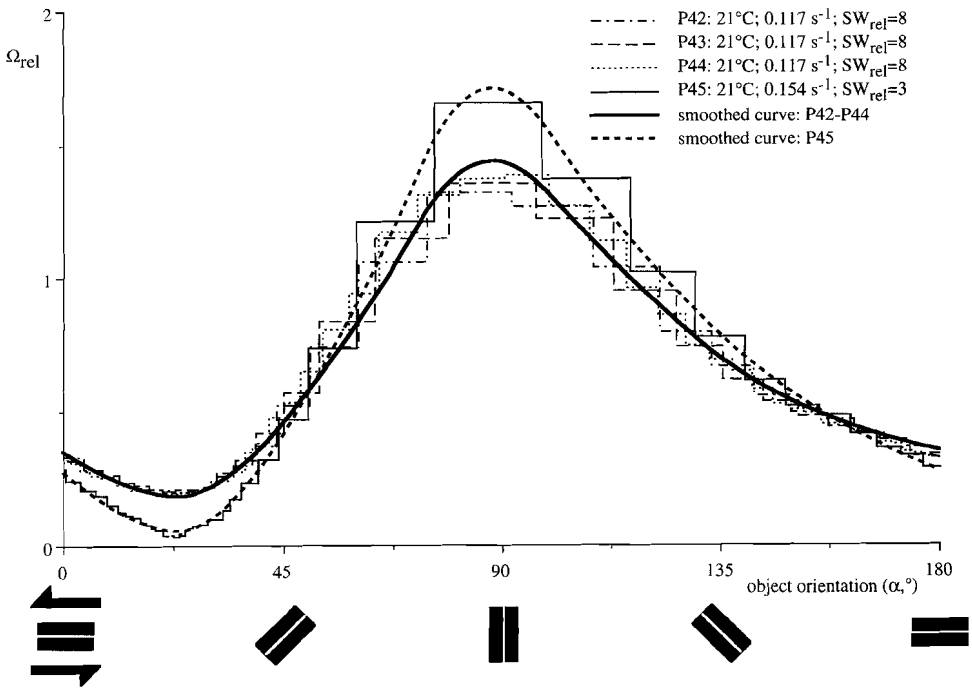

Figure 4.12. Graph showing Ω_{rel}-value versus object orientation of a 3x6 mm oblong object floating in a shearing 0.5%wt pAA-solution; experiments P42-P45 and smooth curves over the data. Note that the minimum value for Ω_{rel} is not found at 0° but ~23°. If the shear zone width is reduced to 15 mm (P45), the rotation rate of the object is very close to 0 when it reaches an orientation of ~23°.

Flow pattern

As for the square object, the flow around oblong objects in the pAA-solution is only shown as an interpretation of the films made during the experiments. The far-field back-flow regions have skewed displacement paths when the object is in orientations other than $\alpha=0°$ or $\alpha=90°$. From these paths, the geometry of the separatrices and position of the stagnation points is interpreted as shown in figure 4.13. At orientations other than $\alpha=0°$ or $\alpha=90°$, there are two intersection points of far-field and central separatrices on either side of the object. As with the square object, these are connected by a segment of the central part of the separatrices where no displacement takes place; a line section of stagnation points (figs. 4.13b,c&e). At an orientation of ~23°, the rotation rate is very low and the surface of the object approximates a surface of stagnation points (object surface shown as thick line in fig. 4.13b). At this orientation, the difference between object rotation rate and fluid velocity and thus shear stress, reaches a maximum at the upper-right and lower-left corners of the object, as indicated in figure 4.13b.

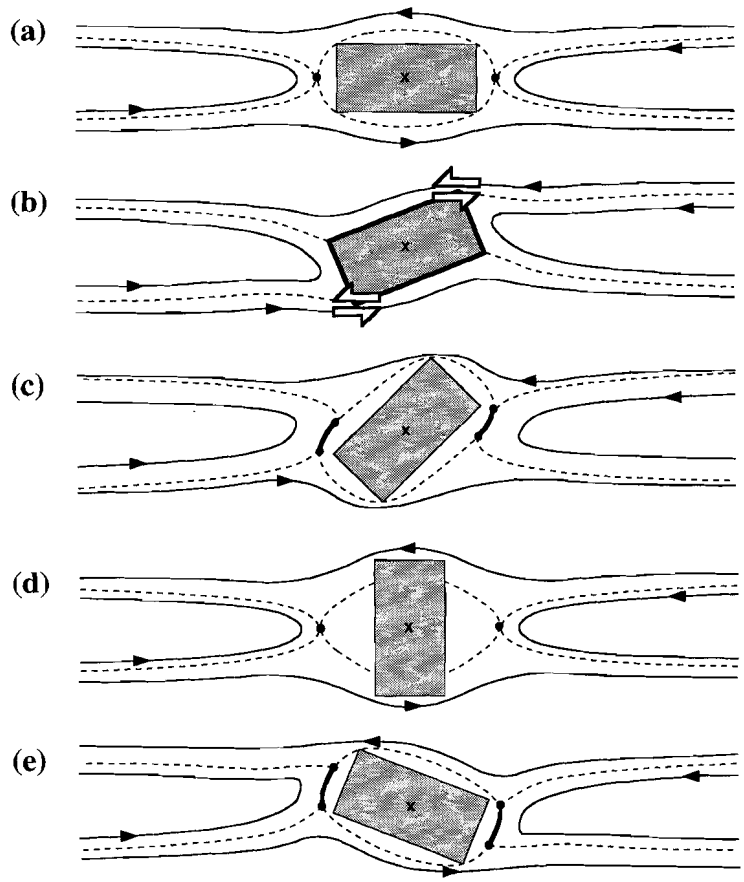

Figure 4.13. Interpretation of one cycle of 180° of the orientation dependent flow around a 3x6 mm oblong object in a shearing 0.5%wt pAA solution. The experimental conditions were: $\dot{\gamma}=0.140\ s^{-1}$, sinistral shear, SZW=16.5 mm, 21°C. Lines with arrows are flow lines, dashed lines and heavy dots are separatrices and stagnation points respectively. The heavy lines indicate line segments of stagnation points in (c) and (e) and a 'surface of stagnation points' in (b). Notice the skewed backflow regions in (b), (c) and (e) and that (e) is not the mirror-image of (b).

4.4 Summary of results

A qualitative pictorial summary of the results in this Chapter is shown in figure 4.14.
In a Newtonian matrix deforming by simple shear, an immersed buoyant object rotates with a rate that depends on the geometry and orientation of the object (figs. 4.14a,b). When one of the axes of the object coincides with the vorticity vector of simple shear flow, the observed rate of rotation can be described by the mathematical functions for ellipsoidal particles given by Jeffery (1922) and Freeman (1985). The rotation of a cube is equivalent to that of a sphere. A rectangular prism shows the pulsating rotational behaviour of an ellipsoid with a 12.5% smaller aspect ratio. Objects with an aspect ratio of 4 or larger have a very low rotation rate when its long axis is parallel to the direction of shear.

The flow pattern around the objects depends on the shear zone width relative to the diameter of the object. If the relative shear zone width is 20 or more, the flow has an eye-shaped geometry (fig. 4.14c). When the relative shear zone width is reduced, the flow pattern shows a bow-tie geometry (fig. 4.14d) and the distance from the object to the stagnation points decreases.

In a shearing non-Newtonian solution of pAA, in which the shear thinning behaviour (and more than likely also the anisotropy) increases with shear strain rate, the rotation rate of objects decreases with increasing shear strain rate (fig. 4.14e). Cubical objects, as well as rectangular prisms, show a rotation rate that is pulsating and a function of the orientation of the objects (fig. 4.14f). The minimum and maximum rotation rates of cubes are found when a side is at an angle of 37.5 and 82.5° resp. to the direction of shear. For a rectangular prism with an axial ratio of 2, the minimum and maximum rates of rotation are reached when the long axis of the object is at an angle of 23 and 87° resp. to the direction of shear. An object with an axial ratio of 4 nearly stops rotating after a semi-stable orientation is reached. This effect is more pronounced when the shear strain rate is increased. In the semi-stable orientation, the long axis of the object has a positive angle with respect to the flow direction. This angle depends on the shear strain rate of the matrix and the axial ratio of the object but not on the relative shear zone width.

A bow-tie flow pattern emerges around the object in the non-Newtonian matrix, even when the shear zone width is 20 times as large as the diameter of the object (figs. 4.14g,h). The flow pattern depends on the shear zone width, the shear strain rate and the geometry and orientation of the immersed object. An increase in shear strain rate or a decrease in shear zone width, decreases the distance of the stagnation points to the object.

Figure 4.14 (next page). Pictorial summery of experimental results. On the left side ((a) to (d)) for glycerol (Newtonian), on the right side ((e) to (f)) for pAA-solution (shear thinning, probably anisotropic) as matrix material. **(a)** and **(e)** show the influence of shear strain rate on the rotation rate of a cylinder. **(b)** and **(f)** show the influence of object orientation of angular objects on rotation rate. **(c)**, **(g)** and **(d)**, **(h)** show the influence of shear zone width on the flow pattern geometry.

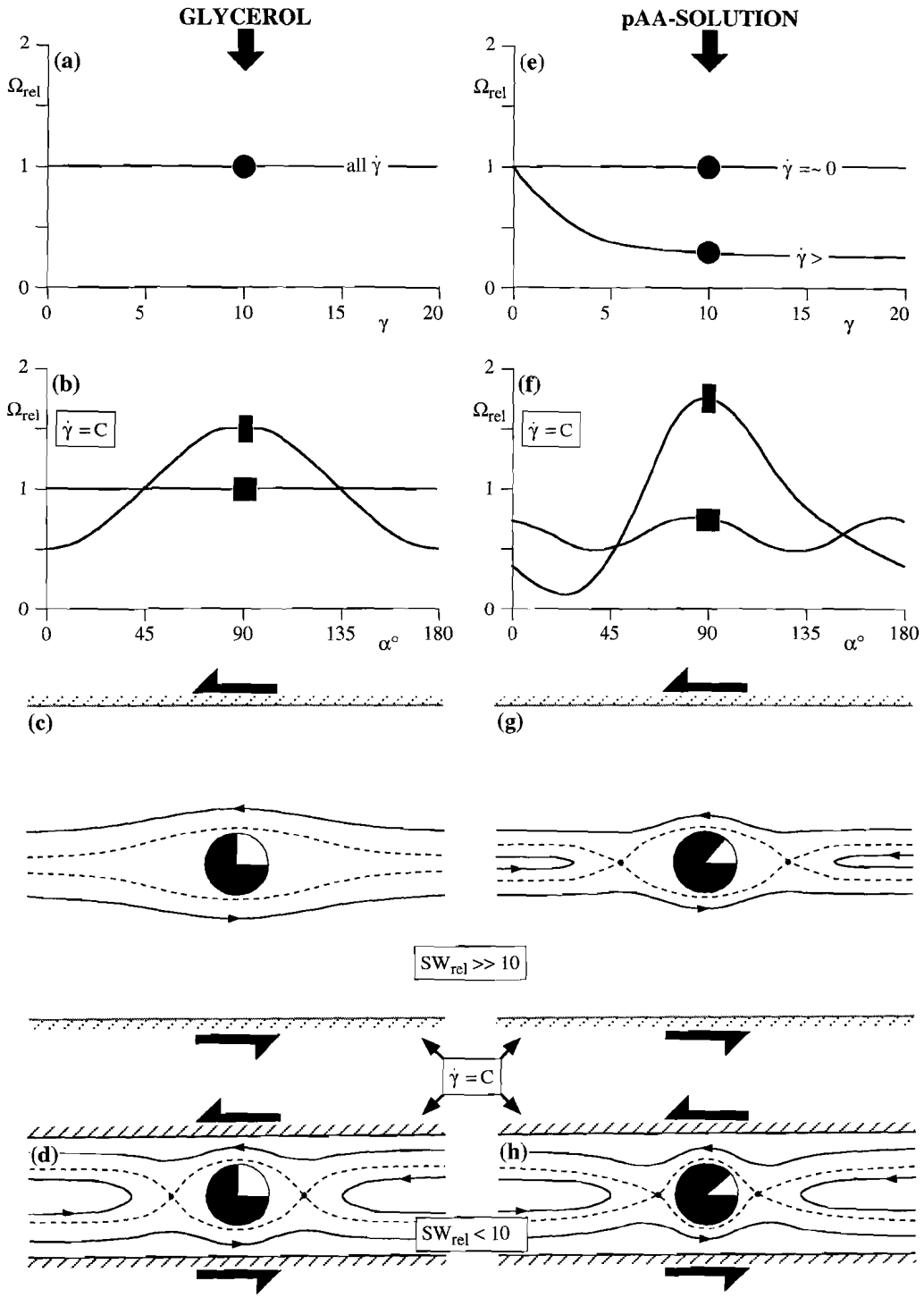
GLYCEROL
pAA-SOLUTION
(a)
(e)
Ω_{rel}
all $\dot{\gamma}$
$\dot{\gamma}$ =~ 0
$\dot{\gamma}$ >
γ
(b)
(f)
$\dot{\gamma}$ = C
$\alpha°$
(c)
(g)
SW_{rel} >> 10
$\dot{\gamma}$ = C
(d)
(h)
SW_{rel} < 10

4.5 Discussion

4.5.1 Rotation rate

It is remarkable that the rotation rate of a cube in a shearing Newtonian matrix does not reflect the geometry of the cube. Furthermore, the experiments with glycerol described in this paper show that the equivalent ellipsoidal shape for an oblong object has a 12.5% smaller aspect ratio than that of the oblong object; 1.75:2.00 for experiments G19-G21 and 3.50:4.00 for experiment G22. Eirich and Mark (1937; Papierfabrikant, 27, 251-258: cited in Freeman 1985) argued that the effect of minor surface imperfections had a negligible effect on particle motion since the liquid contained in cavities and slots in a particle is immobilised. Although a cubical shape can hardly be regarded as a cylinder with cavities or slots, this might account for the similarity in rotational behaviour of cylindrical and square objects in Newtonian media as found in the experiments with glycerol. Bartok and Mason (1957; J. Colloid Sci., 12, 243-262) have shown experimentally that the behaviour of a fused doublet of equal sized spheres corresponds very closely to that of a prolate ellipsoid when the equivalent ellipsoidal shape is accounted for (in their case R_{xy}=2). This indicates that the 'cavities and slots' in a particle can be relatively large before they effectively change the behaviour of the particle.

The most conspicuous result of these experiments is the strain rate dependent rotation rate of a cylinder in a shearing pAA-solution. In the range of increasing shear strain rates studied in this thesis for a cylindrical object (0.006 to 0.70 s^{-1}), the power-law stress exponent (n) of the flow-law for the 0.5%wt pAA-solution increases from 1.5 to 2.3 (at 25°C, see Chapter 3, fig. 3.14). The increase of the stress exponent probably reflects an increase in anisotropy as discussed in Chapter 3. This increase in anisotropy can explain the decrease in rotation rate to a unique plateau value for floating cylinders in a shearing pAA-solution: the steady state anisotropy is only reached after a certain amount of accumulated shear.

The variation and distribution of the anisotropy in the shearing pAA-solution can also explain the reduction of the rotation rate. Because the stress exponent of the matrix is a function of the shear strain rate (in the range 0.03 to 2.5 s^{-1}, see Chapter 3, fig. 3.14), there will be a non-

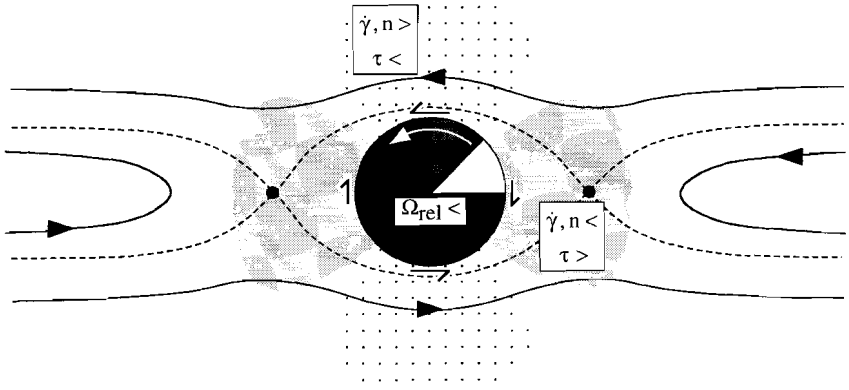

Figure 4.15. Drawing shows where shear stress on the cylinder is reduced (dark shading) and increased (light shading) as the effect of the shear strain rate and hence stress exponent distribution around the object. When the forward rotating torque is lowered with respect to the backward rotating torque, a lower rotation rate of the cylinder results.

homogeneous distribution of the stress exponent around the object due to strain rate variations in the shearing matrix. A close examination of figures 4.3 and 4.9 shows that the velocity-gradient above and below the cylinder is larger than the gradient to the left and right of the object, implying that the stress exponent changes equivalently. This velocity gradient can also be deduced from the geometry of the flow-lines: the gradient increases where flowlines converge, i.e. at the top and bottom of the object. This means that the shear-stress induced 'forward rotating' torque of the faster flowing pAA-solution above and below the cylinder is lowered with respect to the 'impeding' torque imposed by the slowly flowing fluid on the left and right sides of the object. The total torque on the cylinder is thus lowered which results in a decrease in relative rotation rate (fig. 4.15). When the bulk imposed shear strain rate is increased, the variation in local shear strain rates increases concommitantly. As a result, the total torque on the cylinder is decreased and, therefore, the rotation rate of the object will decrease.

When the object is not round but angular, a gradient in shear strain rate is more easily established since material has to be squeezed around the corners of the object. This may account for the somewhat surprising orientations at which the minimum and maximum rotation rates of the square and oblong objects are found.

The rotational behaviour of a cylinder in a shearing pAA-solution gives an indication that the stress exponent of the matrix material has no influence on the rotation rate. When the shear strain rate in the pAA-solution approaches zero, the relative rotation rate is very close to 1 (experiment P10) while the stress exponent of the solution is not 1 but ~1.5 (Chapter 3, fig. 3.14). This phenomenon could be checked at very low shear strain rates, i.e. when the maximum shear strain rate reached locally in the matrix is lower than ~0.02 s^{-1} (at higher shear strain rates the n-value of the pAA-solution starts to increase). It cannot be detected at the imposed shear strain rates examined as the shear strain rate within the matrix has a non-homogeneous distribution: the maximum shear strain rate reached locally in the matrix is thus higher than the imposed bulk shear strain rate (lowest imposed shear strain rate was 0.006 s^{-1}, P10).

Decreasing the relative shear zone width (keeping the bulk shear strain rate constant) will result in higher shear stresses in the direct environment of the object since the material has to be 'squeezed' through a narrower channel in the areas situated perpendicular to the flow with respect to the object. Although the bulk shear strain rate remains constant, the velocities in the aforementioned areas will increase as a result of the converging particle-paths. Since an increase in shear strain rate results in a higher stress exponent (and anisotropy) of the solution and a lower rate of rotation, a decrease in relative shear zone width will have a similar result as an increase in bulk shear strain rate. Figure 4.8b shows that this effect is very small.

It is argued in Chapter 3 that increasing the temperature also increases the 'disorder' of the long pAA-molecules in the liquid which decreases the anisotropy, the shear-thinning behaviour and the power law-exponent of the shearing solution. Figure 4.8c shows that this effect is more pronounced at higher shear rates which can be explained by the idea that the amount of 'disordering' by an increase of 6°C is of the same order, irrespective of shear strain rate. At low shear strain rates, the pAA molecules are still distributed with very low order, which implies that the disordering effect of an increase in temperature has relatively little influence. From experiments P19-P21, P32-P34 and P36-P38 can be concluded that the actual stress exponent of the fluid at 21°C must be higher than the measured value shown in figure 3.14 since the properties of the fluid were determined at 25°C.

4.5.2 Flow pattern

The numerically determined eye-shaped flow patterns of Jeffrey and Sherwood (1980), Mifflin and Schowalter (1986) and Masuda and Ando (1988) for free rotating cylinders in a Newtonian medium were the result of an object in an infinite matrix. The experimentally derived cat's-eye flow pattern of Robertson and Acrivos (1970) in a Newtonian liquid emerged from a SW_{rel} of 39.6. However, Robertson and Acrivos (1970) and Jeffrey and Sherwood (1980) have shown that a bow-tie pattern arises around a cylinder in a Newtonian medium if the cylinder is (forced) to rotate at a lower rate than a suspended one; in the experimental work by Robertson and Acrivos (1970) a D_S of 1.4 was found when the cylinder was slowed down to an Ω_{rel}-value of 0.5. However, in the experiments with glycerol presented in this thesis, the existence of the bow-tie flow pattern is certainly not the effect of low rotation rates of the cylinder since the Ω_{rel}-values are close to unity.

The main difference between the work cited above and the experiments with glycerol described in this Chapter is the relative width of the shear zone. Therefore, the bow-tie flow pattern, as found in the (Newtonian) glycerol experiments, could be the result of a small SW_{rel}. The effect of a large, free floating object in a narrow shear zone, has not been commonly studied. The bow-tie flow pattern has hardly been described before in geological literature. Figure 7c of Passchier and Simpson (1986) clearly shows the bow-tie geometry in a shearbox experiment with silicone putty as matrix and a rigid cylinder that has a large diameter with respect to the shear zone width. They state that there is: 'minor flow crossing the *uw* plane' (the flow plane). The bow-tie flow pattern reported in the pAA-solution experiments can be ascribed to the combined effect of the relative shear zone width and the impeded rotation of the object.

4.6 Conclusions

-In shearing glycerol, which has a Newtonian behaviour (linear stress-strain rate relation), the rotational behaviour of an isolated object can be described by the equations of Jeffery (1922) and Freeman (1985) for ellipsoidal particles. For a cylinder with its rotational axis parallel to the vorticity vector of the flow, the rotation rate is linearly related to the shear strain rate. The rotation rate of a cube is equivalent to that of a sphere and a rectangular prism shows the pulsating rotational behaviour of an ellipsoid with a 12.5% smaller aspect ratio.

-In a shearing watery 0.5%wt pAA-solution, the rotation rate (relative to that in a Newtonian matrix) of a cylinder with its rotational axis parallel to the vorticity vector of the flow is primarily affected by the shear strain rate. Minor influence of changes in temperature and width of the shear zone are found. Shear strain rate and shear zone width have a negative, and temperature has a positive effect on the relative rotation rate. These effects are non-linear and probably related to the development of an anisotropy in the matrix. The relative rotation rate of a rectangular prism is a function of aspect ratio and orientation, even when the aspect ratio is 1 (cube). Minimum and maximum rotation rate are not found at the same orientations of the object when compared to a Newtonian matrix.

-In both glycerol and pAA-solution, objects with a large axial ratio (end member is a line) will rotate to a semi-'steady state' orientation.

-The eye-shaped flow pattern was only found in glycerol (Newtonian) when the width of the shear zone is larger than approximately 20 times the diameter of the immersed cylinder. When the shear zone width is reduced or when a pAA-solution is used as matrix, the flow pattern shows a bow-tie geometry. The bow-tie flow pattern in glycerol is the result of nearby shear zone walls. In the pAA-solution, it is also the result of the reduced rotation rate of the cylinder. Therefore, all flow patterns in a pAA-solution have a bow-tie geometry, even when the shear zone walls are distant from the rigid object.

"Heb je al veel materiaal bij elkaar?" ...
"Al een hele hoop. Maar ik heb zeker nog eens zoveel nodig
voor ik er zelfs maar aan kan denken om aan mijn dissertatie te beginnen."

(Tove Jansson-Pappa Moem en de mysteriën der zee)

Chapter 5

Flow patterns around rigid objects and the development of porphyroclast mantle geometries

5.1 Introduction

5.5.1 General

It was shown in Chapter 2 that natural porphyroclast geometries can be experimentally modelled using a ringshear apparatus with power-law materials as matrix and clast. Similarly, it was demonstrated in Chapter 4 that the bow-tie flow-pattern, reported in Chapter 2 as characteristic of flow around the clasts, can be experimentally reproduced using both Newtonian and non-Newtonian liquids as shearing matrix materials around rigid cylinders. Moreover, the bow-tie flow-pattern was inferred in Chapter 4 to reflect the short distance of the shear zone walls to the inserted floating object (small relative shear zone width), since the flow-pattern modifies towards an eye-shaped configuration when the relative shear zone width is increased. This implies that the relative shear zone width is of major importance for the developing flow-pattern around (nearly) rigid objects. In practice, a shear zone may be much wider than the effective width when deformation is inhomogeneously distributed through the material; this may be the case in natural shear zones. In addition, the bow-tie flow pattern was obtained in all experiments with non-Newtonian liquids, even when the relative width of the shear zone was large. This indicates that, as well as the shear zone width, the properties of the matrix material also have an important effect on the flow-pattern. The results of Chapter 4 are thus in partial agreement with Passchier *et al.* (1993), who predicted that the flow-pattern is dependent on material properties, though they do not support the conclusion by Passchier *et al.* (1993) that a bow-tie flow-pattern is characteristic for non-Newtonian behaviour of the matrix.

Aside from the above, the rotation rate (Ω) of free floating cylindrical objects in the shearing experiments on the Newtonian liquid (glycerol), reported in Chapter 4, was found to be linearly related to the shear strain rate ($\dot{\gamma}$) and identical to the rotation rate predicted by Jeffery (1922) so that $\Omega(\text{rad}\cdot\text{s}^{-1})=0.5\cdot\dot{\gamma}(\text{s}^{-1})$. In contrast, the rotation rate of a free floating cylinder in the non-Newtonian liquid (pAA-solution) was found to be always lower than $\dot{\gamma}/2$ and non-linearly related to the shear strain rate such that the ratio $\Omega_{rel}=\Omega/(0.5\cdot\dot{\gamma})$ decreased with increasing shear strain rate. This was thought to be the effect of anisotropy developing within the liquid (Chapter 4).

These observations on the effects of shear zone width and matrix rheology provide useful insight into the flow-pattern around semi-rigid objects and hence into the development of porphyroclast geometry. However, a fully quantitative description of the flow behaviour is still lacking and the decreased rotation rate seen using non-Newtonian liquids is not understood. Also, the implications for wing development around porphyroclasts with deformable mantles have not been considered.

In the present Chapter, a mathematical description of the flow pattern in Newtonian[1] slow flow around rigid objects in general plane strain deformation is developed. The equations

[1] In this mathematical use, the hypothetical Newtonian fluid is assumed to be incompressible.

obtained are based on the stream function given by Bretherton (1962) for simple shear flow around a rotating cylindrical object. Bretherton's stream function is also applicable for flow around cylinders that rotate at lower rates than a free floating one ($\Omega<0.5\cdot\dot{\gamma}$; $\Omega_{rel}<1$). This Chapter presents Newtonian slow flow patterns around rigid cylinders, for several flow types and object rotation rates. Some of these flow patterns are subsequently used to model the development of passive mantles around rigid cylindrical objects. The equation given by Bretherton is further used to determine the strain rate distribution within the matrix material as a result of the presence of a cylinder, in order to gain insight in the strain (rate) partitioning and anisotropy development around a rigid cylinder. In addition, the effect of nearby shear zone walls on flow patterns is investigated numerically by a finite element analysis applied for a variety of boundary conditions. The finite element modelling (FEM) was done in collaboration with P. D. Bons and T. D. Barr and is described partially in Bons *et al.* (in press). Within the FEM, linear and power-law stress-strain rate relations are ascribed to the elements in order to gain information on the influence of the properties of the matrix material on the flow pattern and the rotation rate of the enclosed object. Furthermore, comparing the results from the analytical solution for a Newtonian matrix with the results of the FEM, the discussion opened in Chapter 4 on the influence of material properties on the rotation rate of enclosed objects, is re-addressed. Finally, the velocity distribution, derived from the stream function by Bretherton (1962), is used to trace the development of winged structures that result from progressive deformation of passive mantles around rigid circular objects.

5.1.2 Definitions

Most of the results obtained in this Chapter are represented by line drawings of the emerging flow patterns. From the outset, it is therefore necessary to define the terms used to describe these patterns. During steady state (time independent) flow, material particles proceed along paths known as *stream lines*. These are lines to which the velocity vectors of particles are tangent. They are thus a representation of the flow pattern without showing the velocity distribution. In all flow patterns given, the positive x-direction is taken to the right, the positive z-direction is taken upwards; simple shear has a flow plane parallel to x and the origin is placed at the centre of the object. When polar co-ordinates are used, r is the distance to the origin ($r^2=x^2+z^2$) and θ is the angle to the positive x-axis ($x=r\cos\theta$, $z=r\sin\theta$). For all figures shown in this Chapter that represent flow, the deformation rate (E) is taken to be 1.0 s^{-1} and all stream function values shown are normalised to a cylinder radius of 1.0 when a cylinder is present, or equivalent scaling in figures without a cylinder.

In the system thus defined, homogeneous dextral simple shear with no central object, will be characterised by straight horizontal stream lines in all model calculations (Ramsay and Graham 1970). The deflection of material by the presence of a rigid cylinder causes the stream lines to be curved and complex stream line patterns may result. Basically, two distinct flow patterns emerge. The *eye-shaped flow pattern* (Robertson and Acrivos 1970, Jeffrey and Sherwood 1980, Masuda and Ando 1988; see fig. 5.1 for a typical example) has three regions with two different types of flow: 1) in the central, 'UFO'-shaped, area adjacent to the object and extending to infinity in the x-direction, stream lines are closed, and 2) above and below the central area, stream lines are open at both ends. The *bow-tie flow pattern* (Robertson and Acrivos 1970, Jeffrey and Sherwood 1980; see fig. 5.11 for a typical example) has five regions with three different types of flow: 1) in the central, ellipse-shaped, area close to the object, stream lines are elliptical and closed, 2) in the back-flow regions left and right of the central area, stream lines

are open at the far field side and closed at the central side, and 3) above and below the central area and back-flow regions, stream lines are open at both ends. Both eye-shaped and bow-tie flow-pattern have a net rotational component. A *separatrix* is a stream line that separates domains with different types of flow, i.e., the domains with closed, half-closed and open flow lines (Ottino 1989; the separatrices in figs. 5.1a and 5.11a have stream function values Ψ=0.250 and Ψ=0.038 resp.). A *stagnation point* is defined as an immobile point (displacement rate is zero) and is found where separatrices meet (Ottino 1989).

5.2 Flow patterns derived from the stream function

In order to model the development of passive mantles around rigid objects, the velocity field of the flow must be completely known. This can be achieved by the use of a stream function. A stream function is a scalar function having constant value along individual stream lines. At any point within a 2-dimensional field, the relation between the stream function ($\Psi(x;z)$ or $\Psi(r;\theta)$) and the velocity components (v_x and v_z or v_r and v_θ) at a point is defined by:

$$v_x = \frac{d\Psi}{dz} \quad \text{and} \quad v_z = -\frac{d\Psi}{dx} \quad \text{(Cartesian co-ordinates), or} \qquad 5.1a$$

$$v_r = \frac{1}{r}\frac{d\Psi}{d\theta} \quad \text{and} \quad v_\theta = -\frac{d\Psi}{dr} \quad \text{(polar co-ordinates).} \qquad 5.1b$$

It follows from this definition that any scalar function Ψ of x and z (or r and θ) that can be differentiated in x and z (or r and θ) describes an incompressible flow field. This means that, with the restriction of constant area (or volume in a 3-dimensional flow) and time-independence, any flow can be represented by a stream function when the appropriate function can be found. Arithmetic operations, such as adding and subtracting, can be applied to stream functions and a complicated stream function can be split into separate components.

Symbols used here in association with the stream function Ψ	
Ω	angular velocity of the cylinder
E	magnitude of imposed deformation rate
W_k	kinematic vorticity number of imposed flow
Ω_{rel}	Ω relative to W_k (for simple shear: $\Omega_{rel} = \Omega / (0.5\dot{\gamma})$)
subscripts have the following significance:	
S	imposed simple shear flow
R	imposed rotational flow
P	imposed pure shear flow
Wk	imposed general flow
*	special case
superscript	
d	deflected around a cylinder of unit radius, centred at the origin (valid for $r \geq 1$; in the absence of d, the stream function is valid for $r \geq 0$)

5.2.1 Simple shear flow deflected around a rotating cylinder

Bretherton (1962) gives the stream function for simple shear Stokes flow with boundaries at infinity, deflected around a cylinder of unit radius, centred at the origin of the reference system, with its rotational axis parallel to the vorticity vector of the flow and rotating at angular velocity Ω. In this case, displacements are restricted to 2 dimensions and the flow in the matrix is completely described by the stream function:

$$\Psi_S{}^d(r;\theta) = \tfrac{1}{4}E\left(r^2 - 2\ln r + 1\right) - \tfrac{1}{4}E\left(r^2 - 2 + \frac{1}{r^2}\right)\cos 2\theta - \Omega \ln r, \qquad 5.2a$$

in which r and θ are polar co-ordinates and where $r \geq 1$. As indicated above, the constant E (s^{-1}) is a measure of the rate of deformation, e.g., in a simple shear geometry it represents the imposed shear strain rate ($\dot{\gamma}$), while in pure shear it represents the imposed strain rate ($\dot{\varepsilon}$). The stream function (eq. 5.2a) can be written in many forms and several others are found in the literature (e.g.: Robertson and Acrivos 1970, Jeffrey and Sherwood 1980).

Using the co-ordinate substitutions: $x = r\cos\theta$, $z = r\sin\theta$ and $x^2 + z^2 = r^2$, the stream function $\Psi_S{}^d$ can also be written as:

$$\Psi_S{}^d(x;z) = \tfrac{1}{4}E\left(r^2 - 2\ln r + 1\right) - \tfrac{1}{4}E\left(x^2 - z^2\right)\left(1 - \frac{2}{r^2} + \frac{1}{r^4}\right) - \Omega \ln r \text{ (with } x^2 + z^2 = r^2\text{).} \qquad 5.2b$$

Both forms of $\Psi_S{}^d$ (eqs. 5.2a,b) can be split into 3 components namely a rotational component of the imposed flow, a pure shear component of the imposed flow and a rotational component related to the rotation of the cylinder:

$$\Psi_S{}^d = \Psi_R{}^d + \Psi_P{}^d + \Psi_{R(\text{cylinder})}. \qquad 5.3$$

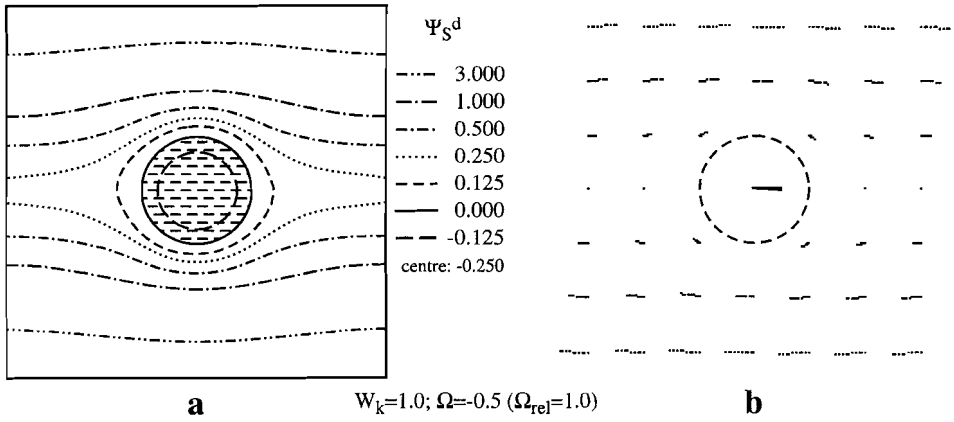

Figure 5.1. (**a**) Stream lines and (**b**) particle displacements during 10 successive deformation increments of 0.02, according to the stream function $\Psi_S{}^d$ for dextral simple shear flow deflected around a free floating cylinder (Ω=-0.5, Ω_{rel}=1.0). Stream lines with Ψ=0.250 represent the separatrices.

Figure 5.1 shows contours of the stream function values (stream lines) of $\Psi_S{}^d$ and the displacements of selected particles when E=1, Ω=-0.5 and each incremental step of deformation (E·dt) is 0.02. This is a typical example of an eye-shaped flow-pattern. It should be noted that the stream lines that touch the x-axis at infinity ($\Psi(\pm\infty;0)=0.25$) are the separatrices since they bound the region with closed stream lines. With the above stream function of Bretherton as a basis, stream functions can be developed for any geologically relevant plane strain deformation in slow Newtonian flow with or without a cylindrical object at the centre. A series of such functions are given in the following and some implications are considered.

5.2.2 Rotational flow deflected around a stationary cylinder

The stream function $\Psi_R{}^d$ represents the rotational flow with boundaries at infinity deflected by a stationary cylinder of radius 1, centred at the origin. It is written:

$$\Psi_R{}^d(r;\theta) = \tfrac{1}{4}E\left(r^2 - 2\ln r + 1\right). \qquad 5.4a$$

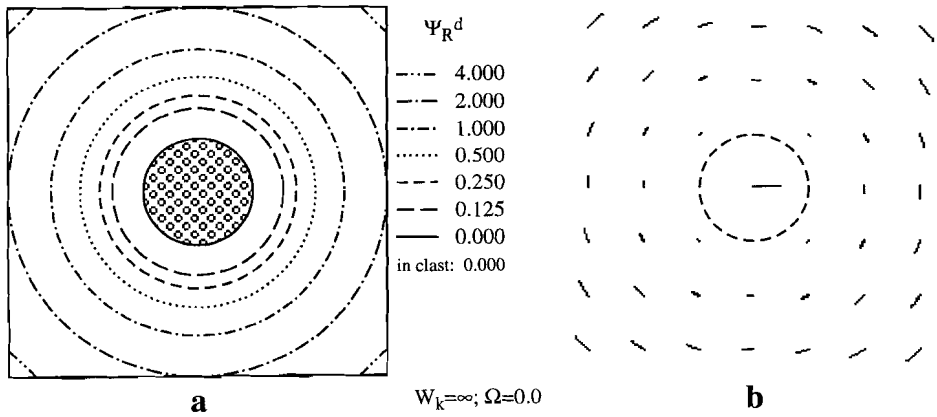

Figure 5.2. (**a**) Stream lines and (**b**) particle displacements during 10 successive deformation increments of 0.02, according to the stream function $\Psi_R{}^d$ for clockwise rotational flow deflected around a stationary cylinder (Ω=0.0).

Figure 5.2 shows contours of this stream function (stream lines) and the displacements of selected particles for E=1 and E·dt=0.02. The function $\Psi_R{}^d$ can be split into 2 components and a constant:

$$\Psi_R{}^d = \Psi_R + \Psi_{R(\text{cylinder}^*)} + C_R. \qquad 5.4b$$

The significance of each of these terms is as follows.

a) $\Psi_R(r;\theta) = \frac{1}{4}Er^2$ or: $\Psi_R(x;z) = \frac{1}{4}E(x^2 + z^2)$. 5.5a,b

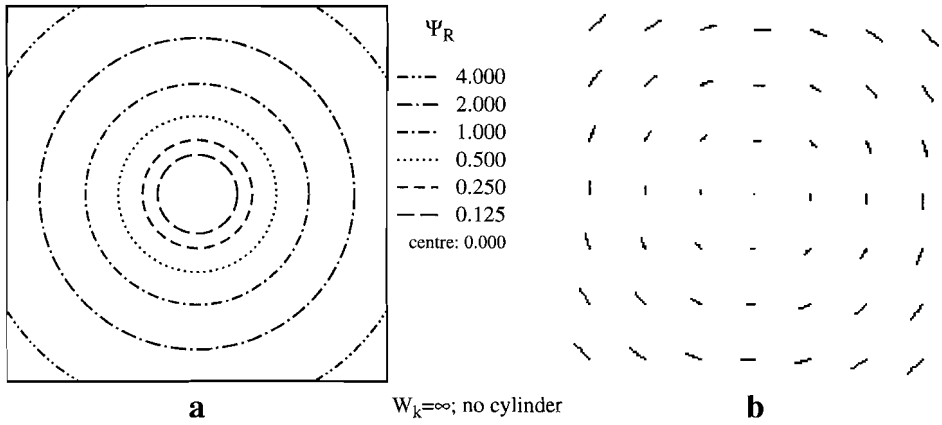

Figure 5.3. (**a**) Stream lines and (**b**) particle displacements during 10 successive deformation increments of 0.02, according to the stream function Ψ_R for clockwise rotational flow.

This corresponds to the rotational component of the matrix flow, i.e., it represents a rotational flow of the matrix with angular velocity $\dot{\omega} = -\frac{1}{2}E$ when no cylinder is present. The flow is clockwise when E>0. Figure 5.3 shows contours of the stream function Ψ_R and displacements of selected particles for E=1 and E·dt=0.02.

b) $\Psi_{R(cylinder^*)}(r;\theta) = -\frac{1}{2}E\ln r$ or: $\Psi_{R(cylinder^*)}(x;z) = -\frac{1}{4}E\ln(x^2 + z^2)$ 5.6a,b

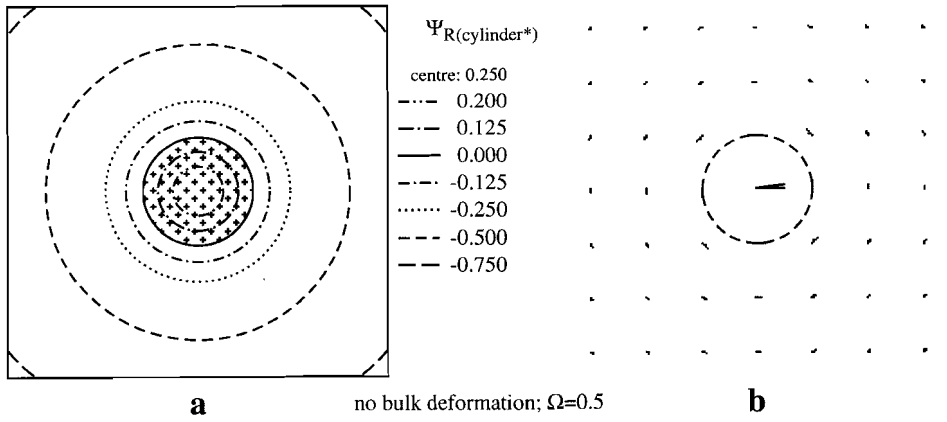

Figure 5.4. (**a**) Stream lines and (**b**) particle displacements during 10 successive deformation increments of 0.04, according to the stream function $\Psi_{R(cylinder^*)}$ for flow generated by a cylinder rotating counter-clockwise with angular velocity Ω=0.5 (rad s^{-1}).

This term represents rotations in the matrix generated by a cylinder of unit radius, rotating at an angular velocity that is related to the magnitude of imposed deformation rate: $\Omega=\frac{1}{2}E$. This special case of $\Psi_{R(cylinder)}$ in $\Psi_R{}^d$ means that the angular velocity of the cylinder is of equal magnitude but in opposite sense to the angular velocity of the matrix at infinity. When E>0 the cylinder rotates anti-clockwise. Figure 5.4 shows stream lines of $\Psi_{R(cylinder*)}$ and the displacements of selected particles for E=1 and E·dt=0.04.

c) $C_R = \frac{1}{4}E$.

This component of the function $\Psi_R{}^d$ is used to make the stream function value zero at the surface of the cylinder ($\Psi_R{}^d$=0 at r=1).

5.2.3 Pure shear flow deflected around a stationary cylinder

The stream function $\Psi_P{}^d$ represents pure shear flow around a stationary cylinder and can be developed from two sub-functions:

$$\Psi_P(r;\theta) = -\tfrac{1}{4}Er^2\cos 2\theta \qquad \text{or: } \Psi_P(x,z) = -\tfrac{1}{4}E\left(x^2 - z^2\right) \qquad 5.7a,b$$

$$\text{and } f(r) = 1 - \frac{2}{r^2} + \frac{1}{r^4}. \qquad 5.8$$

The resulting stream function for $\Psi_P{}^d$ is:

$$\Psi_P{}^d = f(r)\cdot\Psi_P. \qquad 5.9$$

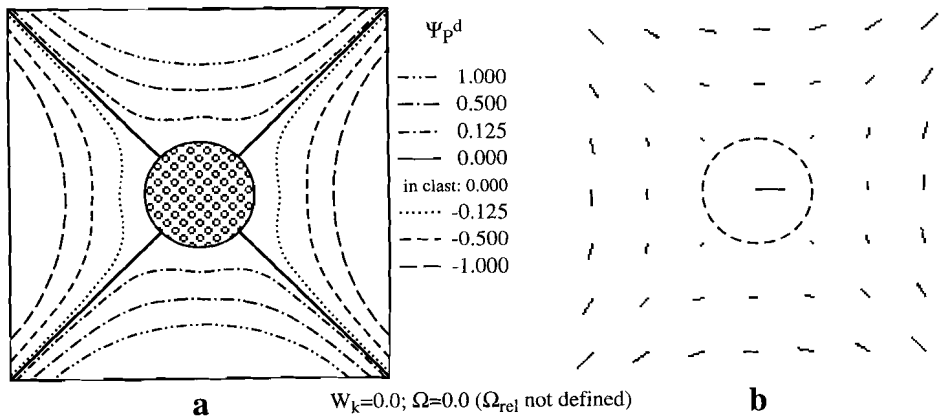

Figure 5.5. (**a**) Stream lines and (**b**) particle displacements during 10 successive deformation increments of 0.02, according to the stream function $\Psi_P{}^d$ for pure shear flow with x=y as extension direction deflected around a stationary cylinder (Ω=0.0).

Stream lines and corresponding displacements of the function $\Psi_P{}^d$ are shown in figure 5.5 for E=1 and E·dt=0.02. In this case, there are no displacements at the cylinder surface. However, only those points where the separatrices meet the cylinder surface are defined as stagnation points. This flow cannot be considered to have a bow-tie pattern since there is no net

rotation component. Equations 5.7a and 5.7b represent unobstructed pure shear flow with x=z as extension direction (when E>0). Figure 5.6 shows stream lines of Ψ_p and particle displacements for E=1 and E·dt=0.02. Equation 5.8 is the function that deflects the unobstructed pure shear flow (Ψ_p) around the stationary cylinder with unit radius, centred at the origin.

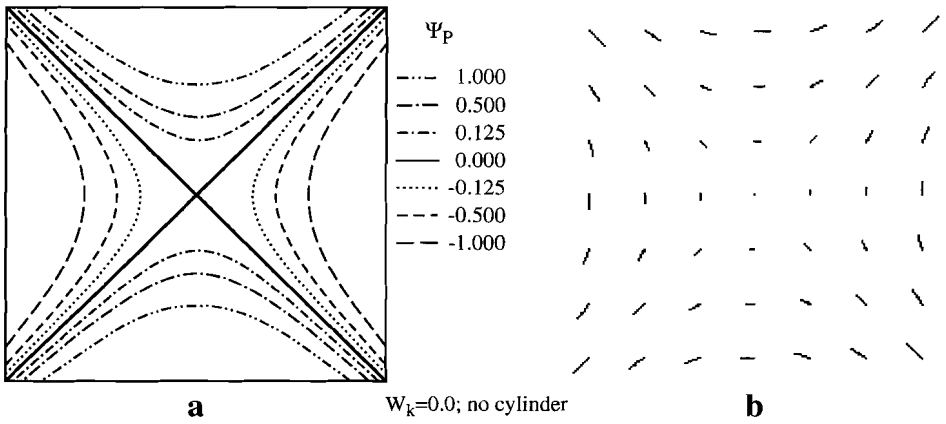

Figure 5.6. (**a**) Stream lines and (**b**) particle displacements during 10 successive deformation increments of 0.02, according to the stream function Ψ_P for pure shear flow with x=y as extension direction.

5.2.4 Flow generated by a rotating cylinder

$\Psi_{R(cylinder)}$ represents the flow, in a matrix that is stationary at infinity, generated by a cylinder of radius 1, centred at the origin and rotating with angular velocity Ω. The function is written:

$$\Psi_{R(cylinder)}(r;\theta) = -\Omega \ln r \qquad \text{or: } \Psi_{R(cylinder)}(x;z) = -\tfrac{1}{2}\Omega \ln\left(x^2 + z^2\right). \qquad 5.10a,b$$

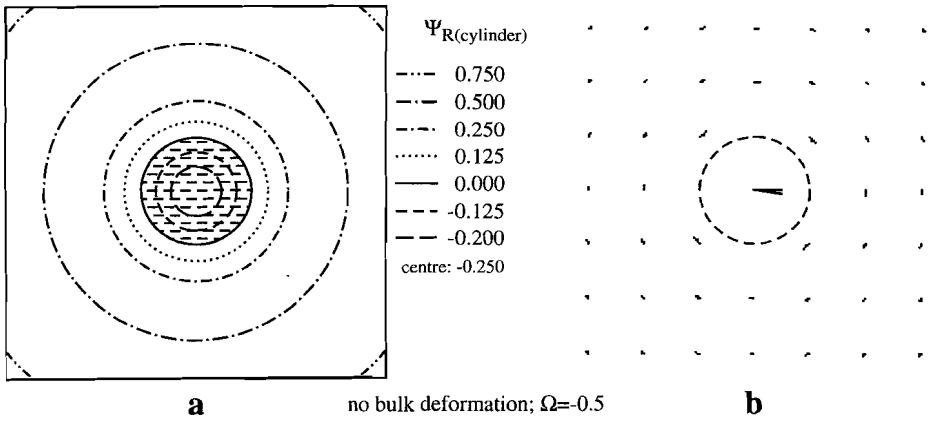

Figure 5.7. (**a**) Stream lines and (**b**) particle displacements during 10 successive deformation increments of 0.04, according to the stream function $\Psi_{R(cylinder)}$ for flow generated by a cylinder rotating clockwise with angular velocity Ω=-0.5 (rad s^{-1}).

When $\Omega>0$, the cylinder rotates anti-clockwise. Figure 5.7 shows stream lines of $\Psi_{R(cylinder)}$ and particle displacements for $\Omega=-0.5$ and $E\cdot dt=0.04$.

5.2.5 General flow with or without a (non-) rotating cylinder

Ψ_R (eq. 5.5) and Ψ_P (eq. 5.7) are the 'building blocks' for the stream function description of any geologically relevant plane strain slow Newtonian flow without obstacles. Accordingly, the stream function for unobstructed simple shear flow with a horizontal flowplane Ψ_S is found by the addition of Ψ_R and Ψ_P so that:

$$\Psi_S = \Psi_R + \Psi_P \text{ or} \qquad 5.11a$$

$$\Psi_S(r;\theta) = \tfrac{1}{4}Er^2 - \tfrac{1}{4}Er^2\cos 2\theta \qquad \text{or: } \Psi_S(x;z) = \tfrac{1}{2}Ez^2 \qquad 5.11b,c$$

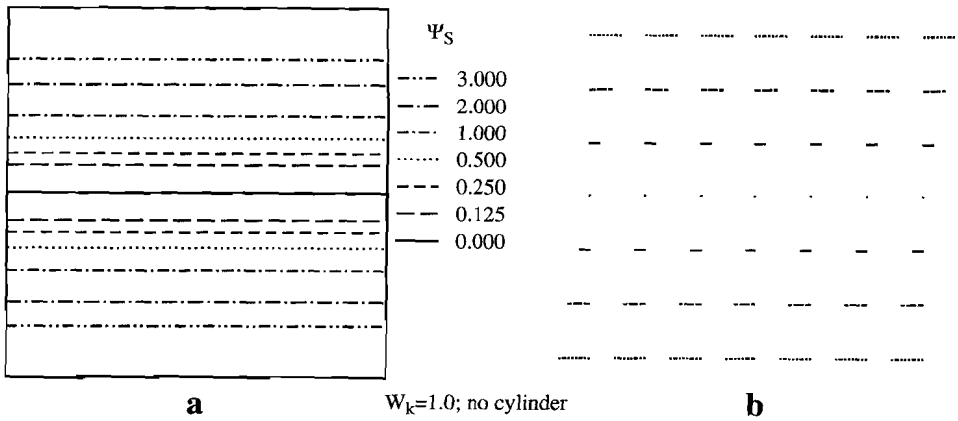

Figure 5.8. (**a**) Stream lines and (**b**) particle displacements during 10 successive deformation increments of 0.02, according to the stream function Ψ_S for dextral simple shear.

Figure 5.8 graphs this function as stream lines and shows displacement trajectories for E=1 and $E\cdot dt=0.02$. Note that all stream lines are straight and horizontal.

A general two-dimensional deformation can be described by changing the rotational component of the flow, by appropriately weighting Ψ_R or Ψ_P:

$$\Psi_{wk} = W_k \cdot \Psi_R + \Psi_P. \qquad 5.12$$

For deformation between pure and simple shear (also known as intermediate shear), W_k falls in the range: $0 \le |W_k| \le 1$. W_k is known as the kinematic vorticity number of the flow and is a measure of the rotational component of the deformation, normalised with respect to strain rate (Truesdell 1953, Means *et al.* 1980). For $|W_k| > 1$, all flow lines are closed which means that, during ongoing deformation, any material particle will eventually return to its original position. In geology, the case of $|W_k| > 1$ is generally not considered. Figure 5.9 shows stream lines of Ψ_{wk} and associated displacements for $W_k=0.5$, E=1 and $E\cdot dt=0.02$.

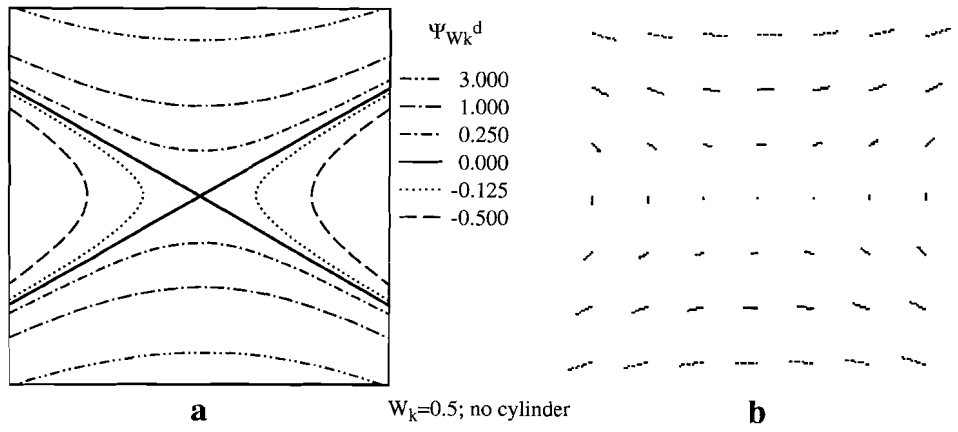

Figure 5.9. (**a**) Stream lines and (**b**) particle displacements during 10 successive deformation increments of 0.02, according to the stream function Ψ_{Wk} for general flow (W_k=0.5).

Ψ_R (eq. 5.5) and $\Psi_P{}^d$ (eq. 5.9) can similarly be used to construct stream functions for general deformation deflected by a free floating cylinder centred at the origin using the function:

$$\Psi_{Wk}{}^{d} = W_k \cdot \Psi_R + \Psi_P{}^{d} + C_{R*}, \qquad 5.13$$

in which C_{R*} ($=W_k \cdot \frac{1}{4}E$) is a constant to make the stream function value zero at the surface of the cylinder. In this case, the cylinder is 'free floating' and will rotate with the same angular velocity as the rotational component of the flow: $\Omega = -W_k \cdot E/2$. I define the relative rotation rate of the cylinder (Ω_{rel}) as: $\Omega_{rel}=\Omega/(-W_k \cdot E/2)$ meaning that a free floating object in Newtonian slow flow has an Ω_{rel}-value of 1.0 (Ω_{rel} is only defined when $W_k \neq 0$, see also Chapter 4). Figure

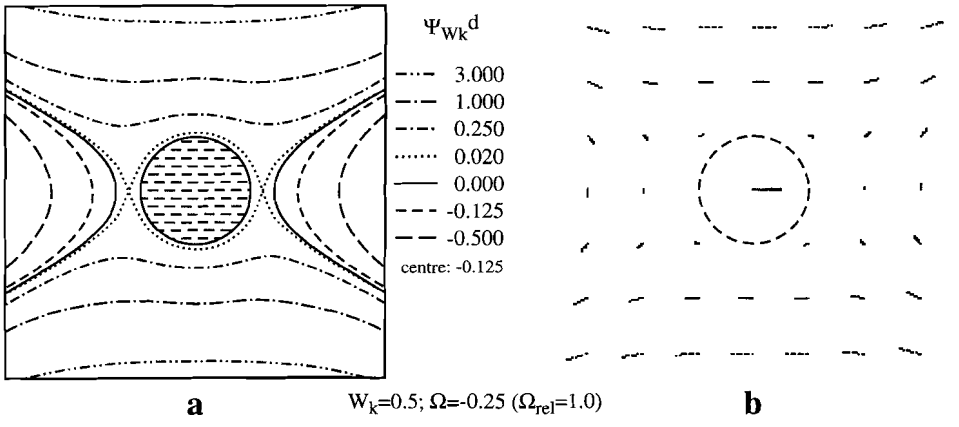

Figure 5.10. (**a**) Stream lines and (**b**) particle displacements during 10 successive deformation increments of 0.02, according to the stream function $\Psi_{Wk}{}^{d}$ for general flow (W_k=0.5) deflected around a free floating cylinder (Ω=-0.25, Ω_{rel}=1.0). Stream lines with Ψ=0.020 represent the separatrices.

5.10 shows contours of $\Psi_{Wk}{}^{d}$ and particle displacements for W_k=0.5, E=1, and E·dt=0.02. The stream lines with a Ψ-value of 0.02 form the separatrices. This pattern can be called a bow-tie pattern since there is a net rotational component and back-flow regions are present.

5.2.6 Flow patterns around a cylinder with Ω_{rel}<1.0

In Chapter 4 it was reported that a cylinder floating in the non-Newtonian pAA-solution rotated up to ~60% slower ($0.4<\Omega_{rel}$(in pAA)<1.0) than the angular velocity, predicted by Jeffery (1922), of a free-floating cylinder in slow Newtonian simple shear flow (Ω_{rel}=1.0). Furthermore, it has been argued that porphyroblasts (which, contrary to clasts, grow during deformation) do not generally rotate in a non-coaxially deforming rock (Bell *et al.* 1992, and references therein). For the purpose of visualising the flow patterns around an object that rotates at a reduced rotation rate, the equation of Bretherton (eq. 5.2) can be used for simple shear flow, imposed at infinite distance.

Figures 5.11 and 5.12 show stream lines of $\Psi_S{}^{d}$ and corresponding displacement trajectories for E=1, E·dt=0.02 and Ω=-0.25 (Ω_{rel}=0.5; fig. 5.11) and Ω=0.0 (Ω_{rel}=0.0; fig. 5.12). Figure 5.11 is a typical example of a bow-tie flow-pattern with stagnation points left and right of the object and is characterised by separatrices at Ψ=0.038. Figure 5.12 shows the limiting example of a bow-tie flow-pattern with stagnation points on the cylinder surface at $\theta=\pm30°$ and separatrices at Ψ=0 but without closed flow lines in the central region. Figure 5.11 shows a close resemblance with the flow pattern in a non-Newtonian liquid around a floating cylinder, as shown in figure 4.9b (Chapter 4).

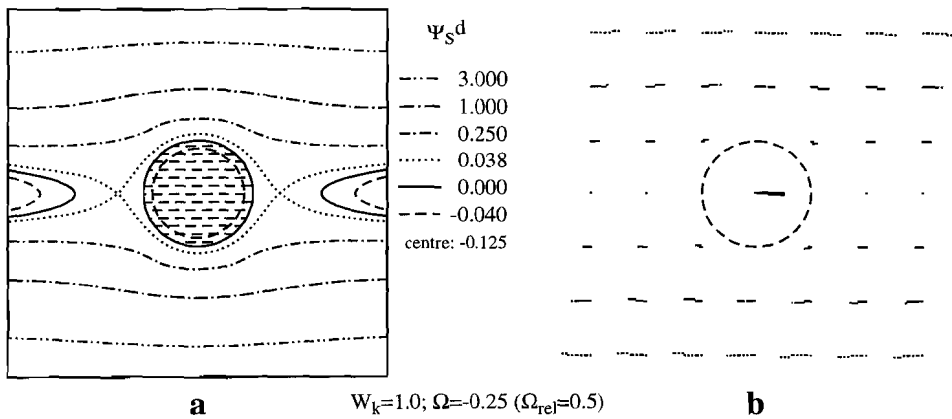

Figure 5.11. (**a**) Stream lines and (**b**) particle displacements during 10 successive deformation increments of 0.02, according to the stream function $\Psi_S{}^{d}$ for dextral simple shear flow deflected around a cylinder with an impeded rotation rate (Ω=-0.25, Ω_{rel}=0.5). Stream lines with Ψ=0.038 represent the separatrices.

The flow patterns as shown in figures 5.1, 5.11 and 5.12 were experimentally produced in a Newtonian liquid by Robertson and Acrivos (1970) in a linear fluid shear apparatus similar to the one described in Chapter 3. The cylinder in their experiments was fixed to the axis of a motor and could thus be forced to rotate at any given rate of rotation. The experiments by Robertson and Acrivos (1970) showed that equation 5.2 describes the observed flow pattern accurately. It is interesting to see that when the rotation rate of the cylinder is lower than Ω_{rel}

back-flow regions occur on either side of the cylinder. The stream line through a given value of z (at x=0) departs less from a straight line when Ω_{rel} of a cylinder is reduced (compare figs. 5.1a, 5.11a and 5.12a).

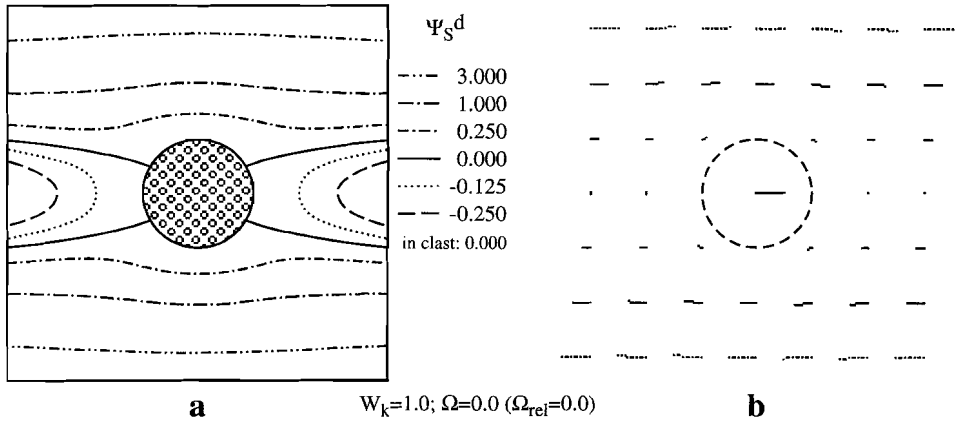

Figure 5.12. (**a**) Stream lines and (**b**) particle displacements during 10 successive deformation increments of 0.02, according to the stream function Ψ_S^d for dextral simple shear flow deflected around a stationary cylinder (Ω=0.0, Ω_{rel}=0.0). Stream lines with Ψ=0.000 represent the separatrices.

5.2.7 Strain rate and stress distribution based on the stream function

With the use of the velocity distribution that can be calculated with the stream function it is also possible to calculate the strain rate ($\dot{\varepsilon}$) distribution around the cylinder (see Appendix). A rotational component of the entire system has no effect on the strain rate. Therefore, the strain rate distribution for pure shear around a stationary cylinder (fig. 5.5; E=1.0, W_k=0.0, Ω=0.0) is equivalent to the strain rate distribution for simple shear with a free floating cylinder (fig. 5.1; E=1.0, W_k=1.0, Ω_{rel}=1.0).

Figure 5.13 shows the strain rate distributions around the cylinder relative to the imposed shear strain rate for the conditions used for figures 5.1 (Ω_{rel}=1.0), 5.11 (Ω_{rel}=0.5), and 5.12 (Ω_{rel}=0.0). The $\dot{\varepsilon}$-values range from 0.0 (within the cylinder) via 1.0 (in the far-field matrix) to a maximum immediately adjacent to the cylinder. The distribution in figure 5.13a has 4-fold symmetry which reduces to 2-fold symmetry when the angular velocity of the cylinder is not the same as the angular velocity of the far-field flow ($\Omega_{rel}\neq$1.0, figs. 5.13b and c). The strain rate immediately adjacent to the cylinder must be the direct result of simple shear (with respect to pure shear) since the velocity-vectors in the matrix are tangent to the cylinder surface. The maximum strain rates in 5.13a, b and c are 2.0, 2.5 and 3.0 respectively and found immediately above and below (5.13a to c) and left and right (only in 5.13a) of the object.

It is obvious that a cylinder in pure shear (fig. 5.5a) will not rotate since the flow pattern is symmetric and no momentum is transferred from the matrix to the cylinder. Adding a rotational component to pure shear flow, in order to get simple shear at infinity (fig. 5.1a), does not change the strain rate distribution in the matrix. When inertial forces are neglected, the rotational component of the matrix has thus no effect on the momentum transferred to the cylinder. Consequently, the angular velocity of a cylinder in simple shear is equal to the angular velocity of the far-field matrix (Ω_{rel}=1.0), provided that simple shear is imposed at infinite

distance from the cylinder. Due to symmetry of the flow, the rotational behaviour of the cylinder is not dependent on the material properties of the matrix[2]. Simple shear flow imposed at infinite distance from the cylinder can for that reason not explain Ω_{rel}-values below 1.0, as was observed in Chapter 4 for cylinders in a non-Newtonian fluid (pAA-solution). The only feasible explanation for the observed slowing down is a progressive development of anisotropy in the pAA-solution, with concomitant establishment of a velocity distribution which departs from that in a Newtonian (isotropic) fluid, and a decrease in momentum transfer from the fluid to the object.

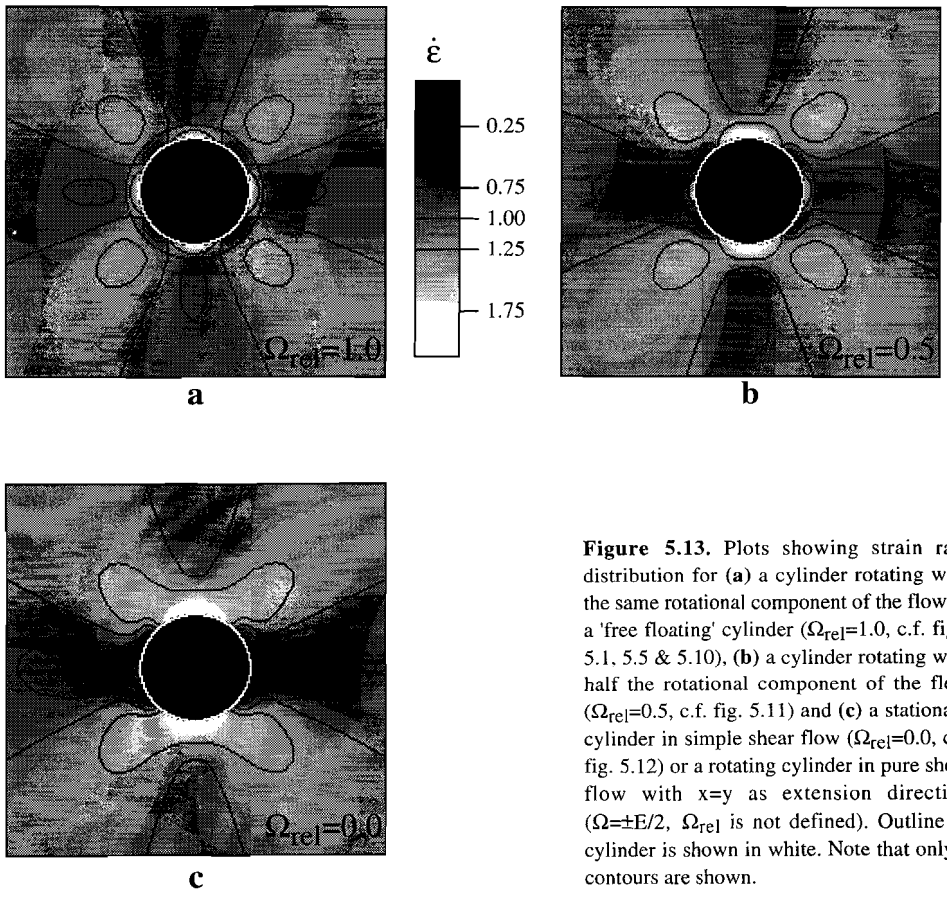

Figure 5.13. Plots showing strain rate distribution for **(a)** a cylinder rotating with the same rotational component of the flow as a 'free floating' cylinder (Ω_{rel}=1.0, c.f. figs. 5.1, 5.5 & 5.10), **(b)** a cylinder rotating with half the rotational component of the flow (Ω_{rel}=0.5, c.f. fig. 5.11) and **(c)** a stationary cylinder in simple shear flow (Ω_{rel}=0.0, c.f. fig. 5.12) or a rotating cylinder in pure shear flow with x=y as extension direction (Ω=±E/2, Ω_{rel} is not defined). Outline of cylinder is shown in white. Note that only 3 contours are shown.

[2] Orientation dependent material properties (anisotropy) in the matrix prior to deformation would lead to a different flow-pattern. When anisotropy develops as a result of this flow-pattern, it will have a symmetric geometry.

5.3 Flow patterns derived from finite element modelling

The stream function as a method of examining the flow in Newtonian matrix materials gives the exact analytical solution when the boundaries of the system are at infinite distance from the origin. The stream function cannot, however, be used to model non-Newtonian rheologies or the influence of shear zone walls on the flow around an object. The effects of non-linear rheology or nearby boundaries on the flow around a rigid cylinder can only be investigated with the aid of numerical techniques. This section starts with a description of the finite element method (FEM) as applied to this problem. It continues with the presentation of the flow patterns that are the results of the finite element modelling conducted in collaboration with Paul Bons and Terence Barr and partially reported in Bons, Barr and Ten Brink (in press[3]).

5.3.1 Numerical technique

The finite element method as applied to the present problem gives solutions for the distribution of stress, strain rate, velocity and flow paths for a system in which a cylindrical, rigid object is embedded in a body of (non-) linear, ductile, material deforming by bulk simple shear. Deformation is at all points incompressible, plane strain. The rotational axis of the cylinder is parallel to the vorticity vector of the flow so that displacements are restricted to the xz-plane and the problem is thus indeed two-dimensional. The assumption is made that both matrix and object material can be described by a constitutive relation of the form:

$$\tau_{ij} = B \cdot I_{II}^{(1/1-n)} \dot{\varepsilon}_{ij}, \tag{5.14}$$

where τ_{ij} is the deviatoric stress , $\dot{\varepsilon}_{ij}$ is the strain rate, I_{II} is the second invariant of the strain rate tensor, n is the exponent that determines the degree of non-linearity of the rheology, and B is a scalable constant. The strain rate is defined as:

$$\dot{\varepsilon}_{ij} = \frac{1}{2}\left(\frac{dv_i}{dx_j} + \frac{dv_j}{dx_i}\right), \tag{5.15}$$

where v_i is the velocity component in the i-direction. In this case, the viscosity (η) is given:

$$\eta = B \cdot \dot{E}^{(1/n-1)}. \tag{5.16}$$

In the FEM-calculations, the constant $B_{object}=100^{1/n} \cdot B_{matrix}$ which makes the effective viscosity of the object 100 times greater than that of the matrix. With equation (5.14), the solution is found for the force balance equations:

$$\frac{d\tau_{ij}}{dx_j} + \frac{dP}{dx_i} = 0 \tag{5.17}$$

---

[3] Bons, P.D., Barr, T.D. and Ten Brink, C.E., in press (accepted May 1996). The development of δ–clasts in non-linear viscous materials: a numerical approach. Tectonophysics.

where P is pressure and summation is implied over the j-index. The assumption of incompressibility requires that:

$$\dot{\varepsilon}_{xx} + \dot{\varepsilon}_{yy} + \dot{\varepsilon}_{zz} = 0. \tag{5.18}$$

The velocity and pressure was calculated for every element intersection point (node) within the medium for infinitesimal deformation using a finite element code (Basil) developed by G. Houseman. When the appropriate boundary-conditions are chosen, it is possible to compare the results of the finite element model to the experiments described in Chapters 2 and 4 as well as to the analytical solutions of §5.2.

5.3.2 Model-conditions

Two different models[4] were studied that represent or approximately represent simple shear (fig. 5.14), but lead to significant differences in the resulting flow field around the rigid cylinder (Bons *et al.* in press). In both models, the central cylinder is 'free floating' which means that any motion of the cylinder will be the sole result of momentum transferred by the matrix to the cylinder. The condition of no-slip implies that matrix material directly adjacent to the cylinder has the same velocity as the cylinder itself. All values in the results presented here are normalised to unit shear strain rate ($\dot{\gamma}$=1.0) with, in contrast to Bons *et al.* (in press), a cylinder of unit radius (R=1.0) positioned at the centre. The margins of the model are at 12·R (d=12 in fig. 5.14) in positive and negative x and z away from the centre which results in a 'relative shear zone width' of 12 (SW_{rel}=12, see §3.3.2).

The first model corresponds to simple shear deformation imposed on margins located at infinite distance from the object, located at the origin (fig. 5.14a, b). When a Newtonian matrix (n=1) is assumed using this model, the solution can be compared to the analytical solution presented in §5.2. By varying the stress-exponent (n) of the matrix within this model, it is thus possible to examine the influence of material properties on flow pattern and rotation rate of the object. In this 'infinity' model (fig. 5.14a), the horizontal velocity component (v_x) at the upper and lower boundaries of the model are set to a constant value: v_x(top)=12 and v_x(bottom)=-12. The vertical velocity component (v_z) at the right and left boundaries of the model are set to zero: v_z(left)=v_z(right)=0. A constant background normal stress is applied to all boundaries: $\sigma_{xx}=\sigma_{zz}=C$. This means that, during deformation, the boundaries (at d=12) are allowed to deform and do not represent shear zone walls in a physical sense. An equivalent notional experimental set-up is drawn in figure 5.14b. Here, the normal pressure could be applied by inserting the apparatus in a pressurised (fluid filled) tank.

The second model resembles deformation between relatively closely spaced (SW_{rel}=12) rigid shear zone walls (fig. 5.14c, d). When the matrix material is taken as Newtonian (n=1), the results should be comparable to the experimentally determined flow around a rigid cylinder floating in glycerol (§4.3.2). When the stress-exponent (n) of the matrix is raised, the flow can be compared to that around a rigid cylinder floating in pAA-solution (non-Newtonian; §4.3.3) and to the experiment described in Chapter 2 (crystalline, power-law matrix and clasts). In this 'shear zone wall' model (fig. 5.14c), the rigid walls are represented by restrictions on the vertical

[4] Bons *et al.* (in press) also reports the results of a third model that simulates shear-box experiments, where deformation is imposed by movement of rigid boundaries on all sides.

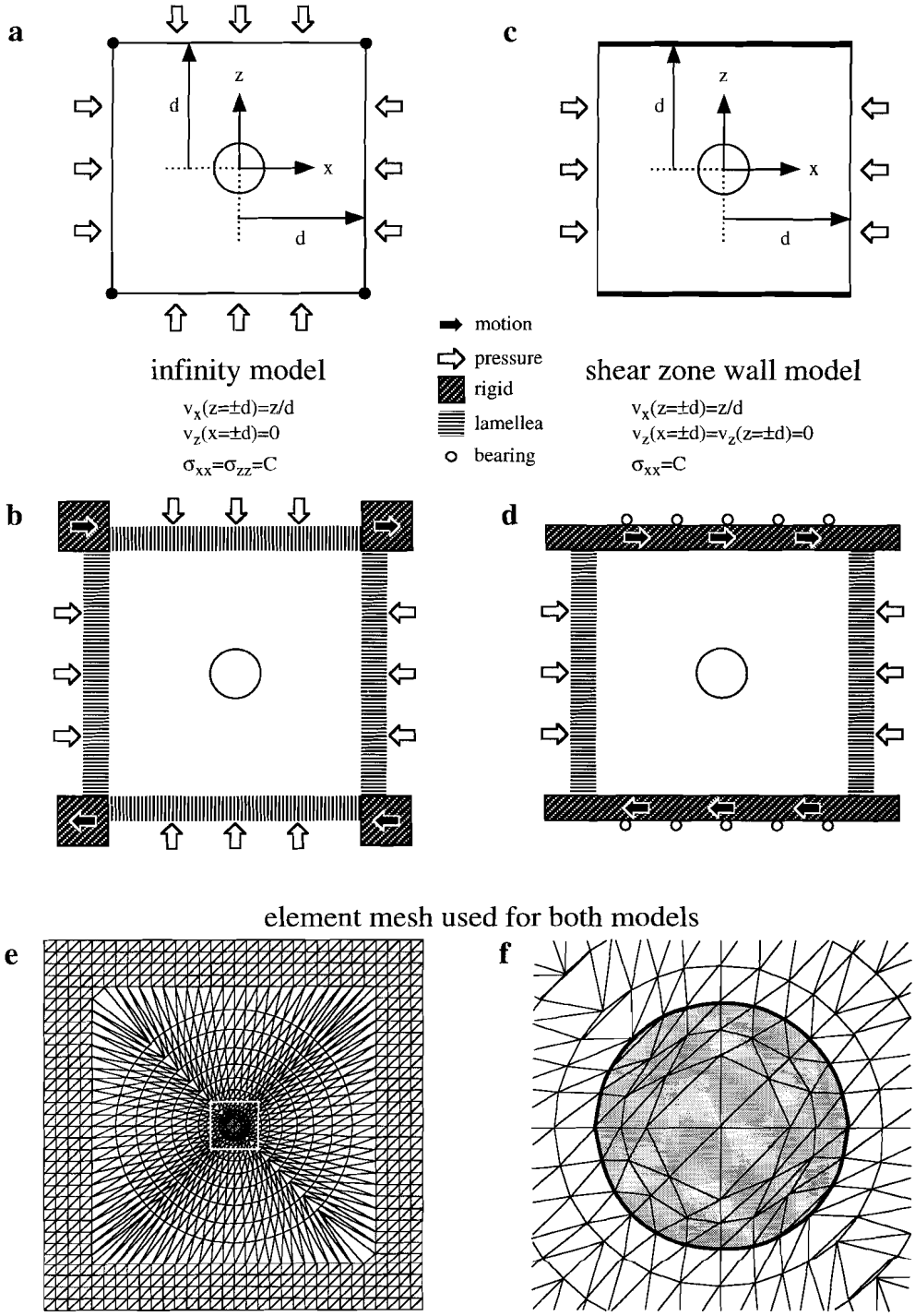
a
z
d
x
d
infinity model
$v_x(z=\pm d)=z/d$
$v_z(x=\pm d)=0$
$\sigma_{xx}=\sigma_{zz}=C$
motion
pressure
rigid
lamellea
bearing
c
z
d
x
d
shear zone wall model
$v_x(z=\pm d)=z/d$
$v_z(x=\pm d)=v_z(z=\pm d)=0$
$\sigma_{xx}=C$
b
d
element mesh used for both models
e
f

Figure 5.14 (previous page). **(a)** Conditions of the infinity model used in the finite element modelling. **(b)** Simplified possible experimental set-up for the infinity model. **(c)** Conditions of the shear zone wall model used in the finite element modelling. **(d)** Simplified possible experimental set-up for the shear zone wall model. Note that object radius is not drawn at the correct scale. **(e)** The element mesh used by the model calculations, the white outline is enlarged in **(f)**.

velocity component at the upper and lower boundaries of the model: $v_z(top)=v_z(bottom)=0$. Other velocity-components are equal to those in the first model: $v_x(top)=12$, $v_x(bottom)=-12$ and $v_z(left)=v_z(right)=0$. A constant background normal stress is applied on the right and left boundaries: $\sigma_{xx}=C$. This means that the shear profile at the right and left boundaries may deviate from the straight line geometry which would result from homogeneous simple shear. A simplified equivalent experimental set-up is drawn in figure 5.14d. The element mesh used for the model calculations is shown in figure 5.14e, f.

5.3.3 Results

As in §5.2, the flow patterns are represented in the form of stream lines (see also Chapter 4). The stream lines are obtained by numerical integration of the instantaneous velocity values calculated by the model. Symmetry of the flow allows representation using only half of the model, the vertical through the centre of the object being a mirror plane. Each box in figure 5.15 represents results obtained for the central area of one stress-exponent plus boundary-condition combination. Stream lines are shown on the left side of each box for the two different models and for the matrix n-values shown (n=1, 3 and 5). Contours of the vertical velocity component (v_z) are shown on the right side of each box.

Both of these models were investigated for various boundary-object distances. While boundary conditions have a profound effect on the flow pattern, only a very minor effect of the relative size of the cylinder was found between $SW_{rel}=2.5$ and $SW_{rel}=25$. Illustrated in this thesis (as in Bons *et al.* in press) are the calculations for $SW_{rel}=12$.

The results show that the 'infinity' model always produces an eye-shaped flow pattern, independent of the stress-exponent n of the matrix (fig. 5.15 left column). The volume of material revolving in closed stream lines around the object increases with the stress exponent. The n=1 solution is almost identical (approximately 1% discrepancy) to the analytical solution for a free floating cylinder of Bretherton (1962) and Chwang and Wu (1975). It should be emphasised that in these calculations $v_z=0$ at $x=\pm 12$, implying that stream lines are horizontal at the left and right margins. Therefore, the stream lines through $z=0$ at $x=\pm 12$ represent the separatrices, and the stagnation points are situated on the margins. This is contrary to the analytical solution for a free floating object where the stagnation point is found at $x=\pm\infty$ and the value of the stream function for the separatrices is 0.250.

In contrast, the 'shear zone wall' model always produces a bow-tie flow pattern (fig. 5.15 right column). The distance of the stagnation point to the object (D_s, see §3.3.2) and, more particularly, the width of the backflow regions at the margins (D_{bfr}), depend on the stress exponent (table 5.1). With increasing stress exponent, D_{bfr} increases while D_s decreases. The separatrices are virtually parallel to the direction of shear at a short distance from the object.

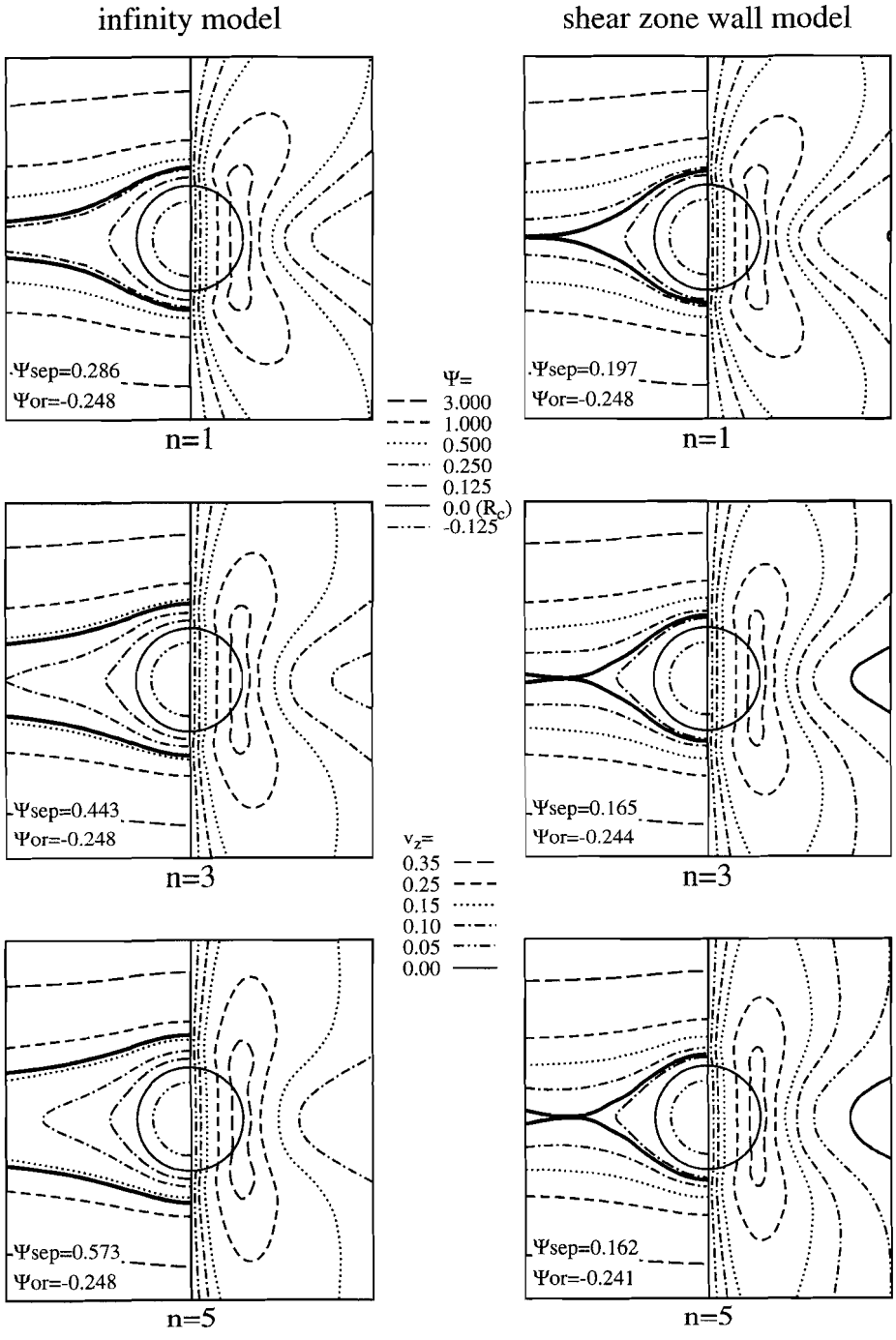
infinity model
shear zone wall model
Ψsep=0.286
Ψor=-0.248
n=1
Ψsep=0.197
Ψor=-0.248
n=1
Ψ=
3.000
1.000
0.500
0.250
0.125
0.0 (Rc)
-0.125
Ψsep=0.443
Ψor=-0.248
n=3
Ψsep=0.165
Ψor=-0.244
n=3
vz=
0.35
0.25
0.15
0.10
0.05
0.00
Ψsep=0.573
Ψor=-0.248
n=5
Ψsep=0.162
Ψor=-0.241
n=5

Figure 5.15 (previous page). Contours of stream line value (left hand side of each box) and vertical velocity component (right hand side of each box) for the infinity model (left column) and shear zone wall model (right column) for three different stress exponents (n=1, 3 and 5). Only the central area of the model is shown. Bold lines are separatrices, Ψsep is stream line value of separatrix, Ψor is stream line value at centre of object. Stream line value at object boundary (R_C) was set to 0.0.

Finally, the rotation rate (Ω) of the object was determined in the simulations. The analytical value of Ω for a free floating cylinder in a Newtonian viscous matrix is $0.5 \cdot \dot{\gamma}$ (Ω_{rel}=1.0, see §3.3.2) and is 0.5 in the simulations. Values of the relative rotation rate (Ω_{rel}) of the central object are given in table 5.1, which shows that they are practically the same as the analytical value (<1% slower) for the 'infinity' model and slightly reduced (up to 3.5% slower) when the 'shear zone wall' model is applied with higher stress-exponents.

SW_{rel}=12	D_{bfr} (at margins)		D_S		Ω_{rel}	
	Infinity	SZW	Infinity	SZW	Infinity	SZW
n=1	--	0.89 (·R)	12	3.42	0.993	0.990
n=3	--	1.20 (·R)	12	2.77	0.993	0.975
n=5	--	1.30 (·R)	12	2.64	0.993	0.965

Table 5.1 The width of the backflow regions (D_{bfr}), the relative distance of the stagnation points (D_S) and the relative rotation rate (Ω_{rel}) calculated for the two models with 3 different stress-exponents (n). Infinity: infinity model, SZW: shear zone wall model.

5.3.4 Strain rate distribution

The strain rate ($\dot{\varepsilon}$) distribution in the immediate vicinity of the central object is depicted in figure 5.16 for four different model conditions. The dimension of the elements (fig. 5.14f), the no-slip condition at the object boundary and the imperfect rigidity of the central object all have a 'smoothing' effect and decrease the strain rate gradient at localised extremes in the modelled area. Therefore, the strain rate maxima immediately adjacent to the object cannot be found.

Figure 5.16a shows that the $\dot{\varepsilon}$-distribution obtained for the infinity model with n=1 is similar to that of the free-floating Newtonian case obtained analytically (c.f. fig. 5.13a). However, the distribution of the elements in the finite element calculations results in a more irregular pattern, and the maximum strain rate value is not found immediately adjacent but diagonally displaced from the object. When the stress exponent of the matrix is increased to 5 (n=5, fig. 5.16b), the range of strain rate values (not considering the values in and immediately adjacent to the central object) increases from $0.60<\dot{\varepsilon}<1.36$ to $0.51<\dot{\varepsilon}<1.37$, and hence minima and maxima are more pronounced.

The strain rate distribution within the shear zone wall model is very similar to the infinity model apart from a larger increase in range between n=1 ($0.60<\dot{\varepsilon}<1.58$; fig. 5.16c) and n=5 ($0.54<\dot{\varepsilon}<1.73$; fig. 5.16d). The strain rate minima and maxima in figures 5.16 (FEM-method) and 5.13a (Ψ-method) are listed in table 5.2.

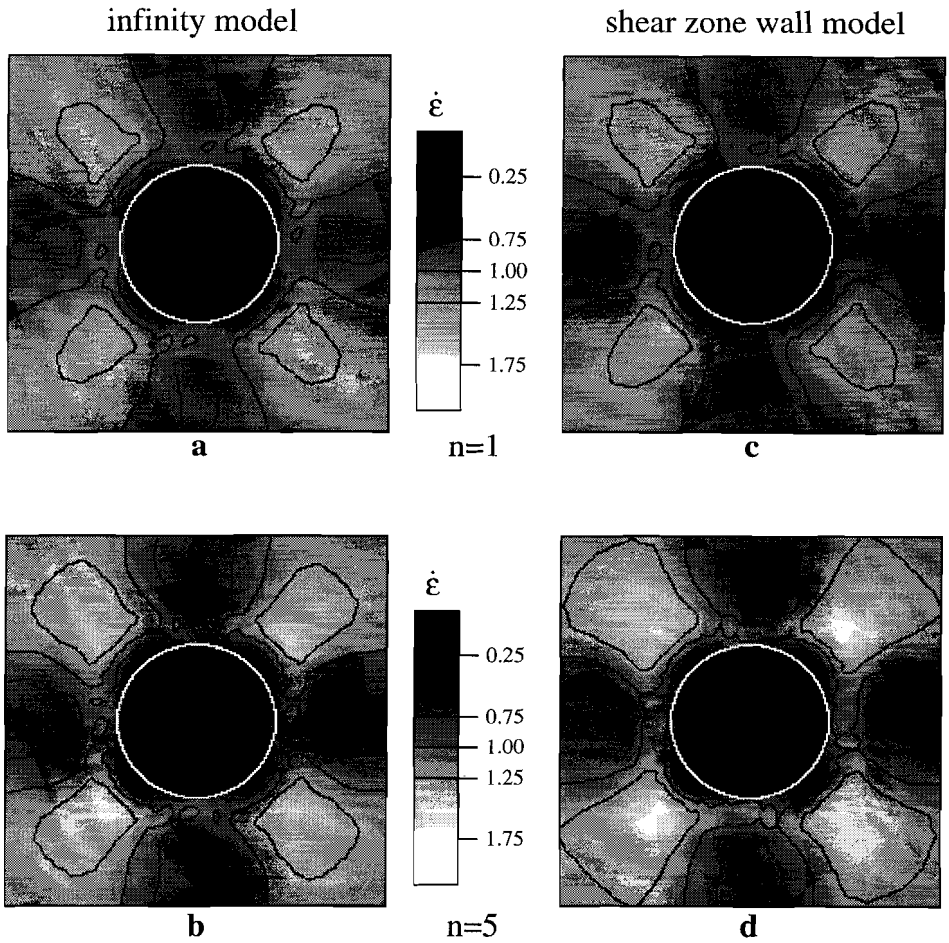

Figure 5.16. Plots showing strain rate distribution for the infinity model (left) and the shear zone wall model (right) for n=1 (top) and n=5 (bottom). Outline of central object is shown in white. Note that only 3 contours are shown and that scale is not the same as in figure 5.13.

	infinity model		shear zone wall model		Ψ-method	
	minimum $\dot{\varepsilon}(+)$	maximum $\dot{\varepsilon}(\times)$	minimum $\dot{\varepsilon}(+)$	maximum $\dot{\varepsilon}(\times)$	minimum $\dot{\varepsilon}(+)$	maximum $\dot{\varepsilon}(\times)$
n=1	0.60	1.36	0.60	1.58	0.78	1.37
n=5	0.51	1.37	0.54	1.73		

Table 5.2. The range of 'far-field' strain rate extremes found with the FEM-method for the 2 models using n=1 and n=5. The values derived with the stream function are shown for comparison. + means horizontally and vertically away from the central object, × means diagonally away from the object.

5.3.5 Discussion

The results of the finite element modelling (FEM) show that a variation in the stress exponent (n) produces only small variations in flow pattern. The type of flow pattern is determined by the boundary conditions (i.e. eye-shaped in 'infinity model' vs. bow-tie in 'shear zone wall' model) for deformation around a rigid clast under incompressible plane-strain. The large effect of the boundary conditions on the type of flow pattern is an interesting observation. It implies that care should be taken in choosing boundary conditions for simulation of these systems, either numerically or experimentally. Since both models investigated, i.e. the infinity and shear zone wall model, result in remarkably different flow patterns, it is important to relate these models to deformation in natural or experimental environments.

The 'infinity' model is characterised by deflection of flow trajectories (stream lines) around the object and vertical velocity components are developed in a wide field around the object. Eye-shaped flow patterns are the result, irrespective of the value of the stress exponent. For a linear viscous matrix (n=1), the solution most closely resembles the analytical solution for simple shear flow imposed at infinity (compare fig. 5.15a to 5.1a). It can thus be inferred that the 'infinity' model is most applicable to isolated inclusions or to inclusions that are small with respect to the width of the shear zone. This situation may be approached in geology, but rarely in geologically relevant experiments. The experiments by Robertson and Acrivos (1970), with a Newtonian matrix surrounding a cylinder, show good agreement between velocities calculated with the stream function and experimentally determined velocities. However, the width of the shear zone in the experiments by Robertson and Acrivos (1970) was 39.6 times the diameter of the cylinder which may account for the lack of shear zone wall effects.

The 'shear zone wall' model approximates the situation where simple shear is imposed by rigid platens parallel to the flow plane, not restricting shear strain rate variations laterally within the matrix. This model is similar to experiments by Handin *et al.* (1960), Jessell and Lister (1991), Passchier *et al.* (1993), Bons and Cox (1994), and the experiments presented in Chapters 2 and 4. The rigidity of the horizontal boundaries enforces back-flow regions to accommodate the inhibited vertical velocity component. A bow tie flow pattern is the result, with separatrices that are parallel to the flowplane at relatively short distance from the object. This model is probably also applicable to many natural shear zones, where relatively hard layers parallel to the flow plane constrain vertical movement above and below the clast, but not laterally.

A further point of interest is the influence of the relative shear zone width (SW_{rel}) on the flow pattern, which is not significant in the FEM-simulations of the shear zone wall model. The FEM results of the shear zone wall model for a large SW_{rel}, should intuitively be equivalent to the results for the infinity model. However, such a trend is not found for SW_{rel}=2.5 to 25. It is possible that the assumption of incompressibility accounts for the absence of shear zone width-effects, however, it is also possible that the boundary conditions and constraints are not chosen correctly.

Lastly, the relative rotation rate (Ω_{rel}) of the objects in the FEM-simulations is up to 3.5% lower than the analytical Ω_{rel}-value for a free-floating cylinder in a Newtonian matrix. A very small decrease of rotation rate (0.7-1.0 %) was found for the n=1 simulation which is consistent with the Ω_{rel}=1.0±0.075 for a free floating cylinder in glycerol (see §4.3.2). However, although

increasing the stress exponent of the matrix material to 5 in the shear zone wall model reduces the relative rotation rate by 3.5%, this cannot account for the 60% reduction in Ω_{rel}-values (i.e. values down to Ω_{rel}=0.4) found for cylinders floating freely in the shearing non-Newtonian medium used in Chapter 4 (pAA-solution; see §4.3.3) where shear strain was imposed by nearby rigid shear zone walls.

5.4 Effect of matrix anisotropy on object rotation rate

When simple shear is imposed by rigid walls, the curvature of the flow lines above and below the object must vanish in the direction of these walls; the velocity-component of the flow in the z-direction (v_z) must be zero at the walls. Therefore, the compressive stress is increased, with respect to the 'infinity' case, in regions where flow lines have to converge as a result of these walls. In horizontal dextral simple shear this will occur in regions above-left and below-right of the cylinder. Similarly, the compressive stress is lowered in regions where flow lines diverge as a result of these walls. On the basis of the experimental results presented in Chapter 4 regarding the Ω_{rel}-values, it was concluded that nearby shear zone walls have no effect on the rotation rate of a cylinder in a Newtonian liquid.

In the shear zone of Chapter 4, Ω_{rel} in the pAA-solution is reduced, but not in the glycerol. At the start of deformation, Ω_{rel}=1.0 in both pAA-solution and glycerol, and the strain rate re-distribution, caused by the presence of the shear zone walls, is presumably similar in both materials. This strain rate re-distribution has no effect on Ω_{rel} in glycerol so the momentum transfer when shear zone walls are present is equivalent to the situation where simple shear is imposed at infinity. In contrast, Ω_{rel} in the pAA-solution decreases with strain to a certain 'steady state' value, during which time the total forwarding torque must thus be gradually lowered with respect to the total restraining torque until a new (and lower) steady state momentum transfer is reached.

The up to 60% reduction of relative rotation rates of the objects in the shearing pAA-solution, as reported in Chapter 4, has been ascribed to the alleged anisotropy of the pAA-solution. Up to the present, geological literature has not given anisotropic behaviour the attention that it should have. Many researchers acknowledge the presence of orientation dependent material properties and anisotropy is recognised in many deformed rocks. This anisotropy can be the result of depositional layering (clays, mass-flow deposits, varves, etc.) or the effect of deformation on an, at the larger scale, initially isotropic material due to rotation of flaky minerals (e.g. gneisses) or redistribution of grain shape and/or crystallographic orientation (e.g. mylonites). No sound model has been proposed yet to model the flow in an anisotropic medium. For that reason, the anisotropic behaviour can only be dealt with in a qualitative manner starting from two extremes: completely isotropic versus highly anisotropic.

From the finite element modelling it is concluded that the rotational behaviour of a cylinder in an isotropic medium (power-law, n>1) is nearly equivalent to that of a cylinder in a shearing Newtonian matrix (n=1), independent of the boundary conditions. The rotation rate of a free-floating cylinder (or sphere) in a Newtonian medium is $0.5 \cdot \dot{\gamma}$ ($rad \cdot s^{-1}$; Jeffery 1922) and is the effect of the rotational component in the flow that exerts an angular momentum to the object. A deck of cards can be regarded as an example of a material with maximum anisotropy, since a stress acting normal to the cards will not deform the deck, while a shear stress acting parallel to

the cards, will make them slide past one another. Within a shearing deck of cards there is no displacement possible normal to the cards. If a cylinder were surrounded by neatly stacked cards and a shear stress acts parallel to the upper card surface, the cylinder will not rotate because velocities tangent to the cylinder surface are only found at the extreme top and bottom of the cylinder. In the limiting case therefore, the cylinder will not rotate (see figure 5.17). Clearly then, when a material is of intermediate anisotropy, the cylinder will rotate at a rate between 0.0 and $0.5 \cdot \dot{\gamma}$ ($rad \cdot s^{-1}$), when that material including the cylinder is being sheared.

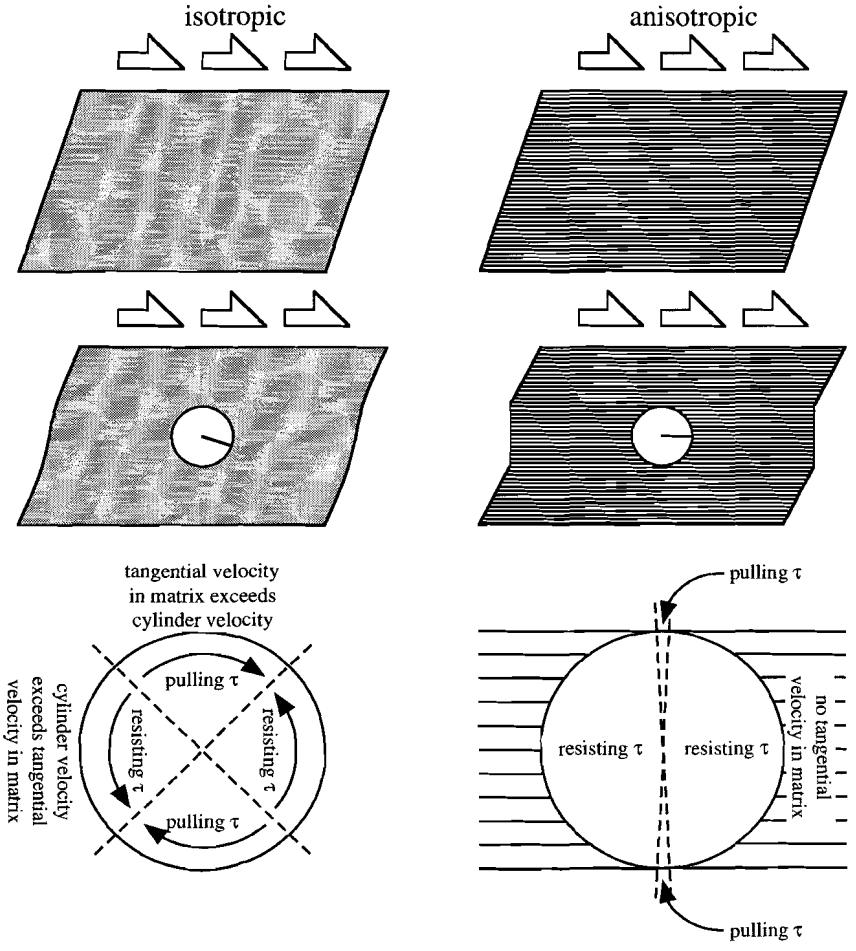

Figure 5.17. Schematic drawing shows that lack of velocity tangential to cylinder surface in anisotropic shearing matrix (right column) results in reduced rotation rate of incorporated cylinder w.r.t. isotropic matrix (left column).

5.5 Wing development around rigid objects with passively deformable mantles

The geometry of the 'wings' or material trails that develop around a rigid porphyroclast object with deformable outer margin (mantle) is directly determined by the flow pattern around the rigid porphyroclast core. During progressive deformation, individual particles trace a single stream line. However, velocities are reduced where stream lines diverge and increased where stream lines converge. Consequently, mantle deformation and shape evolution associated with the flow patterns shown in the previous sections will be complex. For that reason, a computer program has been used to study the development of deformable mantles around a cylindrical rigid objects during progressive bulk simple shear making use of the stream function method already treated, i.e. for boundaries at infinity. The method employed is similar to that used by Bjørnerud and Zhang (1995), for simulation of mantle development around a sphere, but deals with the two-dimensional case. In order to keep the mathematical description simple, the mantle is assumed passive: i.e. its behaviour is exactly the same as that of the matrix surrounding the object (see also Masuda and Ando 1988, Masuda and Mochizuki 1989). The mantle is thus comparable to a passive marker drawn on the matrix material in experimental situations, e.g., Ghosh 1975, Ghosh and Ramberg 1976, Passchier and Simpson 1986, Van Den Driessche and Brun 1987, Ildefonse and Mancktelow 1993.

The most important factor in the development of a (passive) mantle in a steady flow is the initial distribution of mantle material with respect to the flow- or stream lines (Passchier 1994). The characteristic wing geometry of a core-mantle-matrix system is primarily the result of displacements along flow lines that partly intersect both mantle and matrix material. No visible development is present for mantle material that is situated completely within a (closed) flow line, since material cannot escape the area enclosed by that flow line. Mantle material that is situated outside the area of closed flow lines (i.e. outside the separatrices) will never return to its original position and, apart from some possible approach during the early stages of shear, will keep moving away from the core. The stream line with the highest stream function value, which still touches the mantle, bounds the region where mantle material can be found during progressive deformation. When the radius of the rigid core reduces due to syn-kinematic recrystallisation or other microphysical wearing processes (Passchier and Simpson 1986), the flow pattern contracts concomitantly. As a result, mantle material that was first inside the separatrices can be located outside the separatrices.

In the following, structures developing from a cylindrical passive mantle around a cylindrical rigid core are simulated for three different flow patterns namely (1) eye-shaped, (2) bow-tie shaped with flow in the central region, and (3) bow-tie shaped with a stationary central region. These flow patterns are derived from the analytical solution (eq. 5.2) for bulk simple shear and were chosen because they represent the two end members and an intermediate value of the relative rotation rate of the object (Ω_{rel}=1.0, 0.5, 0.0). The influence of the mantle thickness at the onset of deformation ($R_m(0)$) is also examined. Aspects of core deterioration, i.e. generation of passive mantle material from the rigid core, are then considered. Finally, the significance of initial geometry and orientation of a rectangular mantle is considered.

Parameters used in the present mantle geometry development study	
$R_m(0)$	Outer radius of passive mantle (before deformation)
$R_c(t,\gamma)$	Radius of rigid core at time t or after shear strain γ ($R_c(0)$=1.0)
1+dR/dγ	Rigid core deterioration rate

5.5.1 Wing development in an initially cylindrical mantle around a cylindrical core

Consider now the results of the simulations performed for cylindrical, passive mantles of various initial thicknesses around a rigid cylindrical core. Figure 5.18 shows how these mantles, with initial thicknesses of 5, 20 and 40% ($R_m(0)$=1.05, 1.20, 1.40) of the radius of a rigid core of fixed radius ($R_c(t)$=1), develop into wings during progressive bulk simple shear. For a detailed description and the terminology of the different mantle type geometries and stair-stepping, see figure 1.1, Chapter 1. Earliest use of this terminology is found for the θ-type geometry, in Hooper and Hatcher 1988, the ϕ-type in Passchier 1994, the σ- and δ-type in Passchier and Simpson 1986. An offset in asymptotic wing level (fig. 1.1d-f) was first referred to as 'stair-stepping' by Lister and Snoke 1984.

Eye-shaped flow pattern with 'free floating' core (Ω_{rel}=1.0)

In figure 5.18a, the object has a relative rotation rate of Ω_{rel}=1.0 and the flow pattern is eye-shaped (cf. fig. 5.1a). In this flow pattern, an initial mantle thickness of at least 31% is needed in order to have mantle material outside the separatrices at the onset of deformation. A cylindrical mantle with an initial thickness of 5% of the core radius remains nearly circular in section because stream lines close to the core are almost circular. This geometry is referred to as a θ-type geometry.

Still with reference to figure 5.18a, when $R_m(0)$=1.20, the stream line with the highest stream function value that still touches the mantle (Ψ=0.1436) is an ellipse and small bulges of mantle material form during progressive deformation. The geometry evolves from a θ- to a so called early ϕ-type at γ=3. At a shear strain of 5, these bulges have developed into a recognisable winged structure (ϕ- or early σ-type). The divergence of the stream lines is most prominent at distances left and right of the rigid core. Therefore, the velocity at the wing-tips is low with respect to material closer to the core. This results in small embayments of matrix material developing between core and wing (σ- or early δ-type, γ=6). With increasing strain, the velocity at the wing-tips increases, leading to very thin, short wings and thin embayments at γ=10 (I introduce the terminology: '@-type' geometry for this shape). With ongoing deformation, the wings develop into small 'hooks' (γ=14) and eventually to very thin wings that are wrapped around the core (@-type, γ=22).

With an initial mantle thickness of 40% (fig. 5.18a), the outermost stream line that still touches the mantle (Ψ=0.3576) is situated outside the separatrices (Ψ=0.250). This means that during progressive deformation the wing tips keep moving away from the core and that the wings will thus keep stretching. The mantle material inside the stream line with stream function value 0.122, will always revolve around the core. With this initial mantle thickness, the geometry is largely determined by the flow of matrix and mantle material within the stream lines Ψ=0.122 and Ψ=0.250. At a shear strain value of 3, the geometry has developed from a θ- to a ϕ-type. At shear strains between 5 and 6, a σ-shape with rather long and thick extensions is found. The wings have inwardly curved surfaces on both sides (when such a shape is found in a naturally deformed rock it is possible that the flow will be interpreted as a σ-type indicating sinistral shear). The characteristic δ-shape with triangular embayments of mantle material starts to develop after a shear strain of 6. When a line tangent to the end of a wing does not cross the centre of the core, the wings are stair-stepping. In figure 5.18a, a straight dashed line is drawn asymptotic to the ends of both wings, for γ=10 and γ=14. Since these lines cross the centre of the core, the wings are not stair-stepping. The mantle material will eventually form very thin coils around the core (γ≥14, complex δ-type), with extremely elongated wings.

Bow-tie flow pattern with rotating core (Ω_{rel}=0.5)

In figure 5.18b, the intermediate rotation rate of the core (Ω_{rel}=0.5) is shown and the flow pattern has a bow-tie geometry (cf. fig. 5.11a). In this flow pattern, an initial mantle thickness of at least 10% is needed in order to obtain mantle material outside the separatrices at the onset of deformation. As for Ω_{rel}=1.0, an initially cylindrical mantle with a thickness of 5% remains nearly circular in section (θ-type). However, an initial mantle thickness of 20% is more than sufficient for the development of continuously stretching wings. Figure 5.18b shows that a high finite shear strain is needed before the geometry can be used as an indicator of the movement direction when when $R_m(0)$=1.20: the mantle has a nearly perfect orthorhombic symmetry up to γ=6. At a shear strain higher than 8, the symmetry of the mantle is reduced to two-fold, and the δ-shape starts to develop with continuously stretching wings. A line tangent to the end of a wing does not cross the centre of the core (shown at γ=10 and γ=12): the wings are thus stair-stepping, and step-up in the direction of movement. The matrix material will eventually form a coil around the core (complex δ-shape), but not before a very high finite strain has accumulated.

It can be seen from figure 5.18b that an orthorhombic shape symmetry is also found up to γ=5 during the development when $R_m(0)$=1.40. In fact, an initially cylindrical mantle with a thickness of more than 41% has its boundary completely outside the area of closed flow lines. This means that the central area will remain 'filled' with mantle-material, irrespective of the amount of accumulated shear (Passchier 1994). As a consequence, the typical triangular embayments of matrix material of the δ-clast can never develop into a thin coil between core and wing when when $R_m(0)\geq 1.41$. In contrast, with an initial mantle thickness of 40%, there is a small amount of matrix material enclosed in the central area with closed flow lines at the onset of deformation. This will eventually lead to δ-type geometry with a very thin coil of matrix material between core and wing.

Bow-tie flow pattern with non-rotating core (Ω_{rel}=0.0)

As the end-member situation, the mantle development around a non-rotating core is shown in figure 5.18c. In this flow, there is no area with closed flow-lines and all the initially cylindrical mantle material will eventually flow away from the core in the direction of the stretching separatrices (top-right and bottom-left of the core in dextral simple shear). The final geometry will always be a σ-type, with extensions that curve inward on both sides if shear is maintained for long enough. For an initial mantle thickness of 5%, the amount of shear needed before the σ-geometry can be distinguished is extremely high, because velocities near the core are low. In contrast, $R_m(0)$=1.20 or $R_m(0)$=1.40 already reveal the σ-type after an accumulated shear strain of 3. It is interesting to note that an initial mantle thickness of 40% can show opposite geometry, depending on the rotation rate of the core: the structure that forms with Ω_{rel}=0.0 at γ=4 is the mirror image of that obtained for Ω_{rel}=1.0 at γ=5 (compare with fig. 5.18a).

Figure 5.18 (next 3 pages). Development of initially cylindrical mantles with $R_m(0)$=1.05 (small black circle), $R_m(0)$=1.2 (white outlined circle), and $R_m(0)$=1.4 (larger black circle); Note that only $R_m(0)$=1.2 is shown for the entire sequence. Rigid (non-shrinking) cylindrical core is shaded, line in core indicates amount of rotation of the core. Bulk deformation was dextral simple shear. Finite strain (γ) for each stage as indicated. Flow patterns are shown as shaded lines, heavy lines are separatrices, Ψ-values for stream lines and cylinder surface (R_c: Ψ=0.0) are given. Dashed lines are used to clarify stair-stepping (in b), or the lack of stair-stepping (in a). Displacements were calculated with Ψ_S^d for: **(a) (next page)** Ω=-0.5; Ω_{rel}=1.0, **(b) (2nd next page)** Ω=-0.25; Ω_{rel}=0.5 and **(c) (3rd next page)** Ω=0.0; Ω_{rel}=0.0.

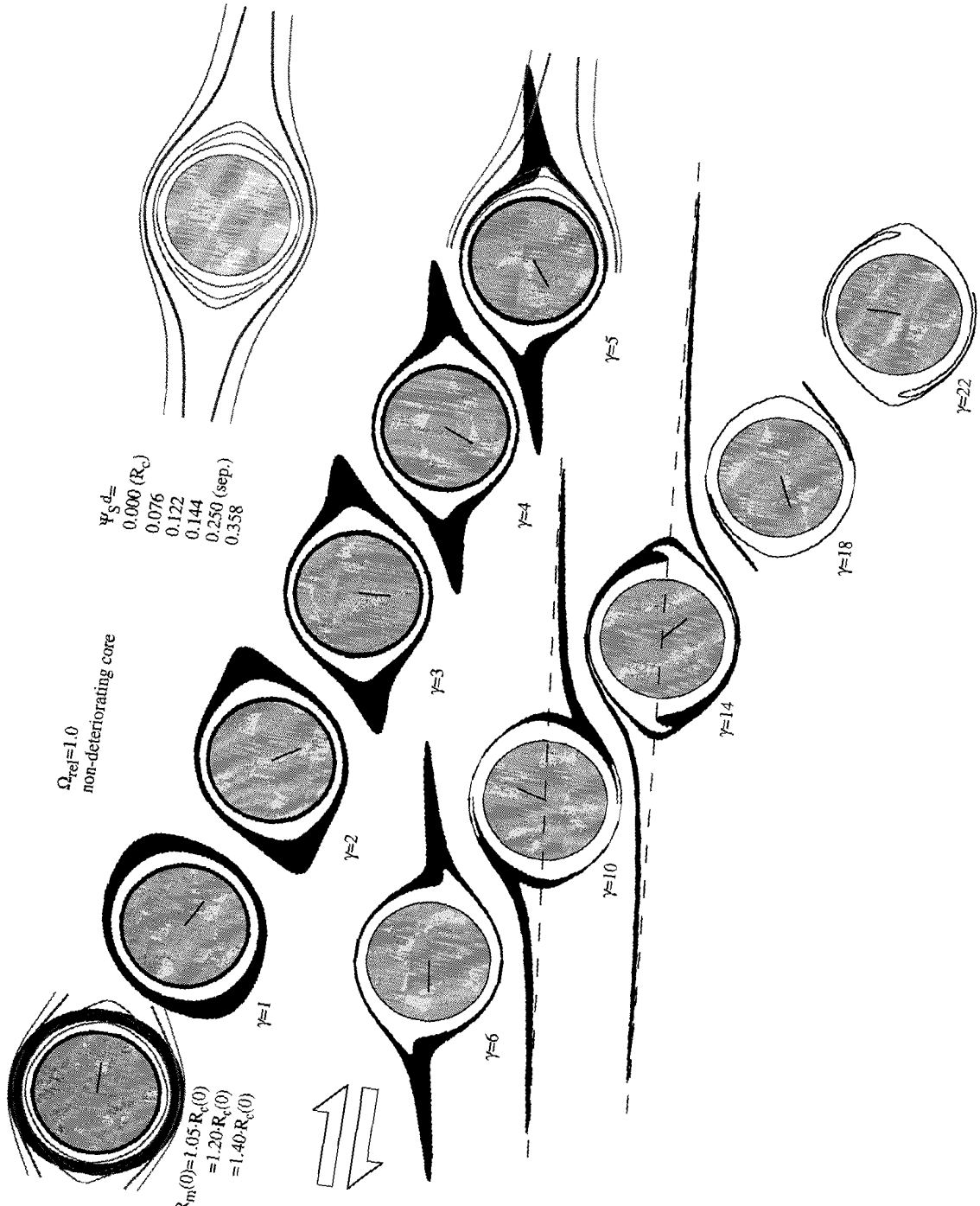
Ω_{rel}=1.0
non-deteriorating core
$R_m(0)$=1.05·$R_c(0)$
=1.20·$R_c(0)$
=1.40·$R_c(0)$
$\Psi_S{}^{d}$=
0.000 (R_c)
0.076
0.122
0.144
0.250 (sep.)
0.358
γ=1
γ=2
γ=3
γ=4
γ=5
γ=6
γ=10
γ=14
γ=18
γ=22

Figure 5.18a

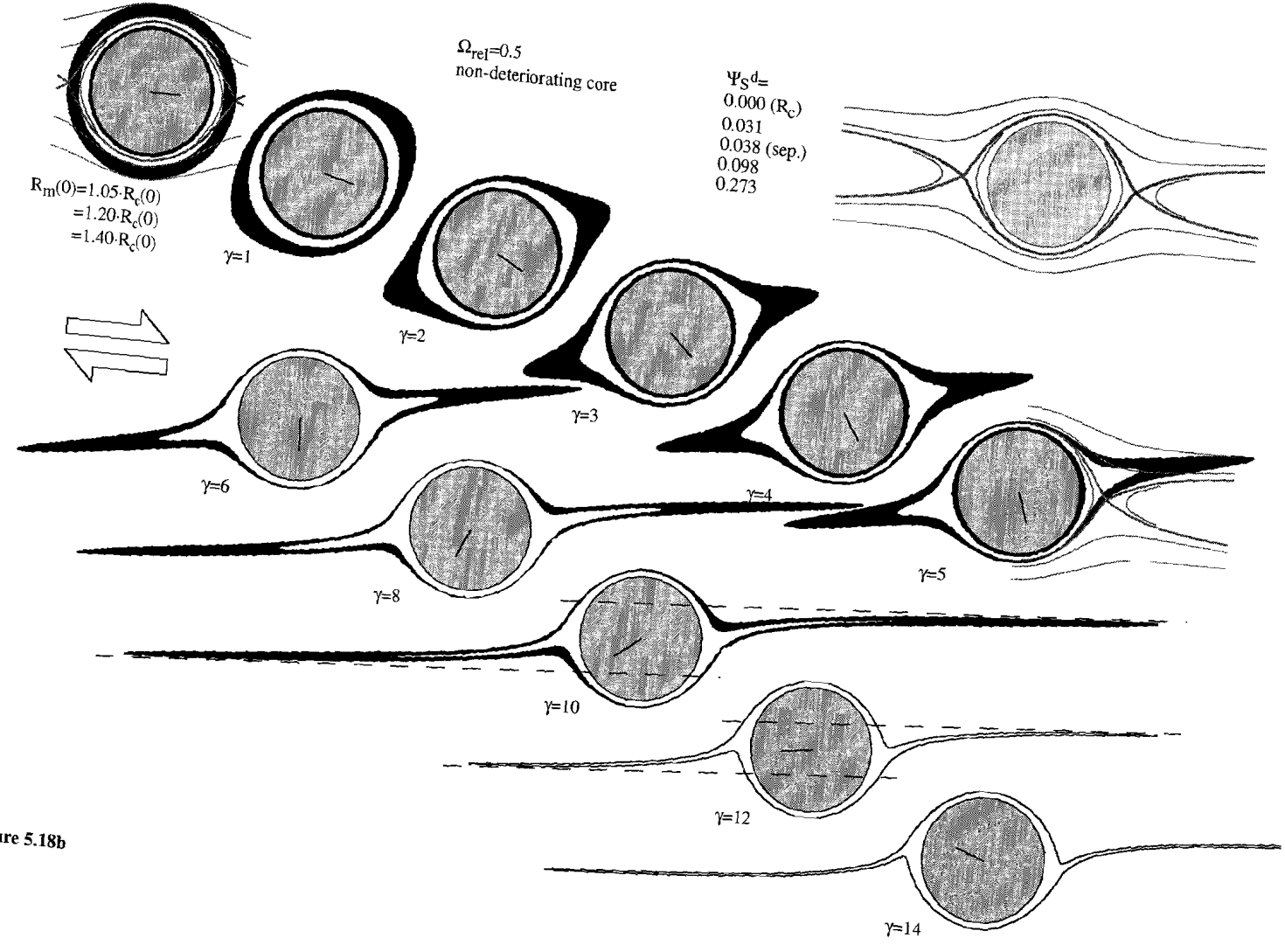
Ω_{rel}=0.5
non-deteriorating core
$\Psi_S{}^d$=
0.000 (R_c)
0.031
0.038 (sep.)
0.098
0.273
$R_m(0)$=1.05·$R_c(0)$
=1.20·$R_c(0)$
=1.40·$R_c(0)$
γ=1
γ=2
γ=3
γ=4
γ=5
γ=6
γ=8
γ=10
γ=12
γ=14

Figure 5.18b

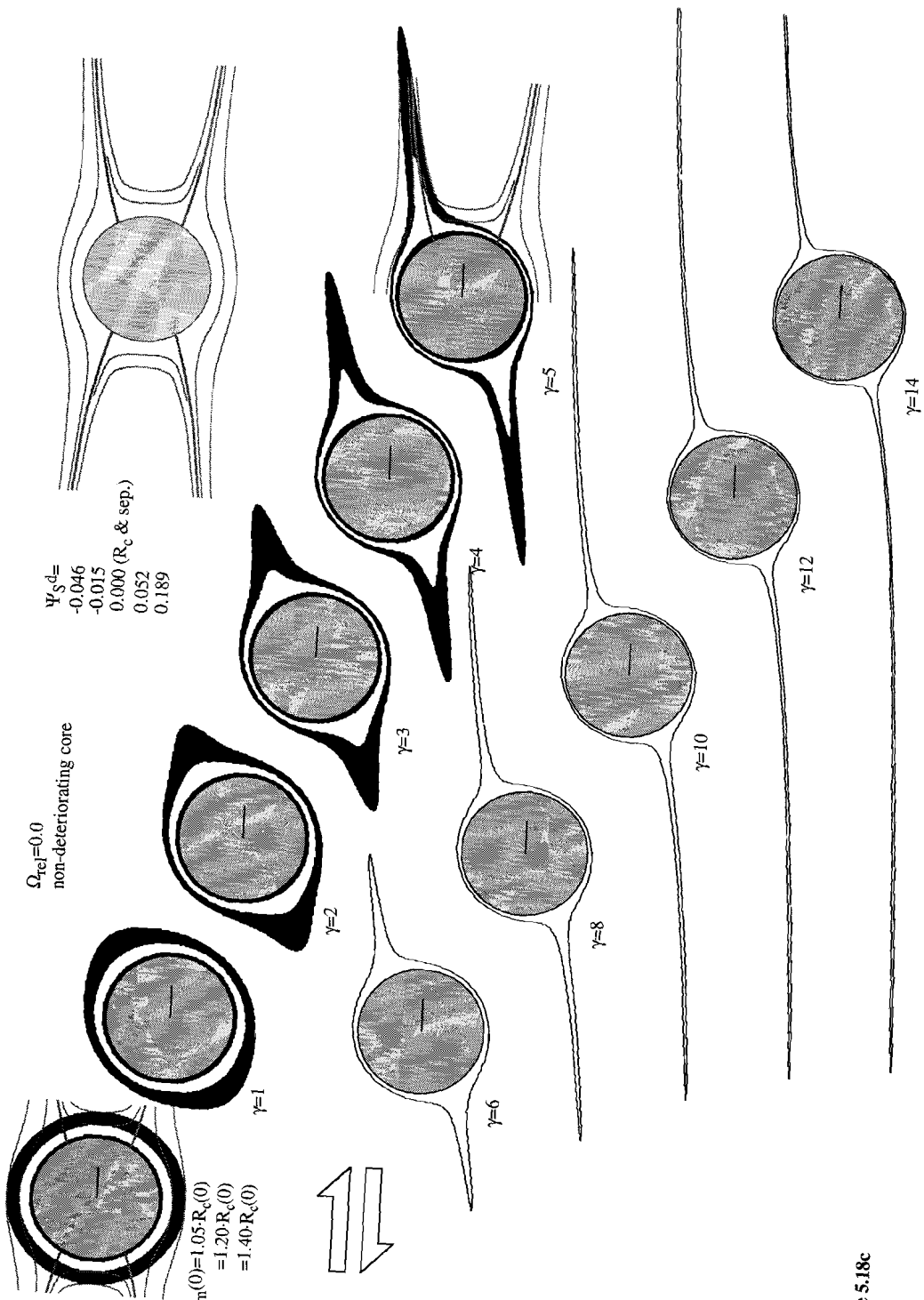
Ω_{rel}=0.0
non-deteriorating core
Ψ_Sd=
-0.046
-0.015
0.000 (R_c & sep.)
0.052
0.189
$R_m(0)$=1.05·$R_c(0)$
=1.20·$R_c(0)$
=1.40·$R_c(0)$
γ=1
γ=2
γ=3
γ=4
γ=5
γ=6
γ=8
γ=10
γ=12
γ=14

Figure 5.18c

Effect of $R_m(0)$ and Ω_{rel} on ultimate stable geometries

Figure 5.19 shows how the initial radius ($R_m(0)$) of the mantle and the relative rotation rate of the core (Ω_{rel}) are of influence on the ultimate stable geometry achieved during ongoing strain. It was constructed by graphing the z-value of the separatrix at x=0 for different values of Ω_{rel} (left curve), and the x-value of the separatrix at z=0 for different values of Ω_{rel} (right curve). It must be stressed that this figure does not represent all possible geometries during deformation but merely the ultimate stable geometries. It will be noted from figures 5.18a-c, that wing geometries can evolve through a series of (not always distinguishable) types until a stable geometric type is reached. As an example, an initial mantle radius of 1.4 around a free floating core (Ω_{rel}=1.0) shows an evolution from θ- to ϕ- (γ=3) to σ- (γ=5) and ultimately to δ-type (γ>6) during progressive shear (fig. 5.18a).

Similar examples worthy of consideration are as follows (circles in fig. 5.19):
(1) $R_m(0)$=1.4; Ω_{rel}=0.8 shows a transition from θ- to ϕ-type at a shear strain of 2. The triangular embayments that are typical for a δ-type geometry become visible at γ=12.
(2) $R_m(0)$=1.1; Ω_{rel}=1.0 still shows a θ-type geometry up to γ=20.
(3) $R_m(0)$=1.1; Ω_{rel}=0.6 starts to develop very small hooks at γ=10. When shear strain continues, the structure will eventually show a @-type geometry with extremely thin extensions of mantle material wrapped around the core.

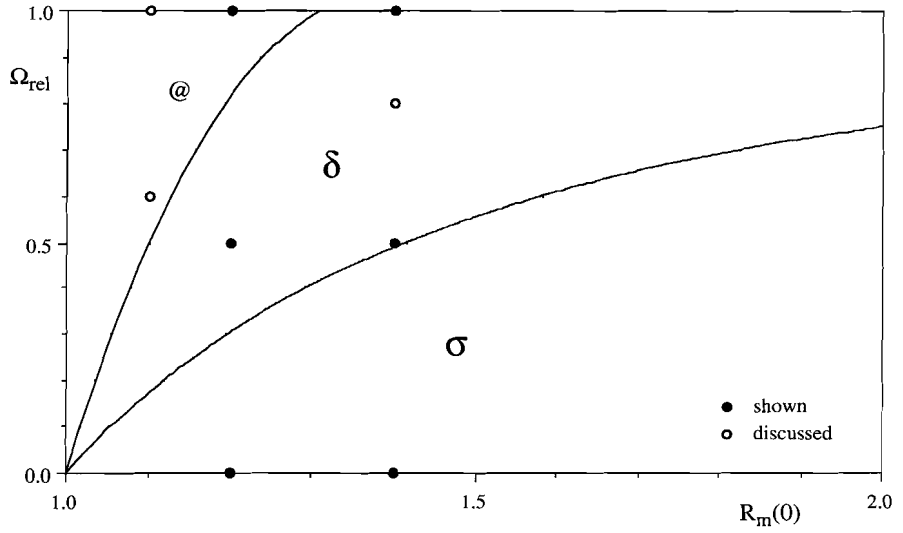

Figure 5.19. Graph showing the three fields of ultimate stable geometries for combinations of initial mantle radius ($R_m(0)$) and relative rotation rate (Ω_{rel}) in bulk simple shear deformation around a rigid, non-shrinking, cylindrical core. Heavy dots are combinations for which the evolutions are shown in figure 5.18a-c. Circles are combinations referred to in the text. See text for further explanation.

5.5.2 Wing development around a deteriorating cylindrical core

The entire picture of wing development changes when passive mantle material is formed as a result of the progressive deterioration of the rigid core, e.g. when there is no mantle material prior to the onset of deformation (Passchier and Simpson 1986). Clearly, the flow pattern will not be time-independent as long as the rigid core reduces in size. In this section, it is shown that the rate and duration of deterioration of the core exert important effects on the developing core-mantle structures in the three different flow types. In the computer program, the radius of the rigid core is reduced with each incremental step of deformation (typically $E \cdot dt=0.02$; the flow types described deal with bulk simple shear such that $E \cdot dt=d\gamma$).

Limited deterioration in an eye-shaped flow pattern with 'free floating' core ($\Omega_{rel}=1.0$)

Figure 5.20a shows the development of winged structures around a cylindrical core, rotating at $\Omega_{rel}=1.0$, that deteriorates until the diameter of the core has reduced to approximately 77% of its initial size. The sequence at the top results from a 'fast' deterioration rate ($1+dR/d\gamma$) of 0.7654, which means that the core only shrinks during the first unit of shear. At $\gamma=4$, the mantle has developed into a ϕ-type with the wing-tips just touching the separatrices. As shear strain accumulates to $\gamma=8$, a δ-shape with curved wings has started to develop. The typical triangular embayments and thin rims of matrix material between core and wings have been formed by $\gamma=12$. With progressive shear, the structure becomes more complex. Because the wing-tips touch the separatrix, they keep moving away from the core. Due to the time-dependent flow during the early stages of deformation, these wings do show stair stepping but they step down in the direction of movement (shown at $\gamma=16$).

The sequence at the bottom of figure 5.20a shows a 'slow' deterioration rate of 0.9353 meaning that the core shrinks up to $\gamma=4$, at which point a θ-shape has been formed. The sequence is quite similar to the faster deteriorating core, although the equivalent geometry requires an extra strain of about 2 to develop. At $\gamma=4$, where the flow becomes time independent, the mantle does not touch the separatrices. The typical δ-shape with triangular embayments and curved wings can now be recognised at $\gamma=10$ (not shown). During progressive shear a more complex geometry evolves but the wing tips remain closer to the core than in the faster shrinking case. Because the separatrices do not touch the mantle, the wing-tips are located in the central area with closed flow lines. At $\gamma=16$, the wing-tips are at a larger distance from the core than at $\gamma=20$. Although the wings remain short, at $\gamma=16$ they can be seen to step down in the direction of shear.

Figure 5.20 (next pages). Development of passive mantles, produced by 'recrystallisation' of an initially 'naked' cylindrical core. Mantle production ceases when the core has deteriorated to ~77% of its original size. Mantle material is black, rigid (shrinking) core is shaded, line in core indicates amount of rotation of the core. Bulk deformation was dextral simple shear. Finite strain (γ) for each stage as indicated. Flow patterns at $\gamma=4$ (mantle production has ceased) are shown as shaded lines, heavy lines are separatrices. In the top sequence of (a), and in (b) and (c), mantle production ceased at $\gamma=1$ (not shown). Dashed lines are used to clarify down-step (a) and up-step (b) of stair-stepping wings. Displacements were calculated with Ψ_S^d for: **(a)** $\Omega=-0.5$; $\Omega_{rel}=1.0$, fast deterioration rate (top sequence: $1+dR/d\gamma=0.7654$) versus slow deterioration rate (bottom sequence: $1+dR/d\gamma=0.9353$). **(b)** $\Omega=-0.25$; $\Omega_{rel}=0.5$, $1+dR/d\gamma=0.7654$ and **(c)** $\Omega=0.0$; $\Omega_{rel}=0.0$, $1+dR/d\gamma=0.7654$.

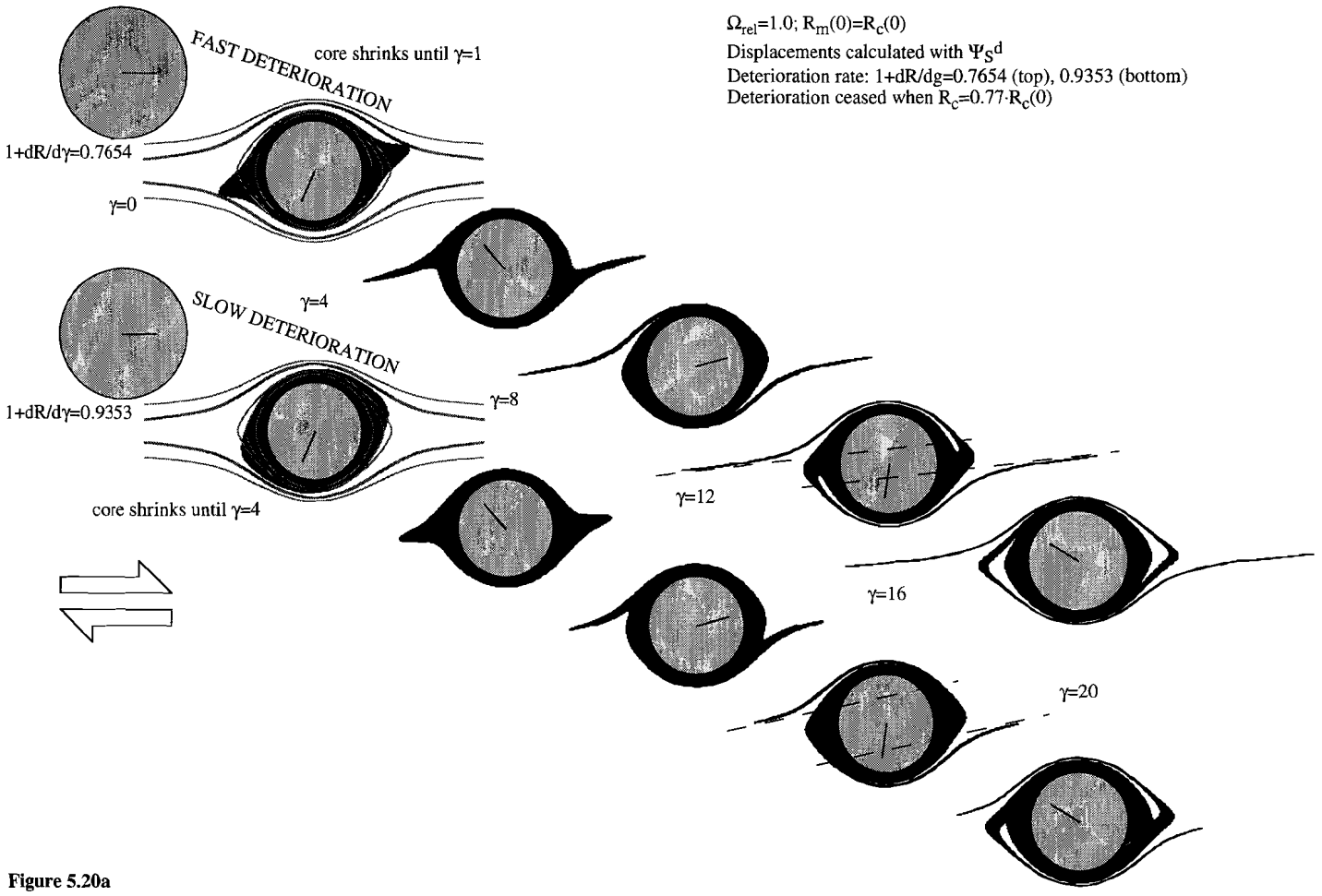
Ω_{rel}=1.0; $R_m(0)=R_c(0)$
Displacements calculated with $\Psi_S{}^d$
Deterioration rate: 1+dR/dg=0.7654 (top), 0.9353 (bottom)
Deterioration ceased when $R_c=0.77 \cdot R_c(0)$
FAST DETERIORATION
core shrinks until γ=1
1+dR/dγ=0.7654
γ=0
γ=4
SLOW DETERIORATION
1+dR/dγ=0.9353
γ=8
core shrinks until γ=4
γ=12
γ=16
γ=20

Figure 5.20a

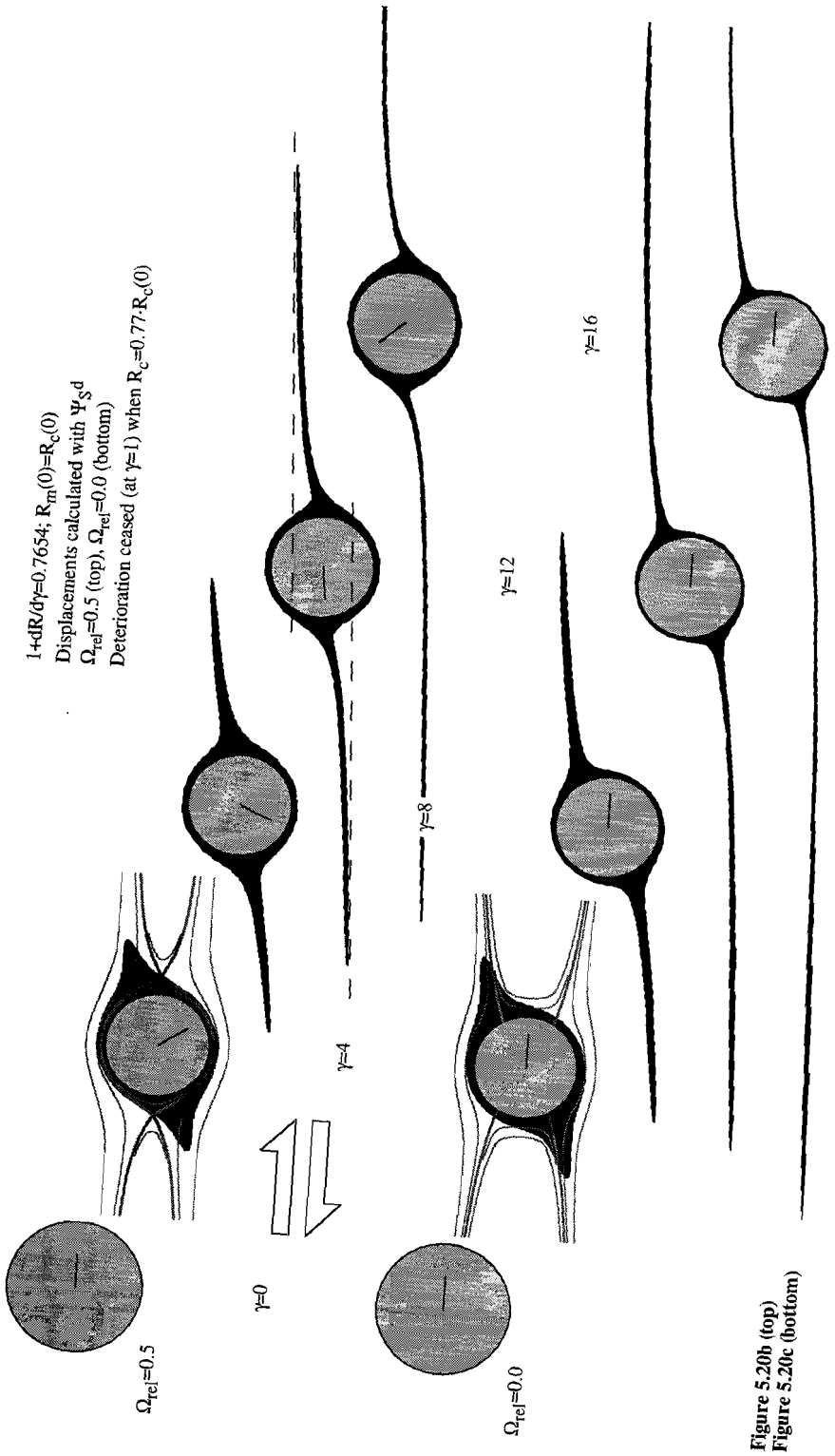

Figure 5.20b (top)
Figure 5.20c (bottom)

Limited deterioration in a bow-tie flow pattern with rotating core (Ω_{rel}=0.5)

The development of the mantle around a core rotating at half the rate of a free-floating one (Ω_{rel}=0.5) shows a similar difference between fast and slow deterioration. Again, an extra accumulated shear of 2 is needed with a slower production of mantle material to yield a given geometry. However, at γ=4 the central area with closed flow lines is completely filled with mantle material (fig. 5.20b), even at the low rate of deterioration. The result is that in both cases the wings remain stretching and thinning during ongoing deformation. At the faster rate of deterioration (1+dR/dγ=0.7654), the orthorhombic symmetry (ϕ-type) of the core-mantle structure is lost at γ=4, and the extensions gradually become stair stepping. With increasing strain, the top-right and bottom-left indentations become more distinct and the geometry starts to resemble a δ-type (γ=12). However, the thin coils of matrix material between core and wings cannot be formed in this type of flow.

Limited deterioration in a bow-tie flow pattern with non-rotating core (Ω_{rel}=0.0)

If the deteriorating core is not rotating (fig. 5.20c, Ω_{rel}=0.0, 1+dR/dγ=0.7654) the deforming mantle material shows a σ-type geometry with wings that curve inwards on both sides by γ>4. With progressive shear the wings are stretched and thinned and eventually nearly all mantle material will flow away from the core. As with the former two examples, a lower deterioration rate of 0.9353 shows similar geometries at an accumulated shear that is 2 units higher than with the faster deterioration rate.

Continuously deteriorating core

When the core is continuously deteriorating into mantle material, the geometry will always be of θ-type at the early stages of deformation, which evolving into a ϕ-type, regardless of the rotation rate of the core. Decreasing deterioration rate only increases the amount of shear needed to produce the same geometry. Obviously, the flow pattern is in this case time-dependent until the core is completely deteriorated into mantle material. A deteriorating core rotating at Ω_{rel}=1.0 (fig. 5.21a) shows an orthorhombic symmetry (θ- or ϕ-type geometry) up to high accumulated shear strains when $1+dR/d\gamma \leq 0.95$. A σ-shape just starts to develop at γ=6 when the rate of deterioration is 0.90, although the extensions of newly formed mantle material are broad with respect to the σ-geometries shown in figures 5.18c, 5.20c and 5.21c. The size of the central area with closed flow lines decreases as the core deteriorates, which prevents matrix material from curling up between core and mantle. As a result, the δ-type geometry can never be formed around a continuously deteriorating core. When the rotation of the deteriorating core is impeded (figs. 5.21b and c: Ω_{rel}=0.5 and Ω_{rel}=0.0 resp., $1+dR/d\gamma$=0.95) the developing structures are very similar to the geometries found with initially existing mantles of 40% (figs. 5.18b, c), although the shear strain has to be doubled to produce a similar geometry.

Figure 5.21 (next pages). Development of passive mantles, produced by 'recrystallisation' of an initially 'naked' cylindrical core. Mantle production is continuous. Mantle material is black, rigid (shrinking) core is shaded, line in core indicates amount of rotation of the core. Bulk deformation was dextral simple shear. Finite strain (γ) for each stage as indicated. Flow patterns are shown as shaded lines, heavy lines are separatrices. Displacements were calculated with Ψ_S^d for: **(a)** Ω=-0.5; Ω_{rel}=1.0. Three deterioration rates are shown; Top: $1+dR/d\gamma$=0.90, middle: $1+dR/d\gamma$=0.98, bottom: $1+dR/d\gamma$=0.98. **(b)** Ω=-0.25; Ω_{rel}=0.5, $1+dR/d\gamma$=0.95 and **(c)** Ω=0.0; Ω_{rel}=0.0, $1+dR/d\gamma$=0.95.

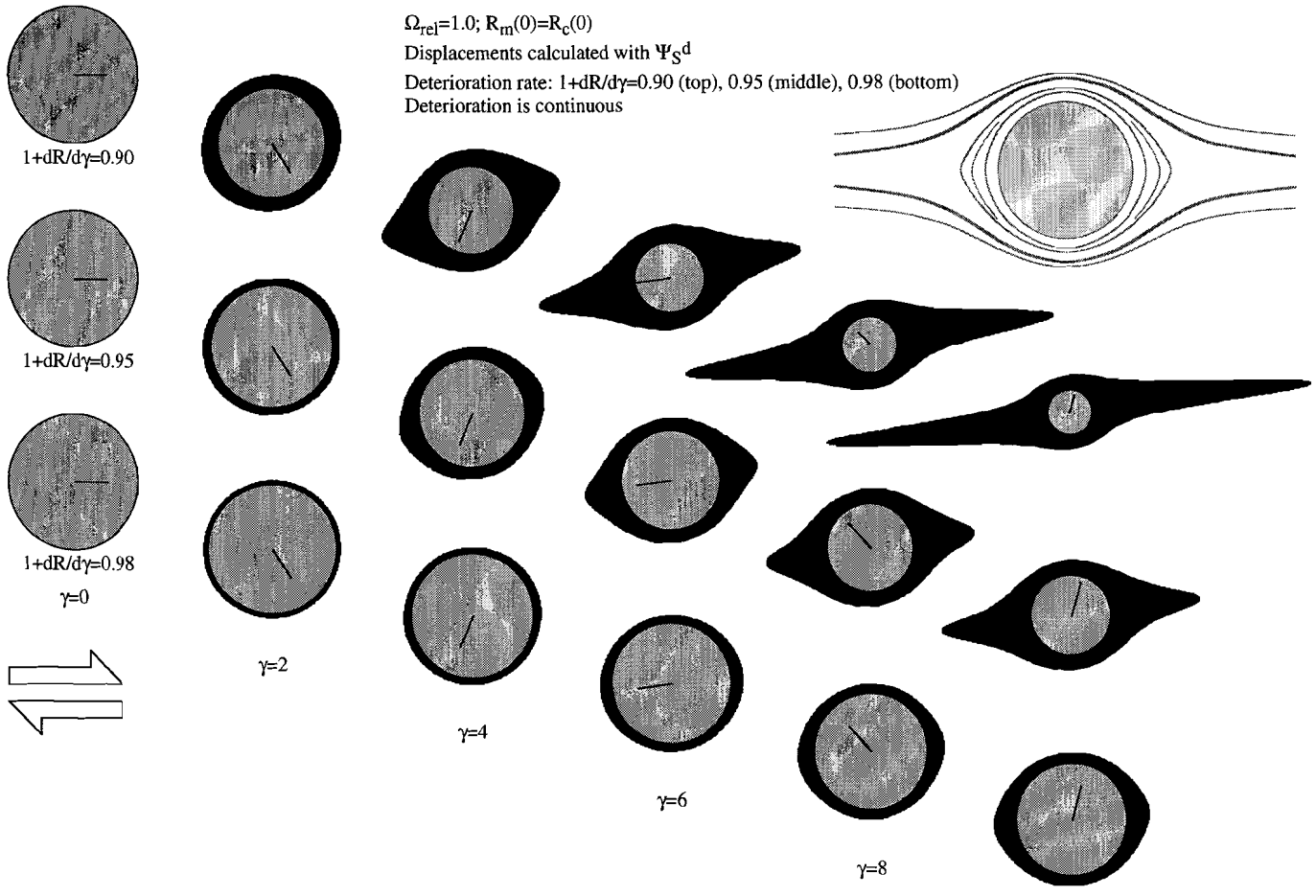
Ω_{rel}=1.0; $R_m(0)=R_c(0)$
Displacements calculated with Ψ_S^d
Deterioration rate: 1+dR/dγ=0.90 (top), 0.95 (middle), 0.98 (bottom)
Deterioration is continuous
1+dR/dγ=0.90
1+dR/dγ=0.95
1+dR/dγ=0.98
γ=0
γ=2
γ=4
γ=6
γ=8
γ=10

Figure 5.21a

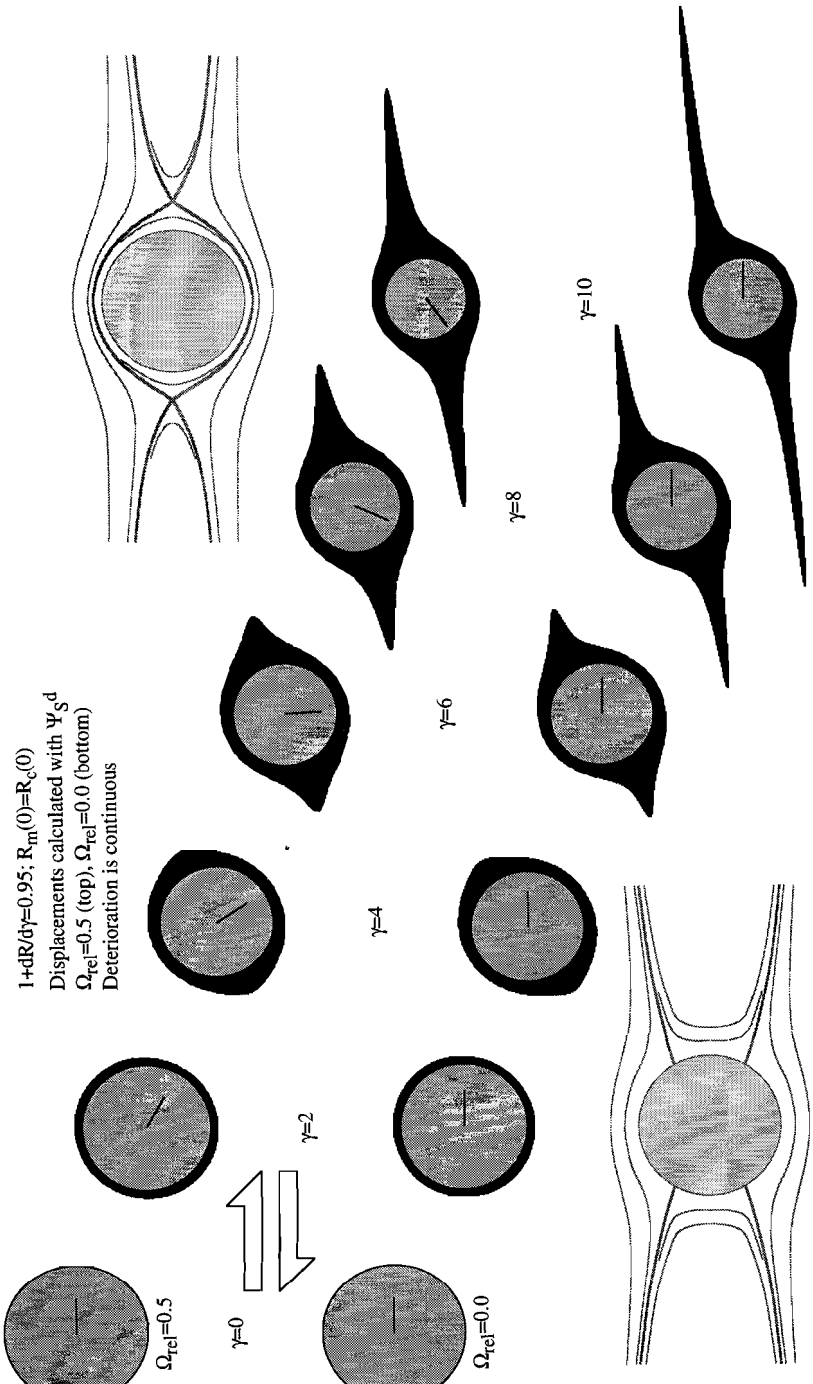

Figure 5.21b (top)
Figure 5.21c (bottom)

5.5.3 Wing development from initially square-sectioned mantles

Most clasts in a natural rock do not have a circular section prior to deformation, but rather show an angular geometry. A well developed garnet can have a sub-spherical shape, but is not commonly found as a mantled clast. Feldspar and Al-silicate porphyroclasts normally grow into rectangular prisms. The experiment described in Chapter 2 has shown that during non-coaxial flow around an initially rectangular clast, the corners are apt to deterioration. This results in a well rounded core and fine-grained clast material taken up by the matrix to form stretching wings. The aspect ratio of the initially rectangular clast remains constant after an initial increase or decrease and the size of the core is hardly affected by ongoing deformation. Unfortunately, the stream function of Bretherton does not allow for the rigid core to be elliptical. For these reasons simulation is restricted to the development of initially square-sectioned passive mantles around a circular core that does not deteriorate during deformation (i.e. is fully rigid).

Figure 5.22 shows the development of a square passive mantle around a rigid core, for three relative rotation rates of the core, when one side of the mantle is initially parallel to the direction of shear. Because the corners of the mantle just touch the separatrix for $\Omega_{rel}=1.0$ and extend well beyond the central area with closed flow lines for $\Omega_{rel}=0.5$ (and $\Omega_{rel}=0.0$), the wing-tips will keep moving away from the core during accumulation of shear. For all rotation rates of the core, the mantle evolves into two wings pointing in the same direction on either side of the clast. When $\Omega_{rel}=1.0$, the geometry has become a complex δ-type by $\gamma=8$, with stair-stepping wings that step down in the direction of shear. With a reduced rotation rate of the core ($\Omega_{rel}=0.5$), all four wings are well developed by $\gamma=8$. At $\gamma=10$, the two long wings show stair stepping (step-up in the direction of shear) and triangular embayments start to develop adjacent to the shorter extensions. Two coils of matrix material between core and wings develop on opposite sides of the core with ongoing shear. When the core is stationary ($\Omega_{rel}=0.0$), two of the corners show a clear σ-type geometry by $\gamma=2$, while the other two corners have become less angular. With increasing shear strain, the last-mentioned corners form bulges and develop into narrow, pointed and doubly bent wings by $\gamma=10$.

Figure 5.22 (next page). Development of initially square mantles with $R_m(0)=R_c(0)$, initially orientated with two sides parallel to x. Mantle material is black, rigid (non-shrinking) cylindrical core is shaded, line in core indicates amount of rotation of the core. Bulk deformation was dextral simple shear. Finite strain (γ) for each stage as indicated. Half of the flow patterns are shown at $\gamma=0$ (shaded lines, heavy lines are separatrices). Displacements were calculated with Ψ_S^d for: **(a)** $\Omega=-0.5$; $\Omega_{rel}=1.0$, **(b)** $\Omega=-0.25$; $\Omega_{rel}=0.5$ and **(c)** $\Omega=0.0$; $\Omega_{rel}=0.0$.

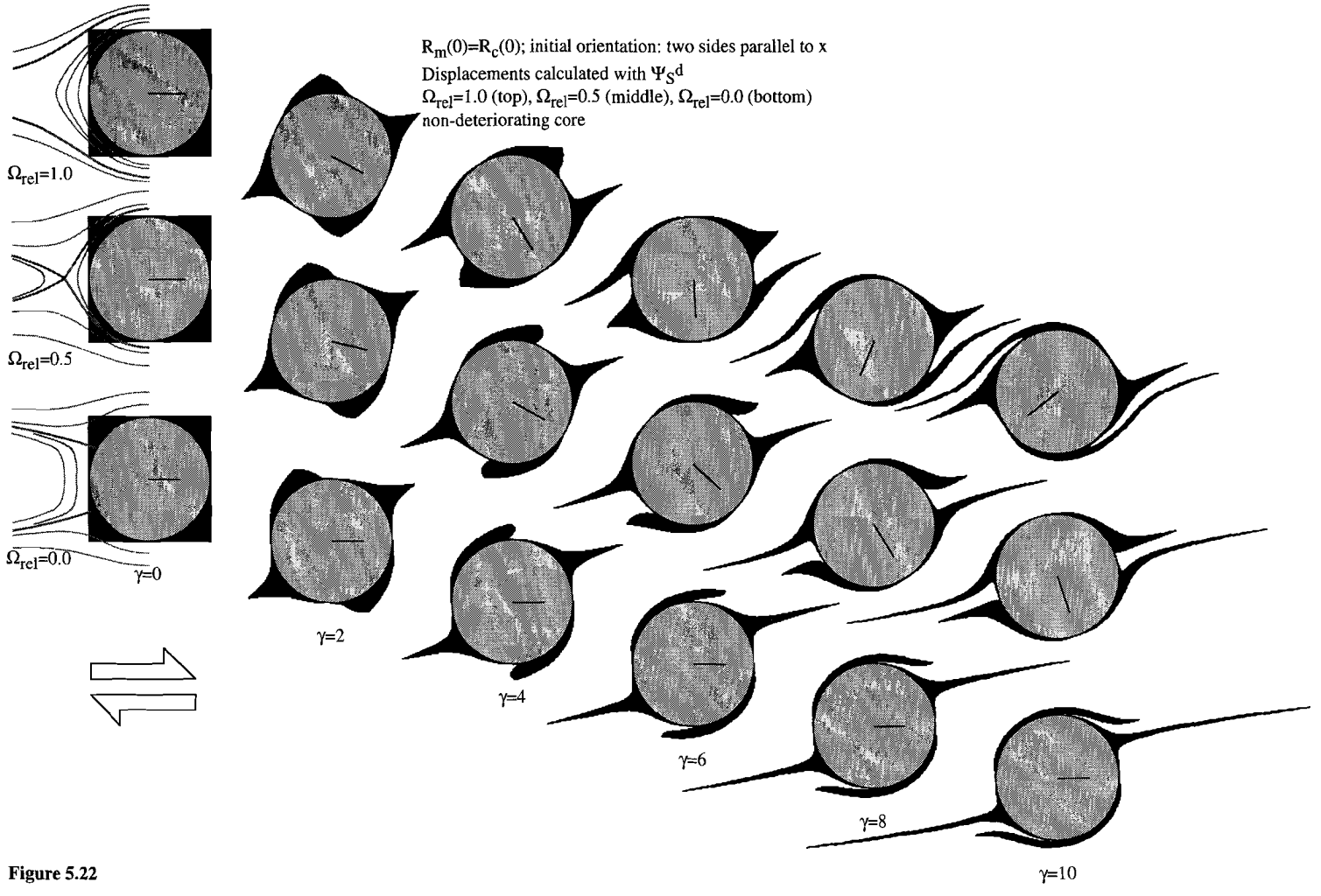
$R_m(0)=R_c(0)$; initial orientation: two sides parallel to x
Displacements calculated with Ψ_S^d
$\Omega_{rel}=1.0$ (top), $\Omega_{rel}=0.5$ (middle), $\Omega_{rel}=0.0$ (bottom)
non-deteriorating core
$\Omega_{rel}=1.0$
$\Omega_{rel}=0.5$
$\Omega_{rel}=0.0$
γ=0
γ=2
γ=4
γ=6
γ=8
γ=10

Figure 5.22

The development of an initially square-sectioned passive mantle in an initial 45° orientation is shown in figure 5.23. When Ω_{rel}=1.0, only two of the corners extend beyond the separatrices. These two corners will continue to move away from the core with on-going deformation. However, since the other two corners are in the central area with closed flow-lines, they will always remain close to the core and eventually form an @-type geometry within the δ-type geometry of the other two wings. When the core has an impeded rotation rate (Ω_{rel}=0.5), the left and right corners of the mantle are positioned exactly at the stagnation points and, as a consequence, the wing-tips remain stationary; thus when $\gamma \geq 10$, the wings show an @-type geometry. In contrast, the top and bottom corners stretch and thin with accumulating strain to form a stair-stepping δ-type geometry when $\gamma \geq 8$. Because of the square shape at the start of deformation, the stretching wings remain relatively straight up to very high shear strains. With a stationary core (Ω_{rel}=0.0) the left and right corners are located in the back-flow regions of the flow pattern and the wing-tips start to move in a sinistral sense within the overall dextral shear, forming a σ-type configuration by γ=6. At the same time, the top and bottom corners are sheared dextrally to form straight and thin σ-type wings.

5.5.4 Summary of main trends and diagnostic features

It is clear from the above that a large number of parameters influence the final geometry of a core-mantle-matrix system, and that small changes in individual parameters can have an important effect on the shape of the developing wings. Although the effect of various parameters have been shown, §5.5 does not give a complete overview of all possibilities. In general, the trends 1 to 8 are observed for mantles that are initially circular-sectioned:

(1) The orthorhombic symmetry, formed during the early stages of deformation, is maintained up to a shear strain value of at least 4 when $\Omega_{rel} \geq 0.5$.

(2) A δ-type geometry can only be formed around a core that is rotating at $\Omega_{rel} \geq 0.5$, in bulk deformation with $0.5 < |W_k| \leq 1$, when a large amount of strain has accumulated. It reflects a relatively thin mantle, that is either pre-existing or the result of a ceased syn-kinematic recrystallisation of the core. A pre-existing mantle results in stair-stepping wings that step-up in the direction of shear. A δ-clast with stair-stepping wings that step-down in the direction of shear is indicative of an initially 'naked' core that has deteriorated during an early stage of deformation. When the rate of deterioration decreases, the down-step of the wings increases.

(3) A δ-type geometry represents the ultimate shape in the evolutionary sequence during progressive deformation: from θ- via φ- and σ- to δ-type.

(4) When mantle thickness exceeds a certain value (which is a function of Ω_{rel}), the σ-type is the ultimate geometry possible, even at very high accumulated strains. A σ-type geometry with long and thin extensions, can only be the result of a core with an impeded rotation rate ($\Omega_{rel} \leq 0.5$).

(5) Relatively thin mantles can only develop extended wings when the core has a reduced relative rotation rate ($\Omega_{rel} < \sim 0.5$). Reduced mantle thickness favours the development of @-type geometries.

(6) A decrease in relative rotation rate ($\Omega_{rel} < 1$) decreases the maximum width of the mantle that may eventually lead to a δ-type geometry. When the mantle completely fills the central area

Figure 5.23 (next page). As figure 5.22 but initial orientation is now 45°.


$R_m(0)=R_c(0)$; initial orientation: sides at 45° to x
Displacements calculated with Ψ_S^d
$\Omega_{rel}=1.0$ (top), $\Omega_{rel}=0.5$ (middle), $\Omega_{rel}=0.0$ (bottom)
non-deteriorating core
$\Omega_{rel}=1.0$
$\Omega_{rel}=0.5$
$\Omega_{rel}=0.0$
γ=0
γ=2
γ=4
γ=6
γ=8
γ=10

Figure 5.23

with closed flow-lines, no thin coils of matrix material can form in between core and wings. Consequently, under no conditions will these coils develop (@- or δ-type) around a non-rotating core.

(7) When the kinematic vorticity number of the flow ($|W_k|$) decreases, any tendancy towards stair-stepping of wings is less pronounced and φ-type geometries are stable up to very high accumulated strains.

(8) Complex (double-winged) geometries, reflect an angular-sectioned initial shape or possibly a second event of mantle material production. Initially square mantles around a rigid circular core develop into geometries with two wings on either side of the core. The distance of the individual wing-tips to the core is related to the initial orientation of the mantle. Circular-sectioned cores that have a single phase of mantle material production cannot develop multiple wings on either side of the core.

(9) The @- and δ-type geometries are reliable shear sense indicators. The shear sense can be determined from the way in which matrix material coils between core and wings. The σ-type geometry with very short wings (e.g. $R_m(0)=1.2$, $\gamma=4$-6, fig. 5.18a) or with wings that are broad near the core (e.g. $R_m(0)=1.4$, $\gamma=4$-6, fig 5.18a) formed in dextral simple shear, may be interpreted to have been formed by sinistral simple shear at a (counter-clockwise) angle to the x-direction. These σ-type geometries should, therefore, not be used as a shear sense indicator when other kinematic information is absent. The σ-shaped geometries with wings that are thin close to the core are reliable sources for sense of shear determination.

5.6 General discussion

5.6.1 Flow-pattern

The absence of influence of the relative shear zone width (SW_{rel}) in the finite element modelling (FEM) is in contrast to the results of the experiments reported in Chapter 4. There, a significant effect of SW_{rel} was found, even when the Newtonian liquid (glycerol; n=1) was used as matrix. It is feasible that the assumption of incompressibility of the matrix, as used in the FEM, does not exactly represent natural and experimental deformation since no material exists that is completely incompressible. Furthermore, it is likely that the free surface of the liquids was not completely flat during the experiments reported in Chapter 4. In that case, flow was not restricted to two-dimensions, and consequently, the flow did not represent a two-dimensional incompressible deformation. Therefore, the experimental conditions do not exactly match the FEM-boundary conditions and constraints. However, it appears unlikely that stowage of the fluid near the object, which would result in a non-flat surface, is responsible for the reported large difference in flow pattern; severe bulging of the fluid would have been noticed. Gravitational forces counteract the bulging effect of stowage in the fluid. Hence, the effect of stowage should decrease with decreasing shear strain rate, but this has not been investigated.

An eye-shaped flow pattern, characterised by a central region of limited extension in the x-direction, is used in the literature to illustrate mantle-geometry development (Passchier and Sokoutis 1993, Passchier *et al.* 1993, Passchier 1994). Theoretically, this particular flow pattern, where the separatrices terminate on a line of immobile points, is non-existent. However, it is possible that strain partitioning in natural rocks allows for this kind of flow perturbation.

An eye-shaped flow pattern can only result around a circular object subjected to bulk simple shear flow (flow with a kinematic vorticity number: $W_k=1$). When $0 \leq W_k < 1$, the resulting flow pattern has two flow-apophyses (without object. With an object, it has four flow-apophyses that

originate (or end) on the object surface; see fig. 5.10) and will thus resemble a bow-tie. The back-flow regions of these bow-tie flow patterns keep increasing in width away from the clast. The amount of divergency of the back-flow-separatrices increases to 90° when W_k decreases to 0.

Preliminary examination of three-dimensional bulk simple shear flow around a sphere, has shown that the central area with closed flowlines contracts with respect to the 'two-dimensional' cylinder case (Appendix; see fig. 5A.1). For 'free floating' objects (Ω_{rel}=1.0), the separatrices intersect the z-axis at ±~1.3 times the diameter of a rigid cylinder and at ±~1.2 times the diameter of a rigid sphere. When the relative rotation rate of the object decreases (Ω_{rel}<1.0), the height of the central area is reduced around both cylinder and sphere. The decrease in height is not linearly related to Ω_{rel}.

5.6.2 Object rotation rate

Power-law behaviour of the matrix and the presence of nearby shear zone walls, have both been rejected as possible causes for object rotation rates lower than that of a free floating cylinder in a Newtonian matrix (Ω_{rel}<1). In materials that show increasingly anisotropic behaviour during deformation, the strain rate will be inhomogeneously distributed throughout the total volume of deforming material. This strain partitioning has been used as explanation for the non-rotation of porphyroblasts (crystals that grow) found within a bulk simple shearing environment in natural rocks (Bell 1985, Bell *et al.* 1986, 1989, 1992a, Bell & Johnson 1989, 1992, Bell & Hayward 1991). In their argument, the strain is partitioned in high strain zones containing phyllosilicates and/or graphite and low strain zones containing quartz, feldspar, garnet and staurolite, for example. The phyllosilicate domains are thought to result from preferential dissolution of non-phyllosilicates in regions with a large component of simple shear deformation. These domains are in contrast to the areas that are 'protected' against simple shear deformation by the presence of relatively large, strong grains and which deform, if at all, by a large component of shortening (pure shear). Due to the layered crystal structure, phyllosilicates and graphite can accommodate progressive shear without necessarily building up large dislocation density gradients within grains. However, most silicates and oxides cannot accommodate strain transitions within grains without associated dislocation density gradients, and hence are susceptible to dissolution and solution transfer. As a consequence, zones of progressive shearing become zones of dissolution of most minerals, and of concentration of phyllosilicates and graphite. Therefore, strain partitioning in most natural rocks results in an anisotropic matrix and hence, a reduced rotation rate of embedded objects, even when the matrix around the larger inclusions is homogeneous at the larger scale prior to deformation.

Although Bell and his colleagues present a strong argument for non-rotation of porphyroblasts by showing that the inclusion trails of numerous blasts have similar orientations over a large area, it must be emphasised that rotation during early stages of the deformation cannot be ruled out. This early rotation of inclusions is supported by the pAA experiments (Chapter 4), where rotation rates of the objects at the start of deformation are equivalent to those of free floating objects in a Newtonian (liquid) medium. When the shearing motion is continued, the anisotropy, and hence the strain gradient, increases until a new stable state is reached at which the object has a steady but reduced rotation rate. Similar processes may take place in a natural rock when progressive deformation causes the development of an anisotropic fabric.

5.6.3 Porphyroclast geometry

A passive mantle that is formed from a 'recrystallising' core, has been simulated experimentally for a 'two-dimensional' cylinder by Passchier and Simpson (1986), and numerically for a sphere by Bjørnerud and Zhang (1995). From these simulations it was concluded that high recrystallisation rates[5] favour the development of σ-type porphyroclast geometries, and that δ-type geometries can only result from a combination of high shear strain and low recrystallisation rate. These findings are in agreement with the results presented in this Chapter. However, for the development of a δ-clast, §5.5.2 shows it is not necessary that an elliptical mantle exists prior to flow in the matrix, as was suggested by Bjørnerud and Zhang (1995). An initially 'naked', circular-sectioned core, that forms passive mantle material by recrystallisation during deformation, can evolve to a δ-type geometry when recrystallisation ceases during continues flow (fig. 5.21a,b). The idea of changes in dynamic recrystallisation rate was addressed by Bjørnerud and Zhang (1995), who suggested that it could result from significant strain softening (with concomitant increase in shear strain rate), or changes in metamorphic conditions (with accompanying decrease in recrystallisation rate).

The @-type geometry, reported in this Chapter (fig. 5.18a) is not in accordance with Passchier (1994), who argued that a thin mantle, located entirely in the central flow region with closed flow lines, will remain a θ-type, irrespective of the amount of accumulated shear strain. However, the experimental observations of Passchier and Sokoutis (1993), used to substantiate this argument, were not based on entirely passive mantles. Although the passive mantle modelling indicates the development of @-type geometries, the 'stiffness' of the mantle (due to a competence contrast) will inhibit such a @-type development and hence, a θ-type geometry results.

Reliable shear sense indicators are δ- and @-type porphyroclasts, and σ-type clasts when wings are either longer than twice the diameter of the core or when wings are narrow at the side of the rigid core. The @-type geometry is not likely to develop in a natural rock and has not been mentioned or shown before in geological reports.

In relation to the non-passive mantles, experimentally modelled by Passchier and Sokoutis (1993), it must be realised that when the mantle has high effective viscosity (η_{eff}), the separatrix expands (the effective core diameter increases). Therefore, the development of θ-geometries is favoured when η_{eff} is very high, while the development of σ- and δ-geometries is more likely when η_{eff} is lower.

In intermediate flow ($0<W_k<1$) around a 'free-floating' object ($\Omega_{rel}=1$), the flow pattern has a distinct bow-tie shape. In spite of this flow pattern, stair-stepping will be less well developed and evolution to ϕ-type geometries is favoured, as was predicted by Passchier (1994) (see figure 5.24).

The presence of shear zone walls at relatively short distance to a porphyroclast results in a bow-tie flow pattern and, therefore, causes stair stepping of wings on developing δ-clasts. The rheological properties of the matrix have only a minor effect on the flow geometry. Stair-stepping of the wings of a δ-type porphyroclast can, consequently, not be used a a gauge for stress sensitivity of strain rate, as was suggested by Passchier *et al.* (1993).

---

[5] For comparison: The values ($\dot{R}$ / $\dot{\gamma}$)=0.13, 0.066 and 0.033 (as used for fig. 8 in Passchier and Simpson, 1986) relate to the values (1+dR/dγ)=~0.91, 0.95 and 0.98 resp.. The dimensionless ratio of recrystallisation rate to shear rate of 0.25 (as used for fig. 2a-h in Bjørnerud and Zhang, 1995) is approximately equivalent to (1+dR/dγ)=0.95.

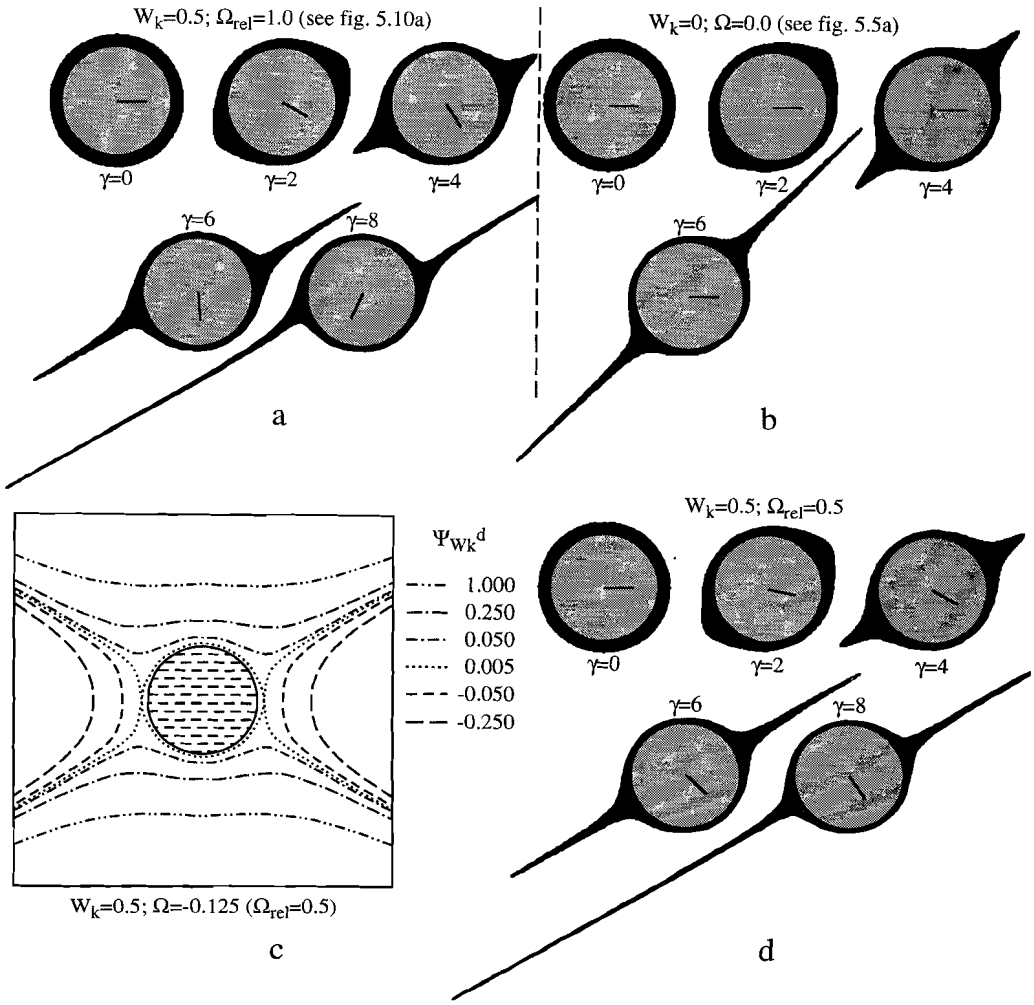

Figure 5.24. Sequences of mantle development from initially cylindrical mantles with $R_m(0)=1.2 \cdot R_c(0)$ around a (non-shrinking) rigid core in flow with $W_k=0.5$, compare to figure 5.18. Displacements were calculated using $\Psi_{Wk}{}^d$. Stream lines with $\Psi=0.005$ represent the separatrices.

In three dimensions, the separatrices in the xz-plane, bounding the central flow region with closed flow lines, are closer to the surface of a sphere than to the surface of a cylinder of the same diameter (Appendix; fig. 5A.1). For that reason, a mantle on a sphere may form extending wings whereas a mantle of equivalent thickness on a cylinder will remain close to the rigid core. Although the primary features of the flow pattern around a cylinder and a sphere are similar, the results of mantle development around a cylinder, as presented in this Chapter, cannot be directly applied to mantle development around a sphere.

5.7 Conclusions

The stream function is a simple starting point for the investigation of two-dimensional flow around rigid cylinders. The velocity field that is obtained from the stream function has been used to model the development of passive mantles around rigid cylinders (or in 3D for spheres). Disadvantages of the stream function are that the flowing medium must be Newtonian and that boundaries of the system are at infinite distance from the origin.

Finite element modelling (FEM) has been used to investigate non-Newtonian flow around semi-rigid objects and allows for boundaries located at short distance from the embedded object. Disadvantages of FEM are the need for powerful computers and the difficulties encountered when boundary-conditions and constraints must be defined. Presently, it is impossible to incorporate all the characteristics of a natural rock in the FEM, e.g. anisotropy development.

Anisotropy (development) in the matrix, which results in strain and strain rate partitioning, is a potential cause for a reduced rotation rate of an object that is embedded in a deforming matrix. Both power-law behaviour of the matrix, and the presence of nearby rigid shear zone walls, have been rejected as possible explanations for reduced rotation rates.

A large number of conditions and parameters influence the final geometry of a core-mantle-matrix system that is subjected to deformation. For bulk simple shear, the most prominent condition is the distribution of mantle material with respect to the surface that bounds the region near the core where flow is closed, i.e., where material can return eventually to its initial position. This condition is directly related to the shape and effective thickness of the mantle with respect to the (relatively) rigid core at any time, and hence, to the rate at which the core material is being transformed into mantle material. Secondly, significant differences in geometry are to be expected from changes in the amount of accumulated shear strain; with increasing deformation, the geometry can evolve from one type to another. Furthermore, a low rotation rate of the core relative to the rotational component of the flow (Ω_{rel}), may prevent the development of certain geometry-types. Finally, a difference in type of flow, e.g., when bulk deformation has a smaller rotational component than that of simple shear (kinematic vorticity number: $0<|W_k|<1$), will result in changes in the developing geometry. General trends can be distinguished (§5.5.4), but it is not feasible to attach specific meaning to each type of evolved geometry, since certain geometries can result from different combinations of parameter-values.

Considering that the trends were found for simplified systems, application of these trends to the interpretation of winged structures in deformed rocks is problematic, and is best limited to the determination of sense of shear and to estimate a possible minimum strain value.

5A.1 Strain rates from the stream function

The strain rate tensor ($\dot{\varepsilon}_{ij}$) is the symmetric part of the velocity gradient tensor (L_{ij}). The velocity gradient tensor is defined as:

$$\dot{x}_i (= v_i) = L_{ij} x_j, \qquad \text{A5.1}$$

in which:

$$L_{ij} = \begin{bmatrix} L_{11} & L_{12} \\ L_{21} & L_{22} \end{bmatrix} = \frac{dv_i}{dx_j}. \qquad \text{A5.2}$$

Since the velocities v_i in the x and y direction are defined by the derivatives of the stream function in Cartesian co-ordinates (§ 5.2) we can write:

$$v_x = \frac{d\Psi}{dy} \text{ and } v_y = -\frac{d\Psi}{dx}. \qquad \text{5.1a}$$

It is thus possible to calculate the strain rate tensor ($\dot{\varepsilon}_{ij}$), from the stream function since:

$$\dot{\varepsilon}_{ij} = \tfrac{1}{2}\left(\frac{dv_i}{dx_j} + \frac{dv_j}{dx_i}\right) \text{ which yields:} \qquad \text{A5.3}$$

$$\dot{\varepsilon}_{11} = \tfrac{1}{2}\left(\frac{dv_1}{dx_1} + \frac{dv_1}{dx_1}\right) = \frac{dv_1}{dx_1} = \frac{d\left(\frac{d\Psi}{dx_2}\right)}{dx_1} = \frac{d^2\Psi}{dx_1 dx_2}, \qquad \text{A5.3a}$$

$$\dot{\varepsilon}_{12} = \dot{\varepsilon}_{21} = \tfrac{1}{2}\left(\frac{dv_1}{dx_2} + \frac{dv_2}{dx_1}\right) = \tfrac{1}{2}\left(\frac{d\left(\frac{d\Psi}{dx_2}\right)}{dx_2} + \frac{d\left(-\frac{d\Psi}{dx_1}\right)}{dx_1}\right) = \tfrac{1}{2}\left(\frac{d^2\Psi}{(dx_2)^2} - \frac{d^2\Psi}{(dx_1)^2}\right), \qquad \text{A5.3b}$$

$$\dot{\varepsilon}_{22} = \tfrac{1}{2}\left(\frac{dv_2}{dx_2} + \frac{dv_2}{dx_2}\right) = \frac{dv_2}{dx_2} = \frac{d\left(-\frac{d\Psi}{dx_1}\right)}{dx_2} = -\frac{d^2\Psi}{dx_1 dx_2}. \qquad \text{A5.3c}$$

From equations A5.3a and A5.3c, it is clear that $\dot{\varepsilon}_{11} = -\dot{\varepsilon}_{22}$ which makes the volumetric strain rate ($\dot{\varepsilon}_v = \dot{\varepsilon}_{11} + \dot{\varepsilon}_{22}$) equal to zero, this is consistent with the fact that the 2D stream function is area conservative by definition. This means that the deviatoric strain rate tensor $\dot{d}_{ij} = \dot{\varepsilon}_{ij} - \delta_{ij}\dot{\varepsilon}_v = \dot{\varepsilon}_{ij}$. The deviatoric strain rate tensor ($\dot{d}_{ij}$) represents the shape-change rate of the deformation and can be plotted as a circle with the centre at the origin in $\dot{\varepsilon}$-ω Mohr space (Passchier 1987a). Following the convention presented by Passchier (1987a), the stretching rate factor (S) of the deformation is the diameter of the Mohr-circle and is related to $\dot{d}_{ij}$ ($=\dot{\varepsilon}_{ij}$ in this case) by:

$$S = \sqrt{(\dot{\varepsilon}_{11} - \dot{\varepsilon}_{22})^2 + (-\dot{\varepsilon}_{21} - \dot{\varepsilon}_{12})^2} = 2\sqrt{\dot{\varepsilon}_{11}{}^2 + \dot{\varepsilon}_{12}{}^2}. \qquad \text{A5.4}$$

S is the value that has been used to plot the strain rate ($\dot{\varepsilon}$) in §5.2 and §5.3.

5A.2 Three-dimensional flow around a sphere

For the purpose of assessing the applicability of the results of the two-dimensional cylinder model to the interpretation of three-dimensional porphyroclast geometries, it is important to compare 2D-flow patterns to 3D-flow patterns. A new approach to a 3D-analysis has recently been attempted by Bons (pers. comm. 1996) for bulk simple shear flow around a sphere rotating with an arbitrary Ω_{rel}. The following equations describe the velocity field in the matrix around a sphere of unit radius, subjected to bulk dextral simple shear flow with the xy-plane as shear plane:

$$\frac{v_x(\Omega_{rel})}{E} = z + \frac{5x^2z}{2}\left(\frac{1}{r^7} - \frac{1}{r^5}\right) - \frac{z}{2r^3}(1-\Omega_{rel}) - \frac{z}{2r^5} \qquad \text{(A5.5a)}$$

$$\frac{v_y(\Omega_{rel})}{E} = \frac{5xyz}{2}\left(\frac{1}{r^7} - \frac{1}{r^5}\right) \qquad \text{(A5.5b)}$$

$$\frac{v_z(\Omega_{rel})}{E} = \frac{5xz^2}{2}\left(\frac{1}{r^7} - \frac{1}{r^5}\right) - \frac{x}{2r^3}(1-\Omega_{rel}) - \frac{x}{2r^5} \qquad \text{(A5.5c)}$$

Here, $r = \sqrt{x^2 + y^2 + z^2}$, and $r \geq 1$. The equations A5.5a-c, kindly provided by Bons, have been used to construct figure 5A.1.

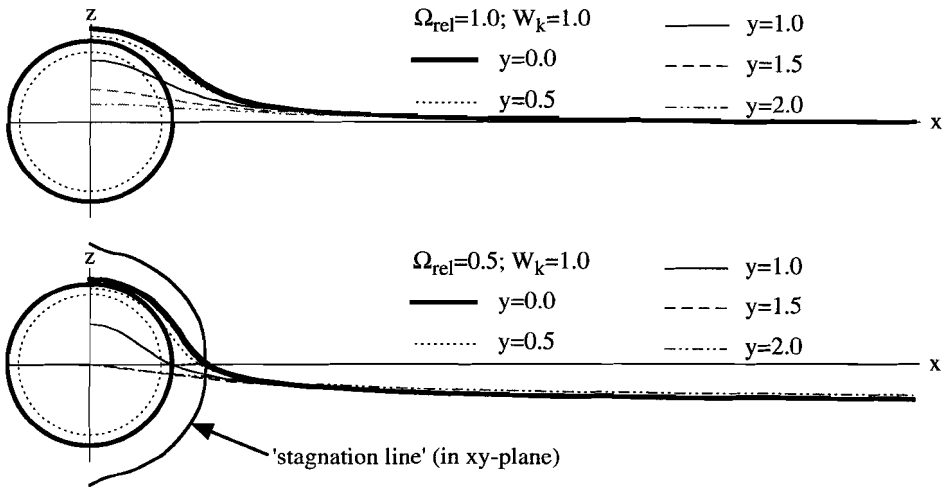

Figure 5A.1. xz-sections for values of y illustrating the positions of points that will eventually end in the 'stagnation line'. They represent (one quart) the 'separating plane' around a sphere of unit radius in three-dimensional bulk simple shear flow. Compare y=0 with figures 5.1a ('2D'-cylinder, Ω_{rel}=1.0 case) and 5.11a (id., Ω_{rel}=0.5), the central region with closed flow lines is contracted w.r.t. the '2D' cylinder case. The hypothetical 'stagnation line' for Ω_{rel}=1.0 reduces to a point located at: x=±∞, y=0, z=0. Note that 'stagnation line' for Ω_{rel}=0.5 is not in the same plane as the sections of the 'separating surface'.

Chapter 6

Conclusions and suggestions for further work

This thesis has studied the development of porphyroclast-mantle geometry during non-coaxial (simple shear) flow in rocks by means of analytical investigations and experiments. The purpose of the present final Chapter is to draw together general conclusions, based on the findings presented in the preceding Chapters. Moreover, questions which remain unanswered are addressed and suggestions are made for further research.

Provided that a deformable mantle exists at the periphery of a relatively rigid porphyroclast, the final geometry of a core-mantle-matrix system is a direct result of the flow pattern, or velocity distribution, in the immediate vicinity of the core. During deformation, the flow pattern is affected by the presence and behaviour of the clast, with respect to the situation where no clast is involved. In order to synthesise the results presented in this thesis into a set of coherent conclusions, conditions that have a primary effect on the flow pattern will be addressed first. Then, the association between flow pattern and clast rotation rate is dealt with. Subsequently, conclusions on the interaction of the mantle material and the flow pattern are considered.

6.1 Flow patterns in simple shear

In a shear zone deforming by homogeneous simple shear, material particles follow straight paths that are parallel to the direction of movement of the shear zone walls. The presence of a relatively rigid object causes strain rate variations within the shear zone matrix and the pattern of rectilinear lines will be disturbed. It has been shown in this thesis that under specific conditions, the velocity distribution around a free floating cylindrical object that is subjected to simple shear flow, can be completely described by a stream function. The relevant conditions are that the matrix material is Newtonian and deforms by slow Stokes flow, and that the boundaries of the modelled area are at infinite distance from the cylindrical object, located at the origin. The flow pattern around a free floating cylinder that results from the stream function theory has an eye-shaped geometry (Bretherton 1962). If the rotation rate of the cylinder is retarded with respect to the rotation rate of a free floating one, the velocity distribution described by the stream function has a bow-tie geometry (Robertson and Acrivos 1970).

Finite element modelling (FEM) was used to investigate non-Newtonian flow around semi-rigid objects and allowed for boundaries located at short distance from the embedded object. Using FEM, it was concluded that eye-shaped flow patterns result when the boundaries of the model are at infinite distance from the object. The eye-shaped flow pattern was found in both Newtonian matrix materials, and in matrix materials that have a power-law stress vs. strain rate behaviour. In contrast, bow-tie shaped flow patterns resulted when FEM was used to simulate flow imposed by relatively nearby rigid shear zone walls. An increase from 1 to 5 of the power-law exponent of the matrix caused only minor changes in both flow patterns.

In experiments performed using a linear fluid shear apparatus, the eye-shaped flow pattern was found in glycerol (Newtonian) only when the shear zone had a width of 20 times the diameter of the immersed cylinder. When the shear zone width was reduced to 10 times the diameter

of the cylinder or less, the flow pattern showed a bow-tie geometry. When a 0.5%wt pAA-solution (non-Newtonian, shear thinning) was used as matrix, the bow-tie flow pattern was found for shear zone widths up to 20 times the diameter of the cylinder. No wider shear zones have been experimentally modelled. The bow-tie flow pattern in glycerol was the result of nearby shear zone walls. In the pAA-solution, it was inferred to be also caused by the effect of the material properties of the fluid.

In ring shear experiments performed with crystalline materials for both matrix (octachloropropane: OCP) and clasts (camphor), the flow pattern around the camphor objects had a bow-tie shape. The circular shear zone in this experiment was approximately four times as wide as the diameter of the clasts. The deformation in the shear zone was strongly variable; it showed a range from approximately simple shear in the far-field to nearly rigid body rotation within the porphyroclast. The shear strain rate, and thus also the accumulated shear, in the circular shear zone was not linearly distributed over the shear zone. The shear strain rate in the immediate vicinity of the clasts was ~50% lower than the 'imposed shear strain rate'.

For distant boundaries, the theory describes the flow patterns that result from the finite element modelling (FEM) when the matrix material is Newtonian or has a power-law stress vs. strain rate behaviour. In a wide shear zone, the flow pattern in glycerol (Newtonian) observed in the fluid shear apparatus corresponds with the theory as well. For narrow shear zones, the flow pattern that results from FEM is equivalent to the flow pattern observed in experiments in the linear fluid shear apparatus when glycerol is used. Flow patterns observed in the pAA-solution in the fluid shear apparatus do not agree with either theory or FEM; this aberration is caused by the anisotropic behaviour of the fluid.

So drawing this together, the theory can be used to model flow patterns and mantle geometry development in both Newtonian and power-law materials, provided that shear zone walls are distant. Furthermore, the shear zone width relative to the diameter of the object has a profound influence on the flow pattern.

6.2 Effects on clast rotation rates

Theory predicts that 'free-floating' cylindrical objects, embedded in a Newtonian matrix that is subjected to simple shear, will rotate at an angular velocity (in rad s^{-1}) equivalent to half the shear strain rate (in s^{-1}). The results of the finite element modelling presented in this thesis showed that nearby shear zone walls caused the cylinder to rotate at a slightly (<1%) reduced rate when compared to the theory. In addition, power-law behaviour of the matrix had a minor effect on the rotation rate of a cylindrical object subjected to bulk simple shear. The largest reduction (3.5%) in the rotation rate of the cylinder was found in the model that simulated nearby rigid shear zone walls and a power-law matrix with a power law exponent of 5.

In fluid shear experiments carried out using glycerol (Newtonian), the rotational behaviour of an isolated object could be described by the equations for ellipsoidal particles given by Jeffery (1922) and Freeman (1985). For a cylinder with its rotational axis parallel to the vorticity vector of the flow, the rotation rate was linearly related to the shear strain rate. The rotation rate of a cube in glycerol was equivalent to that of a sphere and a rectangular prism showed the pulsating rotational behaviour of an ellipsoid with a 12.5% smaller aspect ratio. When a dilute (0.5%wt) pAA-solution (non-Newtonian, shear thinning) was used in the fluid

shear experiments, the rotation rate (relative to the theoretical rate in a Newtonian matrix) of a cylinder was primarily affected by the shear strain rate. Minor influence of changes in temperature and width of the shear zone were found. Shear strain rate and shear zone width had a negative effect, and temperature a positive effect, on the relative rotation rate. These effects were non-linear and presumably related to the development of anisotropy in the pAA matrix. A reduction in relative rotation rate of ~60% was detected for the highest shear strain rate that was experimentally modelled (~0.7 s^{-1}). The relative rotation rate of a rectangular prism was found to be a function of aspect ratio and orientation, even when the aspect ratio is 1 (cube). Minimum and maximum rotation rates were found to occur for different orientations of the object when compared to observations for a Newtonian matrix. In both glycerol and pAA-solution, objects with a large axial ratio (end member is a line) rotates to a semi-'steady state' orientation, i.e. the rotation rate approaches zero.

The rotation rates of the camphor clasts embedded in OCP in the ring shear experiments reported in this thesis were very low (~85% reduced) when compared to the theoretical values for elliptical objects in Newtonian fluids. The non-linear distribution of shear strain rate within the circular shear zone was shown to account for a ~50% reduction of the rotation rates of the clasts. Further reduction of the rotation rates could not be attributed to resisting forces, caused by either friction or a viscous interface layer, between the confining glass plates and the model materials. The observed pulsating rotation rate of the camphor clasts was consistent with the theory for elliptical objects; the highest rotation rates were found when the long axis of the clast was perpendicular to the flow plane and the lowest rotation rates were found when the long axis was parallel to the flow plane.

The rotation rates of embedded objects, observed in the finite element modelling and the linear fluid shear apparatus, agree with the theoretically derived equations for rotation rates of ellipsoidal particles given by Jeffery (1922) and Freeman (1985), provided that no anisotropy is present or developing in the shearing matrix. Anisotropy of the matrix causes a reduction of the rotation rates of the embedded object. Reduction of clast rotation rate in the ring shear apparatus is due to resisting forces between the glass plates and the model material.

6.3 Evolution of core-mantle geometries in simple shear

The velocity field obtained from the stream function has been used to model the development of passive mantles around rigid cylinders subjected to bulk simple shear. It was found that the most prominent factor determining the developing mantle geometry was the distribution of mantle material with respect to the surface that bounds the region near the core where flow is closed, i.e., where material can return eventually to its initial position. This distribution is directly determined by the shape and effective thickness of the mantle with respect to the rigid core at any time. Accordingly, it is related to the rate at which the core material is being transformed into mantle material. Secondly, significant differences in mantle geometry are to be expected from changes in the amount of accumulated shear strain; with increasing deformation, the mantle geometry can evolve from one type to another, e.g., from a θ- to a ϕ- to a σ- to a δ-type geometry. Furthermore, a low rotation rate of the core relative to the rotational component of the flow, may prevent the development of certain geometry-types of the mantle.

In the ring shear experiment, the camphor clasts started to shed material into the surrounding OCP matrix at the early stages of simple shear deformation. As a consequence of the combination of a bow-tie shaped flow pattern and the rotation of the clasts, the camphor objects developed a stair-stepping δ-type geometry. The wings of the δ-objects formed coils around the core. The wings gradually became thin and vague with progressive deformation since no material was added to the wings at later stages while they continued to stretch.

When the object rotation rate in a shear zone is lowered, the shear stresses on parts of the rim of the object will be raised. If the material at the outer bounds of the object is susceptible to degradation, this material can develop into wings with ongoing deformation. Provided that the central area with closed flow-lines is larger than the clasts, no wings will evolve that extend away from the core. This will normally be the case for spherical objects with little degradation at the rim. The material that is shed from the core cannot escape the central area with closed flow-lines and developing wings will wrap around the core. It can be argued that even for cylindrical objects with the axis of revolution in the direction of no deformation (as described here with simple shear), the flat ends of the cylinder will be exposed to shear stresses as the central part of the flow has to change from a (in 2-D) bow-tie, or eye-shaped flow pattern, to flow with straight flow lines in the third dimension (i.e. downwards in the fluid shear apparatus, the flow becomes an undisturbed simple shear flow).

Extending this argument, objects with protruding ends (as the corners of cubes, etc.) will be the most likely objects to develop wings, especially at certain orientations of the object. Since the objects rotate, the material that will eventually form into wings will be shed from the object in a pulsating way. Brick-shaped objects will always develop wings if the object is not rigid but able to form a softer rim. When the degradation of the object is slow, the wings may be very thin and thus difficult to detect. Objects with a larger aspect ratio are more likely to develop wings than spherical objects since rim-material at the 'ends' of these objects can follow particle paths away from the centre when the object reaches an orientation perpendicular to the direction of shear.

A bow-tie flow pattern leads to stair-stepping wings if the object produces material that can escape the central region of the flow. In a relatively narrow shear zone, the central region with closed flow has a smaller diameter than that in a wide shear zone. Therefore, a narrow shear zone will show more prominent stair-stepping than a wide shear zone. Thus, in a single shear zone, the larger clasts are more apt to show stair-stepping than the smaller clasts. Even when stair-stepping wings evolve around an object, they might not be recognised when the far-field back-flow regions are narrow, the wings are short, the stagnation points of the flow are relatively far away from the centre of the object, or if the plane of observation does not section the clast relatively close to the centre.

6.4 Implications for geology

The work reported in this thesis has demonstrated that in a matrix that is deformed by simple shear, (semi-) rigid objects can rotate. The rotation rate of the object depends on the rheological properties of the matrix material (Newtonian or non-Newtonian), the form of the object (sphere, cylinder, cube, etc.) and the orientation of this object. Objects with a large axial ratio will rotate to an orientation at which the rotation rate will be very low.

The present research has extended the basis for the interpretation of porphyroclast system geometries preserved in deformed rocks. The principal conclusions which are relevant to geology are:
(1) It is confirmed that δ-type porphyroclasts are very reliable sense of shear indicators since the geometry can only be formed when the core has rotated with respect to the surrounding matrix (Simpson and Schmid 1983, Passchier and Simpson 1986, Hanmer and Passchier 1991).
(2) σ-type clast geometries can be used as sense of shear indicators, provided that the wings extend far into the matrix and are thin near the associated core. σ-types with very short wings or wings that are thick at the core periphery can be the result of several flow geometries and even opposing sense of shear, they should not be individually used as a kinematic indicator.
(3) It is confirmed that the distance between the wing-tips divided by the diameter of the core gives an estimation of the minimum amount of shear strain accumulated in the immediate vicinity of σ- and δ-type porphyroclast systems (Van den Driessche and Brun 1987).
(4) Stair stepping of the wings of a δ-clast is diagnostic for a bow-tie flow pattern during deformation (Passchier *et al.* 1993, Passchier 1994, Passchier and Trouw 1996). The bow-tie flow pattern indicates either anisotropic behaviour of the matrix or a width of the shear zone that is less than approximately 20 times the diameter of the clast-core.
(5) Stair stepping of the wings of a δ-clast is not a gauge of rock rheology since a bow-tie flow pattern can develop in Newtonian, power-law, and anisotropic materials.
(6) The development of anisotropy in the deforming matrix has a large effect on the flow pattern around and the rotation rate of the core, and accordingly, on the geometry development of a deformable mantle. Strain estimations based on the amount of rotation of the clast, will be too low when the matrix was anisotropic during deformation.

Depending on the dominant deformation mechanism of the rock, it can flow in an either Newtonian or non-Newtonian manner. The deformation mechanism at work is dependent on the conditions during deformation such as temperature, confining pressure, shear stress, rate of shear, and the activity and chemistry of fluids. If enough factors concerning the materials involved can be measured (degradation rate of clast, relative shear zone width, etc.), it may be possible to develop a model that relates winged structures to the flow pattern in the matrix material. However, since for example an increase in temperature will probably result in a faster degradation of the clast, as well as changing the deformation mechanism of the matrix, I conclude that the interpretation of winged porphyroclast systems should be limited to the determination of sense of shear and to estimate a minimum strain accumulated by the adjacent matrix.

6.5 Suggestions for further work

While the present study has addressed a number of questions posed in the introduction, some have remained unanswered and several new ones have been raised. In the following, suggestions for further work are proposed.

(1) From the reported reduction in clast rotation rate when the matrix is anisotropic (Chapter 4), it follows that the theory on the kinematics of flow has to be expanded with a developing anisotropy in the matrix. Although orientation dependent material properties can be dealt with in mechanical models, it may be very difficult to incorporate developing anisotropy in a kinematic model since in such a model, the orientation dependent material properties are also time dependent.
(2) The two-dimensional simulation using finite element modelling (FEM) reported in Chapter 5 has shown that FEM is a powerful tool to model core-matrix systems. Since natural clasts show a variety of shapes and a natural shear zone extends in three dimensions, the FEM should be extended to non-cylindrical shapes of the core, and to three-dimensional systems. Conditions at the boundaries of the model were proven to have a significant effect on the flow pattern. In multi-particle systems, each particle will add 'local boundary conditions' to the system and the flow pattern is thus expected to change accordingly. FEM could be used to extend our knowledge of the kinematics of multi-particle systems, thus approaching natural systems more closely.
(3) The linear fluid shear apparatus was found to be a very user-friendly tool to simulate flow around rigid objects. A different light source would be an advantage to the set-up shown in this thesis. A strobe-light will increase the resolution of the flow patterns, because it allows for the use of photographic material. The anisotropy of the pAA-solution may prove to be very useful to model a natural rock matrix material in which anisotropy development is the rule rather than the exception. Research could be extended to different rheologies, including different anisotropies and the development thereof, by making use of other fluids. A good start on the rheology-effects is probably the use of other concentrations of pAA, or solutions made from pAA-molecules with a different range of molecular weights than the one used in this thesis.
(4) The results of FEM on multi-particle systems need to be verified by experiments with the fluid shear apparatus, for Newtonian as well as anisotropic matrix materials. The particles inserted in the fluid do not have to be of uniform size or shape. The flow pattern in multi-particle systems will be more difficult to trace, as each object creates a shadow in the plane of light. Furthermore, extension can be made to model deteriorating cores, by using lumps of solutions with high pAA-concentrations (~40%wt), or possibly other materials such as sugar-cubes, lumps of dough, chocolate-chips, and honey-drops. Coloured lumps of 40%wt pAA were tried in both glycerol and 0.5%wt pAA solution: they slowly dissolve and, when subjected to shear motion of the liquid, shed streaks of colour into the surrounding matrix. Finally, randomly shaped particles of distributed volume or mass that dissolve at individually different rates could be used in the linear fluid shear apparatus. This may approach deformation in a natural porphyroclast laden shear zone as closely as experimentally possible (see cover).
(5) When a ring shear apparatus is used in future experiments to investigate the kinematics of deformation, a reference frame should be inscribed on at least one, but preferably both glass plates. Such 'external' reference frames are very useful in the determination of particle displacements and were an inconvenient omission in the present work.

References

Bell, T. H. 1985. Deformation partitioning and porphyroblast rotation in metamorphic rocks: a radical reinterpretation. *J. Metamorphic Geol.* 3, 109-118.

Bell, T. H., Duncan, A. C., & Simmons, J. V. 1989. Deformation partitioning, shear zone development and the role of undeformable objects. *Tectonophysics.* 158, 163-171.

Bell, T. H., Forde, A., & Hayward, N. 1992a. Do smoothly curving, spiral-shaped inclusion trails signify porphyroblast rotation? *Geol.* 20, 59-62.

Bell, T. H., Forde, A., & Hayward, N. 1992b. Reply on comment on "Do smoothly curving, spiral-shaped inclusion trails signify porphyroblast rotation?". *Geol.* 20, 1055-1056.

Bell, T. H., & Hayward, N. 1991. Episodic metamorphic reactions during orogenesis: the control of deformation partitioning on reaction sites and reaction duration. *J. Metamorphic Geol.* 9, 619-640.

Bell, T. H., & Johnson, S. E. 1989. Porphyroblast inclusion trails: the key to orogenesis. *J. Metamorphic Geol.* 7, 279-310.

Bell, T. H., & Johnson, S. E. 1992. Shear sense: a new approach that resolves conflicts between criteria in metamorphic rocks. *J. Metamorphic Geol.* 10, 99-124.

Bell, T. H., Johnson, S. E., Davis, B., Forde, A., Hayward, N., & Wilkins, C. 1992c. Porphyroblast inclusion-trail orientation data: eppure non son girate! *J. Metamorphic Geol.* 10, 295-307.

Bell, T. H., Rubenach, M. J., & Fleming, P. D. 1986. Porphyroblast nucleation, growth and dissolution in regional metamorphic rocks as a function of deformation partitioning during foliation development. *J. metamorphic Geol.* 4, 37-67.

Bjørnerud, M. 1989. Mathemathical model for folding of layering near rigid objects in shear deformation. *J. Struct. Geol.* 11, (3), 245-254.

Bjørnerud, M. G., & Zhang, H. 1995. Flow mixing, object-matrix coherence, mantle growth and the development of porphyroclast tails. *J. Struct. Geol.* 17, (9), 1347-1350.

Bons, P. D. 1993. Experimental deformation of polyphase rock analogues. Geologica Ultraiectina, 110, (Publ. PhD. Thesis), Utrecht University, the Netherlands, 207 p.

Bons, P.D., Barr, T.D. & Ten Brink, C.E., in press (accepted May 1996). The development of δ–clasts in non-linear viscous materials: a numerical approach. Tectonophysics.

Bons, P. D. & Cox, S. J. D., 1994. Analogue experiments and numerical modelling on the relation between microgeometry and flow properties of polyphase materials. Mat. Sci. Eng., A175 (1-2): 237-246.

Bretherton, F. P. 1962. Slow viscous motion round a cylinder in a simple shear. *J. Fluid Mech.* 12, 591-613.

Carter, N., & Tseun, M. C. 1987. Flow properties of continental lithosphere. *Tectonophysics.* 136, 27-63.

Chiba, K., Song, K.-W., & Horikawa, A. 1986. Motion of a slender body in quiscent polymer solutions. *Rheol. Acta.* 25, 380-388.

Chwang, A. T., & Wu, T. Y.-T. 1975. Hydromechanics of low-Reynolds-number flow. Part 2. Singularity method for Stokes flow. *J. Fluid Mech.* 67, 787-815.

Cross, M. M. 1965. *J. Coll. Sci.* 20, 417-.

Derby, B. 1990. The dependence of grain size on stress during dynamic recrystallisation. *Acta Metall.* 39, 955-962.

Erskine, B. G., Heidelbach, F., & Wenk, H. R. 1993. Lattice preferred orientations and microstructures of deformed Cordilleran marbles: correlation of shear indicators and determination of strain paths. *J. Struct. Geol.* 15, 1189-1206.

Etchecopar, A., & Malavieille, J. 1987. Computer models of pressure shadows: a method for strain measurement and shear-sense determination. *J. Struct. Geol.* 9, (5/6), 667-677.

Ferguson, C. C. 1979. Rotations of elongate rigid particles in slow Non-Newtonian flows. *Tectonophysics.* 60, 247-262.

Freeman, B. 1985. The motion of rigid ellipsoidal particles in slow flows. *Tectonophysics.* 113, 163-183.

Gauthier, F., Goldsmith, H. L., & Mason, S. G. 1971. Particle motions in non-Newtonian media. I: Couette flow. *Rheol. Acta.* 10, 344-364.

Ghosh, S. K. 1975. Distortion of planar structures around rigid spherical bodies. *Tectonophysics.* 28, 185-208.

Ghosh, S. K., & Ramberg, H. 1976. Reorientation of inclusions by combination of pure shear and simple shear. *Tectonophysics.* 34, 1-70.

Gray, N. H., & Busa, M. D. 1994. The three-dimensional geometry of simulated porphyroblast inclusion trails: inert-marker, viscous-flow models. *J. Metam. Geol.* 12, 575-587.

Handin, J., Higgs, D. V. & O'Brien, J. K., 1960. Torsion of Yule marble under confining pressure. In: D.T. Griggs & J. Handin (editors), Rock Deformation. Geol. Soc. America Mem., 79: 245-274.

Hanmer, S., & Passchier, C. W. 1991. Shear-sense indicators: a review. *Geol. Surv. Can. paper.* 90, (17), 1-72.

Hirth, G., & Tullis, J. 1992. Dislocation creep regimes in quartz aggregates. *J. Struct. Geol.* 14, 145-159.

Hooper, R. J., & Hatcher, R. D. 1988. Mylonites from the Towaliga fault zone, central Georgia: products of heterogeneous non-coaxial deformation. *Tectonophysics.* 152, 1-17.

Ildefonse, B., & Mancktelow, N. S. 1993. Deformation around rigid particles: the influence of slip at the particle/matrix interface. *Tectonophysics.* 221, 345-359.

Ildefonse, B., Sokoutis, D., & Mancktelow, N. S. 1992. Mechanical interactions between rigid particles in a deforming ductile matrix. Analogue experiments in simple shear flow. *J. Struct. Geol.* 14, (10), 1253-1266.

Jeffery, G. B. 1922. The motion of ellipsoidal particles immersed in a viscous fluid. *Proc. Royal Soc. London.* A, (102), 161-179.

Jeffrey, D. J., & Sherwood, J. D. 1980. Streamline patterns and eddies in low-Reynolds-number flow. *J. Fluid Mech.* 96, 315-334.

Jessell, M. W. & Lister, G. S., 1991. Strain localization behaviour in experimental shear zones. PAGEOPH, 137 (4): 421-438.

Karato, S. I. 1984. Grain-size distribution and rheology of the upper mantle. *Tectonophysics.* 104, 155-176.

Kirby, S. H., & Kronenberg, A. K. 1987. Rheology of the lithosphere: Selected topics. *Reviews in Geophysics.* 25, (6), 1219-1244.

Knipe, R. J. 1989. Deformation mechanisms - recognition from natural tectonites. *J. Struct. Geol.* 11, 127-146.

Kohlstedt, D. L., Evans, B., & Mackwell, S. J. 1995. Strength of the lithosphere: Constraints imposed by laboratory experiments. *J. Geoph. Res.* 100, (B9), 17,587-17,602.

Kohlstedt, D. L., & Weathers 1980. Deformation induced microstructures, paleopiezometers, and differential stresses in deeply eroded fault zones. *J. Geoph. Res.* (B) 85, 6269-6285.

Lister, G. S., & Snoke, A. W. 1984. S-C mylonites. *J. Struct. Geol.* 6, 617-638.

Masuda, T., & Ando, S. 1988. Viscous flow around a rigid spherical body: a hydrodynamical approach. *Tectonophysics*. 148, 337-346.

Masuda, T., Mizuno, N., Kobayashi, M., Nam, T., & Otoh, S. 1995. Stress and strain estimates for Newtonian and non-Newtonian materials in a rotational shear zone. *J. Struct. Geol.* 17, (3), 451-454.

Masuda, T., & Mochizuki, S. 1989. Development of snowball structure: numerical simulation of inclusion trails during synkinematic porphyroblast growth in metamorphic rocks. *Tectonophysics*. 170, 141-150.

Means, W. D., Hobbs, B. E., Lister, G. S., & Williams, P. F. 1980. Vorticity and non-coaxiality in progressive deformations. *J. Struct. Geol.* 2, (3), 371-378.

Mena, B., Manero, O., & Leal, L. G. 1987. The influence of rheological properties on the slow flow past spheres. *J. Non-Newt. Fluid Mech.* 26, 247-275.

Mercier, J. C., Anderson, D. A., & Carter, N. L. 1977. Stress in the lithosphere: inferences from steady-state flow of rocks. *Pure Appl. Geophys.* 115, 119-226.

Michibayashi, K. 1993. Syntectonic development of a strain-independent steady-state grain size during mylonitization. *Tectonophysics*. 222, 151-164.

Mifflin, R. T., & Schowalter, W. R. 1986. A numerical technique for three-dimensional steady flows of fluids of the memory-integral type. *J. Non-Newt. Fluid Mech.* 21, 322-337.

Ottino, J. M. 1989. *The kinematics of Mixing, Stretching, Chaos and Transport.* Cambridge University Press, Cambridge. p.

Passchier, C. W. 1987a. Efficient use of the velocity gradients tensor in flow modelling. *Tectonophysics*. 136, 159-136.

Passchier, C. W. 1987b. Stable positions of rigid objects in non-coaxial flow - a study in vorticity analysis. *J. Struct. Geol.* 9, (5/6), 679-690.

Passchier, C. W. 1994. Mixing in flow perturbations: a model for development of mantled porphyroclasts in mylonites. *J. Struct. Geol.* 16, (5), 733-736.

Passchier, C. W., & Simpson, C. 1986. Porphyroclast systems as kinematic indicators. *J. Struct. Geol.* 8, 831-844.

Passchier, C. W., & Sokoutis, D. 1993. Experimental modelling of mantled porphyroclasts. *J. Struct. Geol.* 15, (7), 895-909.

Passchier, C. W., & Speck, P. J. H. R. 1994. The kinematic interpretation of obliquely-transected porphyroblasts: an example from the Trois Seigneurs Massif, France. *J. Struct Geol.* 16, 971-984.

Passchier, C. W., ten Brink, C. E., Bons, P. D., & Sokoutis, D. 1993. δ-objects as a gauge for stress-sensitivity of strain in mylonites. *Earth & Plan. Sci. Letters*. 120, 239-245.

Passchier, C. W., & Trouw, R. A. J. 1996. *Micro-tectonics.* Springer-Verlag, Berlin Heidelberg New York. 289 p.

Passchier, C. W., Trouw, R. A. J., Zwart, H. J., & Vissers, R. L. M. 1992. Porphyroblast rotation: eppur si muove? *J. Metam. Geol.* 10, 283-294.

Poirier, J.-P. 1991. *Introduction to the Physics of the Earth's Interior.* Cambridge University Press, Cambridge. 264 p.

Ramsay, J. G., & Graham, R. H. 1970. Strain variation in shear belts. *Can. J. Earth Scie.* 7, 786-813.

Reiner, M., & Scott Blair, G. M. 1967. Chapter 9. In: *Rheology: Theory and Applications* (edited by F. R. Eirich).4, 461-488.

Robertson, C. R., & Acrivos, A. 1970. Low Reynolds number shear flow past a rotating circular cylinder. Part 1. Momentum transfer. *J. Fluid Mech.* 40, 685-704.

Rosenfeld, J. L. 1970. Rotated garnets in metamorphic rocks. *Geol. Soc. Am. Spec. Pap.* 129, 102.

Ross, J. V., Lallement, H. G., & Carter, N. L. 1980. Stress-dependence of recrystallized-grain and subgrain size in olivine. *Tectonophisics.* 70, 39-61.

Schmid, S. M. 1982. Microfabric studies as indicators of deformation mechanisms and flow laws operative in mountain building. In: *Mountain building processes* (edited by K. J. Hsü).95-110.

Schmid, S. M., Paterson, M. S., & Boland, J. N. 1980. High temperature flow and dynamic recrystallization in Carrara Marble. *Tectonophysics.* 65, 245-280.

Schoneveld, C. 1977. A study of some typical inclusion patterns in strongly paracrystalline-rotated garnets. *Tectonophysics.* 39, 453-471.

Simpson, C., & Schmid, S. M. 1983. An evaluation of criteria to deduce the sense of movement in sheared rocks. *Geol. Soc. Am. Bull.* 94, 1281-1288.

Truesdell, C. 1953. Two measures of vorticity. *J. Rotational Mech. Anal.* 2, 173-217.

Tullis, J., & Yund, R. A. 1985. Dynamic recrystallisation of feldspar: a mechanism for ductile shear zone formation. *Geology.* 13, 238-241.

Tullis, J., & Yund, R. A. 1987. Transition from cataclastic flow to dislocation creep of feldspar: mechanisms and microstructures. *Geol.* 15, 606-609.

Twiss, R. J. 1986. Variable sensitivity piezometric equations for dislocation density and subgrain diameter and their relevance to olivine and quartz. In: *Mineral and rock deformation: laboratory studies, the Paterson volume* (edited by H. C. Heard, & B. E. Hobbs). Geophysical Monographs 36, 247-261.

Urai, J. L., Williams, P. F., & van Roermond, H. L. M. 1991. Kinematics of crystal growth in syntectonic fibrous veins. *J. Struct. Geol.* 13, 823-836.

Van Den Driessche, J., & Brun, J.-P. 1987. Rolling structures at large shear strain. *J. Struc. Geol.* 9, (5/6), 691-704.

Vissers, R. L. M., Drury, M. R., Hoogerduyn Strating, E. H., & Van Der Wal, D. 1991. Shear zones in the upper mantle-a case study in an Alpine lherzolite massif. *Geology.* 19, 990-993.

Wallis, S. 1992. Comment on "Do smoothly curving, spiral-shaped inclusion trails signify porphyroblast rotation?". *Geol.* 20, 1054-1055.

Wenk, H. R., Takeshita, T., Bechler, E., Erskine, B. G., & Matthies, S. 1987. Pure shear and simple shear calcite textures. Comparison of experimental, theoretical and natural data. *J. Struct. Geol.* 9, 731-746.

White, S. H. 1979. Grain and sub-grain size variations across a mylonite. *Contr. Mineral. Petrol.* 70, 193-202.

Yoon, C. K., & Chen, I. W. 1990. Superplastic flow of two-phase ceramics containing rigid inclusions-zirconia/mullite composites. *J. Am. Ceram. Soc.* 73, (6), 1555-1565.

Dankbetuiging

(Acknowledgements)

Aan de ene kant zijn veel problemen het resultaat van de interactie tussen personen. Aan de andere kant kan menig obstakel niet overwonnen worden zonder de hulp van anderen. Een promotie is een horde die beter niet individueel genomen kan worden. Ik was gelukkig omgeven door vele experts in hun eigen gebied: van academici tot zotten.

Tonny en Huib zijn degenen die de basis van mijn karakter kneedden door niet toe te geven aan de gevestigde orde. Daarmee werd tevens het fundament van mijn onderzoekende geest gelegd. Gelukkig zag Teun Abbenhuis mijn houding niet als opstandig, maar als een uitdaging.

Cees Passchier liet mij enkele wonderen van de strukturele geologie zien en door hem werd mijn interesse naar "de klonten in de pap" gewekt. Als begeleider tijdens mijn onderzoek moet hij dat menigmaal betreurd hebben daar ik waarschijnlijk moeilijker te modelleren was dan het gesteente in kwestie. Vanaf het begin van het project had Chris Spiers zo zijn bedenkingen en al discussiërend zijn veel onderwerpen een stuk duidelijker geworden. In Paul Bons had ik een goede medespeler in het bedenken van argumenten en ideeën, die dan weer uitvoerig ter sprake kwamen met Timon, Siese, Rian, Rob, Patrick, Armelle, Marga, Andor, Rachel, Arjen, Tanja, Colin, Martyn, Kabir en Bernard tijdens koffie, borrel en barbeque. Technische ondersteuning kreeg ik van Gert Kastelijn, Colin Peach en Peter van Krieken. Fred Trappenburg, Fred Quint, Brigit Benders en Paul van Oudenallen hielpen met de visuele aspecten. Jan de Groot en Inge Nussgen maakten mooie slijpplaten en lieten mij zien hoe je stenen kan polijsten. De inwendige mens werd altijd vrolijk verzorgd door Margret en Berna. Onuitputtelijk was de alles omvattende helpende hand van Magda Martens.

Het ringshear apparaat werd gemaakt door Gert Kastelijn en Janos Urai, het is afgeleid van een oorspronkelijk idee van Mark Jessell en werd gefinancïeerd door NWO. De OCP werd gesynthetiseerd door Peter van Krieken.

Mr. René Hund de SNF Floerger, Saint-Étienne, France, m'a envoyé l'échantillon de pAA (flocculant AP 30 E). Dr. Ir. G. Peters en Ir. J. Baaiens van de TU-Eindhoven stelden hun apparatuur beschikbaar; Jeroen Schouten en Joris van Dam hielpen met de rheometrische bepalingen van glycerol en de pAA-oplossing. Het lineaire vloeistof shear apparaat kwam tot stand in nauwe samenwerking met Gert Kastelijn, die mijn oorspronkelijke ontwerp enorm wist te vereenvoudigen. De laser werd beschikbaar gesteld door Cees Passchier.

The analytical mantle geometry development would not have been possible without making use of routines written by Mark Jessell and Paul Bons. Terence Barr and Paul Bons were so kind to help confirm my ideas about shear zone walls with the finite element method.

Zonder Janos Urai, die het oorspronkelijke idee van het project had, was ik er niet aan begonnen. Zonder Cees Passchier was ik er wellicht niet mee door gegaan. Zonder Chris Spiers had ik het waarschijnlijk niet "op tijd" afgekregen in de vorm die het nu heeft.

Cees van den Ende heeft me getoont hoe leuk het kan zijn om excursies en veldwerk te begeleiden, zelfs, of juist, als je probeert te vertellen dat geologie meestal niet eenduidig is en dat daardoor theorieën met de tijd evolueren. Helemaal leuk werd het in het veld wanneer Hugo de Boorder, Gert-Jan Weltje of Poppe de Boer met nog meer stukjes van de puzzel aan kwamen. Niemand heeft mij tot nu toe kunnen uitleggen op welke manier een grootschalige homogene verkorting het ruimtegebrek oplost, maar dat kan nog komen.

Marga, Camilla, Mirjam, Siese, Joop en Marjelle, Timon en Ange en, niet te vergeten, Kees en Jifke, wisten de soms diepe dalen waarin ik de afgelopen jaren meermaals zat, op te vullen of zelfs om te buigen naar hoogtepunten. Geduld, vertrouwen en liefde kreeg ik van Elzelien. Bij partijen komt iedereen, maar zonder hen wordt het geen echt feest. En als je dan iets te vieren hebt kan Martijn goed bier tappen.

Natuurlijk ben ik iemand vergeten. Degene die niet genoemd is moet zich troosten met de gedachte dat hij of zij daarin niet alleen staat. Bij deze bedank ik jullie allemaal voor jullie steun en toewijding. I thank you all for your dedication and support.

I betell a friendly atmosphere revolving around seven
Oh that number mystified my soul and captured within feelings
Those of doubt and understanding hand in hand they set me reeling

Met me a stranger he came here to town
Bearing gifts full of promises, discoveries of light
Sold me many reasons why my merry tale
Could be justified and just both together entwined
I tell you a reason, he said "Bless you, you fool, you fool"
You want "so belief" yet you want so much more "you seeker"
Now I see you're baffled yet again you administer fear
Of the unexpected, you don't know the score
Everywhere you look you release parts of your senses
and everywhere there's purpose in answer to all your dreams
I can hear you saying what a dreamer what a fool to life
Isn't it a pity that he won't come back to earth

Haven't you imagination and is it not available
How you can be sooner or later than your thinking
Haven't you imagination and is it so impossible
That you ask of everything so your eyes can see clearly

(Jon Anderson-Song of Seven)

Curriculum Vitea

24-09-1961	Geboren te Amsterdam
1981-1983	VWO, Eindhovens Avond College, Eindhoven
30-09-1989	Doctoraal examen Geologie, Universiteit Utrecht, Hoofdvak Structurele geologie, bijvak Sedimentologie
1989-1996	Assistent in Opleiding, vakgroep Geologie, Universiteit Utrecht